SANDIA REPORT
SAND2001-8111
Unlimited Release
Printed December 2000

From Atom-Picoseconds to Centimeter-Years in Simulation and Experiment

M. F. Horstemeyer, J. C. Hamilton, A. Thompson, M. I. Baskes, S. J. Plimpton, I. Daruka, M. R. Sorenson, A. F. Voter, D. M. Ford, P. S. Rallabandi, G. Tunca

Prepared by
Sandia National Laboratories
Albuquerque, New Mexico 87185 and Livermore, California 94550

Sandia is a multiprogram laboratory operated by Sandia Corporation, a Lockheed Martin Company, for the United States Department of Energy under Contract DE-AC04-94AL85000.

Sandia National Laboratories

Issued by Sandia National Laboratories, operated for the United States Department of Energy by Sandia Corporation.

Available to DOE and DOE contractors from
U.S. Department of Energy
Office of Scientific and Technical Information
P.O. Box 62
Oak Ridge, TN 37831

Telephone: (865)576-8401
Facsimile: (865)576-5728
E-Mail: reports@adonis.osti.gov
Online ordering: http://www.doe.gov/bridge

Available to the public from
U.S. Department of Commerce
National Technical Information Service
5285 Port Royal Rd
Springfield, VA 22161

Telephone: (800)553-6847
Facsimile: (703)605-6900
E-Mail: orders@ntis.fedworld.gov
Online order: http://www.ntis.gov/ordering.htm

SAND2001-8111
Unlimited Release
Printed December 2000

From Atom-Picoseconds to Centimeter-Years in Simulation and Experiment

M.F. Horstemeyer, J.C. Hamilton, I. Daruka
Center for Materials and Engineering Sciences
Sandia National Laboratories
Livermore, CA 94551

A.P. Thompson, S.J. Plimpton
Computation, Computers and Math Center
Sandia National Laboratories
Albuquerque, NM 87185

D.M. Ford, P.S. Rallabandi, C. Tunca
Department of Chemical Engineering
Texas A&M University
College Station, TX 77843

M.I. Baskes, A.F. Voter, M. Sorensen
Theoretical Division
Los Alamos National Laboratory
Los Alamos, NM 87545

Abstract

The final report for a Laboratory Directed Research and Development project entitled, *From Atom-Picoseconds to Centimeter-Years in Simulation and Experiment* is presented. In this project, separate modeling methods at the atomic scale were used to bridge gaps in time and space with higher scales. For understanding of continuum mechanics quantities at various scales atomistic simulations that ranged from nanometers to microns were performed and experiments from centimeters to millimeters were performed. Certain continuum mechanical quantities were clearly defined as a function of size scale, for example, the yield stress. Several techniques were used to extend the time scale of simulations, including calculating prefactors and activation energies for diffusion events and mapping complex atomic motions onto more tractable lattice models. In the case of transport of small molecules in polymeric and nanoporous materials, new Monte Carlo methods for sampling transition rates were developed.

Contents

1. Introduction 14

2. Size Scale and Time Scale Effects on Plastic Flow of FCC Metals (by M. F. Horstemeyer, M. I. Baskes, and S. J. Plimpton) 15

2.1 Atomistic Background 15
2.2 Computational Set-up 17
2.3 Design of Experiments Study 19
2.4 Crystal Orientation Effects 22
2.5 Strain Rate (Time Scale) Effects 28
2.6 Size Scale Effects 31
2.7 Comparison of EAM and FEM Analyses 36
2.8 Summary 52

3. Atomistic Calculations of Diffusion Rates: Compact Surface Cluster Diffusion by Concerted Rotation and Translation (by J. C. Hamilton, M. R. Sorensen and A. F. Voter) 126

4. Multiscale Modeling of Grain Boundary Roughening: A First Order Phase Transition by Atomic Shuffle (by J.C. Hamilton and I. Daruka) 137

5. Single Particle Activated Transport in Amorphous Materials (by P. S. Rallabandi, D. M. Ford and A. P. Thompson) 145

5.1 Determination of Cavities and Transition States in 3-D Space. 146
5.1.1 Cavity Analysis Code 146
5.1.2 Clustering and Percolation Analysis 149
5.1.3 Kinetic Monte Carlo Simulation of Diffusion 151
5.1.4 Results 153

5.2 Determination of Multidimensional Transition States in Flexible Polymers 156
5.2.1 Introduction 156
5.2.2. Transition-state theory 160
5.2.3. Model and potential details 162
5.2.4. Details of Calculation 164
5.2.4.1 Geometric analysis of polymer structures 164
5.2.4.2 Methods for location of transition states and minima 164
5.2.4.3 Implementation of rate calculations 166
5.2.5 Results 169
5.2.6 Discussion 172

6. Multi-Particle Activated Transport of Small Molecules in Ordered Nanoporous Materials (by C. Tunca and D. M. Ford) 197

6.1 Introduction 200
6.2 Theory 201
6.2.1 Background 201
6.2.2 Low-dimensional (LD) approximation 202
6.2.3 Expanded ensemble methods (EEMs) 204
6.3 MODEL SYSTEMS 206
6.3.1 Zeolite and adsorbate models 206
6.3.2 Potentials 206
6.3.3 Evaluation of integrals 207
6.4 Results and discussion 209
6.5 Conclusions 211

7. Achievements 218

Appendix A. Publications Resulting from this LDRD 219

Distribution 220

Figures

Fig. 2.1 Schematic of strain rate and spatial size scale effects on computing and the regions where local and non-local continuum theories are applicable. 53

Fig. 2.2 Schematic of simulation block of atoms at (a) initial state and (b) at large strain in which the clear circles represent the active atoms and the dark circles represent the boundary atoms. 54

Fig. 2.3 Shear stress-strain curve of material blocks at an applied strain rate of $2.4 \times 10^8 s^{-1}$ with (a) ten thousand atoms and (b) ten million atoms showing micro-yield 1 at the proportional limit, micro-yield 2 at 0.2% offset strain, and macro-yield. 55

Fig. 2.4 Shear stress-strain curve for 2242 atoms of nickel illustrating atomic positions and relative displacements (denoted by arrows on atoms) at different strain levels. 56

Fig. 2.5 Stress-strain curves of eight DOE simulations for single crystal nickel. 57

Fig. 2.6 Shear stress-strain response of DOE #8 and correlating shear stress states at (a) yield, (b) 30% shear strain, and (c) unloaded state just beyond yield. The lines show relative displacement of atomic motion. 58

Fig. 2.7 Shear stress-strain curve with plots of centrosymmetry parameter at different strain levels. 59

Fig. 2.8 Normalized DOE (a) yield and (b) plastic energy responses as a function of parameter influence. 60

Fig. 2.9 Different initial orientations in simple shear straining. 61

Fig. 2.10 Stress-strain responses for different initial orientations and pseudopolycrystal under simple shear. 62

Fig. 2.11 Stress-strain responses for different initial orientations under tension. 63

Fig. 2.12 Resolved shear stress-strain curves for different initial orientations that have been modified by a Schmid factor. 64

Fig. 2.13 Contour plots of shear stress at yield and 30% effective strain for the block of atoms initially oriented for single slip under simple shear straining (The dark color is the highest value, and the light color is the lowest). 65

Fig. 2.14 Contour plots of shear stress at yield and 30% effective strain for the block of atoms initially oriented for double slip under simple shear straining (The dark color is the highest value, and the light color is the lowest). 66

Fig. 2.15 Contour plots of shear stress at yield and 30% effective strain for the block of atoms initially oriented for quadruple slip under simple shear straining (The dark color is the highest value, and the light color is the lowest). 67

Fig. 2.16 Contour plots of shear stress at yield and 30% effective strain for the block of atoms initially oriented for octal slip under simple shear straining (The dark color is the highest value, and the light color is the lowest). 68

Fig. 2.17 Distributions of shear stress at yield for (a) single slip, (b) double slip, (c) quadruple slip, and (d) octal slip. 69

Fig. 2.18 Same plot as Fig. 11 with peak atom count at 150 to compare different initial orientations at yield. 70

Fig. 2.19 Distributions of shear stress at 30 effective strain for (a) single slip, (b) double slip, (c) quadruple slip, and (d) octal slip under simple shear. 71

Fig. 2.20 Same plot as Fig. 13 with peak atom count at 150 to compare different initial orientation at 30% effective strain. 72

Fig. 2.21 Comparison of histogram and Gaussian distribution for double slip orientation at 30% effective strain. 73

Fig. 2.22 Comparison of mean, standard deviation, and skewness as a function of effective strain for Gaussian distributions with and without the zero stress atoms included. 74

Fig. 2.23 Shear stress-shear strain curves of material block with 196 atoms (length is 2.8 nm and height is 1.4 nm) at strain rates from $1.5x10^7$/sec to $1.23x10^{11}$ s^{-1} illustrating the increase in yield as a function of strain rate. 75

Fig. 2.24 Shear stress-shear strain curves of material block with 1384 atoms (length is 7.8 nm and height is 4.0 nm) at strain rates from $1.5x10^7$ to $1.23x10^{11}$ s^{-1} illustrating the increase in yield as a function of strain rate. 76

Fig. 2.25 Shear stress-shear strain curves of material block with $2x10^4$ atoms (length is 0.0282 _m and height is 0.014 _m) at strain rates from $1.5x10^{7}$ to $1.23x10^{11}$ s^{-1} illustrating the increase in yield as a function of strain rate. 77

Fig. 2.26 Shear stress-shear strain curves of material block with $1x10^5$ atoms (length is 0.057 _m and height is 0.021 _m) at strain rates from $2.4x10^{8}$ to $1.23x10^{11}$ s^{-1} illustrating the increase in yield as a function of strain rate. 78

Fig. 2.27 Shear stress-shear strain curves of material block with $1x10^6$ atoms (length is 0.18 _m and height is 0.07 _m) at strain rates from $2.4e^{8}$ to $5.26x10^{10}$ s^{-1} illustrating the increase in yield as a function of strain rate. 79

Fig. 2.28 Shear stress-shear strain curves of material block with $1x10^7$ atoms (length is 0.55 _m and height is 0.21 _m) at strain rates from $2.4x10^{8}$ to $1.53x10^{10}$ s^{-1} illustrating the increase in yield as a function of strain rate. 80

Fig. 2.29 Shear stress-shear strain curves of material block with $1x10^8$ atoms (length is 1.7 _m and height is 0.7 _m) at a strain rate of $1.53x10^{10}$ s^{-1}. 81

Fig. 2.30 Yield stress normalized by the shear modulus as a function of strain rate comparing atomistic simulations (dots) and dislocation model (solid line). Various curves represent different model sizes. 82

Fig. 2.31 Experimental data examining yield stress versus applied strain rate from Follansbee (1988) and Edington (1969) for copper. 83

Fig. 2.32 Shear stress-strain curves of various size atomistic models at an applied strain rate of $2.4x10^8$ s^{-1} for (a) 196 atoms, 1384 atoms, and $2x10^4$ atoms and (b) 10^5 atoms, 10^6 atoms, and 10^7 atoms. 84

Fig. 2.33 Shear stress-strain curve of two atomistic models showing the differences in yield and work hardening for single crystal copper at a strain rate of 10^9 s^{-1}. 85

Fig. 2.34 Plateau yield stress normalized by the shear modulus as a function of the size (x-dimension) of the atomistic model. The equation for the power law behavior is shown. 86

Fig. 2.35 Yield stress normalized by the elastic modulus and resolved on a (111) slip plane versus volume/surface area for nickel, gold, and copper for various experiments and atomistic simulations. The equation for power law behavior is shown. 87

Fig. 2.36 Schematic showing the stress-strain responses at four different size scales. 88

Fig. 2.37 Shear stress contour plots at (a) yield-zoom, (b) yield, and (c) 30% strain, illustrating the deformation response for a 64 x 8 unit cell (225 Å by 28 Å) simulation (yellow are low shear stresses and brown are high shear stresses; arrows denote relative displacements of atoms). 89

Fig. 2.38 Average stress-strain response of a 64 x 8 unit cell (225 Å by 28 Å) simulation with the centrosymmetry parameter illustrating the dislocation nucleation, motion, and interaction throughout deformation. 90

Fig. 2.39 Shear stress contours for a one unit cell by one unit cell block at yield for (a) macroscale internal state variable theory (S12), (b) crystal plasticity (S12), and (c) atomistics (yellow are low shear stresses and brown are high shear stresses; arrows denote relative displacements). 91

Fig. 2.40 Shear strain contours for a one unit cell by one unit cell block at yield for (a) macroscale internal state variable theory (E12), (b) crystal plasticity (E12), and (c) atomistics (yellow are low shear strains and brown are high shear strains; arrows denote relative displacements). 92

Fig. 2.41 Shear stress contours for an eight unit cell by one unit cell block at yield for (a) macroscale internal state variable theory (S12), (b) crystal plasticity (S12), and (c) atomistics (yellow are low shear stresses and brown are high shear stresses). ... 93

Fig. 2.42 Shear strain contours for an eight unit cell by one unit cell block at yield for (a) macroscale internal state variable theory (E12), (b) crystal plasticity (E12), and (c) atomistics (yellow are low shear strains and brown are high shear strains). Orientation angle (SDV37) from the crystal plasticity simulation is given in (d). 94

Fig. 2.43 Shear stress contours for a one unit cell by one unit cell block at 30% strain for (a) macroscale internal state variable theory (S12), (b) crystal plasticity (S12), and (c) atomistics (yellow are low shear stresses and brown are high shear stresses; arrows denote relative displacements of atoms). 95

Fig. 2.44 Shear strain contours for a one unit cell by one unit cell block at 30% strain for (a) macroscale internal state variable theory (E12), (b) crystal plasticity (E12), and (c) atomistics (yellow are low shear strains and brown are high shear strains; arrows denote relative displacements of atoms). 96

Fig. 2.45 Shear stress contours for an eight unit cell by one unit cell block at 30% strain for (a) macroscale internal state variable theory (S12), (b) crystal plasticity (S12), and (c) atomistics (yellow are low shear stresses and brown are high shear stresses. 97

Fig. 2.46 Shear strain contours for an eight unit cell by one unit cell block at 30% strain for (a) macroscale internal state variable theory (E12), (b) crystal plasticity (E12) and (c) atomistics (yellow are low shear strains and brown are high shear strains; arrows denote relative displacements of atoms). Crystal orientations (SDV37) are shown from the crystal plasticity simulation in (d). 98

Fig. 2.47 Average yield stress for a block of material of varying aspect ratios computed with different modeling methods: a) constant y, varying x; b) constant x, varying y. 99

Fig. 2.48 Stress distribution normalized by highest local stress from macroscale ISV model finite element analysis for different x/y aspect ratios under simple shear. 100

Fig. 2.49 Shear stress contours (S12) of (a) 1x1 and (b) 8x1 blocks after 30% shear strain. Both blocks show similar distribution of stresses in corners despite different aspect ratios. 101

Fig. 2.50 Shear stress contour plots at (a) yield and (b) 30% strain, illustrating the deformation response for a 4 x 16 unit cell (14 Å by 56 Å) simulation (yellow are low shear stresses and brown are high shear stresses; arrows denote relative displacements of atoms). 102

Fig. 2.51 Comparison of orientation angle distribution at 30% strain from the (a) 1 x 1 and (b) 8 x 1 x/y aspect ratios from the crystal plasticity calculations. 103

Fig. 2.52 Color contours of (a) shear stress and (b) crystal orientation illustrating dependence of stress state on lattice orientation. 104

Fig. 2.53 Relative frequency of local shear stress over the global average stress at yield for a x/y aspect ratio of two for the internal state variable theory, crystal plasticity theory, and three different block sizes of atomistic simulations. 105

Fig. 2.54 Relative frequency of local shear stress over the global average stress at yield for a x/y aspect ratio of two for an atomistic simulation at 10 K and 300 K for 372 atoms of nickel. 106

Fig. 2.55 Pictures of two single Cu crystal torsional specimens. 107

Fig. 2.56 Schematic of MTS multiaxial test system. 108

Fig. 2.57 Torque-rotation curves for two different single crystal Cu specimens that had an axial orientation in the [110] direction. 109

Fig. 2.58. Close-up view of specimens at 35% shear strain illustrating wavy pattern on outside of bar. 110

Fig. 2.59 Plot of atoms showing relative displacements from original positions for (a) small specimen and (b) large specimen under simple shear. 111

Fig. 2.60 Plot of atoms showing relative displacements from original positions for (a) small specimen and (b) large specimen under torsion. 112

Fig. 2.61 Stress-strain responses of small block and large block of atoms simple shear. .113

Fig. 2.62 Finite element simulation of torsion single crystal Cu showing (a) one Euler angle and (b) the correlating displacements to illustrate the oscillating pattern in simple shear. 264

Fig. 2.63 Finite element simulation of torsion single crystal Cu showing (a) one Euler angle and (b) the correlating displacements to illustrate the oscillating pattern in torsion. 115

Fig. 2.64 Yield stress normalized by elastic shear modulus as a function of volume-per-surface-area for copper and nickel (EAM simulations and experiments). 116

Fig. 3.1 Relative energy per atom as a function of position for a single Ir atom on Ir(111) (left plot) and for a pseudomorphic Ir monolayer on Ir(111) (right plot). This figure illustrates the dramatic difference between diffusing a single Ir atom on Ir(111) and shearing an Ir monolayer across Ir(111). For example, the top site is unstable for an adatom and metastable for the monolayer. Contour intervals are 100 meV/atom in both plots. The gray scale is choosen to emphasize the portions of the energy surface most likely to be visited during diffusion. Plots are Fourier fits to computed data. 133

Fig. 3.2 Cluster glide mechanisms discussed in this paper. Bridge-glide and top-glide involve nearly simultaneous translation of all cluster atoms over the bridge and on-top sites respectively. Top-glide was considered as one possible mechanism for long jumps. Cartwheel-glide involves a simultaneous translation of the center atom over the on-top site while the cluster rotates by 60°. Cartwheel-shuffle involves translation of the center atom to the on-top site while the cluster rotates by ~15° to form a metastable state. The cluster then translates to another hollow site while rotating back by ~15°. 134

Fig. 3.3 Calculated energy as a function of translation and rotation during cartwheel-shuffle shown in figure 3.2. Note that the curve is very flat near the maxima (transition states), and steep near the fcc and hcp minima. 135

Fig. 4.1. Elementary excitation along the grain boundary facet junction. (A) The arrows show the atomic displacements associated with the elementary excitation. The atoms also move perpendicular to the plane of the figure because of the 0.7Å offset in the (111) planes between the upper and lower grain. The blue rhombus represents the base of the coincidence site lattice (CSL) primitive cell. (B) The elementary excitation transforms one CSL primitive cell at the grain boundary junction from the lower grain to the upper grain. (C) Schematic view of the elementary excitation that introduces two extra lengths of facet junctions and two extra areas of (111) twin boundary. The corresponding height matrix **h** is also shown. 142

Fig. 4.2. Morphology of the grain boundary obtained by Monte Carlo simulations. We used N_x=80, N_y=48, and α=1 in this calculation. (A) At lower temperatures the grain boundary is faceted as shown here at k_BT/E_{junc}=1.55. (B) Above the de-faceting phase transition temperature a highly disordered structure forms as shown here at k_BT/E_{junc}=1.68. The inset illustrates the normalized average mean-square deviation of the height profile (defined in text). The abrupt change in grain boundary width at $t=k_BT/E_{junc} \approx 1.6$ is characteristic of the de-faceting phase transition. 143

Fig. 5.1 Residence time versus reduced inverse temperature for a single Lennard-Jones particle moving within a fixed cubic array of identical particles. The figure compares the results of the full 3-D transition state theory calculation (circles) with the harmonic approximation (squares and line). The full TST calculation mapped a periodic cell containing 8 atoms and 8 cavities using a grid spacing of 0.03125*a*, or 2 million points. 177

Fig. 5.2 Plot of the calculated diffusion coefficient of nitrogen in zeolite 3A versus the number of grid-points used. The calculation used a 24.6Å x 24.6Å x 24.6Å sample containing 8 unit cells and 8 macrocavities. 178

Fig. 5.3 Visualization of the dividing surfaces obtained using cavity analysis for oxygen in a 60 Å x 60 Å x 60 Å sample of EPDM, assuming no polymer motion. Dividing surfaces are drawn as cylinders joining the centers of adjacent cavities. The radius of each cylinder is scaled proportionally with the logarithm of the configurational integral for the dividing surface, and so gives a measure of the jump rate for that dividing surface. The cavities themselves are not drawn explicitly. The dividing surfaces do not form a percolated network. 179

Fig. 5.4 Plot of mean square displacement versus time for $-CH_2-$ groups in EPDM, obtained from a molecular dynamics simulation. 180

Fig. 5.5 Visualization of the dividing surfaces obtained using cavity analysis for oxygen in a 60 Å x 60 Å x 60 Å sample of EPDM. The polymer motion was represented using the isotropic elastic approximation, with $\langle \_\_^2 \rangle^{1/2}$ = 1.2 Å. Dividing surfaces

are drawn as cylinders joining the centers of adjacent cavities. The radius of each cylinder is scaled proportionally with the logarithm of the configurational integral for the dividing surface, and so gives a measure of the jump rate for that dividing surface. The cavities themselves are not drawn explicitly. The dividing surfaces form a strongly percolated network. 181

Fig. 5.6 Plot of mean square displacement of oxygen molecules in EPDM versus time obtained by kinetic Monte Carlo simulation. The three curves are for $\langle \_\_^2 \rangle^{1/2}$ = 0.6 Å, 0.9 Å and 1.2 Å, going from bottom to top. The thick dashed line serves only to illustrate the expected asymptotic linear behavior. 182

Fig. 5.7 Plot of oxygen diffusion coefficient in EPDM versus RMS polymer displacement. The diamonds are from the kinetic Monte Carlo simulations. The star is from molecular dynamics. The straight line is a power law fit to the kinetic Monte Carlo data. 183

Fig. 5.8 Chemical structure of atactic polypropylene. The bond lengths and angles were constrained, during all calculations, at the values shown here. Energy barriers (a) and entropy barriers (b) during oxygen hopping in the rigid polymer models. *d* is the distance from the location of the transition state to the associated energy minimum. 184

Fig. 5.9 Energy barriers (a) and entropy barriers (b) during oxygen hopping in the rigid polymer models. *d* is the distance from the location of the transition state to the associated energy minimum. 185

Fig. 5.10 Comparison of energy barriers (a) and entropy barriers (b) for oxygen with those for nitrogen in the rigid polymer models. 187

Fig. 5.11 Comparison of energy barriers (a) and entropy barriers (b) for oxygen hopping in the flexible models with those in the rigid polymer models. 189

Fig. 5.12 Rate constants for oxygen (a) and nitrogen (b) hopping in the rigid and flexible polymer models. *d* is the distance from the location of the transition state to the associated energy minimum. 191

Fig. 5.13 Energetic selectivities (a) and entropic selectivities (b) in oxygen/nitrogen separation with the rigid and flexible polymer models. *d* is the distance from the location of the transition state to the associated energy minimum. 193

Fig. 5.14 Ratios of energetic selectivities (a) and entropic selectivities (b) in the rigid polymer to those in the flexible polymer. *d* is the distance from the location of the transition state to the associated energy minimum. 195

Fig. 6.1 Escape rate of a methane molecule from *A* to *B* as a function of N_A, for various N_B. 213

Fig. 6.2 Escape rate of a methane molecule from A to B as a function of N_B, for various N_A. 214

Fig. 6.3 Values of the area integrals $Z_S(N_A,N_B)$ and volume integrals $Z_V(N_A,N_B)$ as functions of N_A, for various N_B. The filled symbols correspond to the area integrals, and the open symbols correspond to the volume integrals. The units for the area and volume integrals are Å^2 and Å^3, respectively. 215

Fig. 6.4 The average Boltzmann factor for the test insertion of a methane molecule, $\langle \exp(-\beta u_t) \rangle$, as a function of N_B. For the filled symbols (area), the test insertion was performed on the surface between cages A and B, with no molecules in cage A. For theopen symbols (volume), the test insertion was performed in cage A, with no other molecules in cage A.. 216

1. Introduction

Stockpile stewardship is perhaps Sandia's most important mission and understanding aging effects is a critical aspect of that stewardship. Couple this with the desire for smaller components for weight-savings, a design must then include complexities of various size and time scales that must be understood. Experiments cannot be performed at all the pertinent size and time scales to satisfy responsible stewardship requirements upon design. Careful experiments coupled with computational tools can, however, allow for better examination of physical phenomena that relate to designs with a concern for aging of small components. As a result, this LDRD was proposed to give mechanistic understanding of the various time/size scales related to various materials. In Chapter 2, we describe results based on molecular dynamic simulations using Embedded-Atom-Method (EAM) potentials that relate to continuum mechanical quantities of interest to mechanical designers. In Chapter 3, we describe atomistic calculations of prefactors and activation rates for clusters of atoms diffusing on surfaces. These calculations illustrate how reaction rates can be derived from atomistic models. In Chapter 4, we describe a mesoscopic model of a grain boundary phase transition. This model allows a statistical mechanical understanding of an important materials process that could not have been derived without an atomistic model. In Chapter 5 we describe methods that we have developed to calculate activated diffusion rates of small molecules in amorphous materials where no *a priori* information about the location of cavities and transition states is available. These calculations assuming a low solute concentration, so that interactions between solues can be ignored. In Chapter 6 new Monte Carlo sampling approaches for the calculation of escape rates in zeolite cavities at arbitrary concentration are presented. In this case, the zeolite structure is very regular, and so locations of the cavities and the transition states are known.

Chapter 2

Size Scale and Time Scale Effects on Plastic Flow of FCC Metals

If one is to determine structure-property relations for plasticity at different size scales, one must be able to bridge concepts from the continuum level down to the atomic level. In this study we probe the kinematic and thermodyamic force variables by running molecular dynamics simulations, finite element simulations (with different material models), and experiments. We mainly focus on the molecular dynamics simulations and build up from lower size specimens. In order to make qualitative correlations in the structure-property relations, we evaluated various parameters (temperature, strain rate, specimen size, deformation path, and crystal orientation) to understand their relative importance on influencing the macroscopic stress. Before quantifying the structure-property relation for a particular parameter, we first examined each parameter's relative importance with respect to each other. To accomplish this, we conducted a Design Of Experiments (DOE) study, which employs orthogonality principles to reduce the number of atomistic simulations, to gain qualitative insight into their relative influence on the continuum stress state. After determining the most important influences, we then focused on each individual parameter to gain quantitative understanding. To support the molecular dynamics results, we also include finite element simulations and physical experiments to help elucidate the size scale effects on the yield stress and kinematics. Before we proceed to the results, we first briefly describe the atomistic modeling background.

2.1 Atomistic Background

For the molecular dynamics simulations we used EAM [Daw and Baskes, 1984; Daw *et al.*, 1993] potentials. The notion of embedding energy was first suggested by Friedel [1952] and further developed by Stott and Zaremba [1980]. Daw and Baskes [1984] proposed a numerical method for calculating atomic energetics. Daw *et al.* [1993] summarize many applications of EAM. Essentially, EAM comprises a cohesive energy of an atom in terms of the local electron density into which that atom is placed. A function, $\rho(r)$, describes the contribution to the electron density at a site due to the neighboring atoms. The embedding energy F is associated with placing an atom in that electron environment. The functional form of the total energy is written as

$$E = \sum_i F^i\left(\sum_{i \neq j} \rho^i\left(r^{ij}\right)\right) + \frac{1}{2}\sum_{ij} \phi^{ij}\left(r^{ij}\right), \tag{2.1}$$

where i refers to the atom in question and j refers to a neighboring atom, r^{ij} is the separation distance between atoms i and j parameterized by their separation, and ϕ^{ij} is the pair potential. Because each atom is counted, contravariant and covariant index notation is not used here. Subscripts denote the rank of the tensor, for example, one subscript denotes a vector, two subscripts denote a second rank tensor, and so on. Superscripts identify the atom of interest. In molecular dynamics, the energy is used to determine the forces on each atom. Once the forces at each atom are determined, the dipole force tensor, $\underline{\beta}$, can be determined and is given by

$$\beta_{km}^{i} = \frac{1}{\Omega^{i}} \sum_{j(\neq i)}^{N} f_{k}^{ij} r_{m}^{ij}, \tag{2.2}$$

where i refers to the atom in question and j refers to the neighboring atom, f_k is the force vector between atoms, r_m is a displacement vector between atoms i and j, N is the number of nearest neighbor atoms, and Ω^i is the atomic volume. In this way, $\underline{\beta}$ would be analogous to the stress tensor at the atomic site. Since stress is defined at a continuum point, we interpret the stress tensor as a volume average over the block of material,

$$\sigma_{mk} = 1/N * \sum_{i}^{N^*} \beta_{mk}^{i}, \tag{2.3}$$

in which N^* is the total number of atoms in the volume.

The correspondence between an atomistic local stress, $\underline{\beta}$, and a global stress, $\underline{\sigma}$, has been the focus of several studies. Irving and Kirkwood [1950] derived a microscopic hydrodynamic formula for stress based on an infinite series expansion that could only be calculated by approximation. The contributions of interatomic forces to the stress tensor were derived on a statistical theory embedded into the continuity equation, equation of motion, and equation of energy transport. Hardy [1982] introduced an envelope function that considers atoms from a surrounding field, in effect a nonlocal quantity, into molecular dynamics calculations to modify the Irving and Kirkwood [1950] stress equation. The notion of including nonlocal terms was implicitly argued by Rowlinson [1993] who stated that unique local thermodynamic functions in inhomogeneous systems could be defined if the spatial length scale of the inhomogeneity is macroscopic, much larger than the interatomic distances. Furthermore, Cheung and Yip [1991] showed that the distribution of local stress could be calculated from the mechanical definition of force per unit area. They derived an expression for a homogeneous system equivalent to the viral theorem (thermodynamic definition); when inhomogeneities are present, the equivalence can be demonstrated when a volume average is considered. These results motivate our use of equation (2.3).

The question of spatial size scale on mechanical properties has been around for sometime now. The Cosserat brothers (1909) developed a nonlocal theory to determine the stress state of a material in which case the stress tensor was asymmetric. Recently, Fleck et al. (1994) have focused on strain gradients that would affect the stress state, and Bammann and Dawson (1997) have developed a dislocation density evolution equation that includes a spatial length scale. This short list of references does not cover the amount of research related to spatial length scale effects on mechanical properties, but at least gives the reader an idea of the various topics related to spatial size scales and continuum level quantities considered.

Because molecular dynamics starts at the scale of an atom and the time on the order of femtoseconds, running simulations to large sizes and times is prohibitive. In fact, there is a competition between the time and size scales as illustrated in Figure 2.1 in terms of computing power. Figure 2.1 shows that as the total time (inversely related to the applied strain rate) needed for a simulation is increased, the computational constraint will allow an upper limit on the size of the atomic block of material. Similarly, as the block size increases, the computational times require and fairly large applied strain rate. Hence, we still cannot achieve macroscopic size scale specimens that include time frames on the order of seconds. Even with these constraints, we performed scoping studies that gave insight into the plastic behavior of metals at different size scales. Strain rates on the order of 10^6/sec or lower are not feasible at this time in atomistic simulations. Later in this chapter we will analyze strain rates down 10^6/sec.

2.2 Computational Set-up

We perform classical molecular dynamics simulations using the following Embedded Atom Method (EAM) potentials (Daw and Baskes, 1984): for nickel (Angelo *et al.* 1995); for copper (Foiles, 1985); and for aluminum (Baskes *et al.*, 1996; Baskes *et al.*, 1997). The EAM potentials were determined from using the lattice parameter, cohesive energy, and elastic moduli for the pertinent metal. Though different deformation paths were examined in this study (torsion, simple shear, tension, and compression), most of the investigation focused on simple shear. In order to illustrate the boundary conditions, we describe fixed-end, simple shear for different cross-sectional sample sizes and crystal orientations. As illustrated in Figure 2.2a, the computational block of material had free surfaces in the x- and y-directions with an aspect ratio of roughly 2:1 in x:y and was periodic in the z-direction. The crystal orientation was $[100,011,0\bar{1}1]$, and the shear loading on y-face was in the [100] direction. In Horstemeyer and Baskes (1999), the global continuum stress saturates if the z-direction is four or more unit cells in thickness; smaller samples introduce a separate size scale effect. Since one of our goals

was to model as large a cross-sectional area as possible, we used a four unit cell z-direction thickness in our simulations.

After creating the sample size, a few planes of atoms at the top and bottom (xz planes at the +y and -y extrema) were frozen on their perfect lattice sites. The remainder of the atoms were allowed to relax to minimum energy to accommodate any surface relaxation at the two remaining free surfaces (yz planes). Velocities of the interior (or active, non-frozen atoms) were then initialized using a Boltzmann distribution at a chosen temperature (300 K). For simple shear, a strain rate was then applied to the block of atoms by setting the x-velocity of the frozen xz planes to a constant value. The bottom atomic plane had a prescribed x-velocity of zero for the duration of the dynamics simulation, and the top atomic plane had a prescribed constant velocity to create a strained sample as shown in Figure 2.2b.

If just the top row of atoms initially experienced the prescribed velocity without the active internal atoms experiencing the same velocity field, a shock would be induced into the block of material because of the high strain rates. In our calculations, we introduced an initial velocity field that mitigated the shock wave and then applied the boundary velocity fields. To accomplish this, the interior atoms in the model were also given an initial x-velocity (superposed on their thermal 300 K velocities) that varied linearly from 0.0 to the prescribed velocity at the top atomic plane depending on their y-coordinates in the simulation box. This initial velocity was introduced to produce the strict simple shear boundary conditions, but only to alleviate the shock. In fact, the rigorous continuum description of simple shear demands that the x-faces remain planar. In these simulations, they are free surfaces. Our goal was to match experiments, which usually have a large length-to-height aspect ratio but with free edges. In these simulations, the prescribed velocity was chosen to model strain rates ranging from 10^7 s^{-1} to 10^{12} s^{-1}.

Following initialization, a constant number of atoms, constant volume, and constant temperature (NVT) simulation was performed with a 0.001 ps time step until the block of atoms had undergone strain sufficient to create yield, typically a few percent strain or more. Because straining via moving the frozen planes adds considerable energy to the active atoms, a Nose-Hoover thermostat (Nose, 1984; Hoover, 1985) was used during the molecular dynamics simulation to keep the active atoms at constant temperature. The thermostat applies a damping (or acceleration) factor to the active atoms based on the difference between their current temperature and the desired temperature (300 K). We computed the instantaneous temperature of the ensemble of active atoms after first subtracting from each atom the non-thermal x-velocity that was initially prescribed, since the active atoms essentially maintain the same component of x-velocity for the simulation.

Before we mention the results, we must first discuss the notion of a yield. In this context, we define two micro-yield points and a macro-yield point. First, the average global stress of the active atoms was computed by using Equation (2.3), and a stress-strain curve was generated. Figure 2.3 shows stress-strain curves for atomistic simulations of ten thousand and ten million atoms just to illustrate the behavior at different material block sizes. We identify three locations on the curve. The first location is defined as micro-yield 1, where the stress-strain behavior first deviates from elastic linearity, i.e., the proportional limit. At this point, initial dislocations are emitted from the surface because of the local stress gradients in the corners due to the boundary conditions. The second location is micro-yield 2, which is defined by the macro-scale continuum concept of a 0.2% offset strain. The third location is defined as macro-yield, the point at which the maximum stress occurs. We also define the quantity $\Delta\varepsilon_{yield}$, which is the difference in strain between the macro-yield and micro-yield 2. Because we start with a perfect lattice, there are no initial defects. As such the stress-strain responses, in terms of the stress drop-off, look very similar to experimental data of metal "whiskers" which have essentially no initial defects (cf. Yoshida et al., 1966). In whiskers, yield is typically defined at the "macro-yield" point. At this point, the stress required to activate a certain density of dislocations is reached and the material plastically deforms precipitating dislocations with subsequent propagation of local Luders bands that lead to irregular fluctuations in the plateau region of the stress-strain curve after the macro-yield stress drop-off. These two curves illustrate that micro-yield 1 and micro-yield 2 are essentially the same and in many cases, as exemplified in the ten thousand atom simulation, macro-yield is very close to the other two micro-yield points.

In determining the yield points in many of the simulations, we also unloaded the material block at each of the micro-yield and macro-yield points to give information regarding permanent set and the influence of dislocations on the yield points. In Figure 2.4, we show the atom positions at different locations along a simple shear deformation path for a block of nickel with 2242 atoms. Here, we unloaded at micro-yield 1 and macro-yield. It is clear from this simulation that the unload at micro-yield 1 returns the atoms to their original positions and at macro-yield almost returns the atoms to their original positions with permanent set realized.

This type of simulation as shown in Figure 2.4 was typical of the ones that we performed with differing block sizes of material that ranged from 100 atoms to 100 million atoms, and the time steps from a few thousand to many millions depending on the applied strain rate. The largest simulations were run using a parallel version of the EAM code designed for distributed memory supercomputers (cf. Plimpton, 1995). Consequently, the CPU cost of the simulations also varied from a few seconds on a single processor workstation to many

hours on hundreds of processors on the Sandia/Intel Teraflop machine. In fact, the largest simulation took 13 CPU hours on 3000 processors.

2.3 Design of Experiments Study

The Design Of Experiment (DOE) analysis of variance approach is a statistical method [Box *et al.*, 1978] that employs orthogonality principles to quantify the relative influence of a set of uncorrelated parameters. In our case we examine the effects of various atomic scale features on the volume averaged single crystal stress state. The DOE approach was intended primarily to give guidance as to which parameters played a dominant role in determining the stress state of a material in an efficient and objective manner. This is especially important since the very high applied strain rates and small sizes inherent to molecular dynamics calculations subject the material to extreme conditions. Once the most important parameter is determined, its levels can be varied for more detailed analyses.

Table 2.1 summarizes the *levels* chosen for each *parameter.* For the DOE, an investigator can select a number of *levels* for each *parameter* in an orthogonal array and then run *numerical experiments* to evaluate the parametric effect in an efficient manner. The levels were chosen based upon physical phenomenology (for example, crystal orientation) and computational constraints (for example, applied strain rate). Certainly, the results might qualitatively change as the levels change, but this method is first good cut at determining qualitative trends and then quantitative simulations can be performed later. Orthogonality refers to statistically independent parameters that make up the columns of the array. Once the number of levels and parameters are determined, an orthogonal array is setup to determine the number of experiments needed. The terminology of orthogonal array $L_x(y^z)$ goes as follows: "x" denotes the number of calculations, "y" denotes the number of levels, and "z" denotes the number of parameters. For example, to examine seven parameters at two levels, one would have an orthogonal array represented by $L_8(2^7)$ which would reduce the number of 128 calculations if done linearly in series to 8, which was used for our study.

Seven parameters were of interest for our study: crystal orientation, temperature, strain rate, deformation path, x-dimension, y-dimension, and z-dimension. For the purpose of understanding the relative influence of the various parameters on the responses (yield and plastic energy resulting from plastic flow) pertaining to this study, only two *levels* were chosen with the seven independent parameters. As such, the appropriate orthogonal array is the L_8 array. The L_8 represents an orthogonal array of equations represented by eight numerical experiments. The L_8 array allows up to seven independent *parameters* with two levels for each parameter. Each *level* can be characterized by an appropriate value. For example, the two

levels for the strain rate were 1.8e9/sec and 1.8e8/sec. Although a full factorial set of calculations could be performed to vary each parameter in a linear fashion, a DOE reduces the set of calculations in a repeatable, timely manner such that data can be easily translated into meaningful and verifiable conclusions. With this technique, relevant data can be extracted from a relatively small number of experiments (or numerical calculations). Clearly, the advantages of DOE as a screening process for parameter influence grow exponentially as the number of parameter variations increases. This type of analysis has been used for examining parametric effects related to void growth in ductile metals [Horstemeyer and Ramaswamy, 2000] and for examining attributes of crystal plasticity [Horstemeyer *et al.*, 1999]. For details of the DOE analysis, the reader can refer to these articles.

Figure 2.5 shows the effective (von Mises) stress-strain curves for each of the DOE calculations, indicating a wide variety of behaviors. Some calculations experienced very large yield stresses compared to the others, and other calculations experienced fairly large elastic strains before plastic flow set in. From these simulations, we used the yield stress and plastic energy to determine the parametric influences.

The yield stress was determined from micro-yield 1, and the plastic energy was determined by integrating the total energy under the stress-strain curve and subtracting the elastic energy. The elastic strain energy is determined from just integrating the area under the elastic region. The plastic energy gives us a measure for the dissipation occurring within the block of material.

Table 2.1 Design of Experiments L_8 orthogonal array.

parameter / calc.	X (nm)	Y (nm)	Z (nm)	strain rate (/sec)	Temp (K)	Def. path	Orient.
1	2.816	2.816	0.704	1.8e9	300	simple shear	(100,011, $0\bar{1}1$)
2	2.816	2.816	0.704	1.8e8	500	tension	(100,010, 001)
3	2.816	5.632	1.408	1.8e9	300	tension	(100,010, 001)
4	2.816	5.632	1.408	1.8e8	500	simple shear	(100,011, $0\bar{1}1$)
5	5.632	2.816	1.408	1.8e9	500	simple shear	(100,010, 001)
6	5.632	2.816	1.408	1.8e8	300	tension	(100,011, $0\bar{1}1$)
7	5.632	5.632	0.704	1.8e9	500	tension	(100,010, 001)
8	5.632	5.632	0.704	1.8e8	300	simple shear	(100,011, $0\bar{1}1$)

It is instructive to discuss the atomic action at yield and sometime later when plastic flow occurs. Figures 2.6 and 2.7 show the shear stress-strain response of calculation DOE #8 and the related atomic positions in Figure 2.6 and the dislocations in Figure 2.7 at different strain levels. In Figure 2.7, the centrosymmetry parameter [Kelchner *et. al.*, 1998] was used to signify the locations of dislocations. At microyield 1, one can observe that dislocation nucleation occurs at the corners of the block. The relative displacement vector at the lower left hand corner of the material block illustrates the local incompatibility evidenced by the presence of a dislocation. As the calculation proceeds, one can observe more dislocations nucleating from the corners and x-face edges until finally at 30% strain, one can observe very large atomic displacements as shown in Figure 2.6b and dislocation interactions in Figure 2.7f. Figure 2.6c also shows the elastically unloaded atomic state after the forward straining proceeded just beyond yield. In this case, the boundary condition on the uppermost atoms was removed and the block of material could return to the elastically unloaded state (that is, the stress free intermediate configuration, not the initial reference configuration).

Figure 2.7 shows clearly the evolution of dislocation nucleation and motion. In macroscale specimens, shear bands can be observed in simple shear experiments, but at this scale, Figure 2.7 clearly shows dislocation glide along crystallographic planes. This may imply that as the scale decreases down to nanodimensions as in this study that underlying mechanisms for macroscopic shear banding is dislocation glide.

Figure 2.8 shows the DOE responses for yield and plastic energy at 15% effective strain. The effective strain (or von Mises strain) equals the shear strain divided by the square root of three for the case of simple shear. The results were normalized by the maximum change of yield and plastic energy, respectively, observed for the eight tests so that the relative influence could easily be determined. Figure 2.8 shows that the crystal orientation had the primary influence on yield and the plastic energy at 15% effective strain, and the strain rate had a secondary influence. The type of boundary condition, spatial length scale, and temperature differences had minor influences compared to the orientation differences. Remember that the relative values depicted in Figure 2.8 arise because of the limits chosen for the parameters. Increasing the limit variations in the size and strain rate leads to a greater effect on both yield and plastic energy, even to the point that the size influence will override that of the orientation at some point. The broader disparate length/time scales are examined next. Regardless, these levels were chosen to determine the relative parametric influences of small size scale differences so that macroscale experimental observations, which also have small size scale differences, might be asserted in the discussion of the crystal orientation results.

2.4 Crystal Orientation Effects

Since the aforementioned DOE study showed that orientation has the strongest influence for these small size scale simulations, we now describe the orientation effects in more detail in the following section. Our goal is to explore the yield and plastic flow behavior with respect to slip within the crystal lattice for these very small size scale and high rate simulations.

The following EAM molecular dynamics simulations were performed under fixed-end, simple shear boundary conditions on a block of atoms that is eight by four by four unit cells of nickel. Each computational block of material had about 1300 atoms and free surfaces in the x- and y-directions with periodicity in the z-direction. Strain rates were approximately ~1e10/sec. Like in the DOE simulations, a displacement was applied to the top row of atoms, and the bottom row of atoms was fixed. A constant number of atoms, constant volume, and constant temperature analysis at 300K was used for all orientations.

The stress state of a metal single crystal is dependent upon the crystallographic orientation, deformation path, temperature, applied strain rate, and size of specimen (if it is at or below the micron range). Extensive experimental studies have shown that yield and plastic flow exhibit a strong dependence on all of these parameters. For example, from the initial experiments of Ludwig and Scheu [1925], many researchers have shown that ductile metals experience a higher work hardening rate, and thus higher flow stress, in tension than in torsion (simple shear) due to texture evolution. Fleck *et al.* [1994] showed that the stress state is dependent upon the specimen size. In particular, as the size decreased, the stress increased. For much smaller sizes, on the order of nanometers, Horstemeyer and Baskes [1999] have shown using the Embedded Atom Method (EAM) that global yield and plastic flow are size dependent. The question of orientation effects has been addressed analytically, initially by Schmid [1931] and more recently by Kocks *et al.* [1998] using crystal plasticity simulations and texture analyses. A summary of early experimental results on FCC single crystals as a function of orientation is found in Nabarro *et al.* [1964].

Important aspects of single crystal experiments related to this study are worth noting. Kochendorfer [1950] tried to perform simple shear on single crystal FCC aluminum specimens but a multiaxial stress state developed. Matsuda [1977] and Rauch *et al.* [1990] performed simple shear experiments on single crystal BCC iron. Phillips [1962] performed direct shear tests on single crystal aluminum and copper specimens to analyze orientation effects. Unlike the case of a polycrystal, torsion of a single crystal may not approximate simple shear too closely, since different slip systems will be active around the circumference of the sample [cf. Boukadia and Sidoroff, 1988].

Orientation effects have changed yield strength and flow stress by up to a factor of four as observed in measurements of tensile, uniaxial compression, and channel die compression

deformation of single crystals at quasi-static strain rates on the order of 10^{-4} to $10^{-2}s^{-1}$ [e.g., Lange and Lucke, 1953; Diehl, 1956; Davis *et al.* 1957; Haasen, 1958; Staubwasser, 1959; Driver, Juul Jensen and Hansen, 1994]. Similar effects were observed in the shock recovery experiments with high strains rates on the order of $10^{5}s^{-1}$ [cf. Follansbee and Gray, 1991]. Trends in the relationship between the yield/flow stress and the orientation, represented by the number of equally and maximally stressed slip systems in the experimental data do not follow a simple rule in simple shear, but depend on deformation path and other factors related to the interactions of the main glide dislocations. For example in tension, <111> oriented single crystals with sextuple slip consistently have the highest yield stress, rather than the <100> with octal slip. This is true for FCC aluminum, nickel and copper single crystals at both quasi-static and shock loading strain rates [Lange and Lucke, 1953; Diehl, 1956; Davis *et al.* 1957; Haasen, 1958; Staubwasser, 1959; Phillips, 1962; Follansbee and Gray, 1991].

Figure 2.9 illustrates four different crystal orientations employed in this study. We oriented the lattice such that a different number of glide planes would be available for crystallographic slip in the different simulations. As Figure 2.9 shows, we examined crystals that were initially oriented for single, double, quadruple, and octal slip.

Figure 2.10a shows shear stress-strain and Figure 2.10b axial-stress, shear-strain curves from crystals oriented for single, double, quadruple, and octal slip under fixed-end simple shear. To determine a polycrystalline response from the single crystal simulations, we averaged the single crystal stress-strain curves. This curve is labeled in Figure 2.10 as "pseudopolycrystal". The shear component of the stress tensor for each single crystal calculation was determined as the average of the shear component of the dipole stress tensor described in equation (2.3). These crystal responses were averaged together to approximate results for a polycrystal and also plotted in Figure 2.10 (in this approximation, intergranular effects are not included). A clear trend is shown in Figure 2.10a with respect to crystal orientation. The flow stress increases with an increase in the number of slip systems. Thus the crystal oriented for octal slip exhibits the highest flow stress with the quadruple slip crystal next and so on. Essentially more active slip systems are in operation thus increasing the dislocation density and resulting stress level. The trends observed for the values of yield, total energy, elastic energy, and plastic strain energy are shown in Table 2.2. Note that the yield stress for the double slip case is nearly double the single slip case. One might suspect this result since the number of active slip systems has doubled. However, the quadruple slip case is less than four times the single slip case, and the octal slip case is less than eight times the single slip case. These two cases indicate that dislocation activity is not just occurring on the primary slip systems. The pseudopolycrystal seems to track with the double slip orientation

(Table 2.2). To our knowledge, these trends have never been examined before in the context of atomistic simulations.

The shape of the stress-strain curves in Figure 2.10 are different than the classical Stage I to III hardening curves measured in bulk FCC single crystals at quasi-static strain rates [Lange and Lucke, 1953; Diehl, 1956]. No initial easy glide region with very low flow stress and strain hardening, Stage I, was observed in the simulations. Instead, an initially high hardening rate to a sharp peak in the flow stress is followed by strain softening occurs for all orientations. If the smaller flow stress oscillations are dampened out, the shape of the stress-strain curve is similar to the shape of the stress-strain curve for single crystal whiskers. Whiskers share a similar characteristic to these simulations in that no dislocations are initially present. Essentially, the stress drops off to a low level as an avalanche of new dislocations that are emitted from the edge [cf. Brenner, 1958]. We should mention that Phillips' [1962] direct shear experiments of single crystal Cu and Al did not experience Stage I hardening and none of the specimens experienced the stress drop-off observed in the atomistic simulations.

Table 2.2 Crystal orientation effects on stress state.

description	yield (GPa)	total strain energy (GPa)	elastic energy (GPa)	plastic energy (GPa)
single slip	2.20	1.08	0.05	1.03
double slip	4.50	1.67	0.13	1.54
quadruple slip	5.31	2.23	0.17	2.06
octal slip	6.13	2.33	0.21	2.22
pseudopolycrystal	4.52	1.78	0.21	1.57

We also show that the axial stress resulting from these fixed-end type simulations was similar in all orientations in Figure 2.10b. This second order response has been attributed to dislocation substructure [Horstemeyer and McDowell, 1998] and texture development [Harren *et al.* 1989, Neale *et al.* 1990]. Although the magnitude of the axial stresses is higher for these atomistic simulations than for large scale polycrystalline material, the slope of the curve is qualitatively similar to the polycrystalline results [cf. Montheillet *et al.* 1984; Lipkin and Lowe, 1989; Anand and Kalidindi, 1994].

Direct comparison of experimental measurements and other types of analyses/simulations with Figure 2.10 do not exist, since the molecular dynamics simulations comprise very small crystal sizes and very high strain rates. No data for single crystal FCC simple shear experiments at these strain rates and sizes could be found, perhaps due to the great difficulty in performing this type of test. Even at a larger size scale and at quasi-static strain rates, few single crystal simple shear or torsion experiments have been conducted.

The results in Table 2.2 and Figure 2.10 illustrate the stress state dependence on crystal orientation in simple shear using atomistic simulations. We also ran various crystal orientations in tension. Figure 2.11 shows that the uniaxial stresses in tension do not follow the trend that simple shear exhibited with respect to crystal orientation. In fact, the sextuple slip case is higher than the octal, single, and double slip cases at early strains. This observation is consistent with experimental observations as discussed in the introduction of this paper.

Since the earliest work on single crystals, these orientation effects have been considered with respect to deformation occurring by slip on discrete glide planes. Schmid [1931] and Schmid and Boas [1935] proposed that a fundamental measure of stress was the stress resolved onto the glide plane and in the glide direction. Slip and thus yield would commence once the resolved shear stress reached a critical value. They further proposed and demonstrated for single glide HCP metals, that the stress-strain curves of single crystals could be normalized to a single curve by plotting the maximum resolved shear stress based on the Schmid factor. This widely used normalization, however, fits the behavior of FCC crystals less well, especially for those orientations in which the direction of the tensile axis is near the boundaries or vertices of the unit stereographic triangle [e.g. Nabarro *et al.*, 1964]. Multiple slip instead of single slip occurs for orientations in these boundary regions. Deviations as large as factor of two occur for the resolved shear stress of multiple slip orientations compared to single slip orientations [Lange and Lucke, 1953; Diehl, 1956; Davis *et al.*, 1957; Haasen, 1958; Staubwasser, 1959]. Note that other normalization schemes such as a Taylor [1938] factor are also common but are not considered herein. To compare the differences between Taylor factors and Schmid factors as a function of orientation see both Calnan and Clews [1951] and Chin and Mammel [1967].

In Figure 2.12, we apply a Schmid factor to the flow stress curves of Figure 2.10 for the four orientations under simple shear straining conditions. The primary slip system has a Schmid factor of 1.0 for initially oriented single slip crystal, 0.707 for the initially oriented double slip crystal, 0.577 for the initially oriented quadruple slip crystal, and 0.408 for the initially oriented octal slip crystal. As shown in Figure 2.12 the stress-strain curves are brought together when normalized by the appropriate Schmid factor, though a maximum of 20% difference exists for the stress value. This difference reflects the additional contribution to yield and flow stress of dislocation-dislocation reactions, interactions, and trapping. These dislocation interactions are more related to the geometry of slip, the dislocation line directions, and Burgers vectors than just by a single parameter related to one slip plane. Deviations of this extent have also been observed experimentally in studies of single crystals [cf. Reid, 1973], but these experiments are conducted with larger specimens and at much lower strain rates.

Various dislocation reactions, interactions, and trappings can break up a single crystal into regions of differing orientations thus inducing differences in the normalized flow stress. This pattern of subdivision in which the regions are separated by dislocation boundaries can affect the flow stress [Huang and Hansen, 1997]. This break up into subdomains has experimentally been shown to occur over two or three spatial length scales. The particular pattern is dependent on the initial orientation and deformation geometry [cf. Driver *et al.*, 1994; Godfrey *et al.*, 1998; Liu and Hansen, 1998; Huang *et al.*, 1998].

One further reason for disparity in the normalized peak flow stress is due to the implicit assumption that only those dislocations in the system with the highest resolved shear stress are active. In reality, even at very low strains, transmission electron microscope analysis shows significant slip activity on other slip systems [Hughes, 1996]. At a strain of 30% in a compressed initial single crystal of aluminum, Hughes [1996] estimated that over 30% of the dislocations stored in the microstructure are not associated with either the primary (highest resolved shear stress) or secondary systems. For this orientation at 30% strain, standard crystal plasticity formulations predict a crystal rotation that is uniform in nature. For a more physically-based continuum level crystal plasticity formulation, one must include other effects, such as, non-Schmid effects.

We now describe the statistical nature of the stress distributions within a crystal. Figures 2.13-2.16 show local shear stresses for each orientation described earlier at yield and at 30% shear strain for each single crystal. The dark colors in Figures 2.13-2.16 represent the highest shear stresses, and the lighter color represents the lowest shear stresses. The values for shear stress used in Table 2.2, and for the stress-strain responses in Figures 2.10 and 2.12 were based on the volume average as described by equation (2.3). In Figures 2.13-2.16, each local value is actually the shear component of the dipole force tensor as described by equation (2.2). At yield, we see that the highest stresses occur at the corners near the free surface of the material block and a fairly uniform low stress state is present within the block interior. This observation illustrates the effect of the local stress gradient on the location where dislocations nucleate. This behavior is fairly consistent for all the orientations. At 30% strain, the distribution of the high and low values for the atomic stresses appears to be more random.

Figures 2.17-2.18 show the distribution of the shear component of the dipole force tensor at yield for the different orientations. Figure 2.17 shows that most of the atoms (several thousand) experience just an elastic shear stress. When the peak atom count is limited to 150 in a bin (for a zoom into the regions of higher stressed regions), we see in Figure 2.18 that the character of the single slip, double slip, and quadruple slip distribution looks similar. Each of these crystals seems to have a lower limit of about –0.5 GPa and an upper limit of about 1.7 GPa. For the octal slip system, a broader distribution is observed wherein the upper limit,

approximately 3 GPa, is greater than the others. At 30% strain, we see in Figure 2.19 that a large number of atoms still experience a small elastic shear stress.

When examining the distribution of local atomic shear stresses, we see some interesting trends. When comparing Figures 2.18 and 2.20, which show the distributions with a peak atom count of 150 in a bin, we see that the double and quadruple slip cases become more diffused but the octal slip case is less diffuse as deformation proceeds. The octal slip case gave a similar distribution as deformation proceeded.

By examining the stress distributions, we find that a Gaussian distribution matches the results extremely well when the small elastic stress atoms are not included. Note that other distributions could be used, for example a Lorentzian distribution, but for simplicity, we use a Gaussian here. Figure 2.21 shows a Gaussian fit versus a histogram of an atomistic simulation at a strain level of 30% effective strain for the local shear stress in the double slip orientation. The other orientations showed similar shear stress distribution comparisons. This evolving distribution predominantly represents the atomic regions experiencing plastic deformation and reflects the plastic work hardening. Figure 2.22 shows the evolving mean value of the Gaussian distribution as a function of strain for the double slip case when all the atoms are included and when the small elastic stress atoms are not included. The mean values follow the stress-strain curve. Figure 2.22 also shows the mean and standard deviation of the actual shear stress distributions as a function of effective strain. Because the evolving distribution becomes more diffuse as strain is applied, the standard deviation (or width) increases. The plastic flow can then be represented as a distribution function, F, with the mean, μ, and standard deviation, sd, functions of applied strain level, γ_{12}. The following equations reflect this evolving stress distribution with constants C_1 through C_6 that are determined from the atomistic simulations,

$$F(\sigma_{12},\gamma_{12}) = \frac{1}{sd(\gamma_{12})\sqrt{2\pi}} \exp\left[-0.5\left(\frac{\sigma_{12}(\gamma_{12}) - \mu(\gamma_{12})}{sd(\gamma_{12})}\right)^2\right] \tag{2.4}$$

$$sd(\gamma_{12}) = C_1 + C_2\gamma_{12} \tag{2.5}$$

$$\mu(\gamma_{12}) = C_3\left(1 - \exp\left[-\gamma_{12}/C_4\right]\right) + C_5\gamma_{12}\exp\left[-\gamma_{12}/C_6\right]. \tag{2.6}$$

In equation (2.6) C_4 and C_6 reflect the short range and long range strain values at which the peak and saturation stress values occur as observed in the stress-strain response from the atomistic simulations. The values for C_5 and C_6 are a function of orientation but since C_3 and C_4 relate to the long range saturation stresses, they essentially remain the same regardless of the orientation. For the double slip case, C_1=0.25, C_2=0.15, C_3=0.1, C_4=0.2, C_5=10, and

C_6=0.04. We note that the constants determined by these limited amount of simulations here may not represent a general deformation field.

The changing yield and work hardening distribution functions based on crystal orientations could be used in a continuum crystal plasticity formulation to account for the orientation changes. From a macroscale continuum perspective, one could develop a shear stress distribution function either by employing a smaller number of bins to capture effects from the lower length scale causes or by approximating the distributions with an evolving orientation function [cf. Prantil *et al.*, 1993]. This work has yet to be done.

2.5 Strain Rate Effects

The two main themes we would like to discuss separately regarding the results, which are the effects of size scale and time scale. Unfortunately, they are linked together so discussing one of these topics independently is difficult without begging questions about the other. However, we will try to do so by first starting with time scale issues as related to strain rate effects on dislocation nucleation, motion, and interaction. Recall from Figure 2.1 that a competition between the size scale and time scale in performing atomistic simulations exists. If a strain rate of 10^7 s^{-1} is to be achieved in the current molecular dynamics paradigm, one must have a small number of atoms. The converse is also true. If a large block of atoms is desired, the applied strain must be rather high (~10^9 s^{-1}). The reason for this time-space relation in the computations is related to the time scale of the atomic period involved, and this in turn affects the applied strain rates. With this in mind, we briefly address the time domains pertinent to our simulations.

There are several time domains to consider when the considering strain rate effects on small specimens. First, the highest frequency component will arise in relation to the atomic frequency. These vibrations occur on the order of 10^{-12} seconds. If shock is involved, then the longitudinal elastic shock wave velocity can be derived from the wave equation given by

$$C_{elastic} = \sqrt{\frac{K + 4/3\,G}{\rho}}, \tag{2.7}$$

and the plastic wave speed as

$$C_{plastic} = \sqrt{\frac{K}{\rho}}, \tag{2.8}$$

and the shear (or distortional) wave speed as

$$C_{shear} = \sqrt{\frac{G}{\rho}} \tag{2.9}$$

in which ρ is the density of nickel, K is the bulk modulus, and G is the shear modulus. Typical sound speeds are ~20 Å-ps^{-1}. Since our blocks of material are small, shock waves propagate through the material many times on the time scale of our simulations which achieve large strains (~30%). However, in our simulations, we avoid the shock by initializing all the atoms with an initial velocity gradient in the x-direction as discussed above, thus alleviating the time issue with the shock wave.

Another time domain to consider is that of the dislocation motion. Baskes and Daw (1990) showed that the modified Leibfried (1950) continuum equation for dislocation velocity can be used to explain the atomistic simulations in simple shear for nickel:

$$\frac{d}{dt}\frac{mv}{\sqrt{1-\left(v/c\right)^2}} = (\sigma-\sigma_o)b - \alpha\frac{3kT}{10b^2}\frac{\left(v/c\right)}{\sqrt{1-\left(v/c\right)^2}} \tag{2.10}$$

where m is the dislocation per unit mass length (0.2 atoms/Burger's distance), c is the dislocation terminal velocity or sound speed (20 A-ps^{-1}), σ is the applied stress, σ_o is the friction stress (4 MPa), b is the Burger's vector of the dislocation (2.5 Å for nickel), and α is a dimensionless drag constant (0.98). The above values for nickel were determined in Baskes and Daw (1990). A closed form solution can then be used to track the dislocation motion. The left-hand-side is the time rate of change of the dislocation momentum. The first term on the right hand side is the driving force for motion, and the second term is the dissipation due to dislocation-phonon drag, which is the important factor related to the applied strain rate. Consider a dislocation nucleated a distance x_0 from a free surface. We modify equation (2.10) where σ_I is the stress due to image forces and is related to the nucleation stress, σ^*, as follows:

$$\sigma_I = \frac{x_0}{x}\sigma^* \tag{2.13}$$

where x is the current dislocation position, and M is the orientation factor related to the resolved shear stress. Here, we assume that the dislocation is nucleated at time zero at position x_0 from the surface when the applied shear stress equals the nucleation stress. The dislocation accelerates under increasing load. When a 0.2% plastic strain offset is assumed for yield, the only free parameter in the model is the nucleation stress σ^*, which is chosen to agree with the atomistic simulations. The nucleation stress is the only size dependent quantity in the model.

The next important time domain of importance is related to the applied strain rate. In our simulations, we start with a strain rate on the order of the atomic period (10^{12} s^{-1}) and then decrease it five orders of magnitude (10^7 s^{-1}). A critical peak strain rate exists in which the stress is so high that the lattice strength of the crystal is reached and immediate fracture occurs between the atoms with the applied boundary condition and the adjacent atoms. The results

that we show do not include these data, since we are not concerned with fracture in our study. When the applied strain rate is between the peak fracture strain rate and the time domain in which dislocation inertial effects are important, the global yield stress increases with increasing model size. When the applied strain rate is below this regime, then the yield stress increases with decreasing spatial size. In any event, as the applied strain rate increases, the yield stress and the magnitude of the stress-drop increases as expected from phonon drag.

Given this information, we ran several atomistic simulations at different sizes and applied strain rates and determined the yield stresses based on a 0.2% strain offset. The stress strain curves are presented in Figures 2.23-2.29 for different atomistic model sizes. These figures show that as the strain rate increases, the flow stress increases. The yield stresses, normalized by the shear modulus, for the different nickel simulations are shown in Figure 2.30. The full gamut of strain rate behavior as discussed above is only seen for the intermediate size samples. For these samples we see that at relatively small strain rates, the yield stress is independent of strain rate, while at higher strain rates the yield stress increases rapidly. For the small samples the extreme increase in yield stress is subsumed by the fracture regime (not shown). For the large samples, due to computer limitations, we were not able to calculate strain rates low enough to reach the strain rate independent regime. In Figure 2.30 we also compare the same atomistic data to the simple model presented above. The choice of the nucleation stress as a function of size is discussed below. We see that the simple model captures the qualitative features of the data: strain rate independence at low strain rate; a rapid increase in yield stress at a critical strain rate; and an increase in the critical strain rate with decreasing sample size. The decrease in the low strain rate plateau with increasing sample size is not a prediction of the model, but was input as the size dependence of the dislocation nucleation stress. The dislocation model predicts an increase in yield stress at high strain rates more rapid than the atomistic simulations. This effect is due to the fact that we have only allowed the nucleation of one dislocation, that is, the dislocation density is constant. At the higher strain rates, multiple dislocations are nucleated, lowering the yield stress from the model calculation prediction. To analyze the trend, Figure 2.31 shows experimental curves for single crystal copper illustrating that the trend for increasing flow stress with increasing applied strain rate occurs for other metals as well. All of the strain rate features noted above for the simulations and the dislocation model have also seen in the experimental data (cf, Edington, 1969; Follansbee, 1988).

Again referring to Figures 2.23-2.29, we see that the micro-yield points and macro-yield point both increase with increasing applied strain rate. However, an increase in applied strain rate increases the strain difference ($\Delta\varepsilon_{yield}$) between the micro-yield points and macro-

yield point. This effect also occurs as the model size increases as shown in Figure 2.3. For the high applied strain rate, the reason that the strain difference increases between the micro-yield points and macro-yield point point is due to the time domains in which the dislocation nucleation rate and velocity are of different magnitudes than the applied strain rate. As such, at low dislocation densities and at low dislocation velocities, the applied strain cannot be fully accommodated by dislocation propagation, so a lower modulus arises that looks like work hardening between the micro-yield points and macro-yield point. The larger size blocks of atoms exacerbate this effect.

2.6 Size Scale Effects

These simulations comprise sizes from 100 atoms to 100 million atoms and strain rates ranging from 10^7 to 10^{12} s^{-1}. We compare our atomistic simulation results to experimental data obtained from interfacial force microscopy (IFM), nano-indentation, micro-indentation, and small-scale torsion. The data is found to scale with a geometric length scale parameter defined by the ratio of volume to surface area of the samples. The atomistic simulations reveal that dislocations nucleating at free surfaces are critical to causing micro-yield and macro-yield in pristine material. The increase of flow stress at increasing strain rates results from phonon drag, and a simple model is developed to demonstrate this effect. Another important aspect of this study reveals that plasticity as reflected by the global averaged stress-strain behavior is characterized by four different length scales: (1) below 10^4 atoms, (2) between 10^4 to 10^6 atoms (2 μm), (3) between 2 μm and 300 μm, and (4) above 300 μm.

Analysis of size scale effects and strain rate effects related to plasticity are studied in the context of molecular dynamics simulations. Few studies, if any, couple these size scale and strain rate effects in plasticity. At the macro-scale, strain rate and temperature effects have been studied for many ductile metals (Johnson and Holmquist, 1989; Bammann et al., 1993; Gray et al., 1994).

Attention to plasticity at smaller size scales has included independent studies of indentation experiments, thin wire torsion tests, and atomistic simulations. Experimental and some theoretical studies on size scale dependence related to plastic deformation follow after the seminal work of Hall (1951) and Petch (1953). For example, recent studies such as Ma and Clarke (1995), McElhaney et al. (1997), and Michalske and Houston (1998) examined grain size effects on yield and hardness for different FCC metals. Nix and Gao (1998) and Begley and Hutchinson (1998) explained this plastic indentor size effect by modifying classical plasticity theory to include strain gradients, which are attributed to the presence of geometrically necessary dislocations. Thin wire experiments like those of Fleck et al. (1994)

included wires with diameters down to 12 μm. In these experiments, a definite size scale effect was observed in torsion on the yield stress and plasticity of the wires. Fleck and Hutchinson (1993, 1997) later applied a strain gradient theory to analyze the size scale effects they found. Holian and Lomdahl (1998), Daw and Baskes (1990), and Hoagland and Baskes (1998) have studied effects of dislocations on plastic response using atomistic methods. Kitamura et al. (1997) examined nano-scale tensile bars of nickel employing molecular dynamics. The purpose of our study is to analyze spatial size scale and strain rate issues on yield and plasticity at the atomic scale since little work has focused on this coupling.

The upper limit of atomic size is determined by the capability of the computing platform. In our simulations, we were trying to reach a certain strain level. As the model size is increased, the strain rates must be large to run the simulation in a reasonable time. This trade-off of model size and strain rate is illustrated schematically in Figure 2.1. If lower strain rates are desired, it is necessary to decrease the size of the atomic model. Our purpose in this manuscript is to broach the limits of current atomistic computing for examination of yield and plasticity of single crystal metals (mostly nickel) by using serial and parallel computing platforms. The schematic in Figure 2.1 indicates the regions where local and non-local continuum theories are applicable based on this study. Here, a nonlocal continuum theory is one in which a size scale is included within the structure of the governing equations.

When the nickel data in Figures 2.23-2.29 are rearranged according to spatial size, we can see that a size scale effect arises as shown by the stress-strain curves in Figure 2.32 at a strain rate of 2.4×10^8 s^{-1}. This size scale effect is also observed in copper as shown in Figure 2.33 at a strain rate of 10^9 s^{-1}.

We may also compare the rate-independent (plateau) yield stresses as a function of specimen size. In Figure 2.34 we show the normalized yield stress as a function of the x-dimension size of the model. Note that the models considered here have the z-dimension constant and the x:y aspect ratio fixed at ~2:1, so that the single x-dimension fully characterizes the model. We see a clear power law dependence of the rate-independent yield stress with the stress varying as model size to the -1/4 power. This dependence was used to define the size dependence of the dislocation nucleation stress σ^* in the dislocation model calculations presented above in Fig. 2.30.

Figures 2.32and 2.33 show size scale effects in the stress-strain response for single crystal nickel and copper. The goal here was to illustrate that another FCC metal, besides nickel, experiences a similar size scale effect in terms of increasing size decreases the yield stress. If this size scale effect is universal, what is an appropriate length scale parameter?

In trying to understand yield at different length scales, we need to have a common length scale parameter. For this purpose, we choose a volume-to-surface-area as our metric. This volume-to-surface area can be defined very clearly for each test method and atomistic simulation. Table 2.3 summarizes the values for the analysis performed in this study related to the specimen geometries.

Table 2.3. Volume-to-surface areas for various geometries.

Geometry	volume	surface area	volume/surface area
simple shear (cell dimensions, x_c, y_c,z_c)	$x_c y_c z_c$	$2y_c z_c$	$x_c/2$
torsion (cylinder radius, r; height, h)	$\pi r^2 h$	$2\pi rh$	r/2
IFM (contact radius, a;)	$2/3\pi a^3$	πa^2	2/3a
indentation (contact radius, a; indentation depth, h; indentor tip angle, θ)	$2/3\pi a^3$	πa^2	$2/3a=2/3*h/\tan\theta$

Figure 2.35 shows a log-log plot of yield stress under simple shear (atomistics) and torsion and indentation (experiment) normalized by elastic shear modulus and resolved on a (111) slip plane as a function of the characteristic length scale given by the volume-to-surface-area ratio. This plot shows a clear size scale effect. The atomistic results come from the current molecular dynamics calculations in the rate-independent region of strain rates. A resolved shear stress factor of 0.577 was applied to the data of Figure 2.34.

The experimental torsion data (Fleck et al. 1994) shown in Figure 2.35 is from small-scale torsion tests of polycrystalline copper at a strain rate of 10^{-3} s^{-1} at room temperature. The volume-to-surface-area was chosen to be the torsion specimen radius divided by two (Table 2.3). To obtain the maximum shear stress at the surface of the cylinder, the normalized torque data presented in the manuscript was multiplied by $\pi/3$ and divided by the shear modulus of copper. It was assumed that at least one grain in the polycrystalline sample was orientated perfectly for slip, hence no resolution factor was applied. This analysis gives an upper bound on the resolved yield stress.

Indentation hardness, H of ductile metals is considered a measure of the yield stress in compression, H=3*yield (Tabor, 1951). Although inadequate measurement techniques and surface contaminants can cause apparent increases in hardness at small loads, the bulk of the data from many experimenters illustrates a common thread of increased hardness, and subsequently yield, as the size scale decreases. McElhaney et al. (1997) illustrated the size dependence on yield for both single crystal and polycrystalline copper. The McElhaney et al. (1997) single crystal data is included in Figure 2.35. To determine the appropriate length

scale, we consider the size of the volume of copper under the indentor that is has plastically deformed. A reasonable assumption is to take that volume as a hemisphere with radius equal to the contact radius (Nix and Gao, 1998). The surface area is taken as the contact area. A resolved shear stress factor of 0.228 (Kiely and Houston, 1998) and tip angle of $\tan\theta = 0.358$ were used.

Interfacial force microscopy (IFM) data for gold from Michalske and Houston (1998), which is also plotted on Figure 2.35, appears to align very nicely, albeit a bit higher, with the atomistic results. The difference may be due to the fact that the atomistic data are quasi-static values and a higher, changing strain rate occurs in the IFM data. Here, the total-volume-to-surface area was determined for the spherical indentor as 2/3 of the contact radius (see Table I), which is determined by simple geometry from the tip radius and the indentor depth at yield. The yield stress was calculated using the Hertz model and the shear stress data presented in the experimental manuscript. A resolution factor of 0.228 (Kiely and Houston, 1998) was applied to the applied stress. Michalske and Houston's argument that dislocation nucleation governs yield stress at this length scale compares extremely well with the work of Horstemeyer and Baskes (1999).

We have also examined nanocrystalline metals in the context of the volume-to-surface area but found much scatter in the data and as such the data is not plotted here. Masumura et al. (1998) have reviewed many studies on nanocrystalline materials and concluded that above a certain length scale, the Hall-Petch relation operates but not below that particular level. Their data indicate that that the Hall-Petch relation does not work in tension. As mentioned earlier, by analyzing the length scale effect in tension other competing dissipative mechanisms can contribute to the stress-strain or hardness behavior, in particular, void nucleation or growth. With these different mechanisms involved we deemed it unfruitful to pursue this data.

One last comment regarding the size scale effect is warranted. In Figure 2.35 are the results of a simple model using the concept of geometrically necessary dislocations by Nix and Gao (1998). The model was fit to the McElhaney et al. (1997) single crystal data. We see that extrapolation of this model to smaller length scales yields good agreement with the Michalske and Houston (1998) data and fair agreement with the atomistic simulations. Note that the model does not agree at all with the torsion data. In contrast, a simple power law seems to represent all of the data reasonably well in which the only argument needed is that related to dislocation nucleation.

By examining the global stress-strain responses of the atomistic simulations, we observed two forms of bulk plastic behavior depending on the size of blocks of atoms. Coupling this computational information with experimental data from others (cf. Fleck et al.,

1994), we assert that four regions of bulk plastic behavior exist based upon the size scale of the solid medium as summarized by the schematic in Figure 2.36. The first spatial domain is roughly below about ten thousand atoms, less than 200Å. The exact size varies depending upon the crystal orientation, strain rate, temperature, and boundary conditions but it is approximately this scale. Here, the local atomic vibrations play a critical role, and three characteristics of the stress-strain curve are demonstrated: high frequency stress oscillations throughout the stress-strain curve, a large difference between micro-yield and macro-yield, and a stress drop-off after macro-yield. To employ a continuum plasticity model in this spatial domain, a vibration analogy with a size scale parameter would be appropriate (cf. Horstemeyer and Baskes, 1999). In terms of computations, these simulations were performed in a serial environment.

Above several thousand atoms and below one hundred million atoms (about 2 μm), the high frequency stress oscillations are damped out because of the averaging procedure used to determine the global continuum stress. However, the stress drop-off occurs at a macro-yield still giving rise to a difference between the micro-yield points and the macro-yield point. To model this spatial domain with a continuum plasticity model, a theory that includes a size scale is needed. In terms of computations, these simulations were performed in a parallel environment.

Both of these regions are dominated by dislocation nucleation and not by the morphological distribution or number density of dislocations, because the material is initially dislocation free. As discussed earlier, the stress-strain response looks much like a whisker in this region. Figure 2.36 shows a comparison of stress-strain responses for two different sizes illustrating the two different plasticity regions. Note as the size increases, the yield stress decreases. We discuss these trends with relatively small blocks of atoms in Horstemeyer and Baskes (1999).

In the third spatial domain between 2 μm (approximately) and 300 μm, the stress drop-off does not exist and micro-yield and macro-yield start to converge, but a length scale dependence is still obtained as evidenced in Fleck *et al.* (1994). Above 300 μm, a power law function without a size scale parameter can describe the stress-strain response. Although single crystal whiskers can be obtained in spatial domains 2 and 3, the Fleck *et al.* (1994) data relate to polycrystalline metals. For the polycrystals, dislocation nucleation is not as dominant as the dislocation number density and morphological distribution in determining the stress state. Hence, there is a gradual influence change from dislocation nucleation at much smaller scales to dislocation number density and distribution at larger scales. Fleck et al. (1994) conducted

torsion tests of polycrystalline copper that ranged from 12 μm to about 300 μm. Their data revealed that a stress drop-off did not exist after macro-yield but a length scale effect did indeed exist when determining yield and the work hardening rate. The length scale effect seems to disappear at about 300 um thus defining the demarcation between the third and fourth spatial domains of plasticity. In this fourth spatial domain, atomistic simulations are currently out of reach for even parallel computing. However, as computers get faster, atomistic simulations will be able to be performed in this region in the near future. As far as continuum modeling, Fleck and Hutchinson (1993; 1997) have employed a strain gradient theory to analyze the length scale effects.

The fourth spatial domain is above 300 microns. For the most part, one can expect different stress-strain behavior between a single crystal and polycrystal, yet qualitatively once both types of materials reach a large enough size the dislocation distribution and morphology is such that a size scale dependence is not realized. One can think of it in terms of a plastic zone size. Once the plastic zone is on the order of the material block, size scale effects can be expected. In considering a polycrystal without second phases, once the plastic zone is small compared to the material block of interest, no stress oscillations, stress drop-offs, or size scale dependence are observed. Local continuum models have been used to solve engineering problems in this spatial domain fairly well.

2.7 Comparisons of EAM and FEM Analysis

In this section, we examine FCC nickel undergoing simple shear by using three different numerical frameworks formulated at three different size scales. The three frameworks included Embedded Atom Method (EAM) potentials used in molecular dynamics simulations, crystal plasticity used in finite element simulations, and a macroscale internal state variable formulation used in finite element simulations. Simple shear simulations were performed in which the specimen aspect ratio was varied to give insight into the homogeneous and inhomogeneous aspects of large deformation. This study revealed that as the length-to-height aspect ratio of the specimen increased, the yield stress increased until the ratio reached about 8:1 in which the yield stress saturated. The three disparate numerical frameworks also gave similar qualitative responses related to inhomogeneous stress and strain distributions in the corner regions of the specimens and also similar responses in the centralized homogeneous deformation region. However, when comparing the shear stress distribution for the finite element analyses to the atomistic simulations, a much narrower distribution arose for the finite element analyses due to the lack of thermal vibrations experienced in the atomistic simulations at 300K. At 10K an atomistic simulation which dampened out the high frequency thermal vibrations verified this reasoning. Three different sizes of blocks of atoms were also used in

the atomistic simulations and the results showed very similar stress and strain distributions with respect to each other indicating that no size scale effect is evidenced in the morphology when normalized by the global shear stress. However, a size scale effect exists related to the global (volume average) shear stress in the block of material. As the specimen size increased, the yield stress decreased. Finally, when comparing the three different numerical frameworks, the location of maximum dislocation nucleation occurred at the location of the maximum plastic spin, stress gradients, and strain gradients.

Starting from the atomistic to the crystal plasticity and then to the macroscale internal state variable frameworks, the degrees of freedom in the simulations decrease. The atomistic simulations start from one atom and build up. The crystal plasticity formulation starts at the scale of the grain and builds up. And the macroscale internal state variable starts from a macroscale continuum point, which usually represents a polycrystalline material but in this case was tuned to single crystal experiments. As such, the macroscale internal state variable formulation does not include explicit details about the plastic spin (texture effect), but the crystal plasticity and atomistic formulations do. Furthermore, the macroscale internal state variable theory and crystal plasticity formulations do not include the thermal velocity (and vibration) effects related to atomic rearrangement or subgrain division arising from large strains, but the atomistic formulation does.

In order to bridge length scales, one can perform physical experiments to quantify the appropriate cause-effect relations between the microstructure and mechanical properties. However, these experiments are costly and to date are wanting. An alternative view is to use "numerical" experiments by using different numerical methods that clearly describe the cause-effect relations at different size scales. This is the motivation for the current study. Before this writing, neither multiscale physical experiments nor multiscale numerical experiments have been performed on a material like single crystal nickel; hence, this is our contribution.

Researchers have examined constitutive models via simple shear or torsion for years, because crystallographic slip occurs on shear planes. In this study, we do not strictly examine simple shear although the terminology is used henceforth for ease of communication. Simple shear requires that the traction-free face of the continuum point planar and parallel, strictly speaking. We loosen that requirement to analyze the inhomogeneous and homogeneous portions of the material block for the modeling frameworks. Our ultimate goal was to examine simple shear experiments, which do not constrain the x-faces to be planar and parallel and as such our boundary conditions are more applicable to simple shear experiments.

In this section, we briefly describe the pertinent attributes of the three numerical methods related plasticity at different length scales for nickel. The atomistic simulations were

conducted using Embedded Atom Method (EAM) potentials (Daw and Baskes, 1984). Finite element simulations using ABAQUS were conducted using two different constitutive models.

One model was a crystal plasticity formulation based on the Cuitino and Ortiz (1992) kinematics but with the hardening equations from Horstemeyer *et al.* (1999). Another constitutive model used was a macroscale internal state variable theory from the work of the Bammann *et al.* (1990; 1993; 1996).

For the single crystal kinematics, the multiplicative decomposition of the deformation gradient into elastic (including rigid lattice rotation) and plastic parts is assumed, i.e. $\underline{F}=\underline{F}^e\underline{F}^p$. $\underline{F}^p$ is computed at the end of the time step by applying the Cayley-Hamilton theorem,

$$\underline{F}^p_{t+\Delta t} = \exp\left(\underline{L}^p \Delta t\right)\underline{F}^p_t \tag{2.14}$$

where $\underline{F}^p_t$ and $\underline{F}^p_{t+\Delta t}$ are the plastic deformation gradients at the beginning and end of the time step, respectively. $\underline{L}^p$ is the plastic velocity gradient in the intermediate configuration that occurs during the time step, which is determined by (Asaro, 1983)

$$\underline{L}^p = \sum_{i=1}^{N} \dot{\gamma}_i \left(\underline{s}_i \otimes \underline{m}_i\right) \tag{2.15}$$

where N is the number of slip systems, $\dot{\gamma}_i$ is the continuum slip or shear rate on the i^{th} slip system, $\underline{s}_i$ is the slip direction vector, and $\underline{m}_i$ is the slip plane normal vector. The hyperelastic stress-strain relation is specified in the intermediate, or stress-free, configuration as

$$\hat{\underline{\sigma}}\left(\hat{\underline{E}}\right) = \underline{\underline{C}} : \hat{\underline{E}}, \tag{2.16}$$

where the elastic stiffness tensor, $\underline{\underline{C}}$, is invariant for a given crystal in the intermediate configuration (cf. Asaro, 1983). The intermediate configuration is aligned with the crystalline axes. $\hat{\underline{\sigma}}$ is the second Piola-Kirchhoff stress in the intermediate configuration, and $\hat{\underline{E}}$ is the conjugate Green elastic strain.

The viscoplastic kinetic relation used is a kinematic hardening generalization of the form employed by Hutchinson (1976), i.e.

$$\dot{\gamma}_i = \dot{\gamma}_o sgn\left(\tau_i - \alpha_i\right)\left|\frac{\tau_i - \alpha_i}{g_i}\right|^M , \tag{2.17}$$

where the plastic slip rate on the i^{th} slip system, $\dot{\gamma}_i$, is a function of a fixed reference strain rate, $\dot{\gamma}_o$, the reference shear strength, g_i, the resolved shear stress on the slip system, τ_i, the rate sensitivity exponent for the material, M, and an internal state variable representing kinematic hardening effects resulting from backstress at the slip system level, α_i. The isotropic hardening evolution law for the internal hardening state variable, g_i, on i^{th} slip system is given by

$$\dot{g}_i = \sum_{i,j=1}^{12} h_{ij}\dot{\gamma}_j \tag{2.18}$$

where h_{ij} are the hardening (or plastic) moduli. The self-hardening components arise when $i=j$ and the latent hardening components arise when $i \neq j$. The increase or decrease of flow stress on a secondary slip system due to crystallographic slip on an active slip system is referred to as latent hardening. A modified hardening-recovery equation was used with the PAN rule (Peirce *et al.*, 1982) given by

$$h_{ij} = F(\gamma)\left(\delta_{ij} + lhr\left(1-\delta_{ij}\right)\right), \tag{2.19}$$

where lhr is the latent hardening ratio. The modified Armstrong and Frederick (1966) hardening-recovery equation that was also used is given by

$$F(\gamma) = h_0 - Rg(\gamma), \tag{2.20}$$

where R is a material constant. We employ a substructural internal variable evolution equation (Horstemeyer and McDowell, 1998) that is assumed to evolve at the level of the grain. For the Armstrong-Frederick form, we employ the following form for each crystal

$$\dot{\alpha}_i = C_{rate}\left(C_{sat}\dot{\gamma}_i - \alpha_i\|\dot{\gamma}_i\|\right), \tag{2.21}$$

where C_{rate} controls the rate of evolution, and C_{sat} is the saturation level of the backstress and were chosen to fit the experimental data. The substructural hardening internal state variable reflects dislocation interactions within the grain (cf. Rice, 1971) and follows the Coleman and Gurtin (1967) postulate that the rate must be governed by a differential equation in which the plastic rate of deformation appears.

Once the material constants were determined from single crystal nickel experiments (Edington, 1969), simple shear simulations were run with different geometries, and the volume average of the shear stress was used for the discussion purposes to follow.

For the internal state variable (ISV) plasticity model (Bammann *et al.*, 1990; 1993; 1996) used in this study, the kinematics and work hardening equations are similar to the crystal plasticity formulation except that the intermediate configuration is not aligned necessarily to the crystalline axis of a single crystal due to the absence of a plastic spin component. The pertinent equations in this model are denoted by the rate of change of the observable and internal state variables. The equations used within the context of the finite element method are given by,

$$\overset{\circ}{\underline{\sigma}} = \dot{\underline{\sigma}} - \underline{W}^e\underline{\sigma} - \underline{\sigma}\underline{W}^e = \lambda tr\left(\underline{D}^e\right)\underline{I} + 2\mu\underline{D}^e \tag{2.22}$$

$$\underline{D}^e = \underline{D} - \underline{D}^{in} \tag{2.23}$$

$$\underline{D}^{in} = f(T)\sinh\left[\frac{\|\underline{\sigma}'-\underline{\alpha}\| - \{R+Y(T)\}}{V(T)}\right]\frac{\underline{\sigma}'-\underline{\alpha}}{\|\underline{\sigma}'-\underline{\alpha}\|} \tag{2.24}$$

$$\overset{o}{\underline{\alpha}} = \dot{\underline{\alpha}} - \underline{W}^e\underline{\alpha} + \underline{\alpha}\underline{W}^e = \left\{h(T)\underline{D}^{in} - \left[\sqrt{\frac{2}{3}}r_d(T)\|\underline{D}^{in}\| + r_s(T)\right]\|\underline{\alpha}\|\underline{\alpha}\right\} \tag{2.25}$$

$$\dot{R} = \left\{ H(T)\underline{D}^{in} - \left[\sqrt{\frac{2}{3}} R_d(T) \left\| \underline{D}^{in} \right\| + R_s(T) \right] R^2 \right\} \tag{2.26}$$

The rate equations are generally written as objective rates ($\overset{o}{\underline{\sigma}}, \overset{o}{\underline{\alpha}}$) with indifference to the continuum frame of reference assuming a Jaumann rate in which the continuum spin equals the elastic spin ($\underline{W} = \underline{W}^e$). The internal state variable (ISV) Equations (2.25)-(2.26) are functions of the observable variables (temperature, stress state, and rate of deformation). In general, the rate equations of generalized displacements, or thermodynamics fluxes, describing the rate of change may be written as independent equations for each ISV or as derivatives of a suitably chosen potential function arising from the hypothesis of generalized normality (Rice, 1971). In Equation (2.22), the elastic Lame constants are denoted by λ and μ. The elastic rate of deformation ($\underline{D}^e$) results when the flow rule as shown in Equation (2.24) is subtracted from the total deformation ($\underline{D}$), which is defined by the boundary conditions.

The independent variables for the inelastic rate of deformation are given in Equation (2.24) as the stress, temperature, and internal state variables. The deviatoric inelastic flow rule, $\underline{D}^{in}$, encompasses the regimes of creep and plasticity and is a function of the temperature, the kinematic hardening internal state variable ($\underline{\alpha}$), the isotropic hardening internal state variable (R), and the functions $f(T)$, $V(T)$, and $Y(T)$, which are related to yielding with Arrhenius-type temperature dependence. The function $Y(T)$ is the rate-independent yield stress. The function $f(T)$ determines when the rate-dependence affects initial yielding. The function $V(T)$ determines the magnitude of rate-dependence on yielding. These functions are determined from isothermal compression tests with different strain rates and temperatures.

$$V(T) = C_1 \exp\left(-C_2/T\right), \; Y(T) = C_3 \exp\left(C_4/T\right), \; f(T) = C_5 \exp\left(-C_6/T\right). \tag{2.27}$$

The kinematic hardening internal state variable, $\underline{\alpha}$, reflects the effect of anisotropic dislocation density, and the isotropic hardening internal state variable R, reflects the effect of the global dislocation density. The functions $r_s(T)$ and $R_s(T)$ are scalar in nature and describe the diffusion-controlled static or thermal recovery, while $r_d(T)$ and $R_d(T)$ are scalar functions describing dynamic recovery. Hence, the two main types of recovery that are exhibited by populations of dislocations within crystallographic materials are captured in the ISVs. Note that the discrete dislocations that are present in the EAM similuations are not explicitly included here. In the context of this paper, the static recovery terms are set to zero. The anisotropic hardening modulus is $h(T)$, and the isotropic hardening modulus is $H(T)$.

$$r_d(T) = C_7 \exp\left(-C_8/T\right) \tag{2.28}$$

$$h(T) = C_9 - C_{10}T \tag{2.29}$$

$$r_s(T) = C_{11} \exp\left(-C_{12}/T\right) \tag{2.30}$$

$$R_d(T) = C_{13} \exp\left(-C_{14}/T\right) \tag{2.31}$$

$$H = C_{15} - C_{16}T \tag{2.32}$$

$$R_s(T) = C_{17} \exp\left(-C_{18}/T\right) \tag{2.33}$$

Once the material constants were determined from single nickel experiments (Edington, 1969), simple shear simulations were run with different geometries, and the volume average of the shear stress in the elements was used for the discussion purposes to follow.

For all three numerical frameworks, fixed-end simple shear boundary conditions were prescribed in which the computational block of material had free surfaces in the x- and y-directions and was periodic in the z-direction. The initial temperature was set at 300 K. The applied strain rate for the atomistic simulations was very large (~1e9/sec), while the parameters for the crystal plasticity and macroscale ISV models were determined from rate independent strain rates (~1e4/sec). This introduces a contrast in stresses since the larger applied strain rate would induce a larger stress level. Hence, there exists not only a size scale difference but a time scale difference between the atomistic simulations and the continuum level simulations. For the EAM and crystal plasticity simulations, the crystal orientation was $[100, 011, 0\bar{1}1]$, and the loading on y-face was in the [100] direction. For the macroscale ISV model, single crystal properties were used but the crystallographic orientation cannot be represented discretely. In a sense, it responds like an isotropic polycrystal.

A few other notes are warranted. First, we focused on fixed-end simple shear at the three size scales because we had planned a complementary experimental study that is yet to be completed with different size specimens in this condition. Second, we discuss the qualitative comparisons of the results from the three types of simulations and then discuss the quantitative differences and describe the underlying mechanisms that are attributed to the aspect ratio of the specimen, material model, stress state, and kinetics.

In all of the atomistic simulations, dislocations would nucleate from the free-surfaces of the x-faces and in particular, near the specimen corners where inhomogeneous deformation arose. Figure 2.37 illustrates this point for an eight-by-one x/y aspect ratio. Figure 2.37a shows a close-up view of the corner in which the dislocations were nucleated. Clearly, the shear stresses as designated by the brown colors are higher near the corner when contrasted with the bulk atomic

shear stresses, which show an almost homogeneous distribution of yellow atoms in Figure 2.37b. Figure 2.37c shows that as deformation proceeds to 30% strain that the dislocations populate the whole material bulk.

To further illustrate the flow of dislocations, we employ the centrosymmetry parameter of Kelchner et al. (1998), which shows deviations of the atomic positions from original lattice positions. Figure 2.38 shows color contours of the centrosymmetry parameter at different strains in the stress-strain response. The second picture in Figure 2.38 approximately corresponds to Figure 2.37a and Figure 2.37b near yield. Also, Figure 2.37c corresponds to the last picture in Figure 2.38 at 30% strain. When comparing Figures 2.37 and 2.38, one can see that the stress response (Figure 2.37) and centrosymmetry parameter (Figure 2.38) correlate fairly well in signifying the dislocation nucleation, motion, and interaction.

Figures 2.39 and 2.40 compare the shear stress and shear strain responses, respectively, of the three numerical frameworks for the one-by-one block of material. Figures 2.41 and 2.42 show the same comparisons for the eight-by-one block of material. Interestingly, the material response at the corners due to the simple shear boundary conditions is the same for each numerical framework whether you examine the stress or strain. Although the magnitude of the stress is different for each framework (because of the size scale and applied strain rate), the kinematic response is essentially the same. This is extremely important for development of the kinematics of higher scale modeling such as a crystal plasticity model or a macroscale ISV model. One can also see that the center region of the crystal plasticity simulation is qualitatively different than the macroscale ISV simulation due to the rate of change of the crystal orientation. Figure 2.42d shows that for one of the Euler angles with an initialization of 90 degrees throughout the bulk at yield we see an angle decrease in some elements by 5 degrees at the corners indicating that local rotations play a role in accommodating the simple shear boundary conditions. When you couple this information with the atomistic simulation results of dislocation nucleation, you can deduce that the gradient in rotation plays a role in the nucleation of dislocations.

Similar to Figures 2.39-2.42 at yield, we show the simulation responses at 30% strain, which puts the simulations well into the plasticity region in Figures 2.43-2.46. The stress and strain plots in Figures 2.43-2.46 shows similar trends as the yield plots. The similarities between the three different numerical methods is again very close when considering the kinematic responses and is qualitatively similar for the stress distributions. One interesting observation related to Figure 2.46d is that the crystal orientation has changed from an initial orientation of 90 degrees to almost 30 degrees for some elements for the x/y aspect ratio of eight, indicating a very large difference in rotations for some elements of the crystal plasticity simulation.

Another similarity between the three computational methods can be seen in Figure 2.47. Figure 2.47 shows the volume averaged yield stresses normalized by the shear modulus over the block of material with varying aspect ratios for the macroscale internal state variable theory

simulations, crystal plasticity simulations, and the atomistic simulations. This plot illustrates that as the x/y aspect ratio of the specimen increases, the yield stress increases until a saturation is achieved. Further, as the y/x aspect ratio of the specimen increases, the yield stress decreases. In Figure 2.47a, the yield stress increases as the x/y ratio increases until a saturation level is reached at an aspect ratio of approximately eight. Horstemeyer and Baskes (1999) proposed that this could arise for two reasons. Because the stress gradients near corners induced dislocations that determine the yield point, as more bulk response arises as the material in the x-direction is increased, then the global effect of dislocations nucleating from the corner decreases. Another notion to describe the x/y ratio increase in shear stress comes from an argument that image force effects could aid the nucleation event. However, the crystal plasticity and macroscale ISV theory show the same qualitative stress and strain gradients, and these numerical treatments do not include explicit functions for dislocation nucleation or image force effects.

Now that we have discussed the qualitative similarities of the three computational methods, we know discuss their quantitative differences. In Figures 2.39-2.46, at yield and at large strains, we saw similar trends in the kinematic and stress response. In Figure 2.47, we saw that the specimen aspect ratio differences gave similar trends in the stress response. However, in each of the cases the stress magnitudes are different for the three different numerical methods.

In Figure 2.47 note that the ordinate has logarithmic units so as the size of the material decreases, the yield stress significantly increases. This occurs because the strength of a solid is inversely proportional to the material size as described by Horstemeyer and Baskes (1999). For the atomistic simulations, we conducted simulations with the same aspect ratios for the blocks of material but with different absolute sizes to illustrate the length scale effect. The macroscale ISV theory and crystal plasticity formulation do not have an inherent length scale included. However, with the crystal plasticity and macroscale ISV theory do show the general trend of size scale dependence as the material model parameters were determined from large scale single crystal data and polycrystalline data

Now we would like to discuss the contrasting results from the varying aspect ratios of the specimens. Using the macroscale ISV theory Figure 2.48 illustrates that when the x/y aspect ratio transitions from eight to unity, the stress distribution is more diffuse because of the influence of the gradients. When the y/x aspect ratio transitions from unity to eight, the stress distribution becomes less diffuse as shown in Figure 2.48. One can think of large x/y ratios as "pure" shear and large y/x ratios as "pure" bending. When the ratio approaches unity, a combined response results. Note that if the distribution of stresses is averaged, like in the data in Figure 2.47, as the x/y aspect ratio increases, the stress increases. This occurs even though a very similar stress distribution occurs in the corners of specimens for the x/y aspect ratios of unity and eight as shown in Figure 2.49 (which exaggerates the effect from the yield point because these stress contours at shown at 30% strain). However, when the x/y aspect ratio is near unity, the gradients

in stress from the corners play more of role than the average values in the center of the specimen. Essentially, the corners introduce inhomogeneous deformation, but the center of the specimen accommodates homogeneous deformation. As the aspect ratio size increases in either direction, the average stress swamps out the gradient effects. Based on these observations, we can conclude that the stress gradients drive the atomic level dislocation nucleation events as well.

From Figure 2.47b, one can see that as the y/x ratio increases, the yield stress decreases. Horstemeyer and Baskes (1999) claimed that volume per surface area of the block of material represents a length scale that correlates to yield and is illustrated by increasing the surface area on the y-face of the material block. This is indeed true, but the crystal plasticity and macroscale ISV theory also provide some insight into the response. Essentially, as the height increases, the mechanism for inducing yield changes because the stress state changes from simple shear to one in which normal stresses are dramatically increased. As such, the volume averaged yield is lowered. Figure 2.50 shows the relative displacements of the atoms and the corresponding shear stress by the color at yield and 30% strain. Clearly, the response in Figure 2.51 is different when compared to Figure 2.37, which shows a block of material with a y/x ratio of 0.125. The larger y/x ratio appears to not only have more surface area available for dislocation nucleation, but experiences material thinning and a inhomogeneous deformation from beam bending, where the smaller x/y ratio (or larger x/y ratio) shows a more "homogeneous" deformation.

When a distribution of the angles is monitored and compared to the x/y aspect ratio of unity as shown in Figure 2.51, we see that the x/y aspect ratio of eight has a less diffuse distribution of angles than the x/y aspect ratio of unity. The smaller x/y aspect ratio almost has an even distribution from 69 to 75 degrees, but the larger x/y aspect ratio has a distribution that mostly saturates at 77 degrees. Hence, the width and mean value of the distributions are different. This observation is consistent with those made with the stresses. In fact, the gradient in crystal rotation corresponds well with the gradients shown by the shear stresses and shear strains as illustrated in Figure 2.52, which shows the x/y aspect ratio of unity at 30% strain.

Although these three different numerical frameworks show stress and strain gradients at the same locations within the block of material, the magnitude of the stress gradients are slightly different and can be illustrated when the results from the different simulations are normalized as shown in Figure 2.53. The ordinate in Figure 2.53 is the relative frequency of the local value for the shear stress divided by the total number of elements (for the FEM simulations) or number of atoms (for the EAM simulations). This helps to normalize the number density of the different simulations. The abscissa in Figure 2.53 is the local shear stress (eqtn 2.2) divided by the average global stress (eqtn 2.3). The results in Figure 2.53 show that the mean values are normalized at unity. The data to the right of the mean value illustrates the stress gradients that arise from the specimen corners with higher local shear stresses than average. The data to the left of the mean value represent the atoms and elements on the left and right x-faces away from the

corners. The stress and strain gradients that arise from the transition of the corner to the face occur where the dislocations nucleate in the atomistic simulations. Note from the atomistic simulations that as the size increases, the normalized distribution does not change. However, the crystal plasticity and internal state variable theory distributions have a much narrower distribution than the atomistic simulations. Furthermore, the lower bump that is observed to the right of the mean value in the atomistic simulations is to the left in the finite element simulations at 300 K. These two differences can be explained from a kinetics perspective. The 300 K simulations include fluctuations of local stresses from thermal vibrations, and these vibrations do not exist in the finite element simulations. To illustrate this point, we ran the smallest block of atoms (372 atoms) at almost 0 K (actually 10 K) with the same boundary conditions. The results in Figure 2.54 show that the 10 K simulation has a much narrower distribution and a lower bump to the left of the mean, much like the finite element simulations. In the 10 K simulation, the thermal vibrations are reduced to a minimum.

Other analyses that we performed were on simple shear and torsion of single crystal copper by employing experiments, molecular dynamics simulations, and finite element simulations. In particular, we focused on micro/macroyield stress and the kinematic response.

Pure FCC Cu has enjoyed a breadth of mechanical property studies. Although many Cu compression and tension tests have been done, few torsion and simple shear tests been conducted. Moreover, even fewer torsion and simple shear tests have been conducted on single crystals. Schmid and Boas (1950), Phillips (1962), Jackson and Basinski (1967), Honeycombe (1984), and Quilici *et al.* (1998) have noted critical resolved shear stresses under various loading conditions for single crystal Cu. In this work, we perform torsion tests of solid bars of single crystal Cu. Historically, little research has been presented with this type of test for several reasons. First, it is a difficult test to achieve accurate load-rotation responses. In this paper, we describe how our method yields repeatable responses. Second, researchers typically would use compression or tension tests to determine the yield strength. Third, researchers typically used thin-walled torsion tests to achieve large strains. By performing the single crystal solid bar torsion test (performed by W.Y. Lu and J. Lim) with a "minimal" amount of dislocations present, we show qualitatively the effects of dislocation nucleation on the yield point.

Two Cu single crystal bars with 99.999% purity were grown from a seed. The diameter of the specimens was 13 mm and the length was 50 mm with the [110] crystallographic direction parallel to the axial direction of the specimen. This orientation allowed for quadruple slip. Referring to Figure 2.55, in order to clamp the specimen to the torsional testing machine, each end of the specimen was epoxied inside an aluminum end cap. Figure 2.56 shows that the aluminum end caps were then clamped to a MTS multiaxial test system with one end clamped to the torque cell and the other end to the torsional actuator. The effective gage length of the specimen then became 17.6 mm.

Rotations were applied by the torsional actuator at a rotation rate of 0.25°/s. The torque-rotation curves of two different specimens (1 and 2) are plotted in Figure 2.57. The stress state can accurately be calculated using an elastic analysis at yield but will become more inaccurate as the deformation proceeds into the plastic regime. As such, we quote only stresses using the elastic formula near yield. Both curves in Figure 2.57 show that Cu single crystal yields at a very low stress level (near 10 MPa), but the work hardening rate after yield is very high. In the context of this section, we use microyield 1 and 2 for the analysis. Recall that microyield 2 is defined from the 0.2% strain offset. Microyield 1 is defined at the proportional limit, when deviation from linearity starts. Table 1 shows the microyield 1 and 2 values for the two specimens. The stress values in Table 2.4 were evaluated at the outer radius of the specimen only since the specimens experienced a gradient in plastic stresses as the deformation proceeded.

Table 2.4. Yield values of the torsion specimens.

Specimen #	Microyield 1	Microyield 2
1	3.5 MPa	9.8 MPa
2	4.8 MPa	10.6 MPa

An observation related to the kinematics of deformation on the outside surface of the specimen was made. As evidenced in Figure 2.58 from the machining marks on the surface of the specimens, a wavy pattern developed during torsion. These machining marks were initially straight before torsion. The sinusoidal wave illustrates material motion and is comprised of four periods resulting from the fourfold symmetry of the dislocation glide planes around the circumference with an average "amplitude" of approximately 0.35 mm at the center of the gage section. This wavy periodic deformation is shown in Figure 2.58 at strain level of 35%.

Table 2.5 summarizes the atomistic simulation parameters for simple shear and torsion. For the simple shear simulations, the two different size computational blocks of material had free surfaces in the x- and y-directions with periodicity in the z-direction. The x/y ratio was identical to the ratio of the circumference of the torsion specimen to its axial length for both the large and small atomistic specimens. For simple shear, the atoms in the top row in the y-direction were prescribed to move in the x-direction and the bottom row of atoms were fixed. For the torsion simulations, two different size computational blocks of material were fixed on one end with a rotation prescribed at the other end. An applied strain rate of ~1e9/sec was used for both types of simulations. A constant volume, a fixed number of atoms, and temperature of 300 K were used for the material that was oriented initially for quadruple slip. No initial defects were introduced into the material. An initial velocity in the x-direction scaled according to the height (y-direction) was introduced to alleviate a shock that would have otherwise been introduced. The atoms inside of the boundary atoms were used to determine the average stress of the block.

Table 2.5. Summary of information regarding atomistic simulations.

attribute	Large block torsion	Small block torsion	Large block simple shear	Small block simple shear
number of atoms	41,630	5298	23,628	332
length (x-dir)	-	-	250 Å	28 Å
heighth (y-dir)	20 Å	14 Å	108 Å	12 Å
depth (z-dir), periodic	-	-	7 Å	7 Å
radius	85 Å	41 Å	-	-
lattice parameter (Cu)	3.615 Å	3.615 Å	3.615 Å	3.615 Å
boundary condition	torsion [100]	torsion [100]	simple shear [100]	simple shear [100]
crystal orientation	$(001,110,1\bar{1}0)$	$(001,110,1\bar{1}0)$	$(001,110,1\bar{1}0)$	$(001,110,1\bar{1}0)$
temperature	300 K	300 K	300 K	300 K
applied strain rate	1e9/sec	1e9/sec	1e9/sec	1e9/sec

Figure 2.59 shows relative displacement results from a simulation at 35% shear strain for both sizes of material under simple shear. Similarly, Figure 2.60 shows relative displacement results from a simulation at 24% shear strain for both sizes of material under torsion. The vectors show the relative displacements from the original positions. One can see that the sinusoidal wave observed in the torsional experiment is also observed here in both types of simulations and at different size specimens. One thing is clear: that dislocations are emitted from the corners of the block of material (cf. Horstemeyer and Baskes, 1999). After the dislocations are nucleated, they propagate into the interior of the block of material and the wavy pattern results.

The simple shear simulations showed that the microyield 1 and 2 stresses from the atomistic simulations for the small block of atoms were 7.25 and 7.62 GPa, respectively. For the large block of atoms, the microyield 1 and 2 stresses were 1.95 and 3.1 GPa, respectively. Figure 2.61 shows the stress-strain responses of the two blocks of atoms. Note that the yield stress is higher for the smaller specimen.

Finite element simulations employing the crystal plasticity constitutive model described earlier was used to give insight into the rotations related to the observed pattern on the outside surface of the experimental torsion specimen. The crystal orientation, rotational rate, gage length, and diameter were the same as the experiment. A simple shear simulation was also performed with the correlating geometry. Figures 2.62 and 2.63 show the relation of one of the Euler angles and the relative displacement of the material at large strain under simple shear and torsion, respectively. For the simple shear case, note that two peaks are observed in the specimen (Figure 2.62b) and this arises because of the plastic spin that was induced by the continuum spin (Figure 2.62a). For the torsion simulation shown in Figure 2.63, we observe that rotation angles are of

opposite sign on opposite sides of the specimen. On the left hand side, we see a peak CW rotation and on the right hand side, we see a peak CCW rotation. These opposing rotations push material up and down in the specimen to induce the wavy pattern. Note that the minimum and maximum rotation angles correlate with the peaks and troughs of the displacement oscillations.

We now discuss the similarities and differences in the experiments, molecular dynamics simulations, and finite element simulations. First, we will discuss the wavy pattern (kinematics) observed on the outside circumference of the specimen and then differences in the kinematics and in micro-yield stress responses. Before we make comparisons though, we must first clarify a point regarding simple shear and torsion. If one assumes that the curvature in the circumferential normal strain is negligible, then the stress response in simple shear and torsion is the same from a continuum perspective. In moving from the cylindrical coordinate system for torsion to the Cartesian coordinate system for simple shear the coordinates r, θ, z map to z, x, y, respectively. Note then that in the torsion experiments and simulations, the free surface is the θ z plane, but the free surface in the simple shear simulations is the zy plane.

The main similarity observed in all the simulations and experiments was a wavy pattern that was observed on the outer radius of the specimen. The wavy pattern occurred because the kinematics are qualitatively the same in the MD, finite element simulations, and experiments. However, the magnitude and period of the oscillating waves are different in simple shear and torsion. The waviness arises because the cubic symmetry of the FCC crystal and the symmetry of the loading are not identical, since the θz shear plane changes orientation around the circumference of the specimen. The finite element simulation shows this in Figures 2.62 and 2.63. For the torsion case (experiments, MD simulations, and finite element simulations), four peaks were observed, but in the simple shear case (MD simulations and finite element simulations) only two peaks were observed. The differences between torsion and simple shear were also observed by Boukadia and Sidoroff (1988) but at much larger strains. In this study, the four peaks in the torsion and two peaks in the simple shear start to develop at the beginning of the deformation. This reflects the fourfold slip activity revealed in the torsion experiment and planar double slip exhibited in the simple shear simulations. These two types of slip activity clearly reflect that the plastic spin operates differently when comparing simple shear to torsion.

Not only are the number of periods different between torsion and simple shear, but the wave amplitudes were also different when we compare the ratio of the wave amplitude divided by the cylinder circumference for torsion and length for simple shear. We kept the ratio of the circumference of the cylinder to the axial gage length of the torsion equal to the ratio of the length to height in the atomistic simulation (0.43). Similarly, we kept the same ratio for simple shear when comparing the length-to-height. Table 2.6. shows a comparison of the wave amplitude ratios at 35% strain.

Table 2.6. Ratio of wave amplitude divided by circumference (torsion) or length (simple shear) of different boundary conditions and methods at large strain.

Condition/Method	*wave amplitude ratio*
Torsion	
experiment	0.02
finite elements	0.05
molecular dynamics (large specimen)	0.06
molecular dynamics (small specimen)	0.07
Simple Shear	
finite elements	0.25
molecular dynamics (large specimen)	0.23
molecular dynamics (small specimen)	0.26

The value of the peak and trough to determine the wave amplitude is fairly simple for the experiment, but these values need to be considered only approximate for the MD simulations and finite element simulations. Note that both the torsion wave amplitude ratio and simple shear wave amplitude ratio were consistent within their own domains, but different when comparing torsion to simple shear. For torsion, the wave amplitude was much smaller than in simple shear. This difference may have to do with either the differences in plastic spin related to slip activity as discussed earlier or related to different free surfaces in each type of boundary condition. Although both have traction free planes orthogonal to the loading direction, the planes are opposite to the coordinate mapping from a cylindrical to the Cartesian coordinate system as r, θ, z map to z, x, y, respectively. If torsion and simple shear were identical, the θz plane in torsion would map to the xy plane in simple shear. The θz plane in torsion is traction free, but the xy plane is not traction free but is constrained by periodic conditions. The yz plane in simple shear is traction free.

Table 2.6 makes three points. (1) Simple shear and torsion boundary conditions incur different kinematics. (2) The wave amplitude is very similar in torsion for the experiments, finite elements, and atomistic simulations, although there is minor trend from the larger specimen having a wave amplitude ratio of 0.02 and the smaller atomistic simulation having a wave amplitude ratio of 0.07. Also, there exists a difference between the crystal plasticity simulation and the experiment from 0.02 to 0.05, respectively, even though these two simulations are considered to be on the same scale. The difference could arise for several reasons, but the main one is that the crystal plasticity formulation does not explicitly account for substructural development that is observed in finite deformations (cf. Hughes, 1995). (3) The simple shear wave amplitude ratio is essentially the same for the finite element simulations and the atomistic

simulations. This result reveals that no specimen size scale effect exists related to the kinematics in torsion.

Now we turn from the kinematics to the stress response of the different methods and boundary conditions. For the MD simulations in this study, the microyield stresses were 7.25/7.62 GPa (small block of atoms) and 1.95/3.1 GPa (large block of atoms) compared to 3.5-4.8/10 MPa for the larger scale torsion experiment. Hence, three orders of magnitude difference were observed when comparing the atomistic to experimental results. Other experiments qualitatively validate the experimental yield stresses observed in our experiments. Schmid and Boas (1950) experimentally showed a microyield stress of 4.5 MPa for single crystal Cu in tension. Phillips (1962) performed direct shear on single crystal Cu with different orientations and observed a value of 0.6 MPa for yield. Jackson and Basinski (1967) conducted tension tests on single crystal Cu specimens with different crystal orientations and found a range of 0.50-1.24 MPa for the critical resolved shear stress. Honeycombe (1984) experimentally showed a critical resolved shear stress of 0.34-0.98 MPa for single crystal Cu depending on the purity level. These values are on the same order as our large scale torsion results. Quilici et al. (1998) obtained a critical resolved shear stress of 0.8 MPa for 1 mm diameter torsion specimens of single crystal Cu. Even for polycrystalline Cu this size scale trend has been observed. Fleck et al. (1994) performed micron scale solid torsion experiments of polycrystalline Cu with different radii. The radii were 12, 15, 20, 30, and 170 μm, and the corresponding yield stresses taken from a 0.2% strain offset were 229, 205, 140, 130, and 120 MPa, respectively. Again, as the size increased, the yield stress decreased. Figure 2.64 shows the yield stress divided by elastic shear modulus as a function of volume-per-surface-area of various copper and nickel experiments with the atomistic data.

In summary of this section, we compared and contrasted three disparate numerical methods representing three different size scales of simulations (atomistic modeling, crystal plasticity using finite elements, and internal state variable theory using finite elements). Qualitative similarities were found related to the yield stress of the specimens as a function of aspect ratio. As the x/y aspect ratio of the block of material increased (close to simple shear conditions), the yield stress increased until the ratio reached about 8:1 in which the yield stress saturated. Similarly, as the y/x aspect ratio of the block of material increased (close to bending conditions), the yield stress decreased until the ratio reached about 8:1 in which the yield stress saturated. The three different numerical methods also gave similar qualitative responses related to inhomogeneous stress and strain distributions in the corner regions of the specimens and a centralized homogeneous deformation region. However, several differences in the three numerical methods were evidenced. When comparing the distribution for the finite element analyses to the atomistic simulations, a much narrower stress distribution arose for the finite element analyses due to the lack of thermal vibrations experienced in the atomistic simulations. A 10 K atomistic

simulation which dampened out the high frequency thermal vibrations verified this notion. A size scale effect related to the volume averaged shear stress in the block of material was evidenced. As the specimen size increased, the yield stress decreased. Finally, when comparing the three different numerical methods, the place of highest dislocation nucleation occurred where the highest plastic spin, highest stress gradients, and highest strain gradients occurred.

2.8 Summary

In this scoping study, atomistic simulations were performed in order to understand structure-property relations at different size scale as related to plasticity of metals. In particular, various parametric effects on the stress state and kinematics has been quantified. The parameters included the following: crystal orientation (single slip, double slip, quadruple slip, octal slip), temperature (300 K and 500 K), applied strain rate (10^6 to 10^{12}/sec), specimen size (10 atoms to 2 microns), specimen aspect ratio size (1:8 to 8:1), deformation path (compression, tension, simple shear, and torsion), and material (nickel, aluminum, and copper). Although many conclusions can be drawn from these studies and has provided fodder for more studies, several major conclusions can be drawn.

(1) The yield stress is a function of a size scale parameter (volume-per-surface-area) that was determined from atomistic simulations coupled with experiments. As the size decreases, the yield stress increases.

(2) Although the thermodynamic force (stress) varies at different size scales, the kinematics of deformation appears to be very similar based on atomistic simulations, finite element simulations, and physical experiments.

(3) Atomistic simulations, although inherently including extreme strain rates and size scales, give results that agree with the phenomenological attributes of plasticity observed in macroscale experiments. These include (I) strain rate dependence of the flow stress into a rate independent regime, (II) approximate Schmid type behavior, (III) size scale dependence on the flow stress, (IV) kinematic behavior of large deformation plasticity, (V).

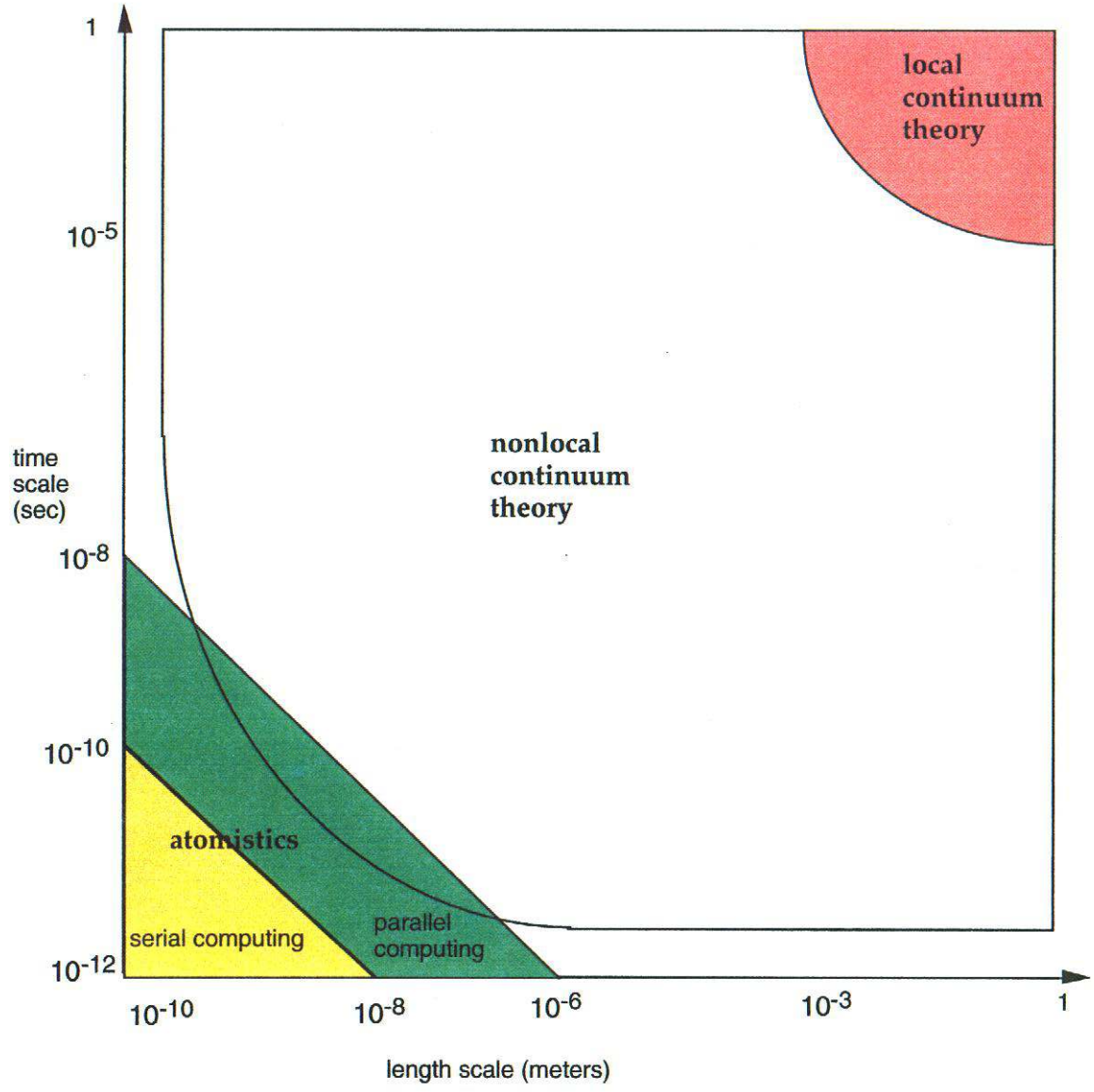

Fig. 2.1. Schematic of strain rate and spatial size scale effects on computing and the regions where local and non-local continuum theories are applicable.

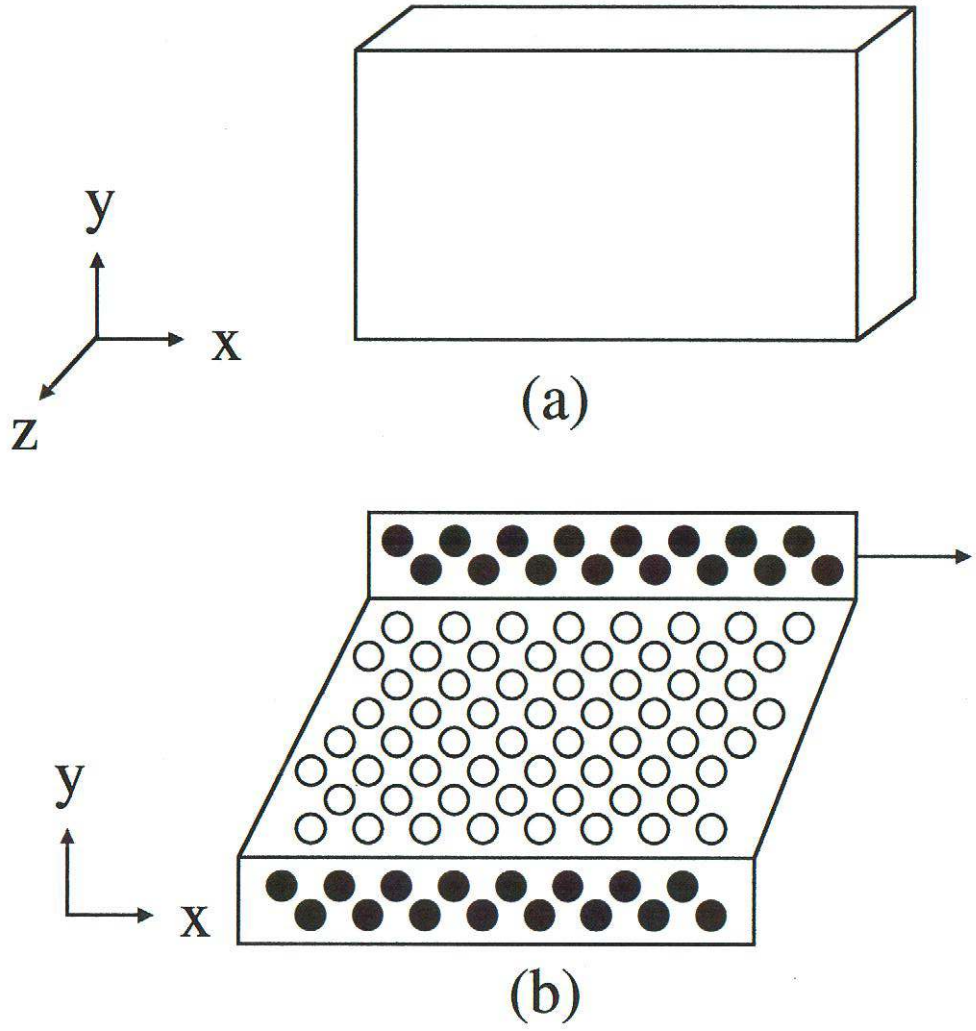

Fig. 2.2. Schematic of simulation block of atoms at (a) initial state and (b) at large strain in which the clear circles represent the active atoms and the dark circles represent the boundary atoms.

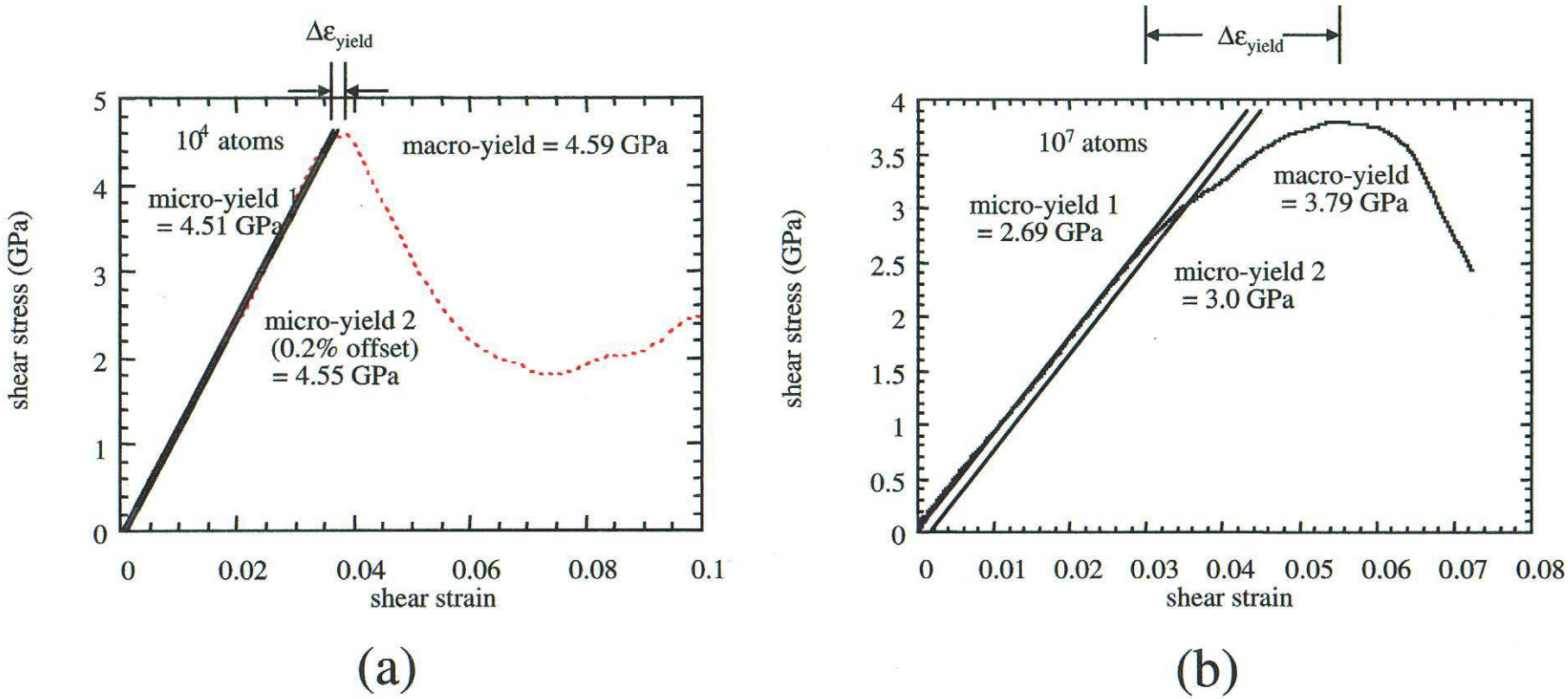

Fig. 2.3. Shear stress-strain curve of material blocks at an applied strain rate of 2.4×10^8 s^{-1} with (a) ten thousand atoms and (b) ten million atoms showing micro-yield 1 at the proportional limit, micro-yield 2 at 0.2% offset strain, and macro-yield.

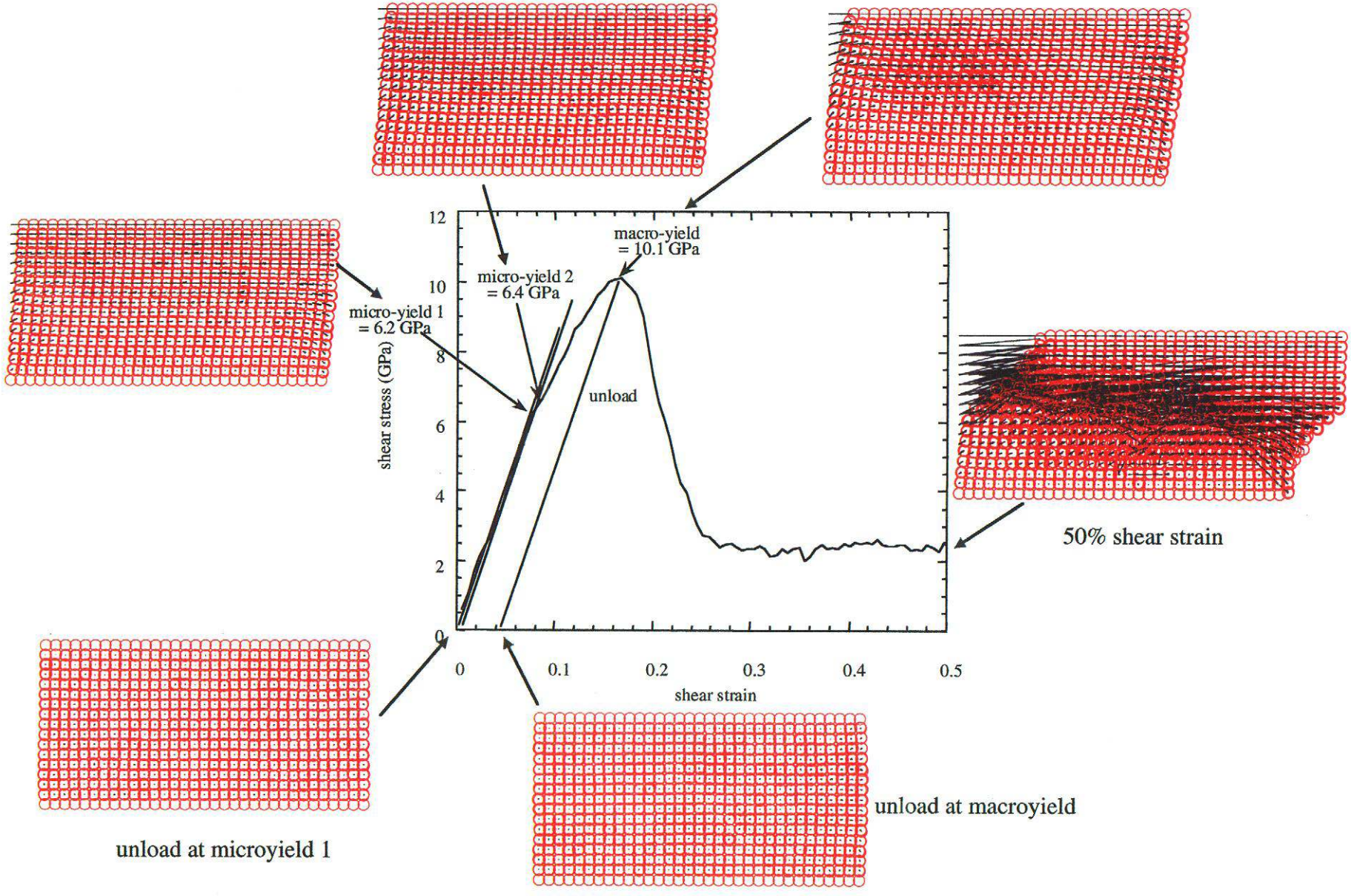

Fig. 2. 4. Shear stress-strain curve for 2242 atoms of nickel illustrating atomic positions and relative displacements (denoted by arrows on atoms) at different strain levels.

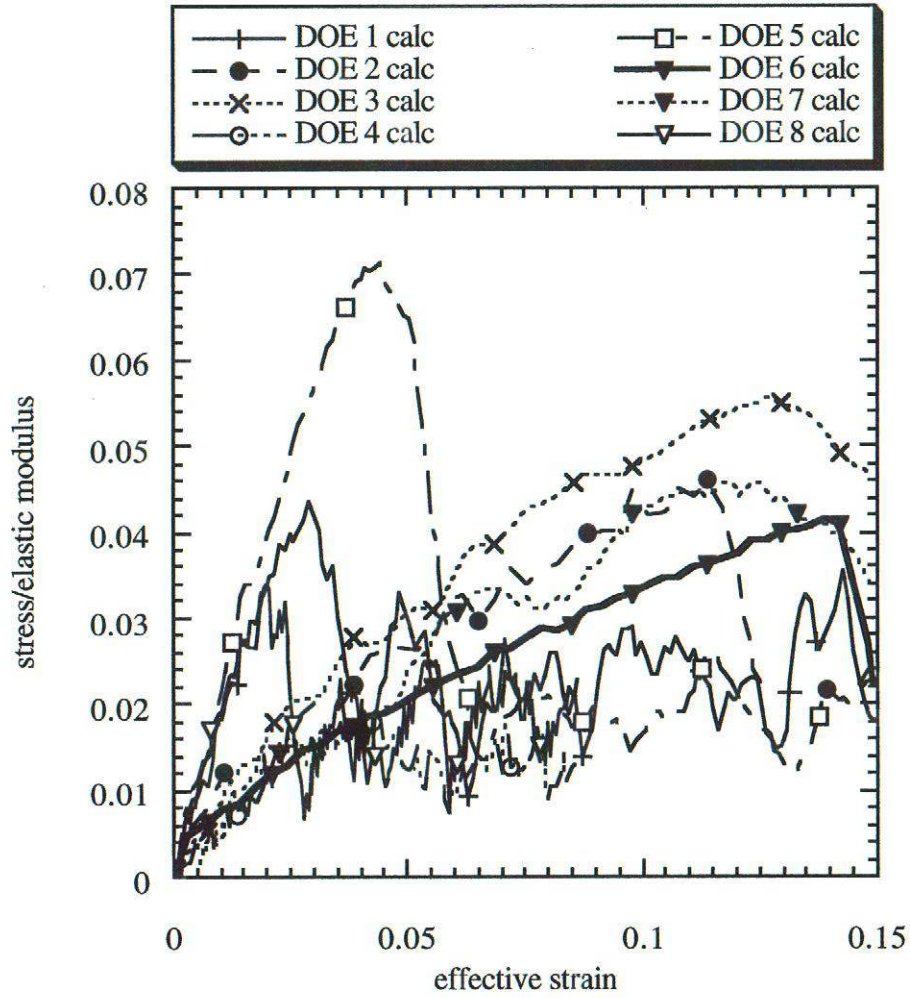

Fig. 2.5. Stress-strain curves of eight DOE simulations for single crystal nickel.

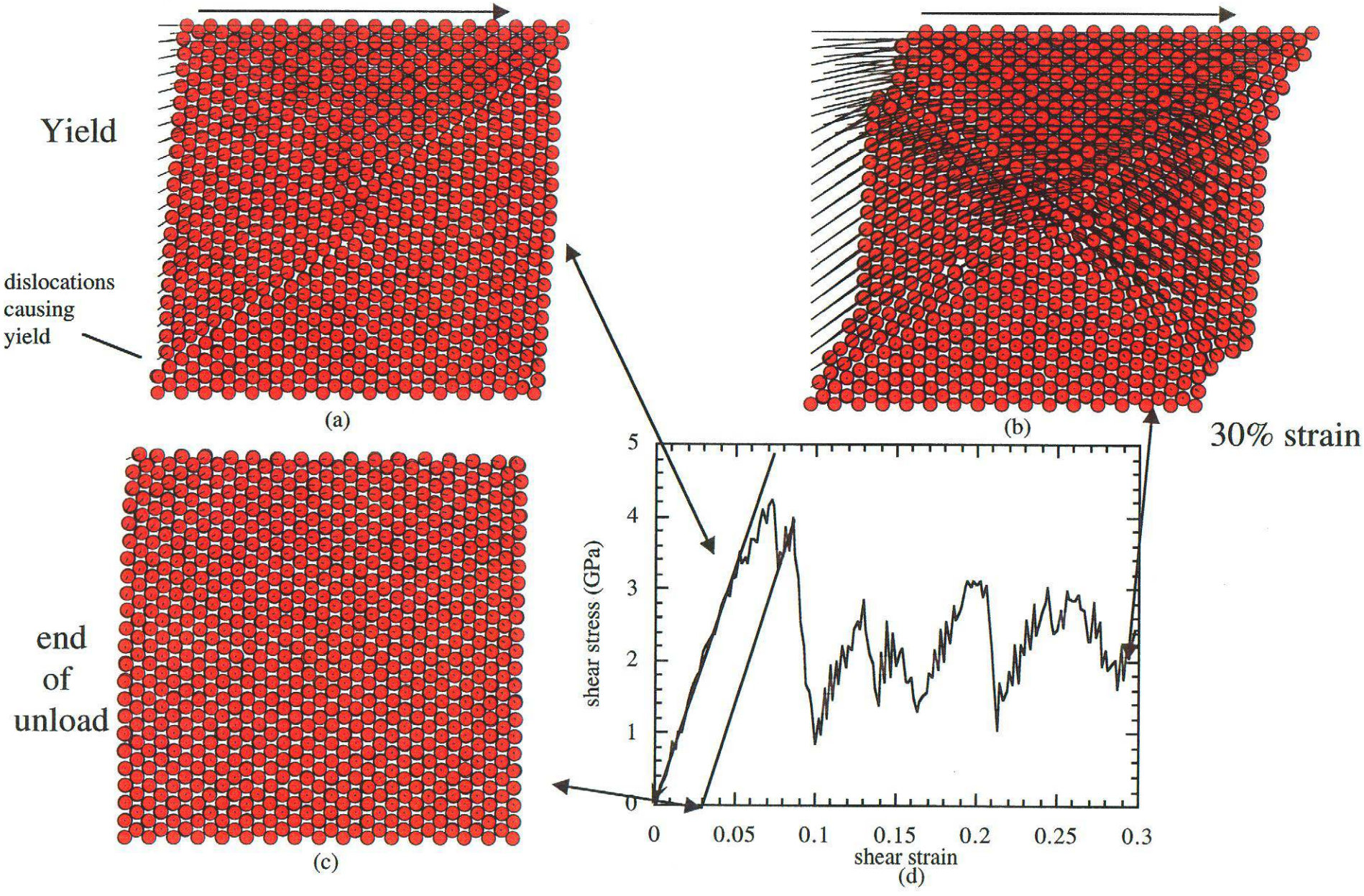

Fig. 2.6. Shear stress-strain response of DOE #8 and correlating shear stress states at (a) yield, (b) 30% shear strain, and (c) unloaded state just beyond yield. The lines show relative displacements of atomic motion.

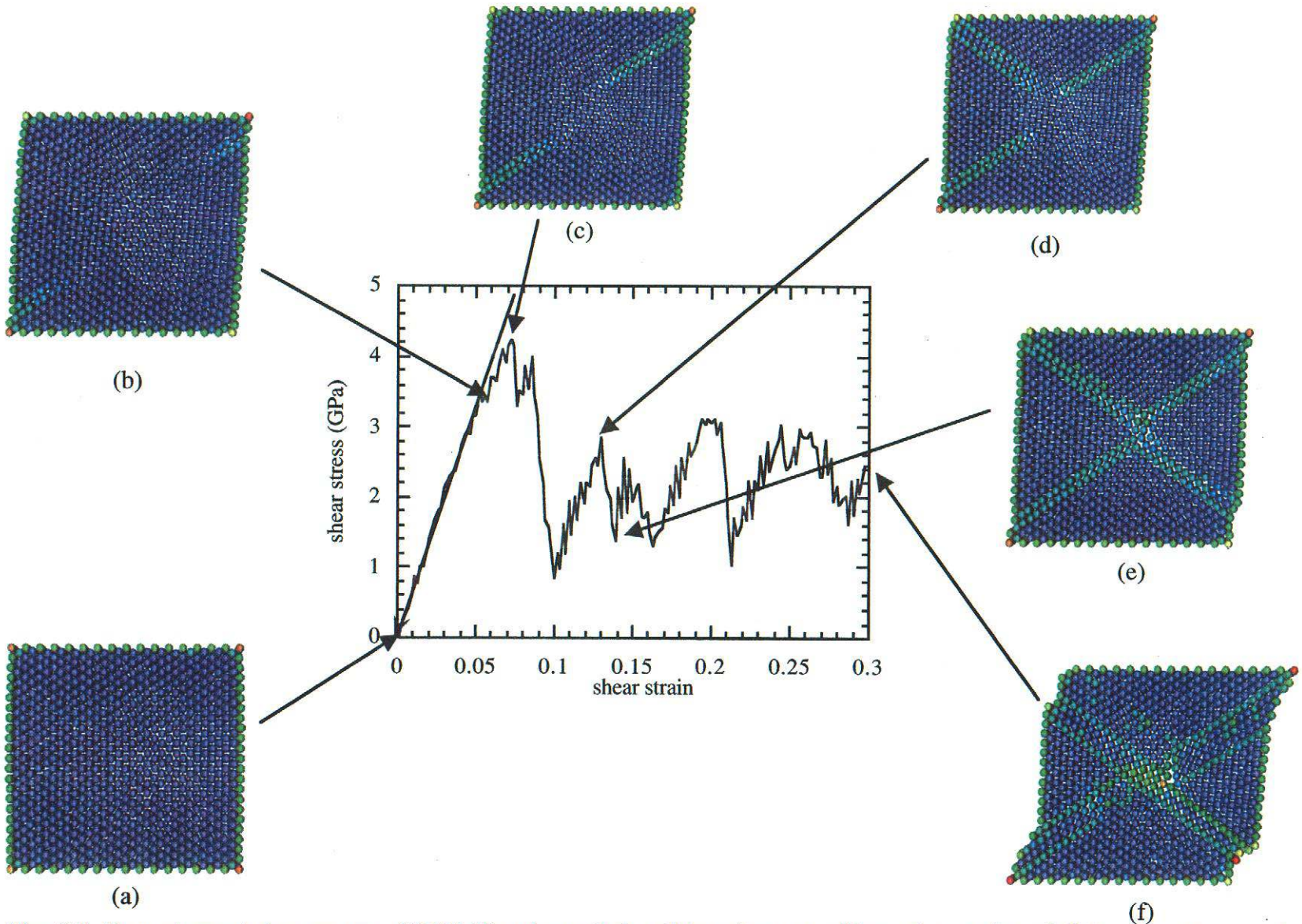

Fig. 2.7. Shear stress-strain response of DOE #8 and correlating dislocation states illustrating motion of dislocations by use of centrosymmetry parameter at (a) start, (b) just after microyield, (c) peak stress, (d) 12% strain, (e)13.5% strain, and (f) 30% strain.

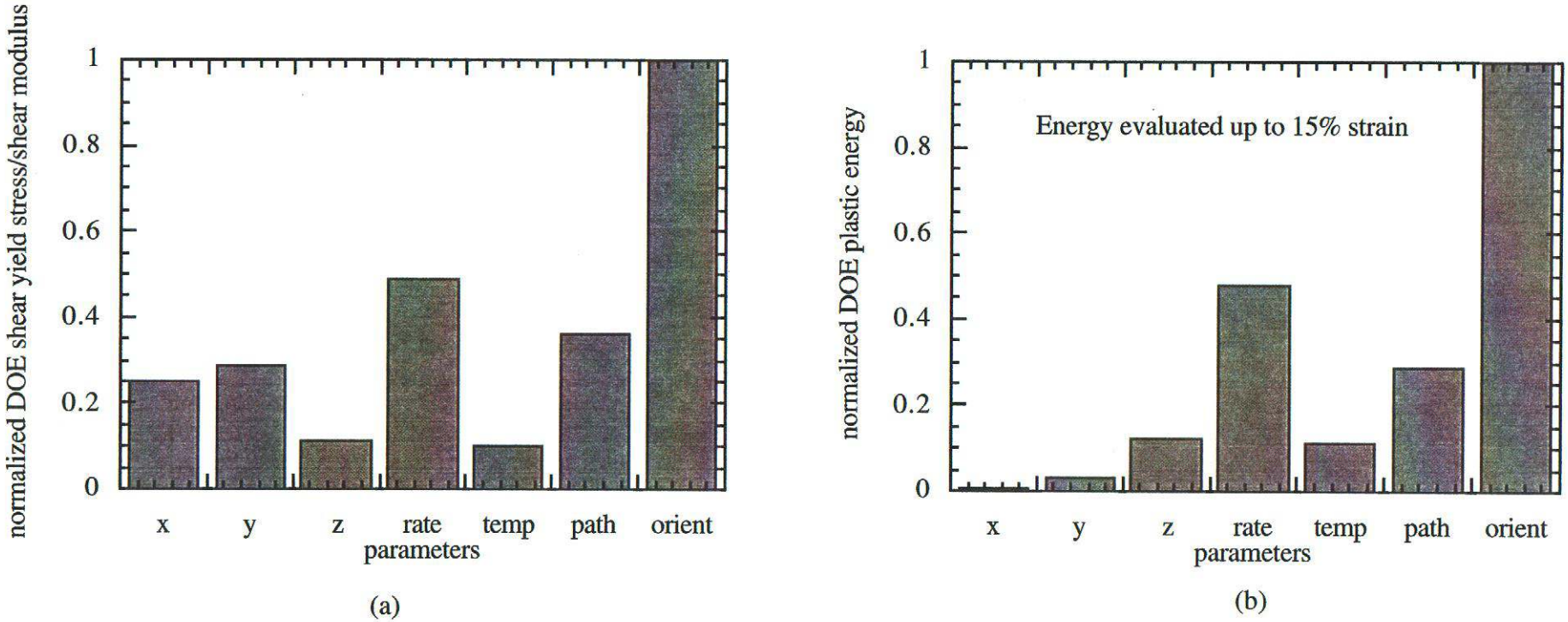

Fig. 2.8. Normalized DOE (a) yield and (b) plastic energy response as a function of parameter influence.

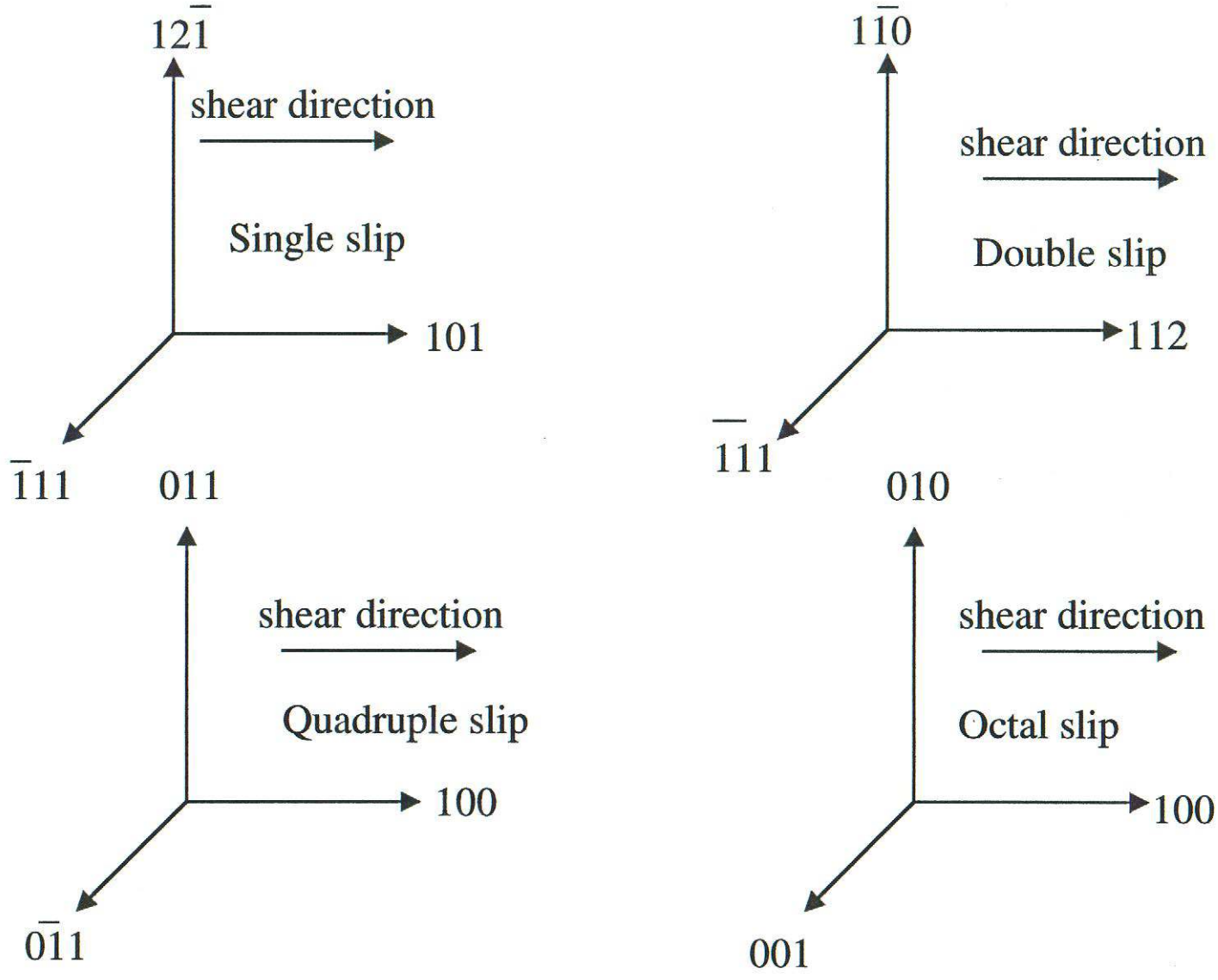

Fig. 2.9. Different initial orientations in simple shear straining.

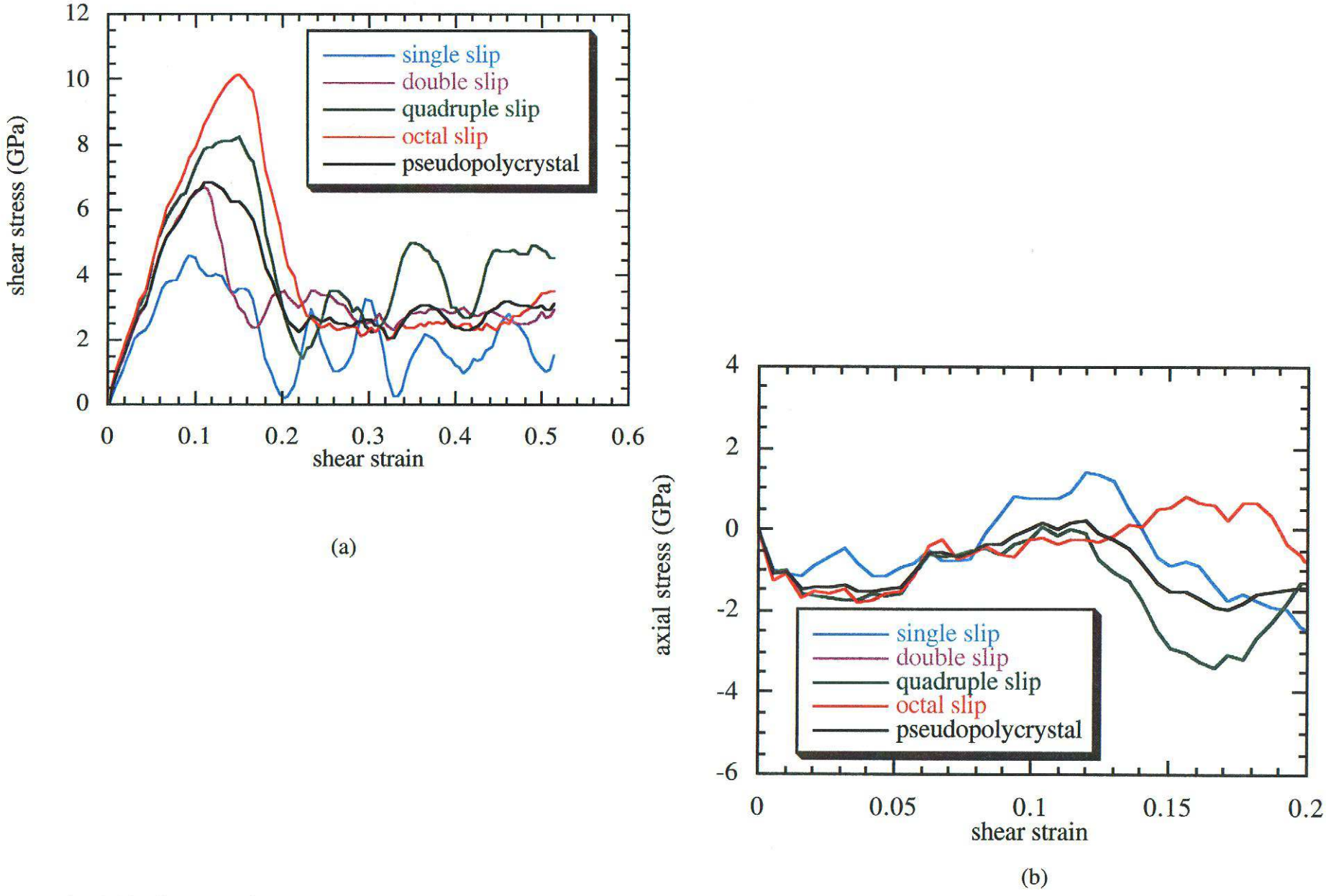

Fig. 2.10. Stress-strain responses for different initial orientations and pseudopolycrystal under simple shear : (a) shear and (b) axial.

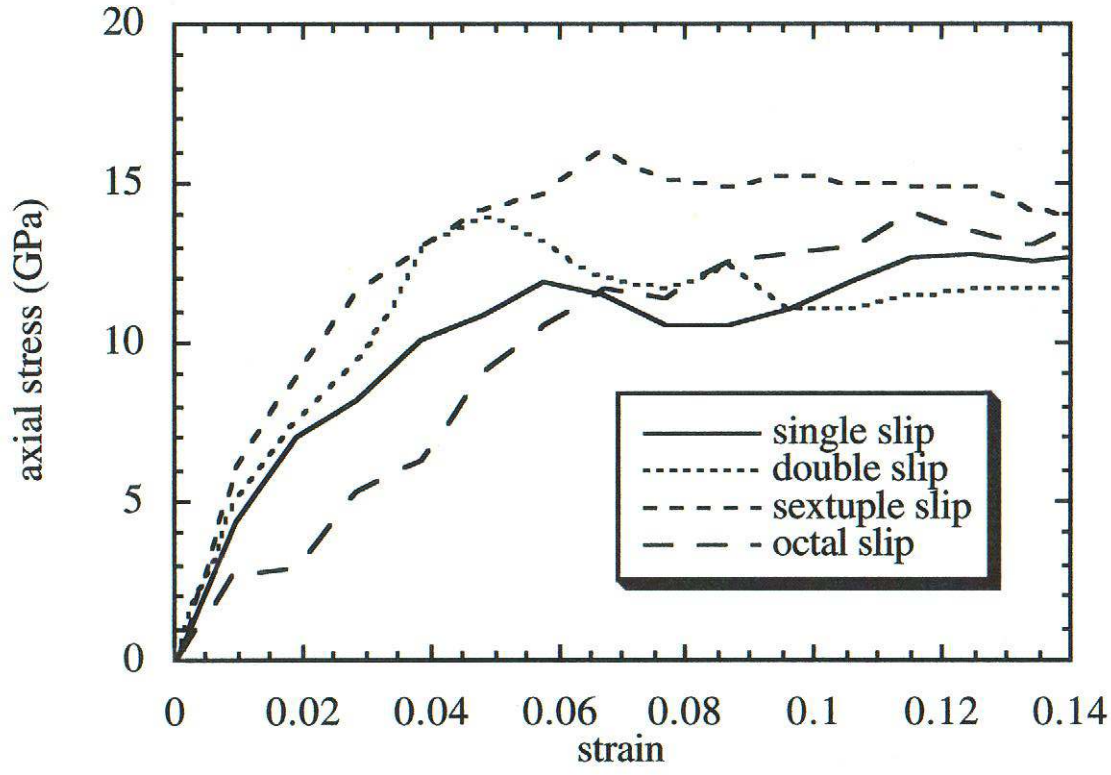

Fig. 2.11. Stress-strain responses for different initial orientations under tension.

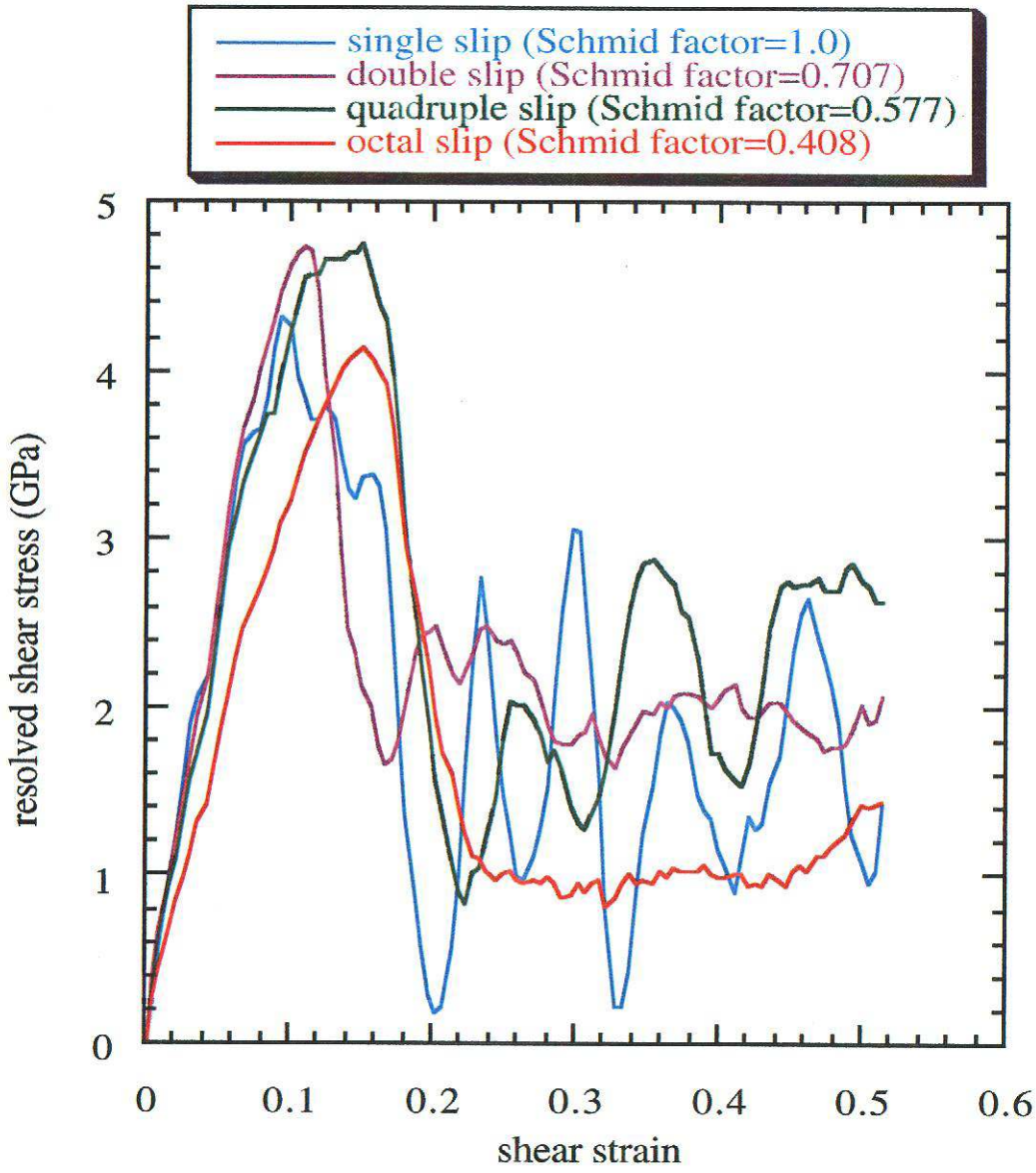

Fig. 2.12. Resolved shear stress-strain curves for different initial orientations that have been modified by a Schmid factor.

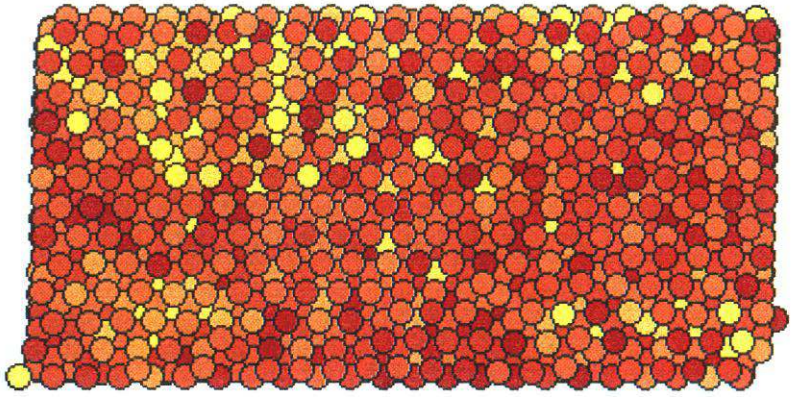

(a)

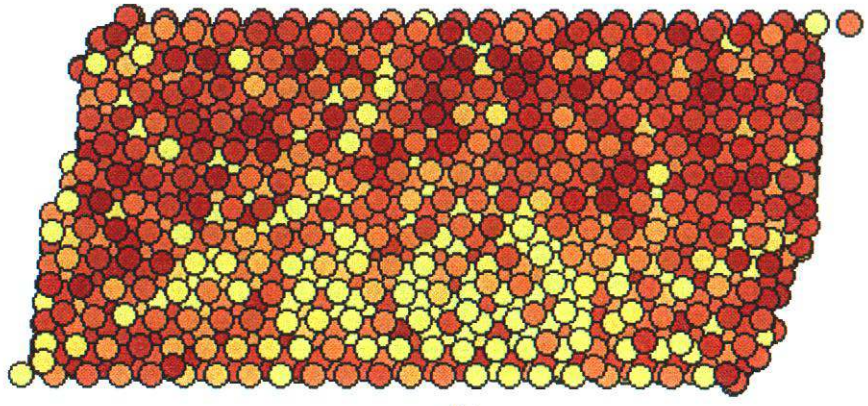

(b)

Fig. 2.13. Contour plots of shear stress at (a) yield and (b) 30% effective strain for the block of atoms initially oriented for single slip under simple shear straining (The dark color is the highest value, and the light color is the lowest).

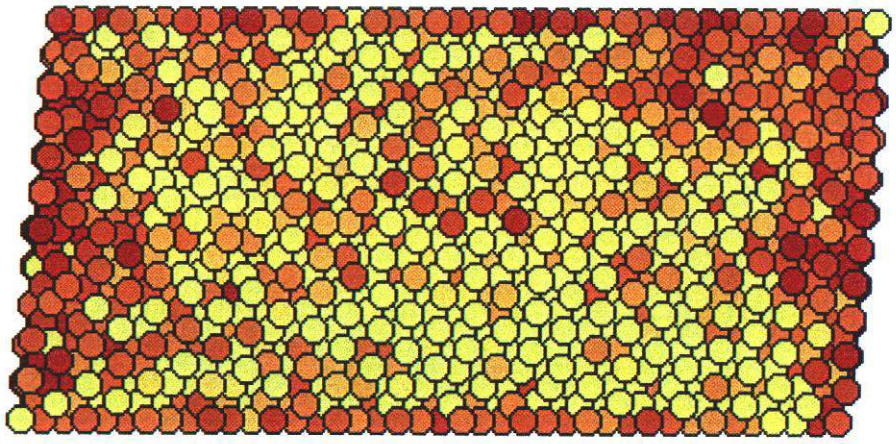

(a)

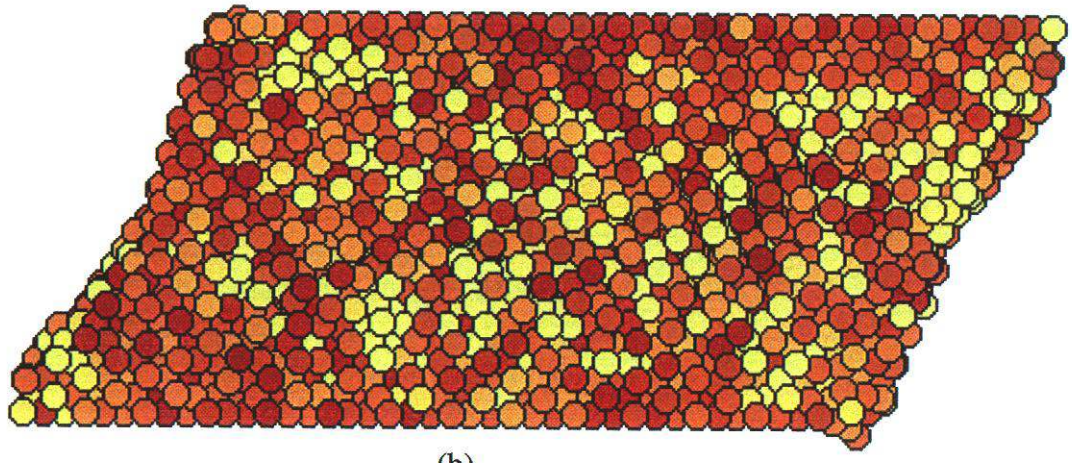

(b)

Fig. 2.14. Contour plots of shear stress at (a) yield and (b) 30% effective strain for the block of atoms initially oriented for double slip under simple shear straining (The dark color is the highest value, and the light color is the lowest).

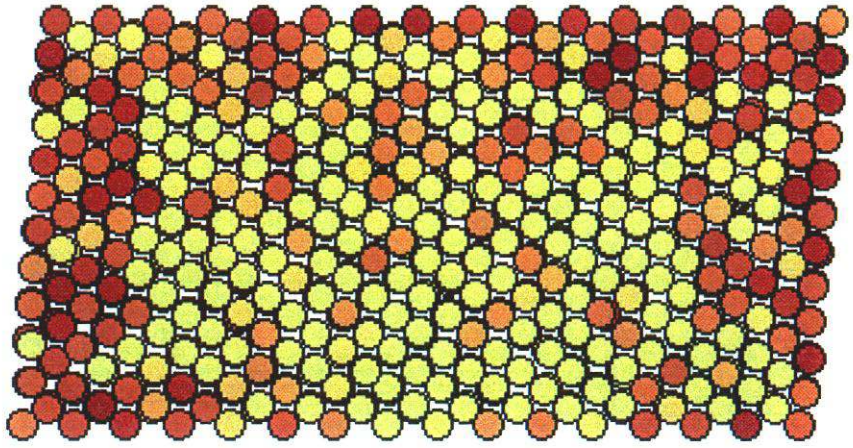

(a)

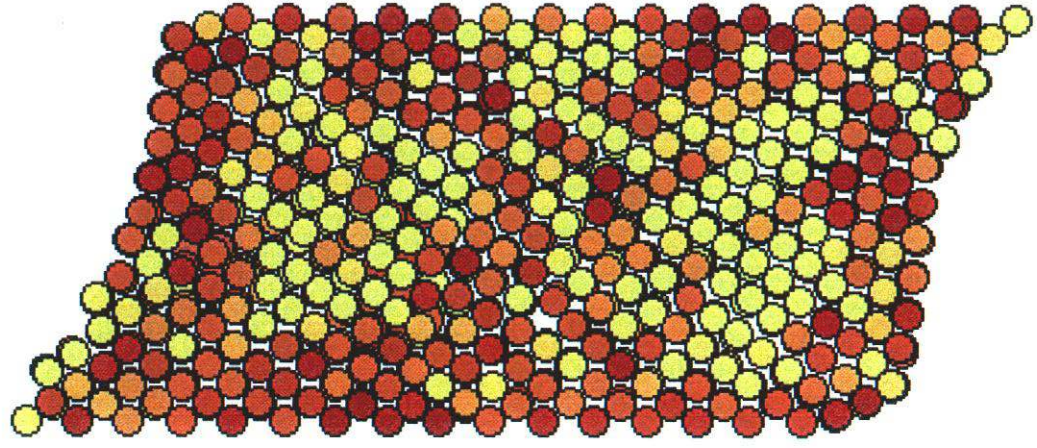

(b)

Fig.2.15. Contour plots of shear stress at (a) yield and (b) 30% effective strain for the block of atoms initially oriented for quadruple slip under simple shear straining (The dark color is the highest value, and the light color is the lowest).

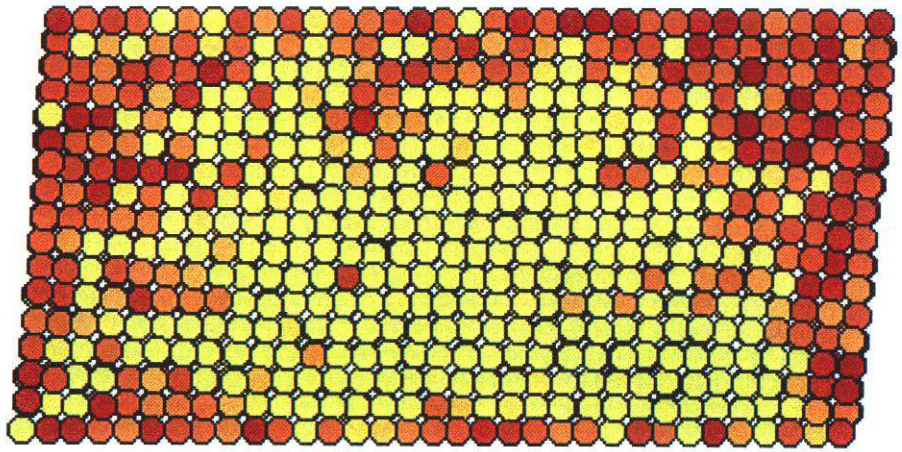

(a)

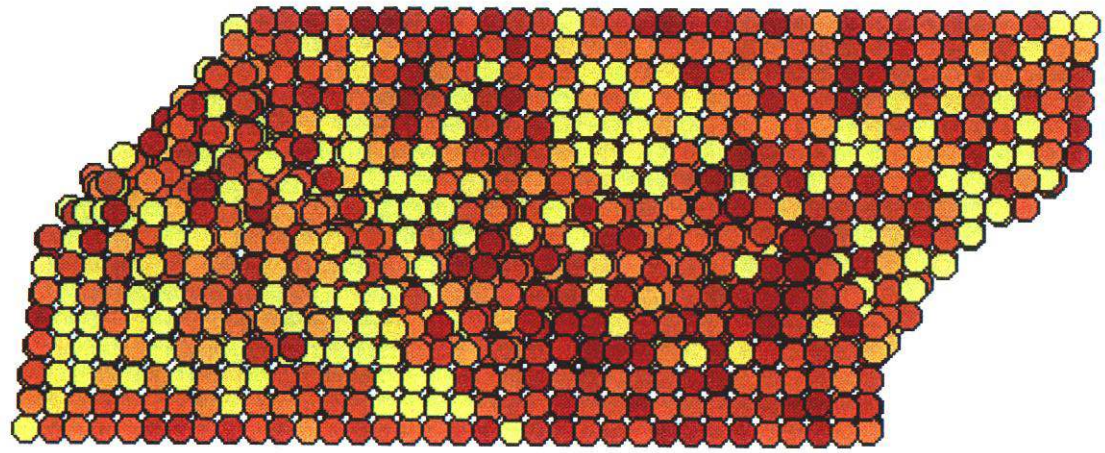

(b)

Fig. 2.16. Contour plots of shear stress at (a) yield and (b) 30% effective strain for the block of atoms initially oriented for octal slip under simple shear straining (The dark color is the highest value, and the light color is the lowest).

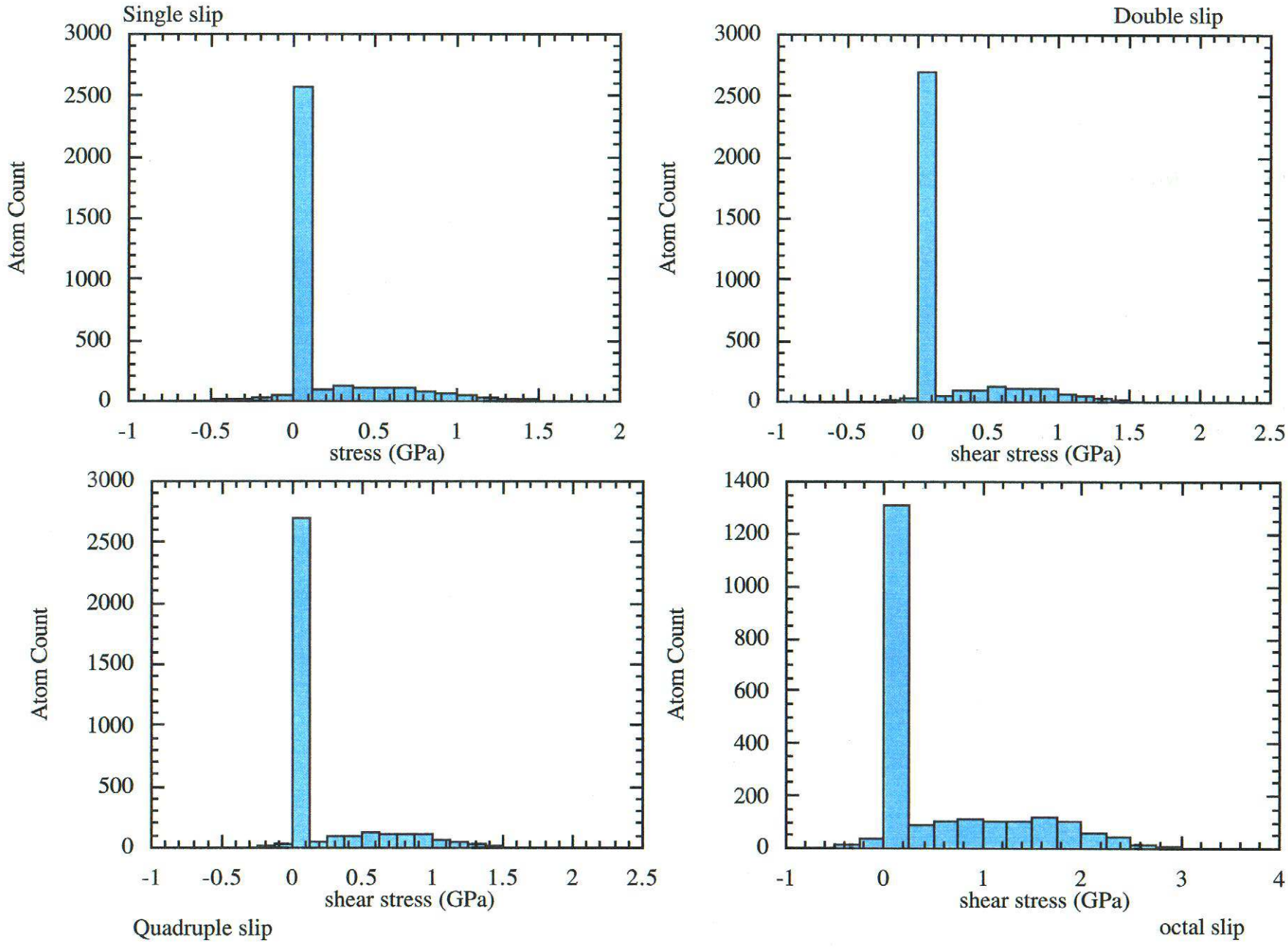

Fig. 2.17. Distributions of shear stress at yield for (a) single slip, (b) double slip, (c) quadruple slip, and (d) octal slip under simple shear.

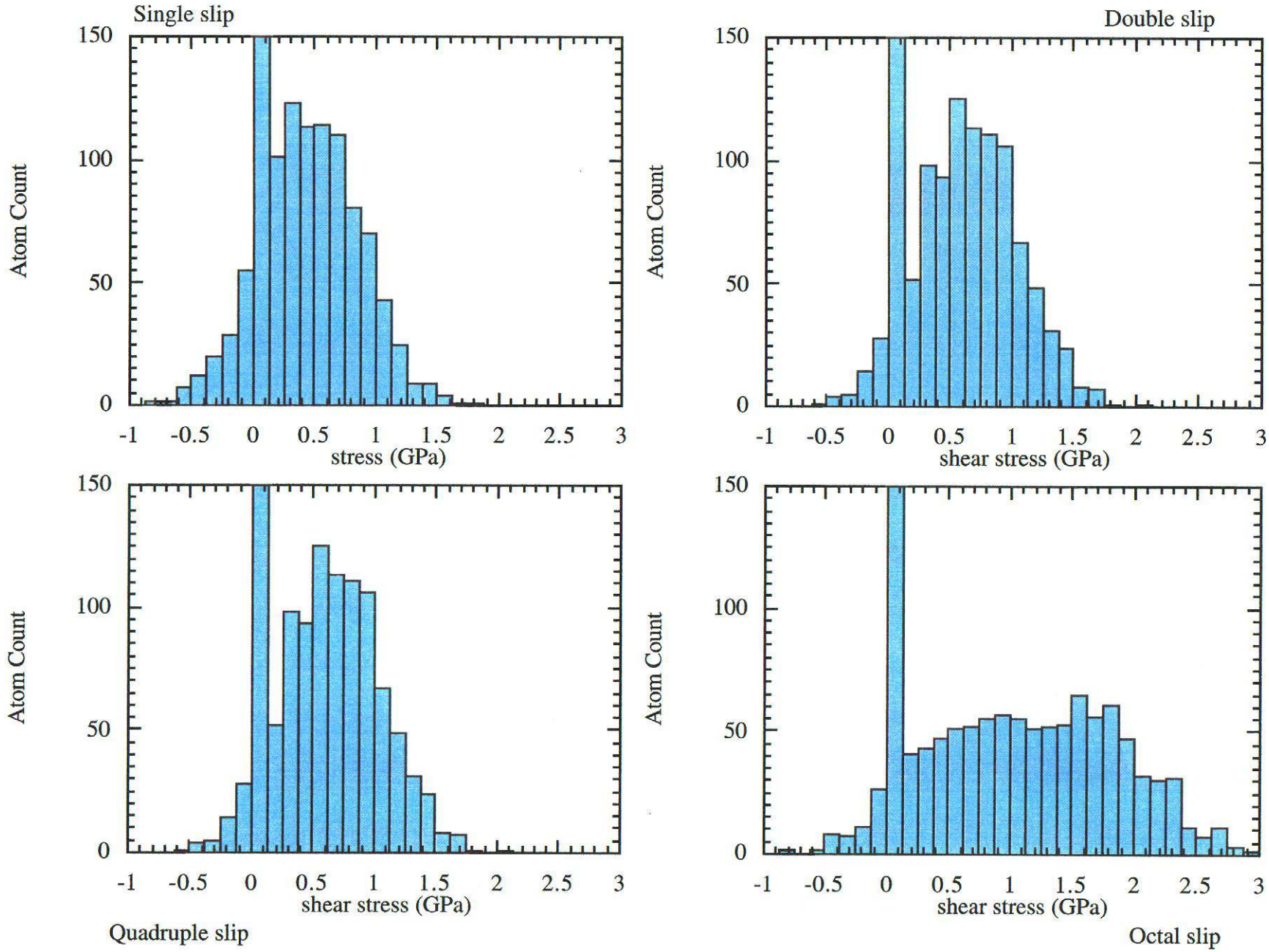

Fig. 2.18. Same plot as Fig. 2.17 with peak atom count at 150 to compare different initial orientations at yield.

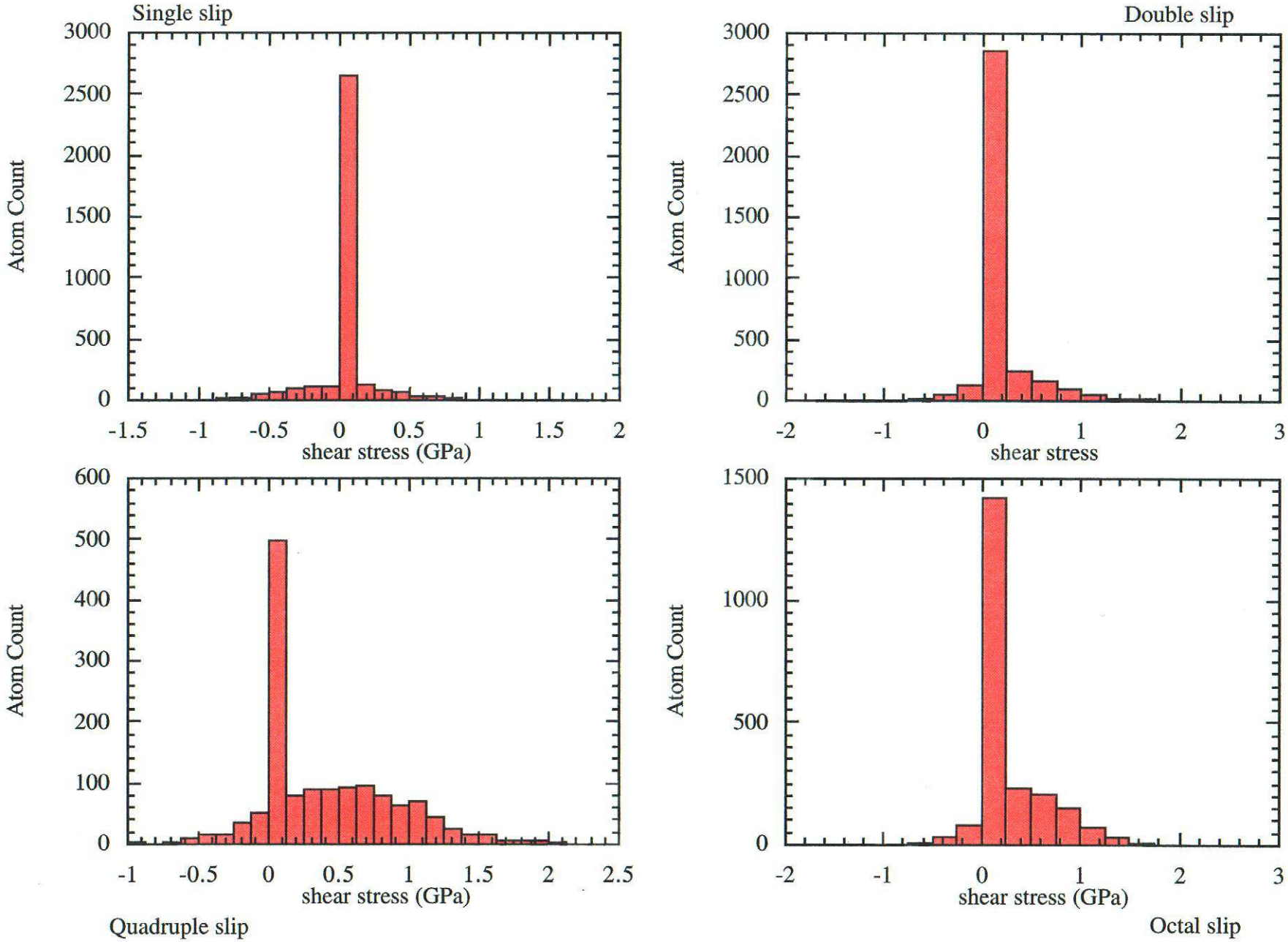

Fig. 2.19. Distributions of shear stress at 30% effective strain for (a) single slip, (b) double slip, (c) quadruple slip, and (d) octal slip under simple shear.

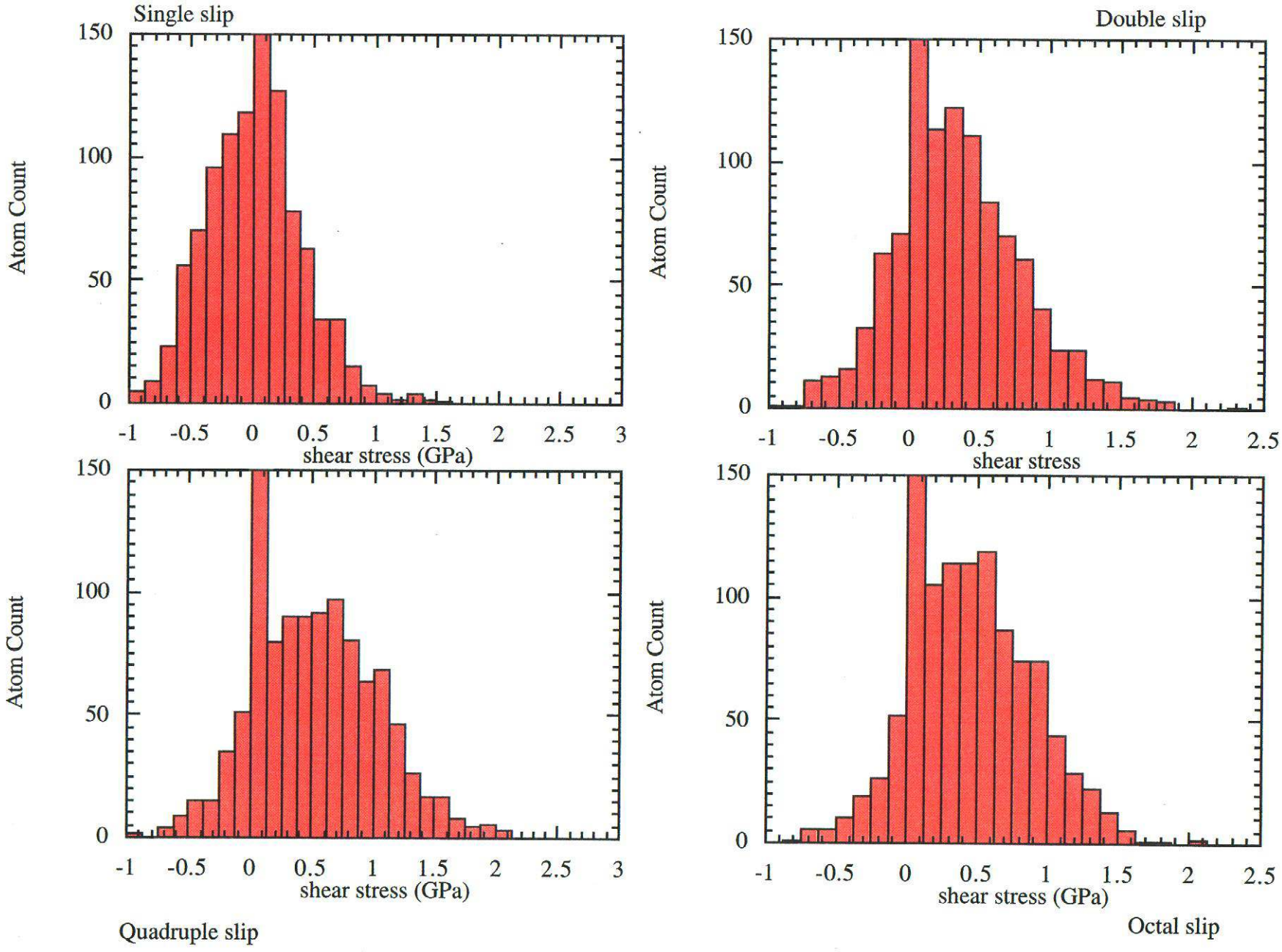

Fig. 2.20. Same plot as Fig. 2.19 with peak atom count at 150 to compare different initial orientation at 30% effective strain.

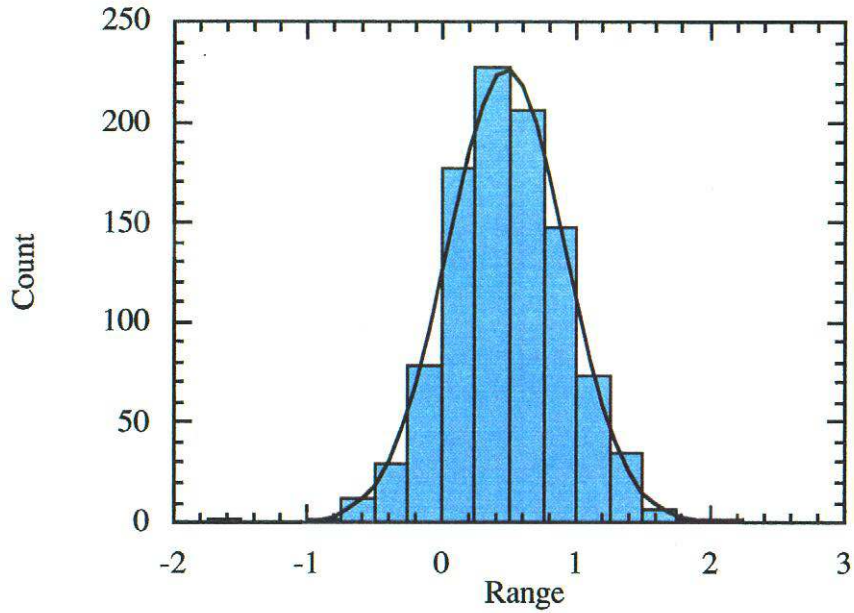

Fig. 2.21. Comparison of histogram and Gaussian distribution for double slip orientation at 30% effective strain.

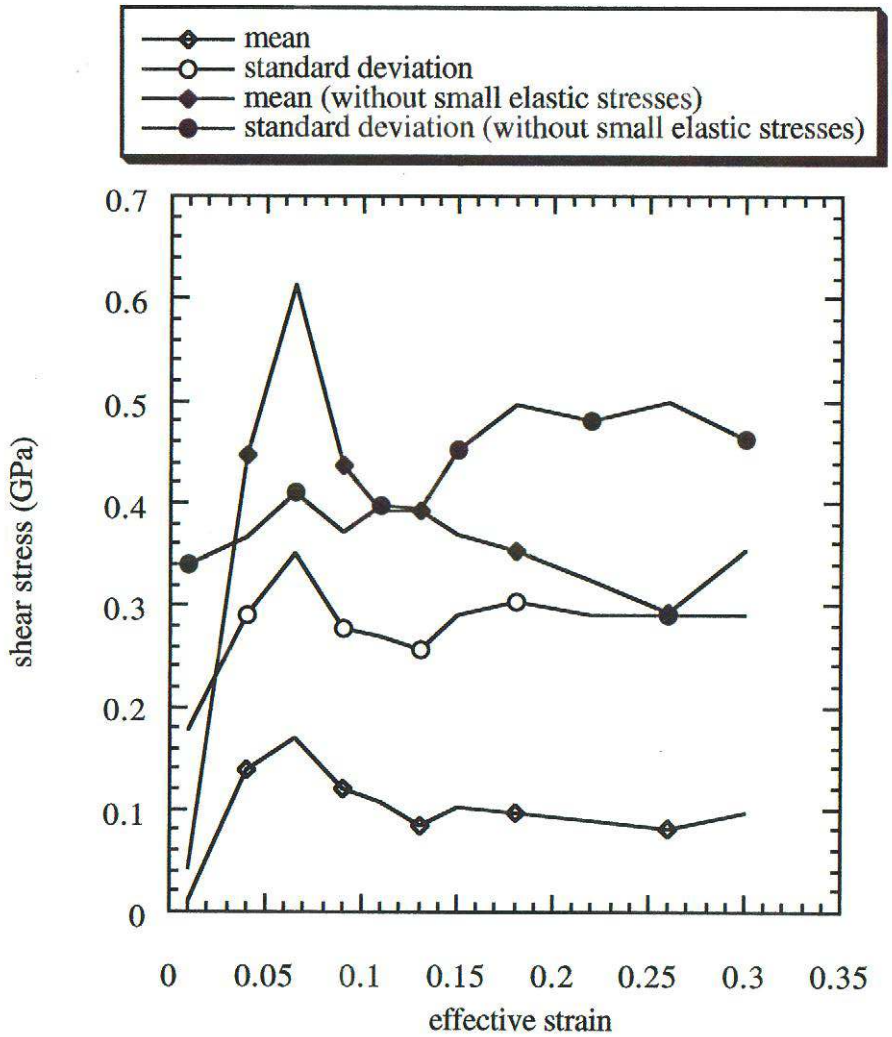

Fig. 2.22. Comparison of mean, standard deviation, and skewness as a function of effective strain for Gaussian distributions with and without the small elastic stresses included.

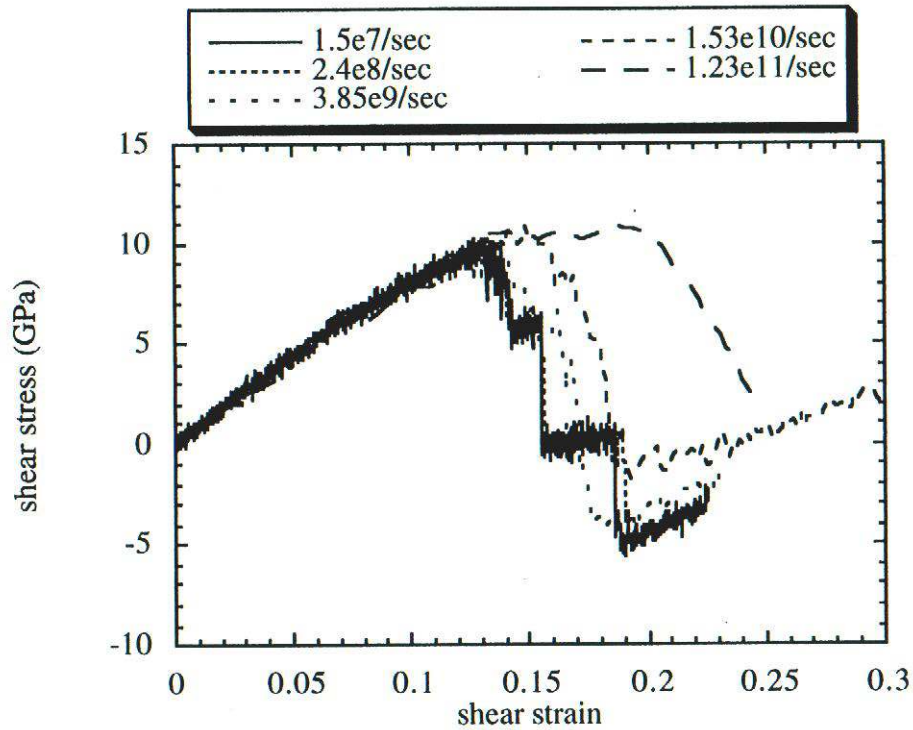

Fig. 2.23. Shear stress-shear strain curves of material block with 196 atoms (length is 2.8 nm and height is 1.4 nm) at strain rates from 1.5×10^{7}/sec to 1.23×10^{11} s^{-1} illustrating the increase in yield as a function of strain rate.

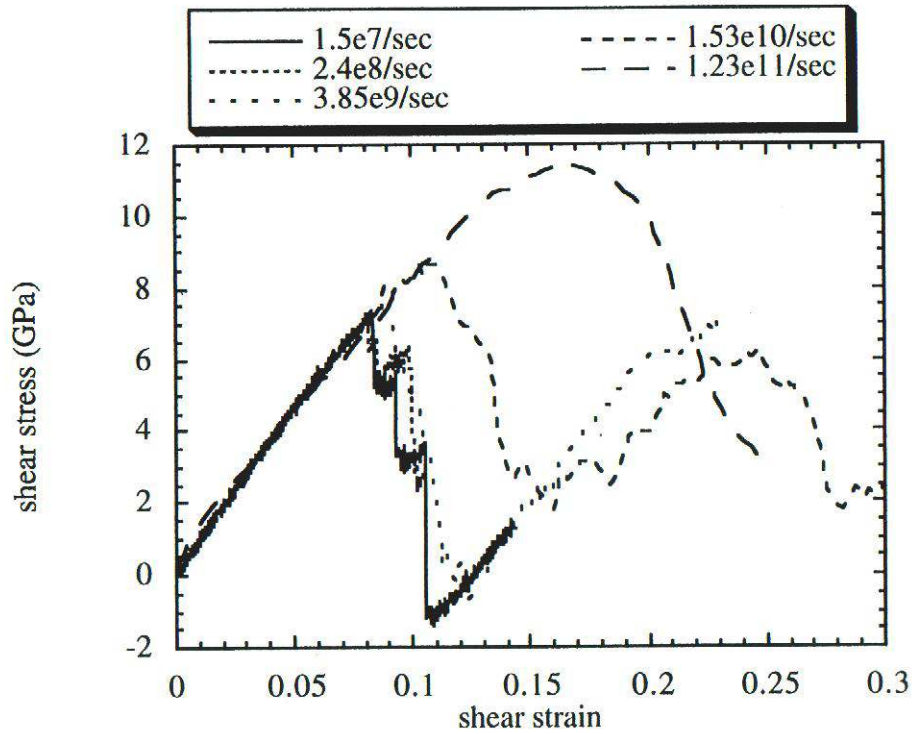

Fig. 2.24. Shear stress-shear strain curves of material block with 1384 atoms (length is 7.8 nm and height is 4.0 nm) at strain rates from 1.5×10^{7} to 1.23×10^{11} s^{-1} illustrating the increase in yield as a function of strain rate.

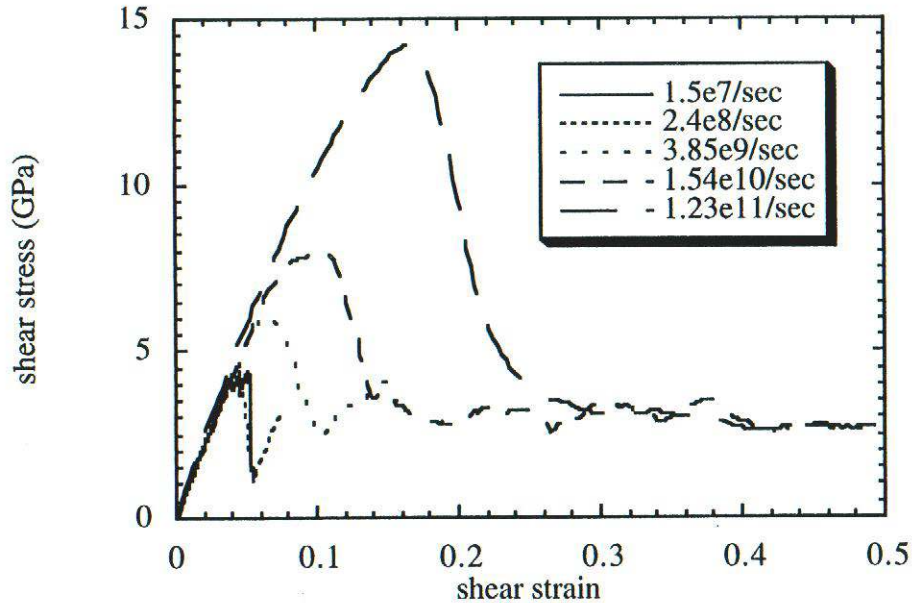

Fig. 2.25. Shear stress-shear strain curves of material block with $2x10^4$ atoms (length is 0.0282 μm and height is 0.014 μm) at strain rates from $1.5x10^7$ to $1.23x10^{11}$ s^{-1} illustrating the increase in yield as a function of strain rate.

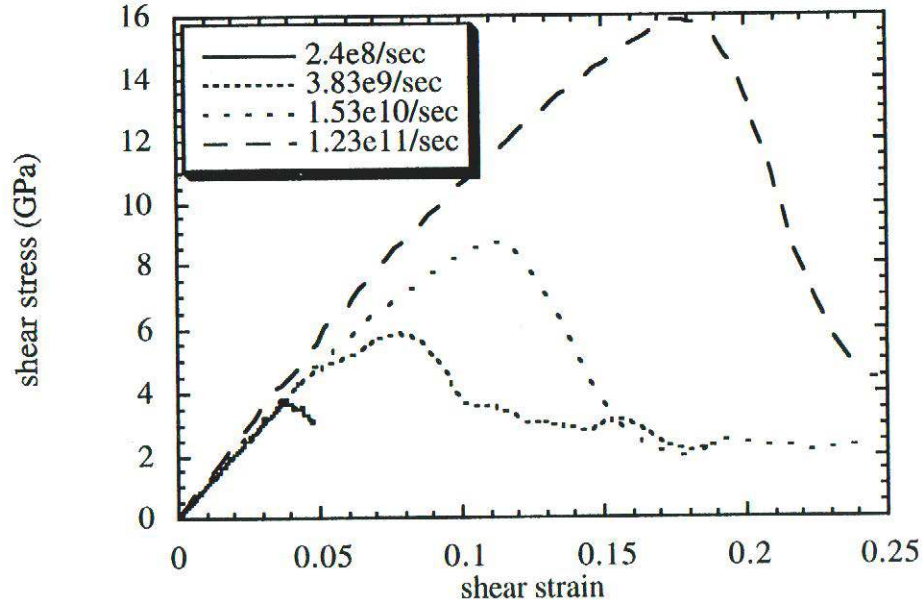

Fig. 2.26. Shear stress-shear strain curves of material block with $1x10^5$ atoms (length is 0.057 μm and height is 0.021 μm) at strain rates from $2.4x10^8$ to $1.23x10^{11}$ s^{-1} illustrating the increase in yield as a function of strain rate.

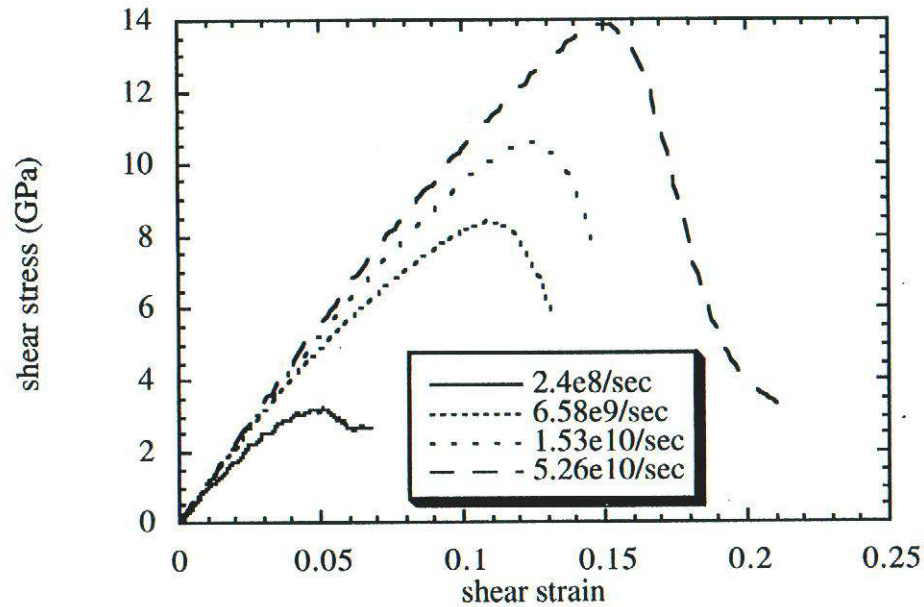

Fig. 2.27. Shear stress-shear strain curves of material block with $1x10^6$ atoms (length is 0.18 μm and height is 0.07 μm) at strain rates from $2.4e^8$ to $5.26x10^{10}$ s^{-1} illustrating the increase in yield as a function of strain rate.

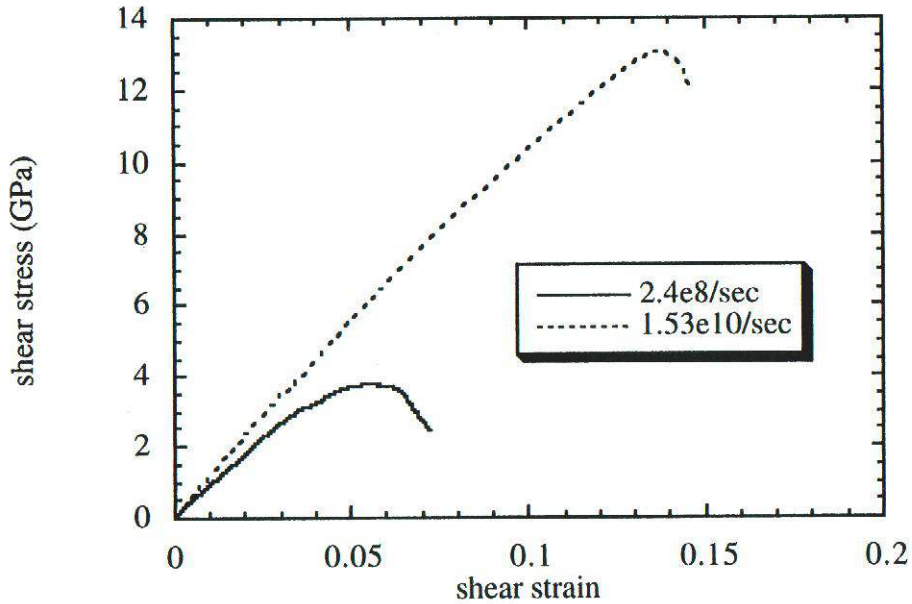

Fig. 2.28. Shear stress-shear strain curves of material block with $1x10^7$ atoms (length is 0.55 μm and height is 0.21 μm) at strain rates from $2.4x10^8$ to $1.53x10^{10}$ s^{-1} illustrating the increase in yield as a function of strain rate.

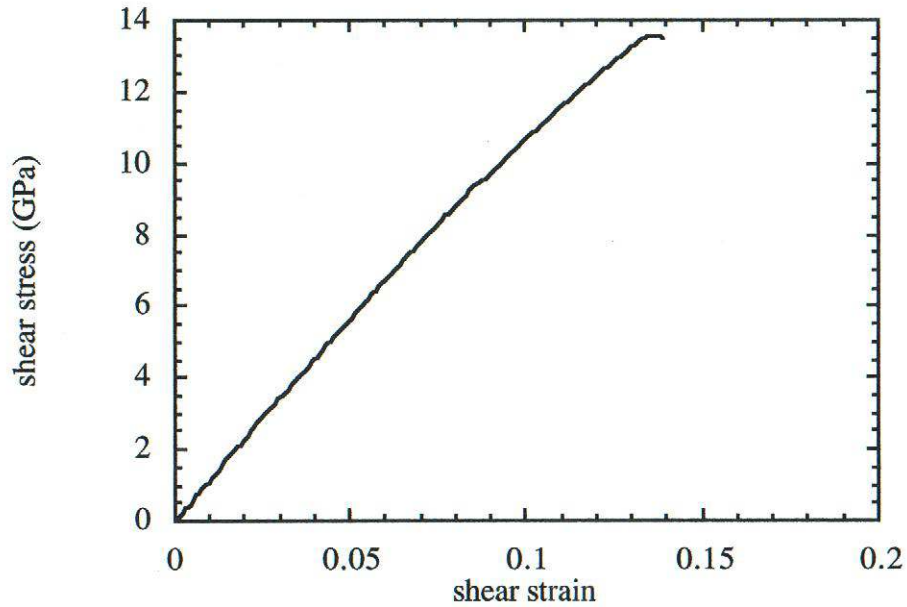

Fig. 2.29. Shear stress-shear strain curves of material block with $1x10^8$ atoms (length is 1.7 μm and height is 0.7 μm) at a strain rate of $1.53x10^{10}$ s^{-1}.

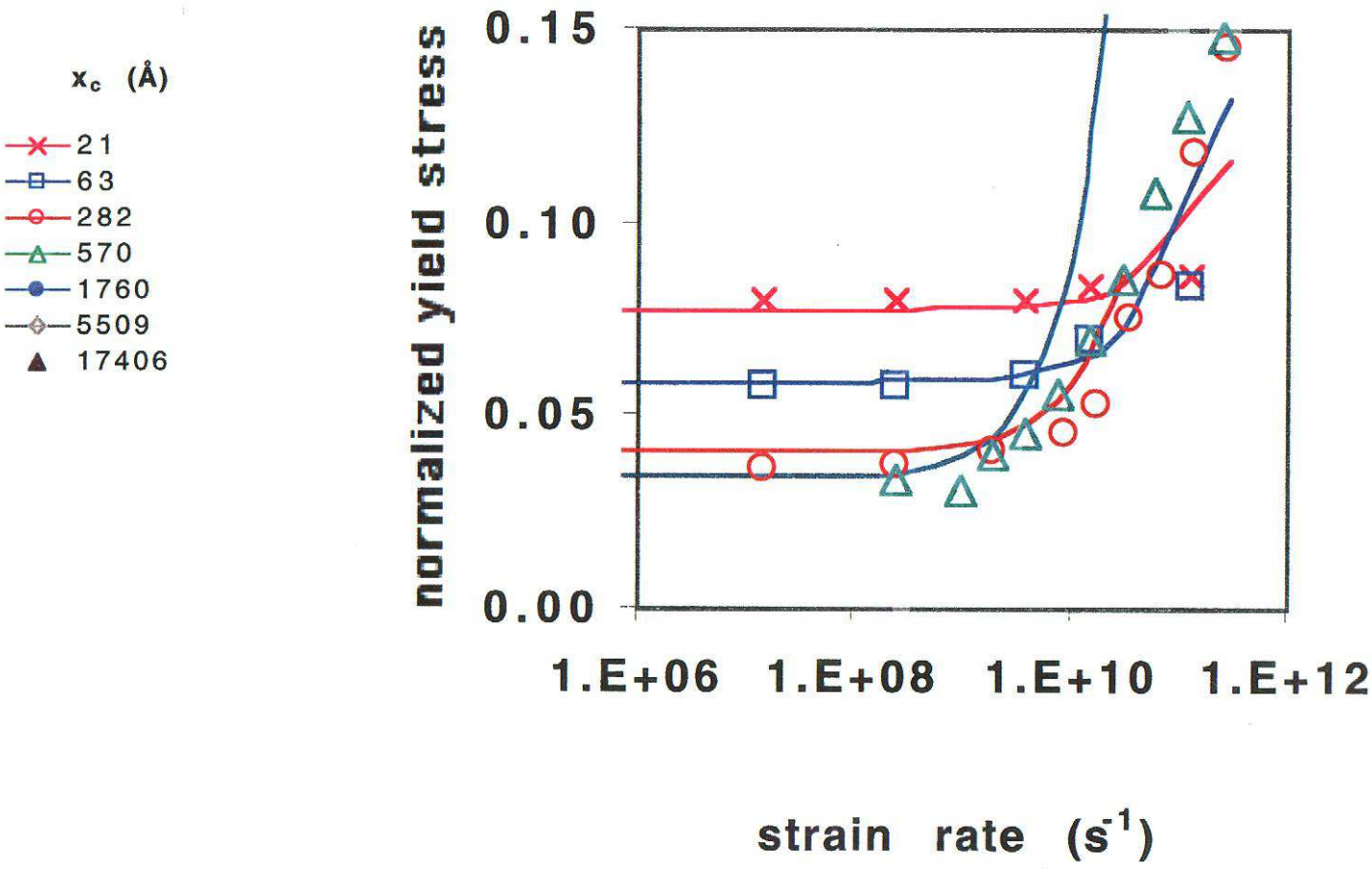

Fig. 2.30.. Yield stress normalized by the shear modulus as a function of strain rate comparing atomistic simulations (dots) and dislocation model (solid line). Various curves represent different model sizes.

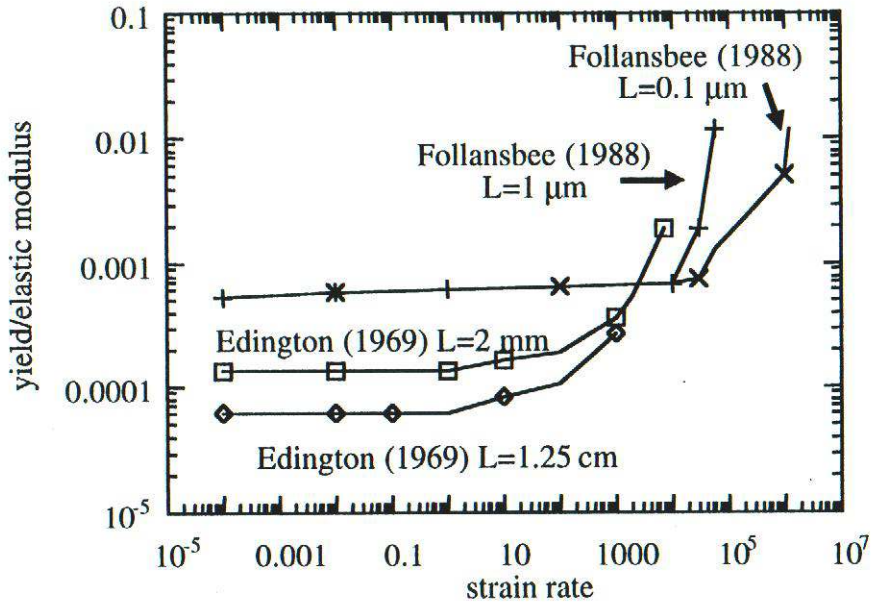

Fig. 2.31. Experimental data examining yield stress versus applied strain rate from Follansbee (1988) and Edington (1969) for copper.

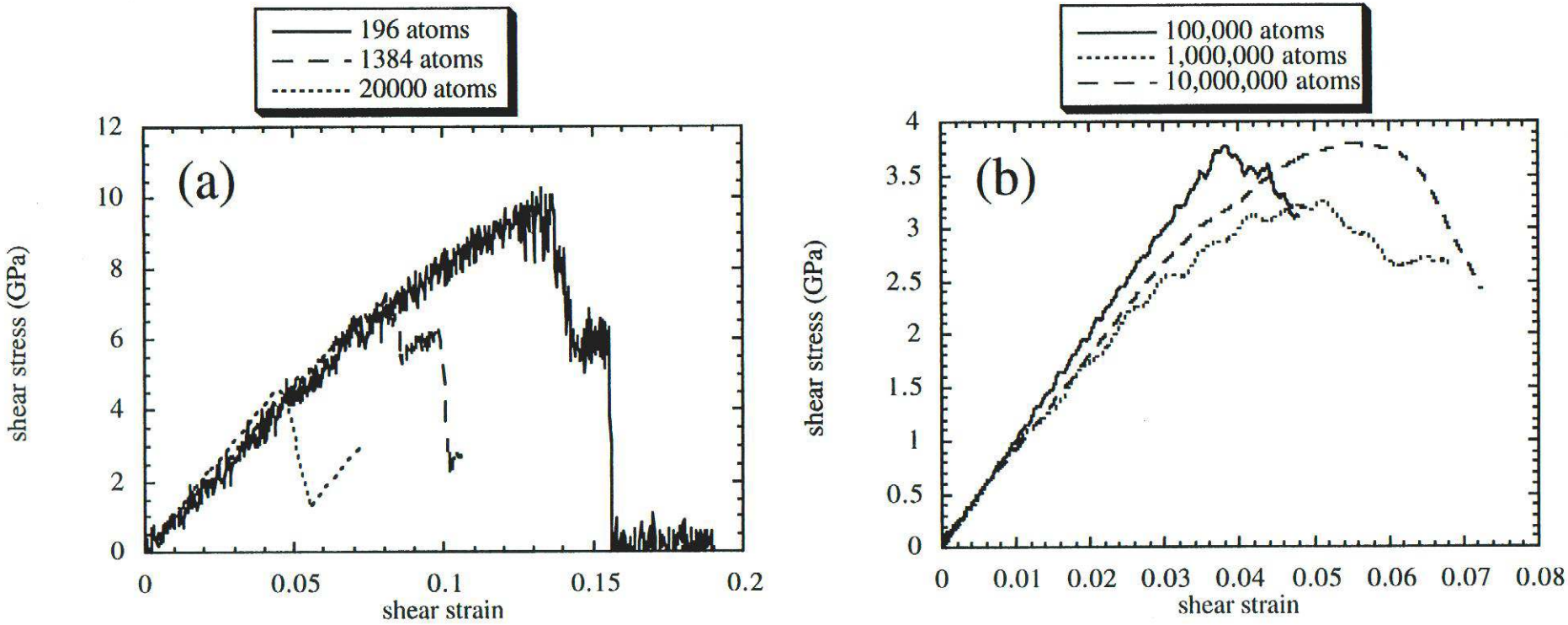

Fig. 2.32. Shear stress-strain curves of various size atomistic models at an applied strain rate of 2.4×10^8 s^{-1} for (a) 196 atoms, 1384 atoms, and 2×10^4 atoms and (b) 10^5 atoms, 10^6 atoms, and 10^7 atoms.

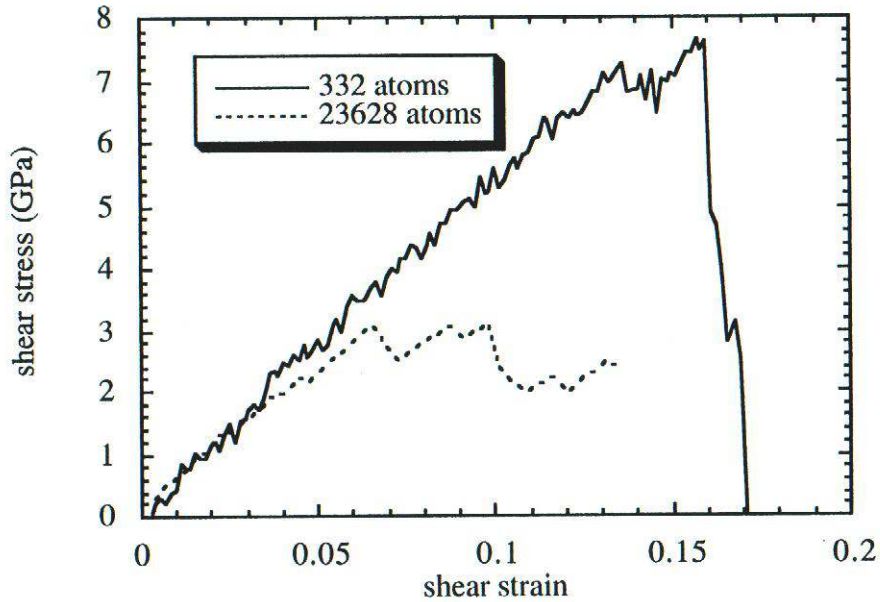

Fig. 2.33. Shear stress-strain curve of two atomistic models showing the differences in yield and work hardening for single crystal copper at a strain rate of 10^9 s^{-1}.

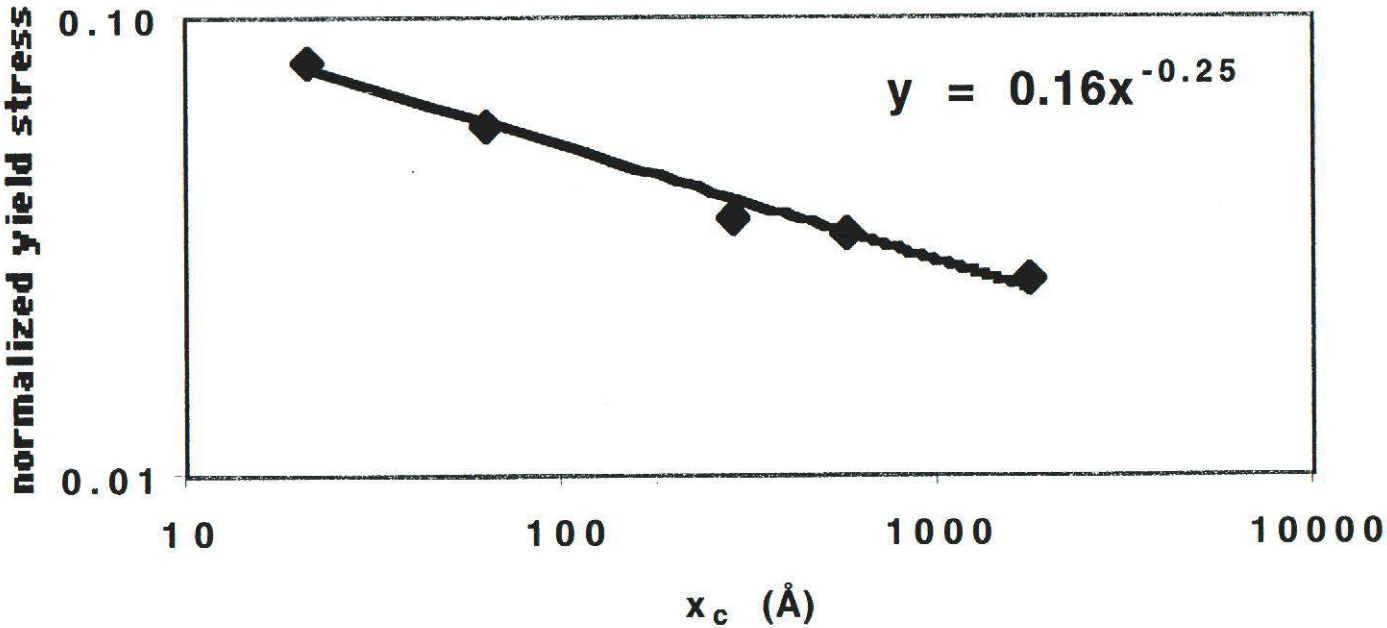

Fig. 2.34. Plateau yield stress normalized by the shear modulus as a function of the size (x-dimension) of the atomistic model. The equation for the power law behavior is shown.

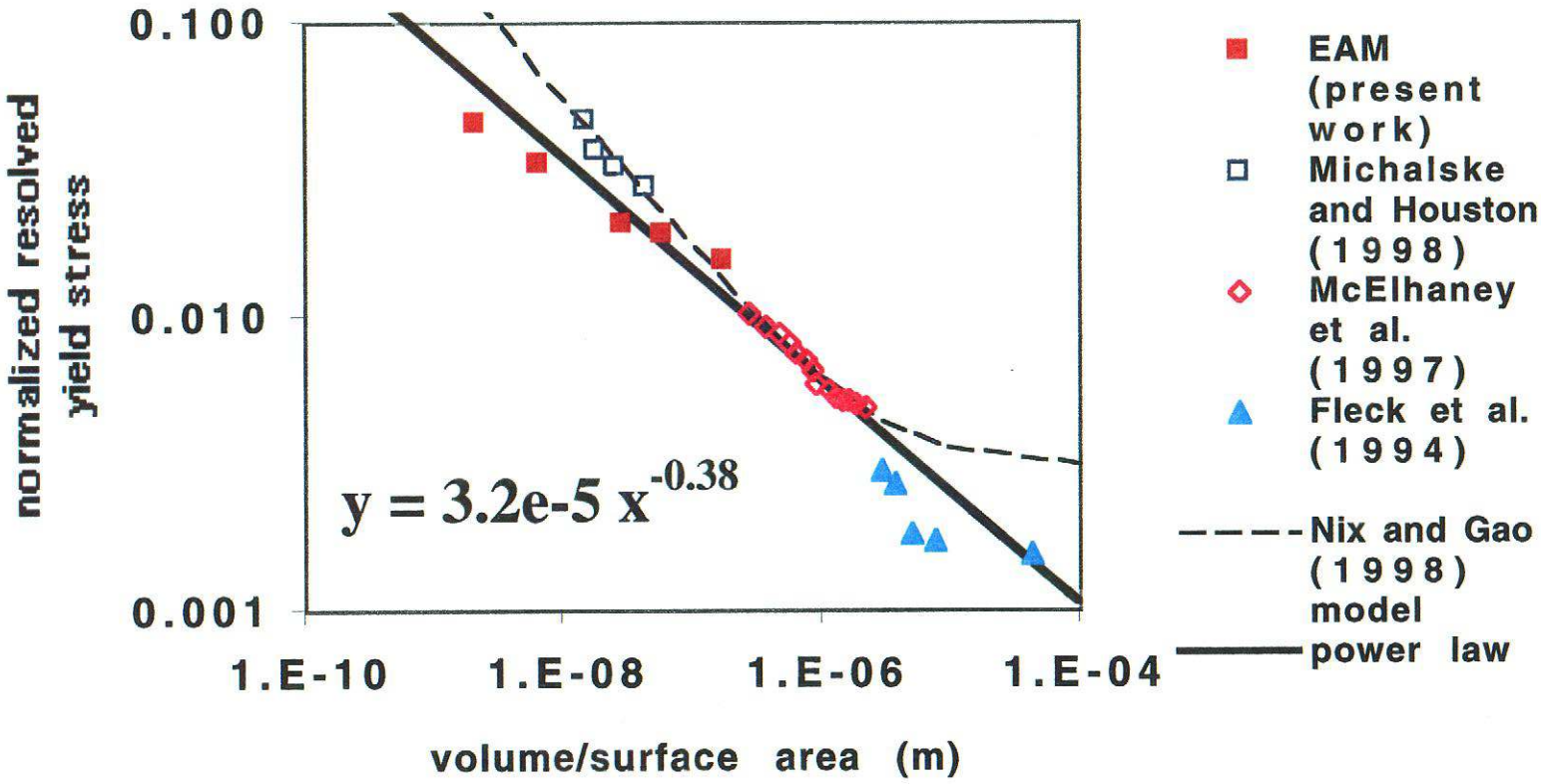

Fig. 2.35. Log-log yield stress normalized by the elastic modulus and resolved on a (111) slip plane versus volume/surface area for nickel, gold, and copper for various experiments and atomistic simulations. The equation for power law behavior is shown.

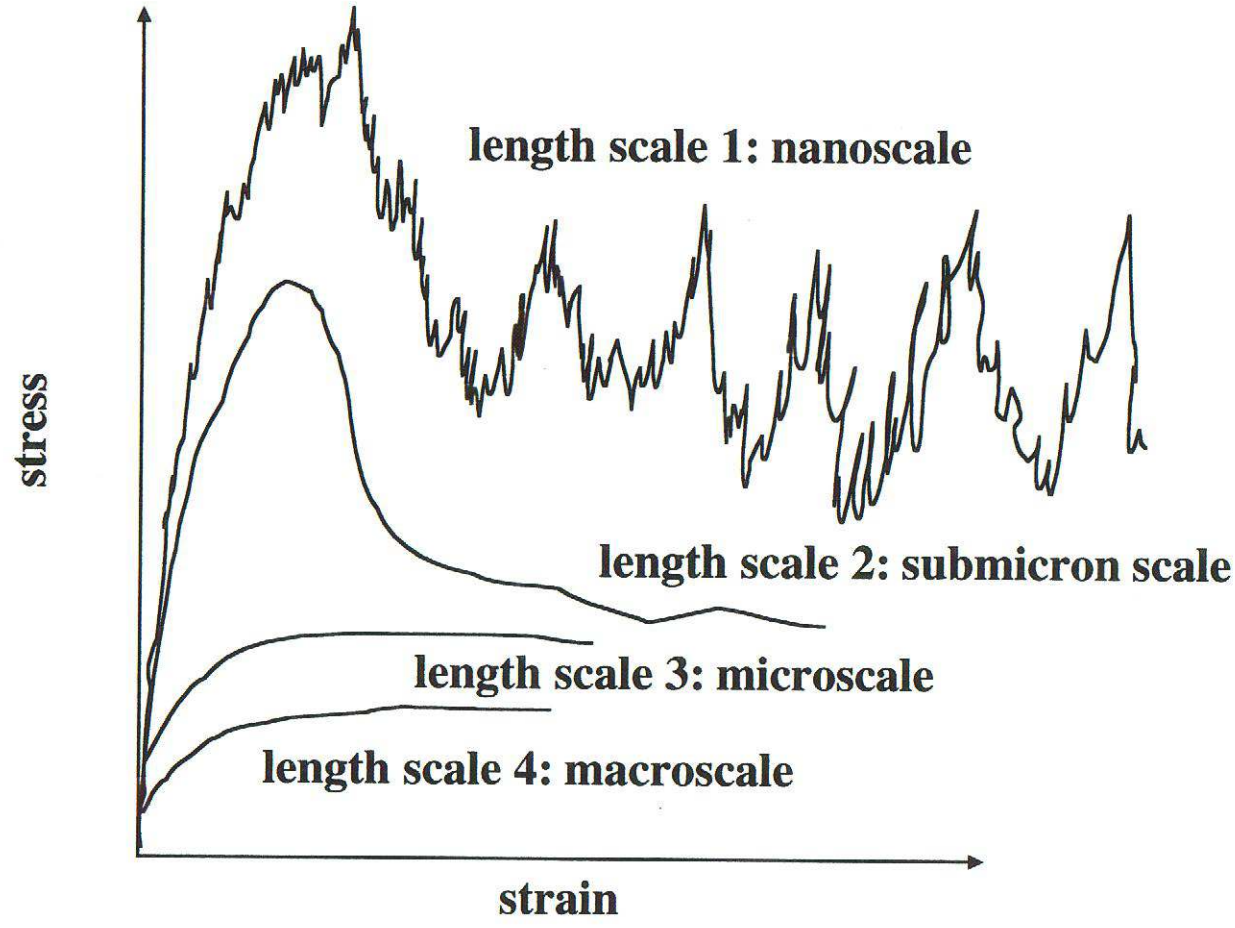

Fig. 2.36. Schematic showing the stress-strain responses at four different size scales.

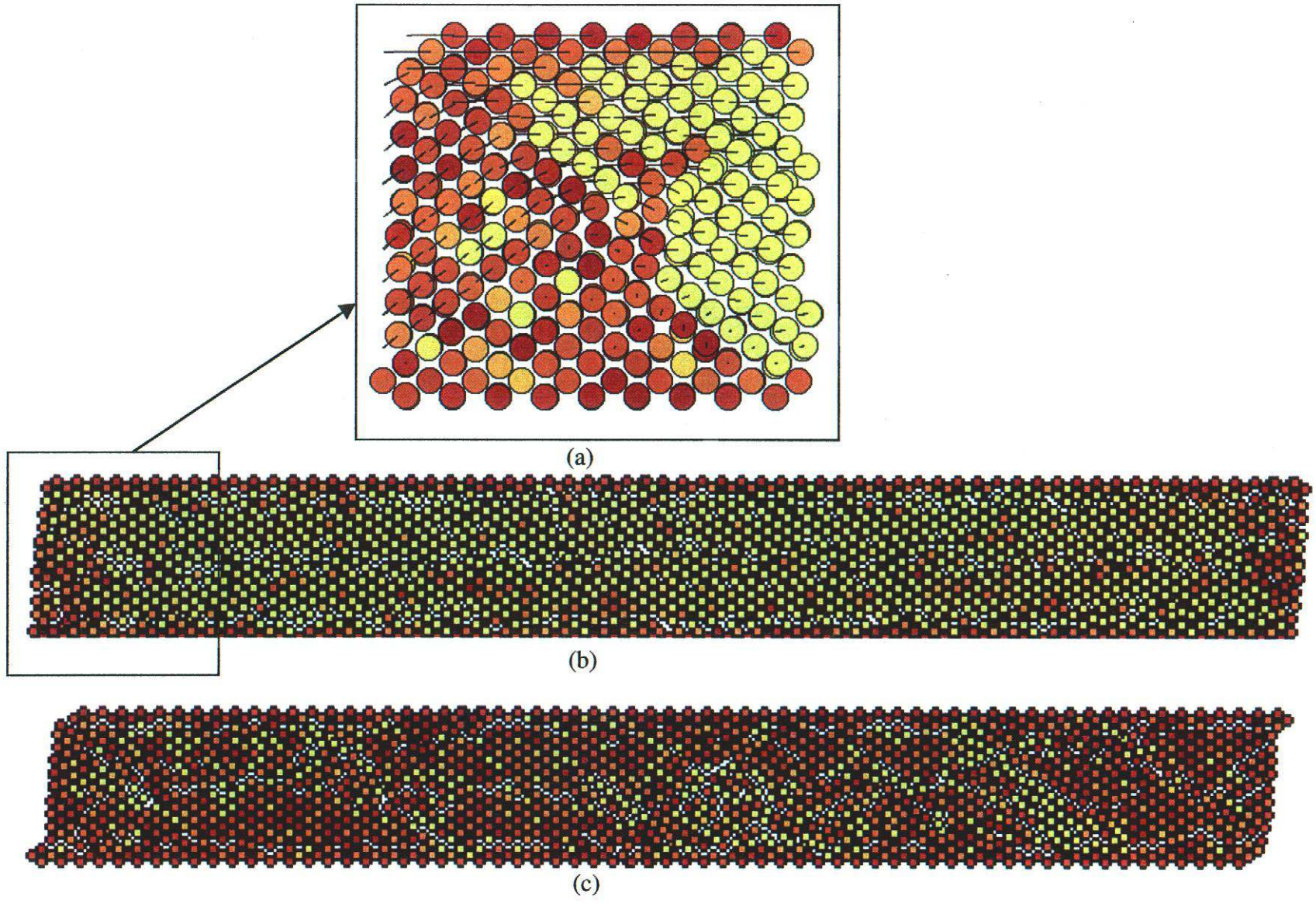

Fig. 2.37. Shear stress contour plots at (a) yield-zoom, (b) yield, and (c) 30% strain, illustrating the deformation response for a length-to-height ratio of approximately 8:1 (225 Å by 28 Å) simulation (yellow are low shear stresses and brown are high shear stresses; arrows denote relative displacements of atoms).

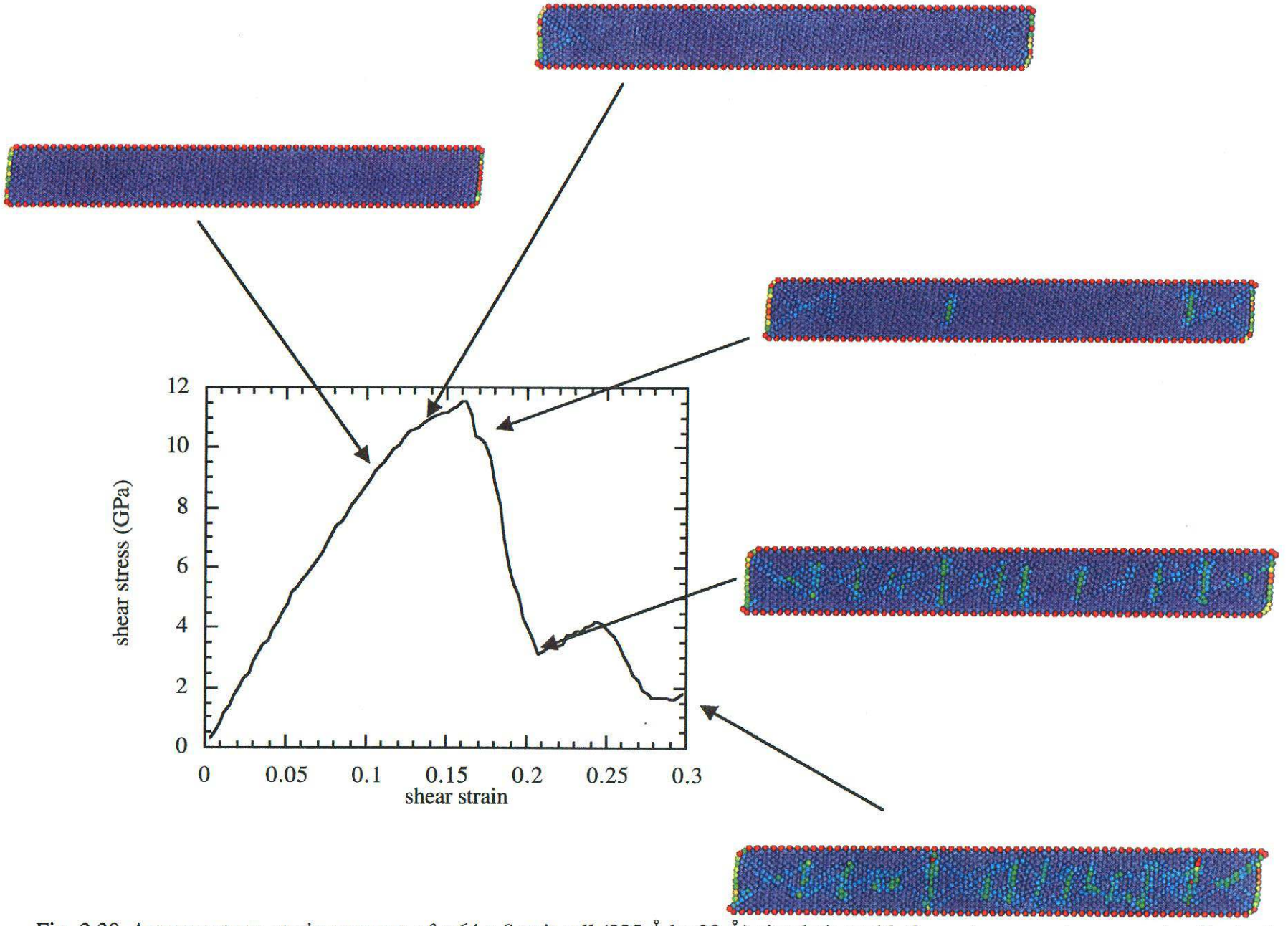

Fig. 2.38. Average stress-strain response of a 64 x 8 unit cell (225 Å by 28 Å) simulation with the centrosymmetry parameter illustrating the dislocation nucleation, motion, and interaction throughout deformation.

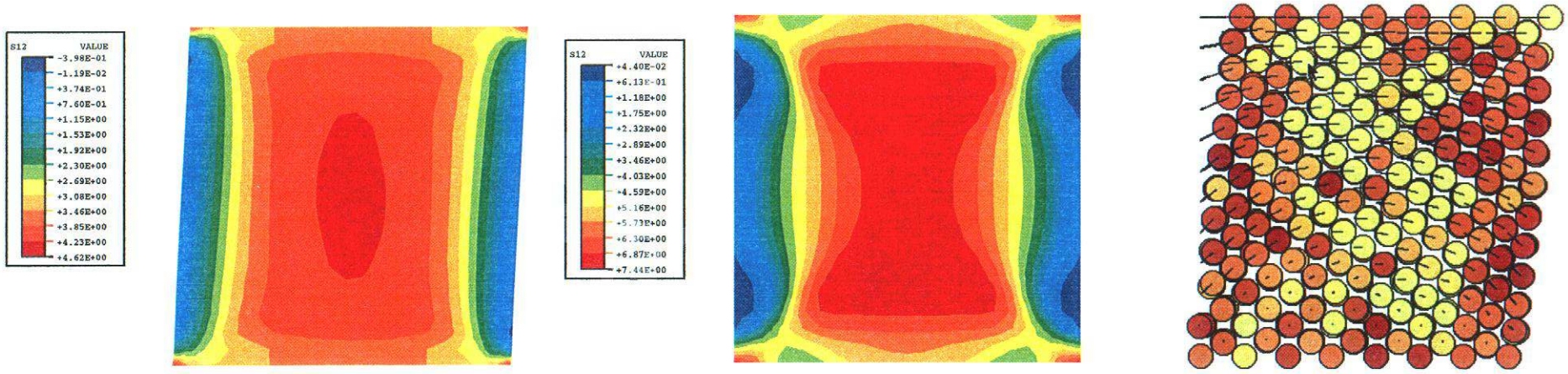

(a) (b) (c)

Figure 2.39. Shear stress contours for a one unit cell by one unit cell block at yield for (a) macroscale internal state variable theory (S12), (b) crystal plasticity (S12), and (c) atomistics (yellow are low shear stresses and brown are high shear stresses; arrows denote relative displacements).

(a)

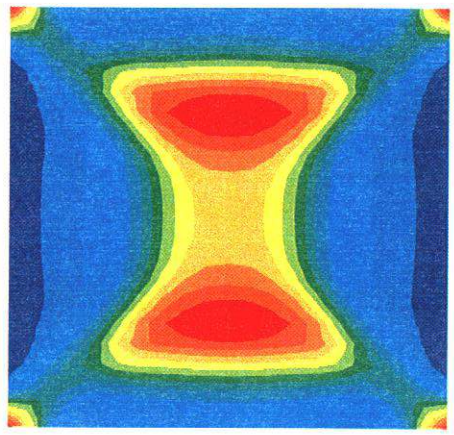

(b)

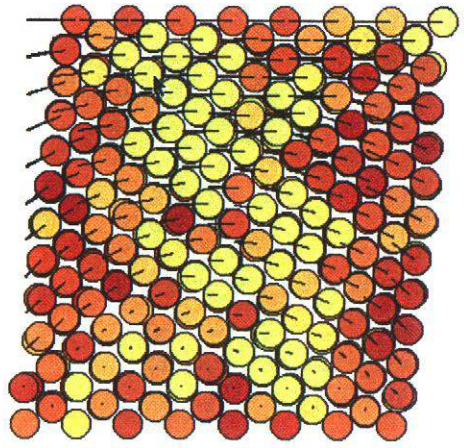

(c)

Fig. 2.40. Shear strain contours for a one unit cell by one unit cell block at yield for (a) macroscale internal state variable theory (E12), (b) crystal plasticity (E12), and (c) atomistics (yellow are low shear strains and brown are high shear strains; arrows denote relative displacements).

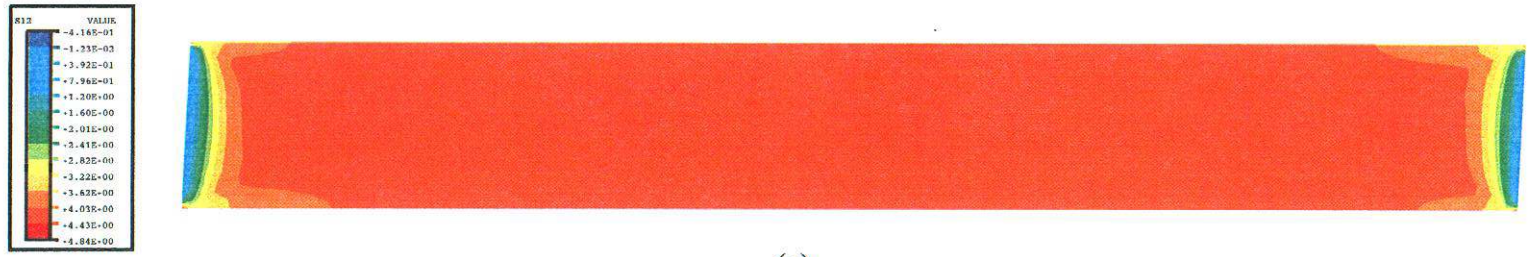

(a)

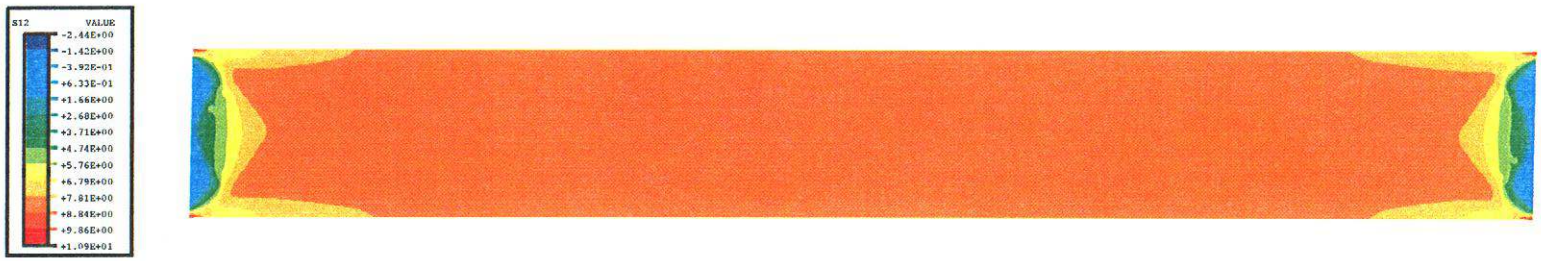

(b)

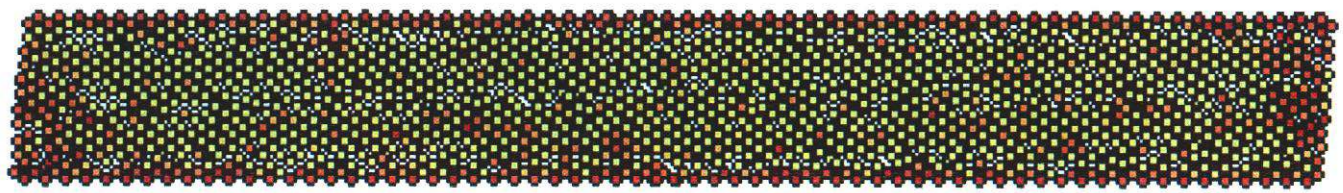

(c)

Fig. 2.41. Shear stress contours for an eight unit cell by one unit cell block at yield for (a) macroscale internal state variable theory (S12), (b) crystal plasticity (S12), and (c) atomistics (yellow are low shear stresses and brown are high shear stresses).

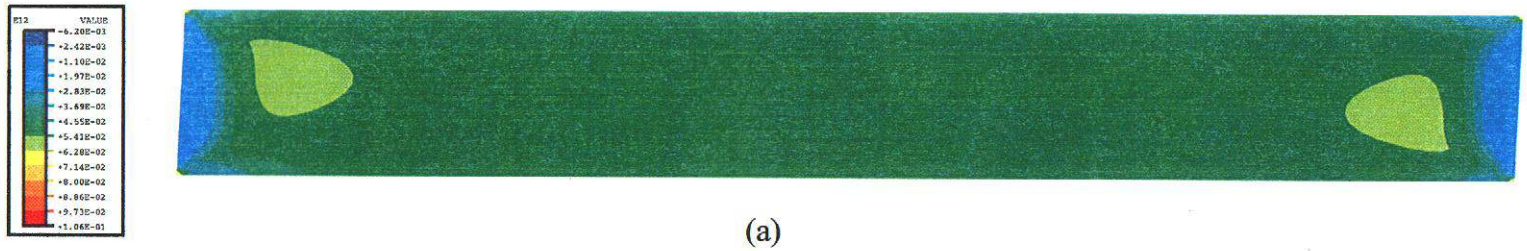

(a)

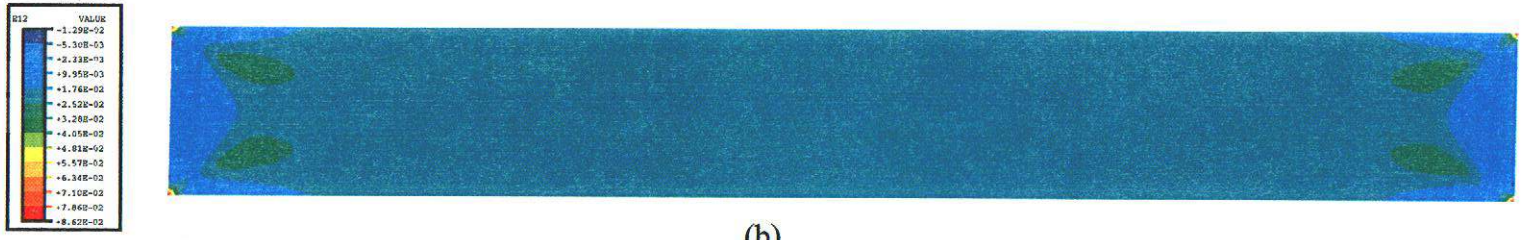

(b)

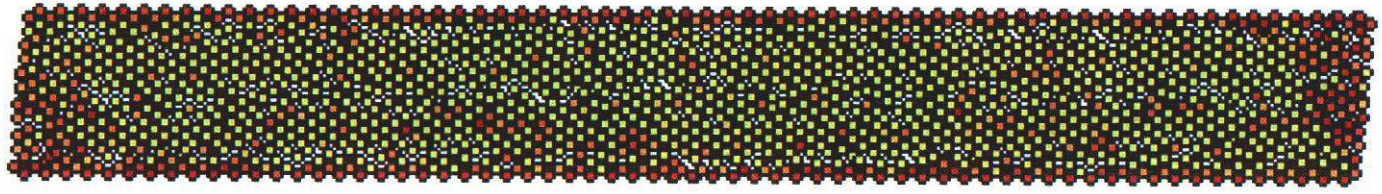

(c)

(d)

Fig. 2.42. Shear strain contours for an eight unit cell by one unit cell block at yield for (a) macroscale internal state variable theory (E12), (b) crystal plasticity (E12),and (c) atomistics (yellow are low shear strains and brown are high shear strains). Orientation angle (SDV37) from the crystal plasticity simulation is given in (d).

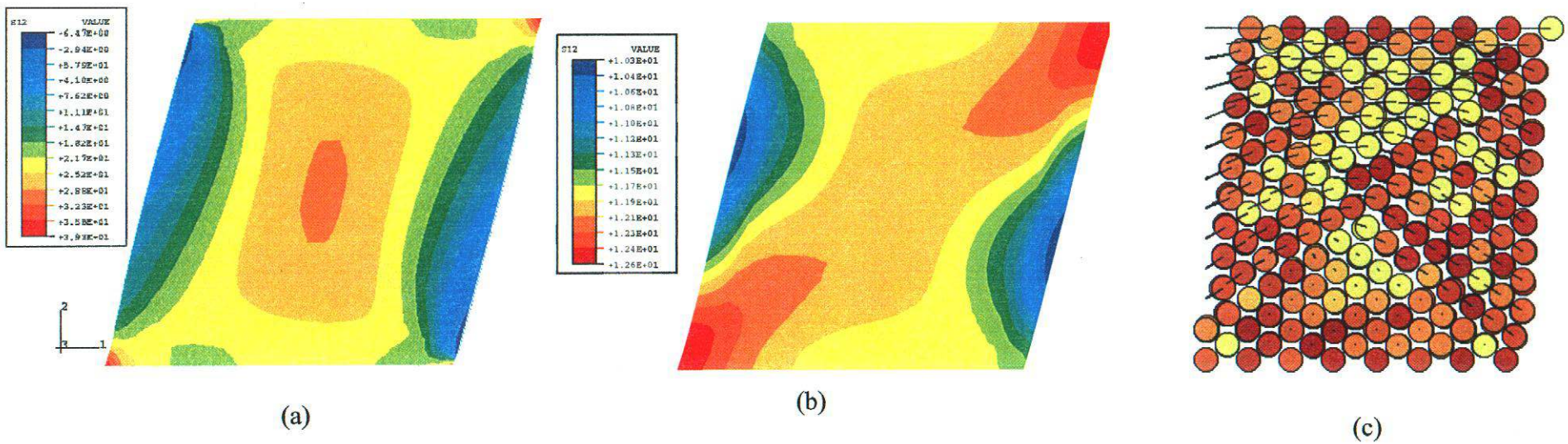

(a) (b) (c)

Fig. 2.43. Shear stress contours for a one unit cell by one unit cell block at 30% strain for (a) macroscale internal state variable theory (S12), (b) crystal plasticity (S12), and (c) atomistics (yellow are low shear stresses and brown are high shear stresses; arrows denote relative displacements of atoms).

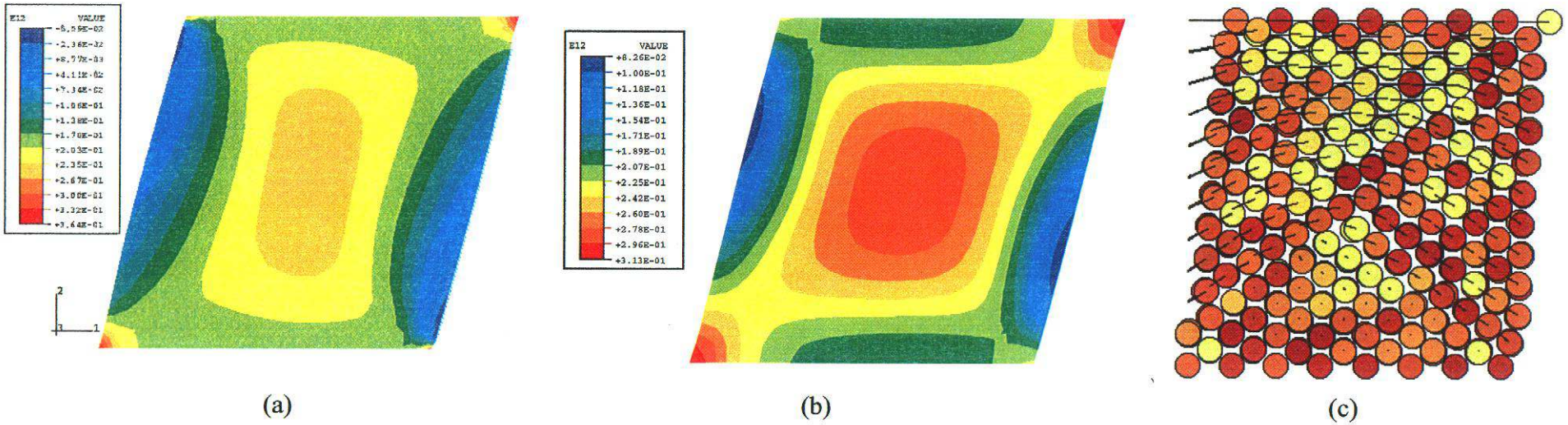

(a) (b) (c)

Fig. 2.44. Shear strain contours for a one unit cell by one unit cell block at 30% strain for (a) macroscale internal state variable theory (E12), (b) crystal plasticity (E12), and (c) atomistics (yellow are high shear strains and brown are low shear strains; arrows denote relative displacements of atoms).

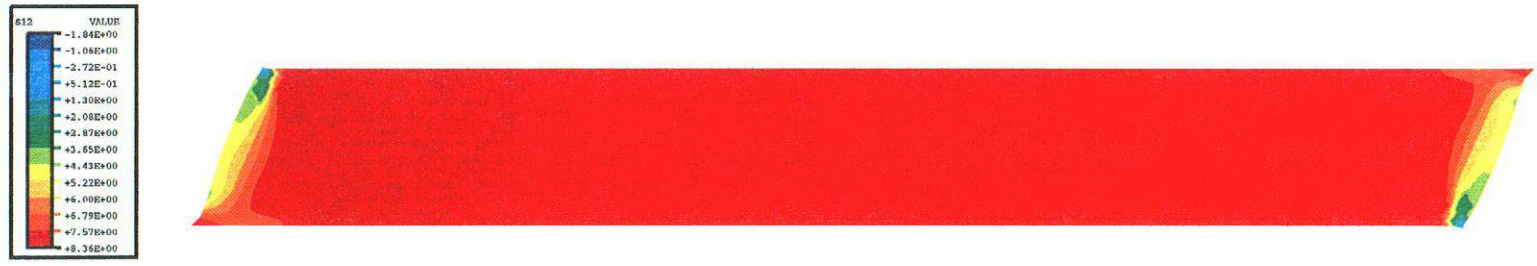

(a)

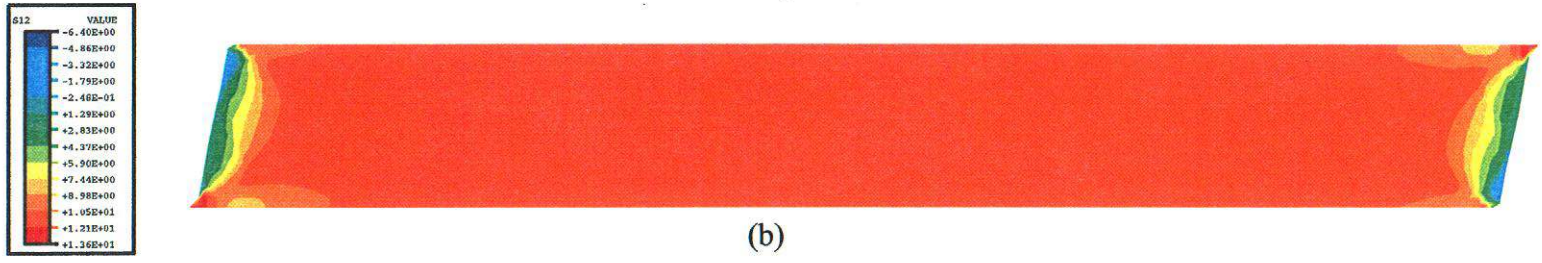

(b)

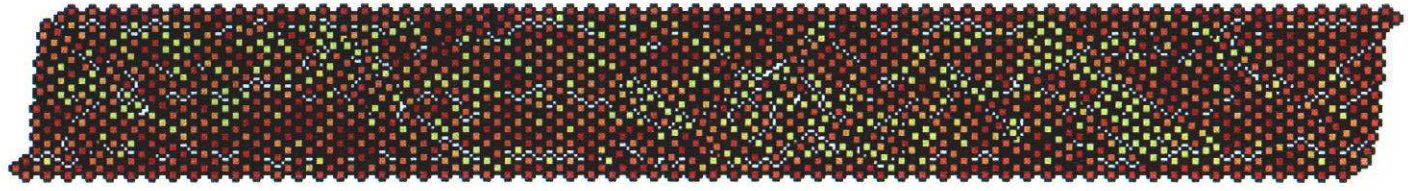

(c)

Fig. 2.45. Shear stress contours for an eight unit cell by one unit cell block at 30% strain for (a) macroscale internal state variable theory (S12), (b) crystal plasticity (S12) and (c) atomistics (yellow are low shear stresses and brown are high shear stresses).

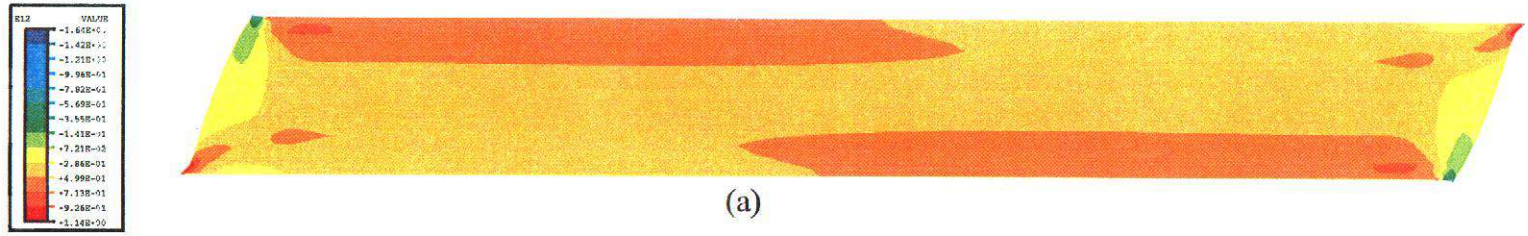

(a)

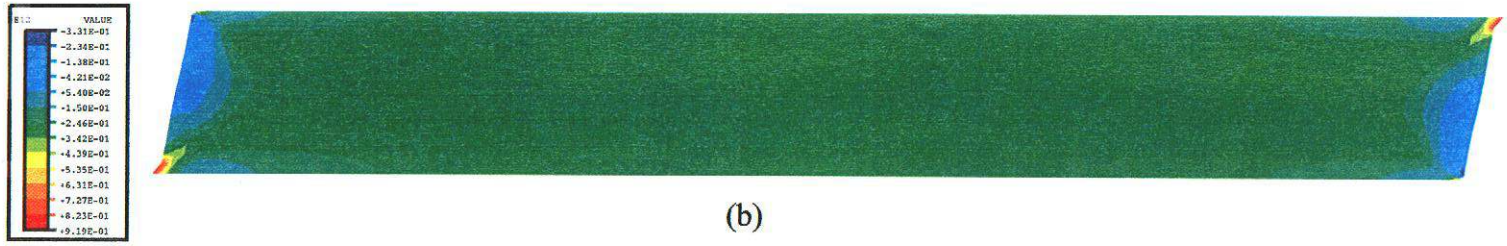

(b)

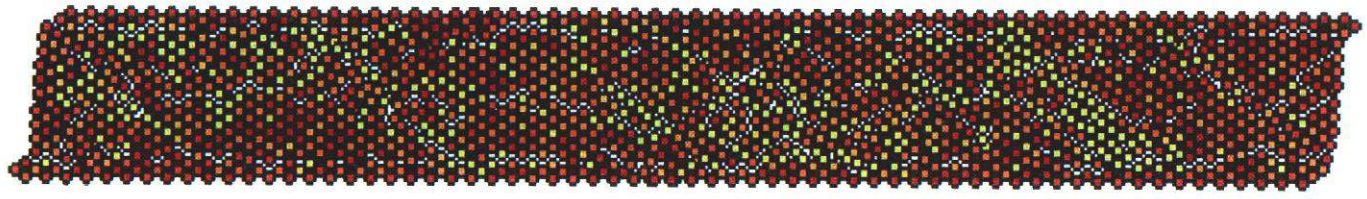

(c)

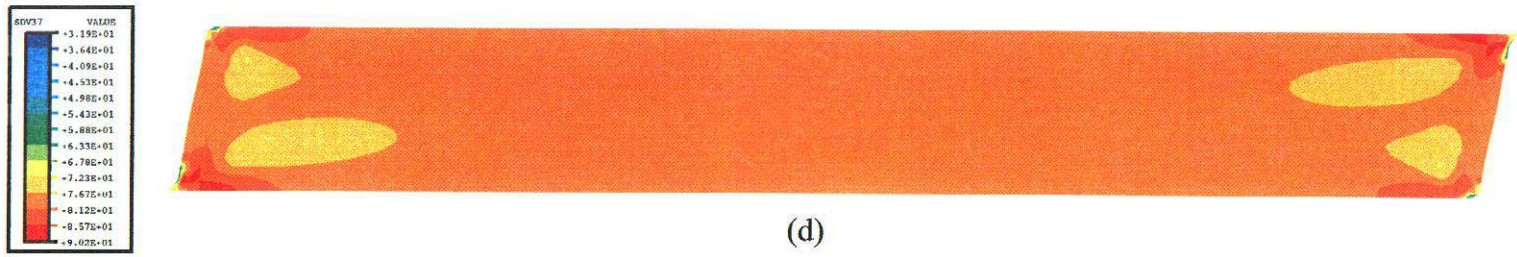

(d)

Fig. 2.46. Shear strain contours for an eight unit cell by one unit cell block at 30% strain for (a) macroscale internal state variable theory (E12), (b) crystal plasticity (E12) and (c) atomistics (yellow are low shear strains and brown are high shear strains). Crystal orientations (SDV37) are shown from the crystal plasticity simulation in (d).

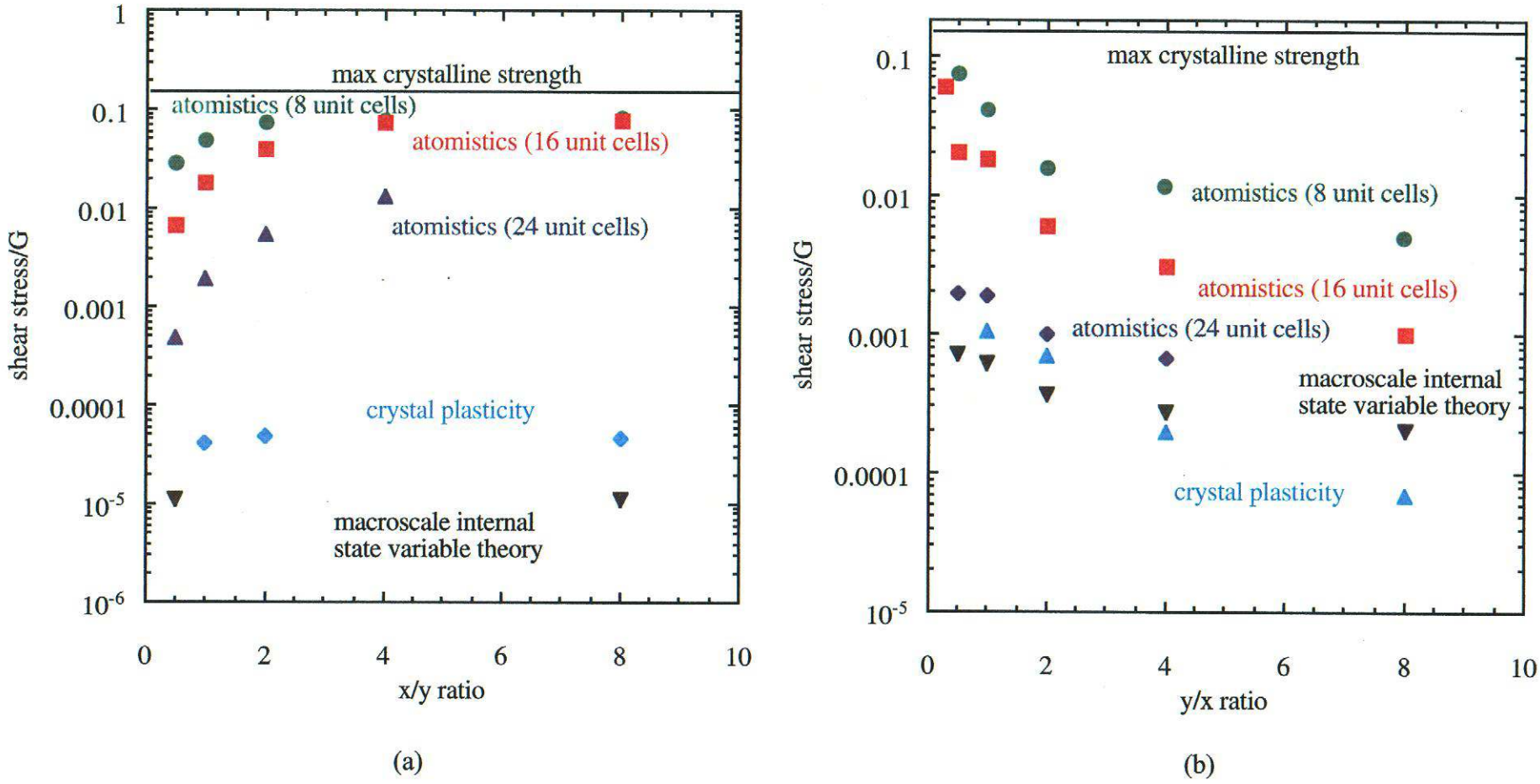

Fig. 2.47. Average yield stress for a block of material of varying aspect ratios computed with different modeling methods: a) constant y, varying x; b) constant x, varying y.

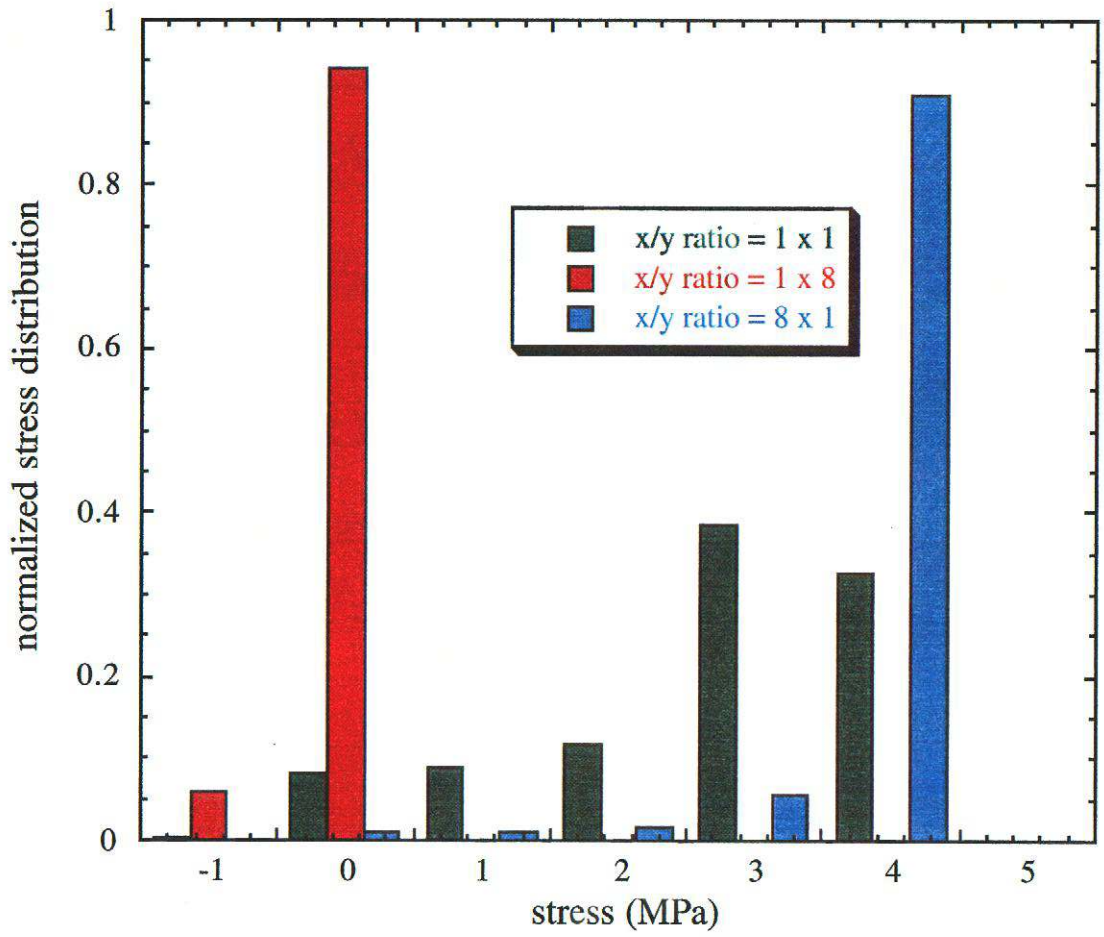

Fig. 2.48. Stress distribution normalized by highest local stress from macroscale ISV model finite element analysis for different x/y aspect ratios under simple shear.

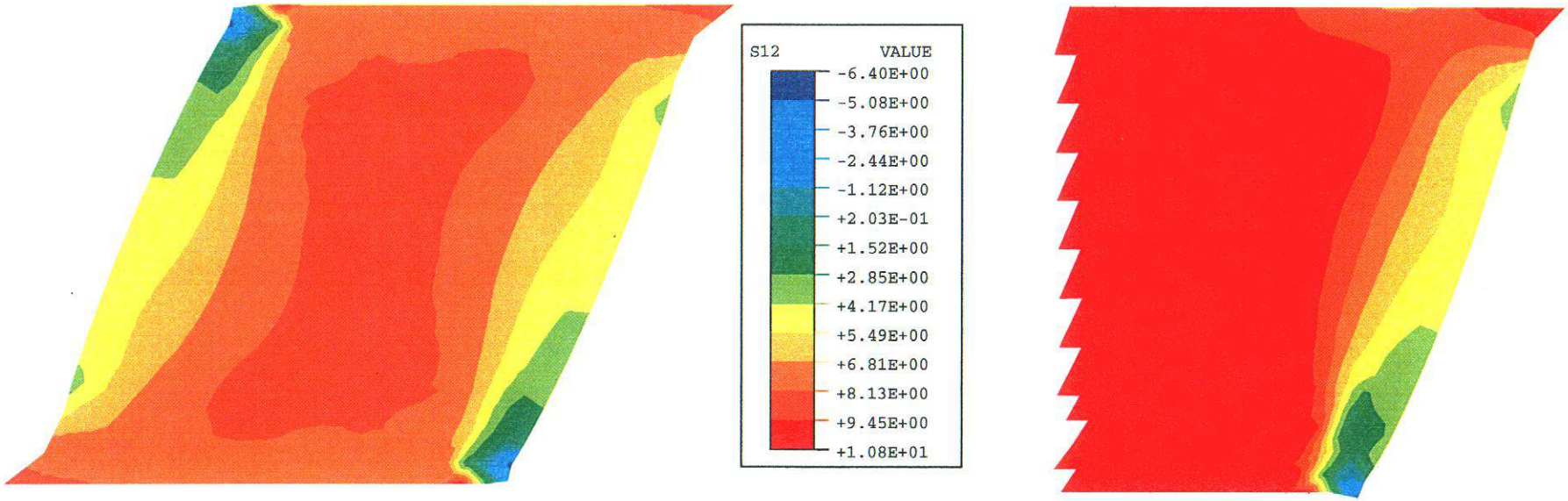

(a) (b)

Fig. 2.49. Shear stress contours (S12) of (a) 1x1 and (b) 8x1 blocks after 30% shear strain. Both blocks show similar distribution of stresses in corners despite different aspect ratios.

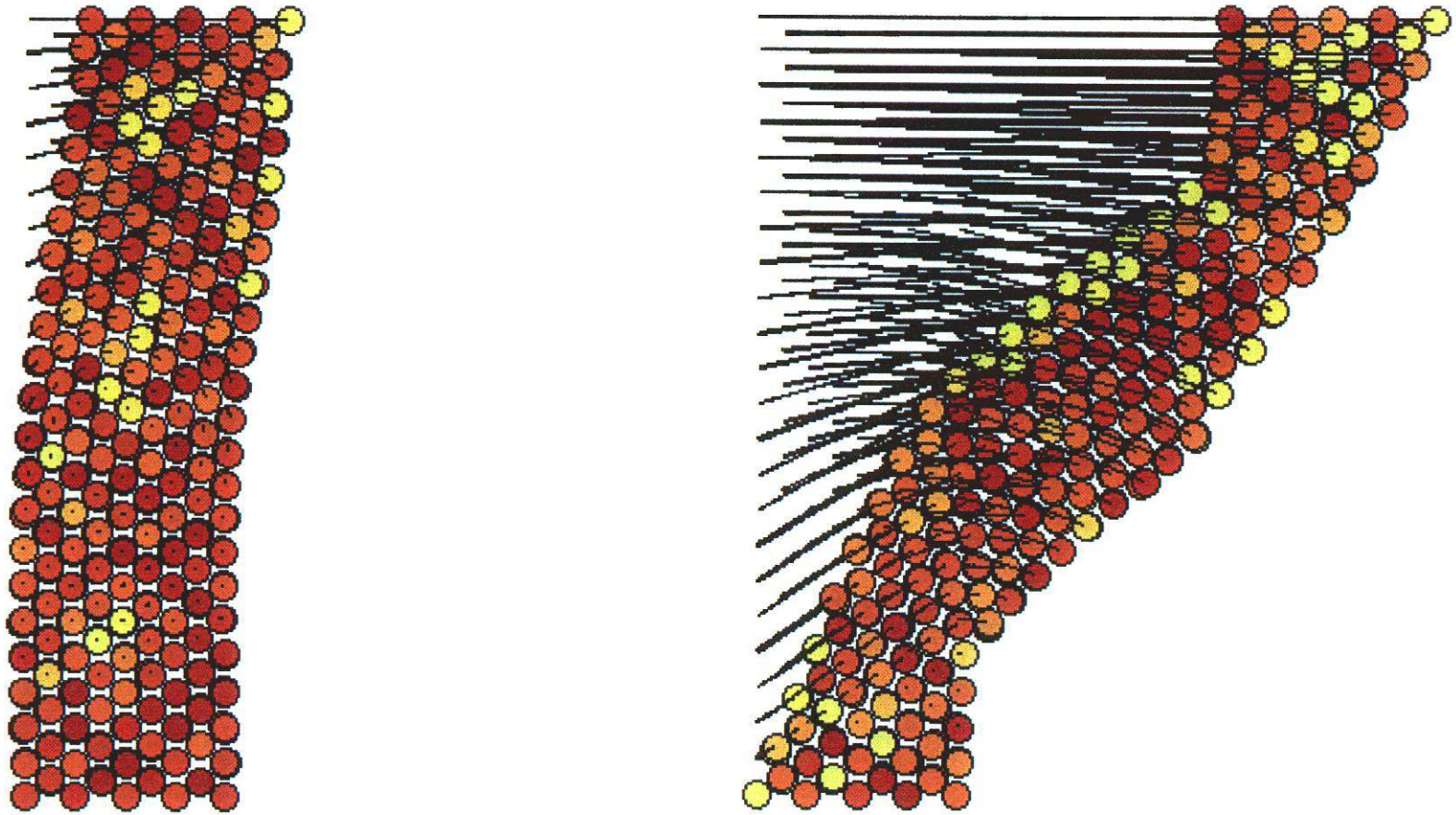

(a) (b)

Fig. 2.50. Shear stress contour plots at (a) yield and (b) 30% strain, illustrating the deformation response for a 4 x 16 unit cell (14 Å by 56 Å) simulation (yellow are high shear stresses and brown are low shear stresses; arrows denote relative displacements of atoms).

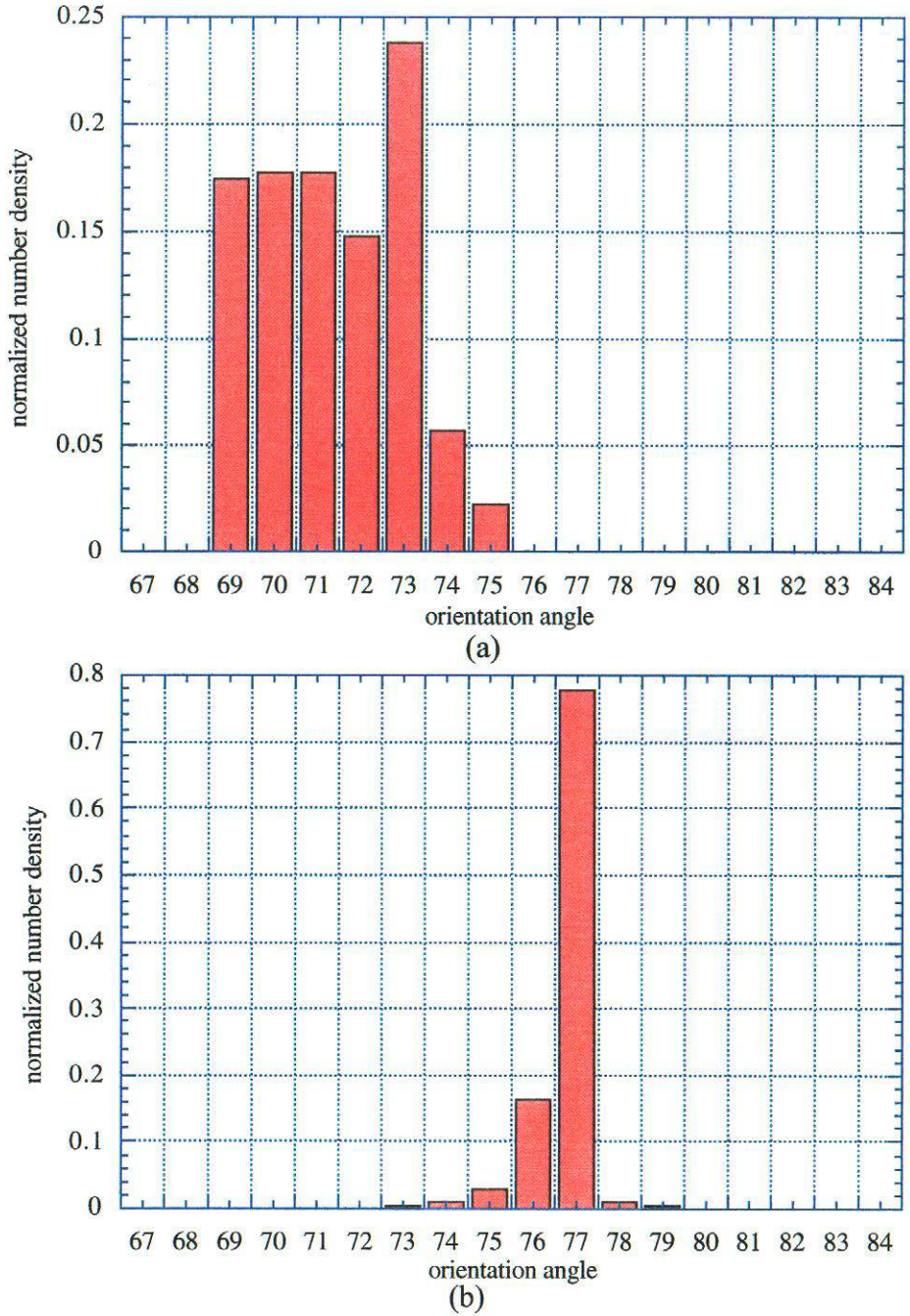

Fig. 2.51. Comparison of orientation angle distribution at 30% strain from the (a) 1 x 1 and (b) 8 x 1 x/y aspect ratios from the crystal plasticity calculations.

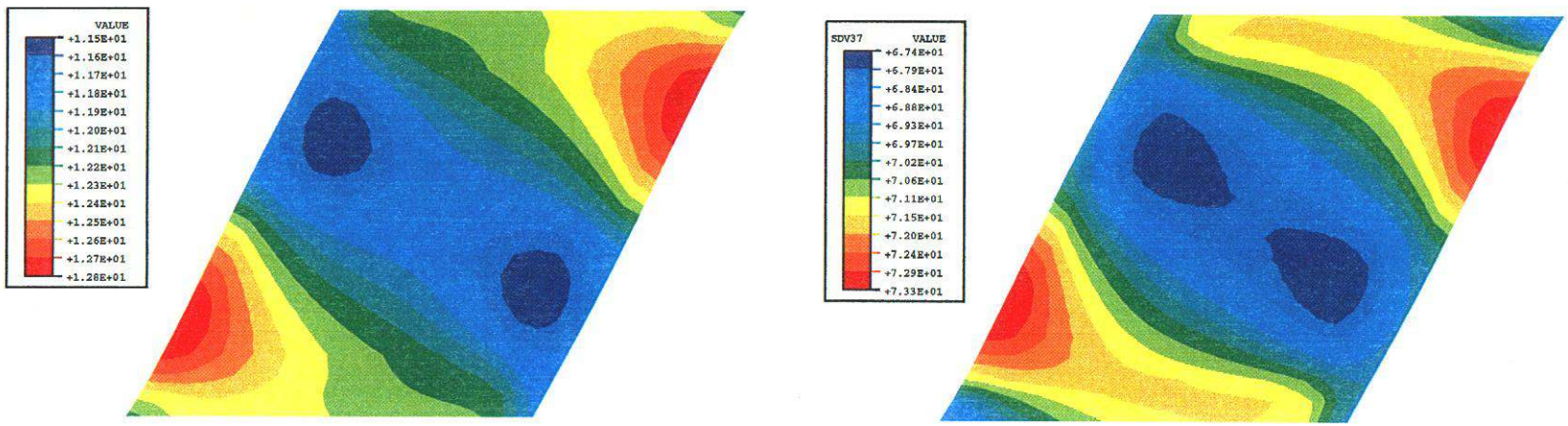

(a) (b)

Fig. 2.52. Color contours of (a) shear stress (S12) and (b) crystal orientation (SDV37) illustrating dependence of stress state on lattice orientation.

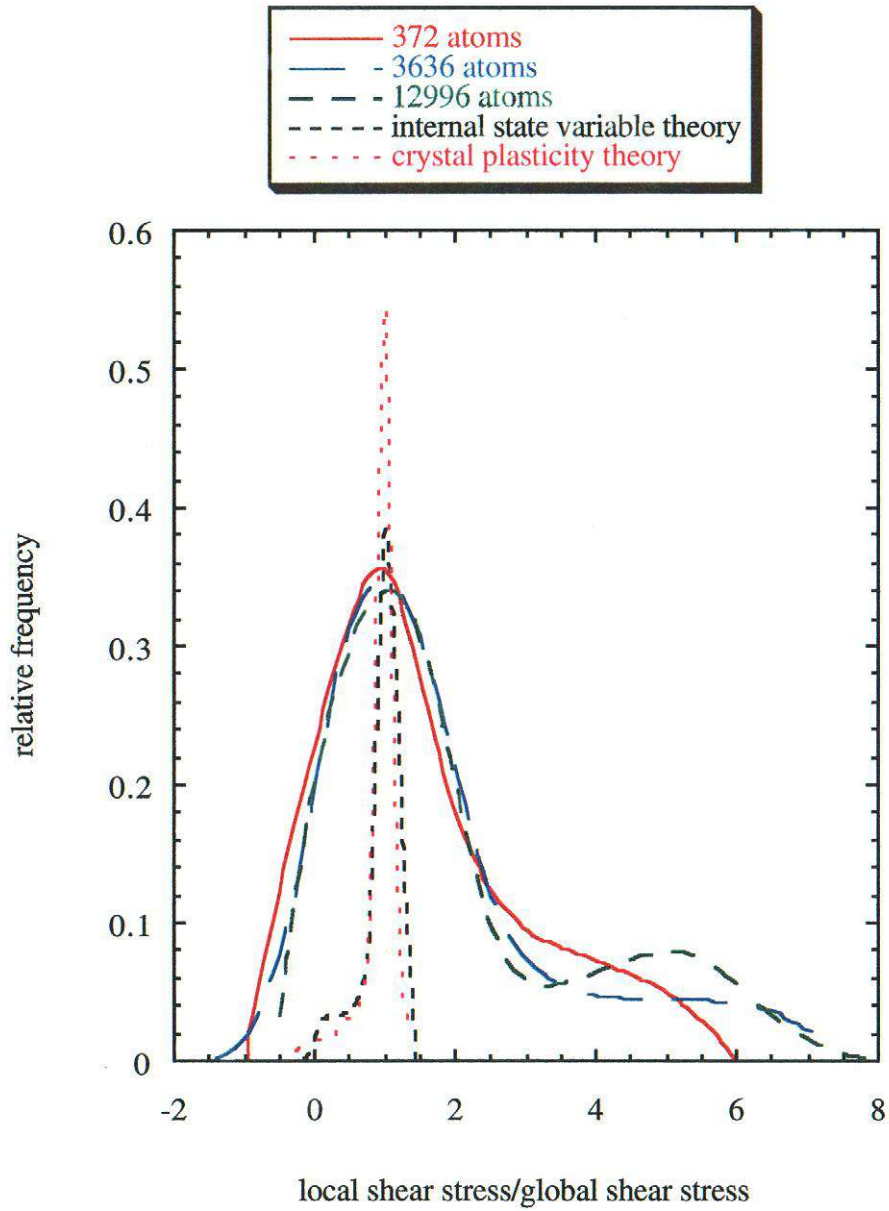

Fig. 2.53. Relative frequency of local shear stress over the global average stress at yield for a x/y aspect ratio of two for the internal state variable theory, crystal plasticity theory, and three different block sizes of atomistic simulations.

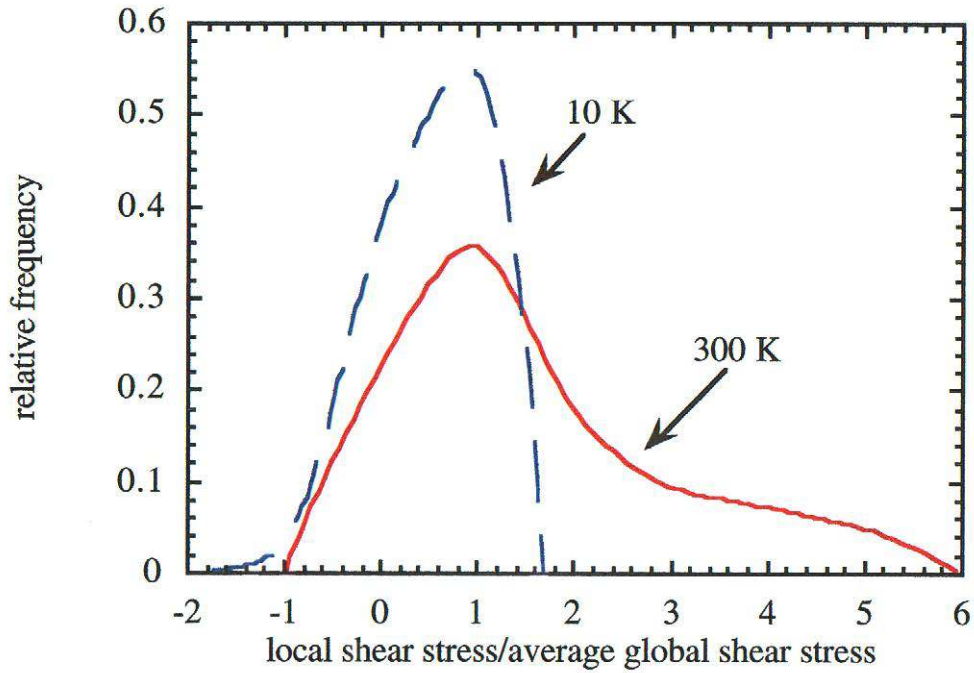

Fig. 2.54. Relative frequency of local shear stress over the global average stress at yield for a x/y aspect ratio of two for an atomistic simulation at 10 K and 300 K for 372 atoms of nickel.

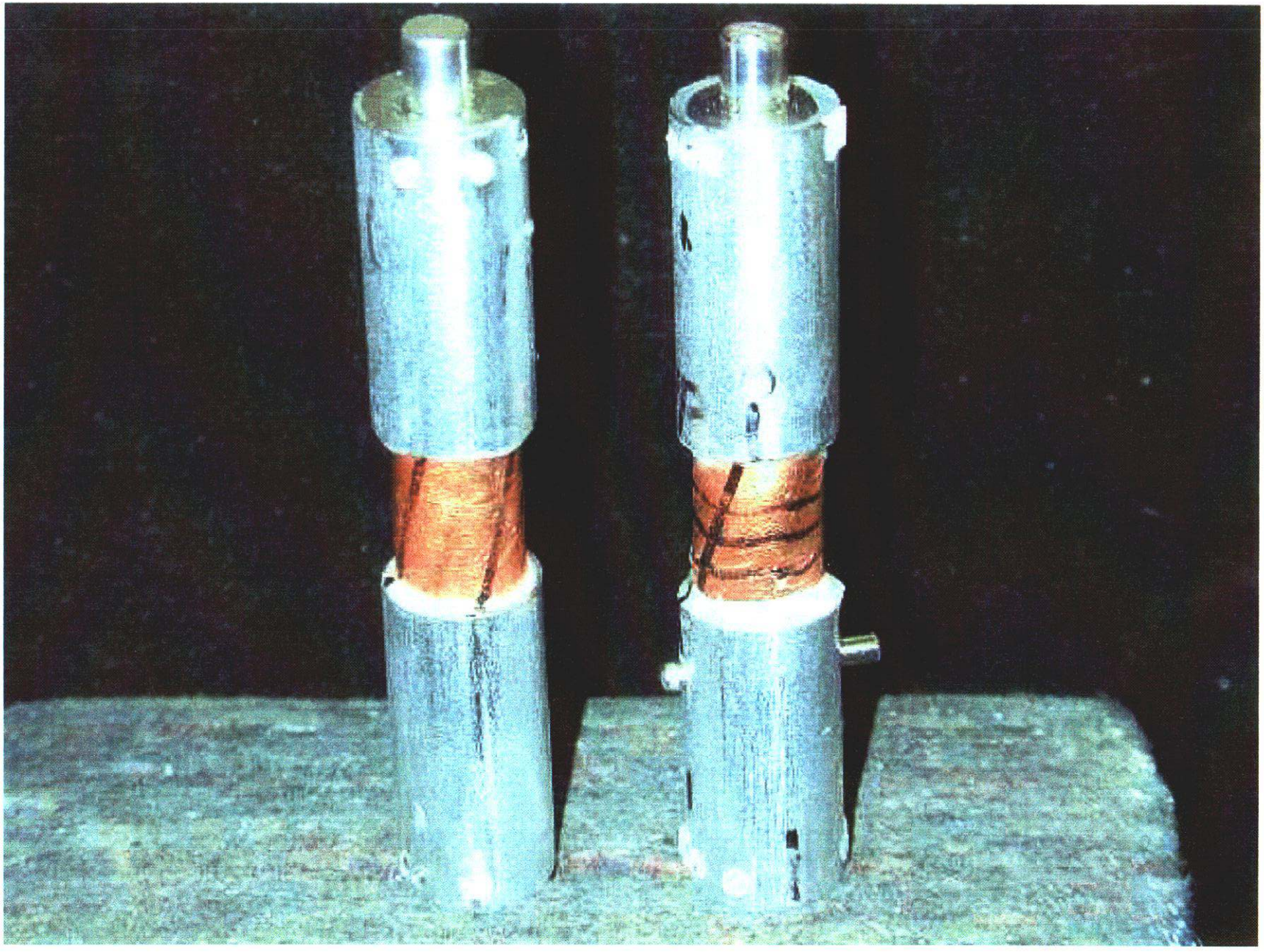

Fig. 2.55. Pictures of two single crystal Cu torsional specimens.

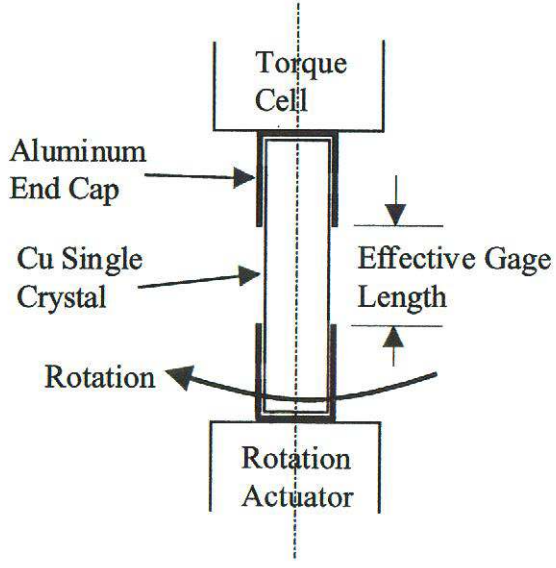

Fig. 2.56. Schematic of MTS multiaxial test system.

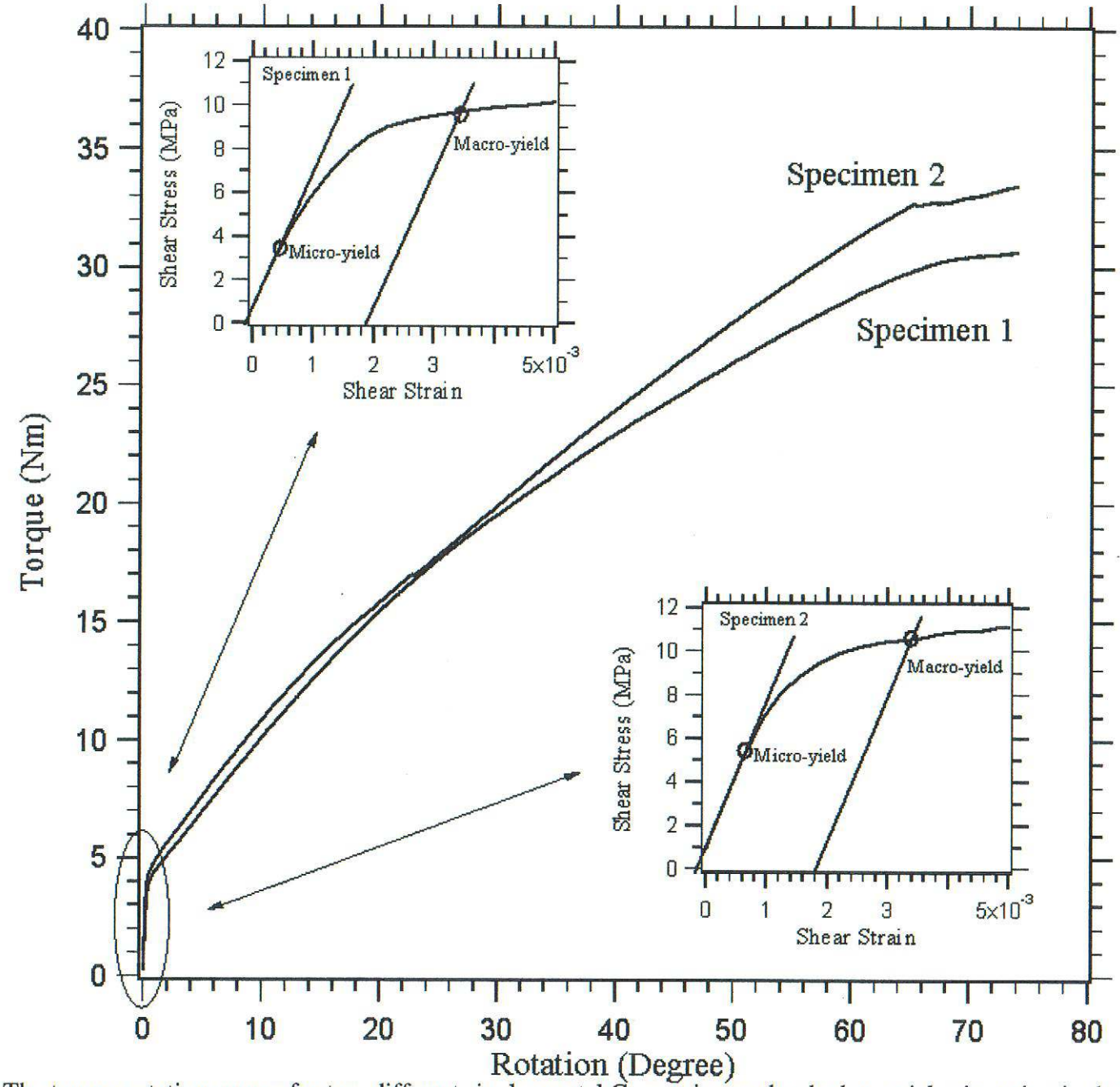

Fig. 2.57. The torque-rotation curves for two different single crystal Cu specimens that had an axial orientation in the [110] direction.

(a) (b)

Fig. 2.58. Close-up view of two specimens at 35% shear strain illustrating wavy pattern on outside of torsion bar.

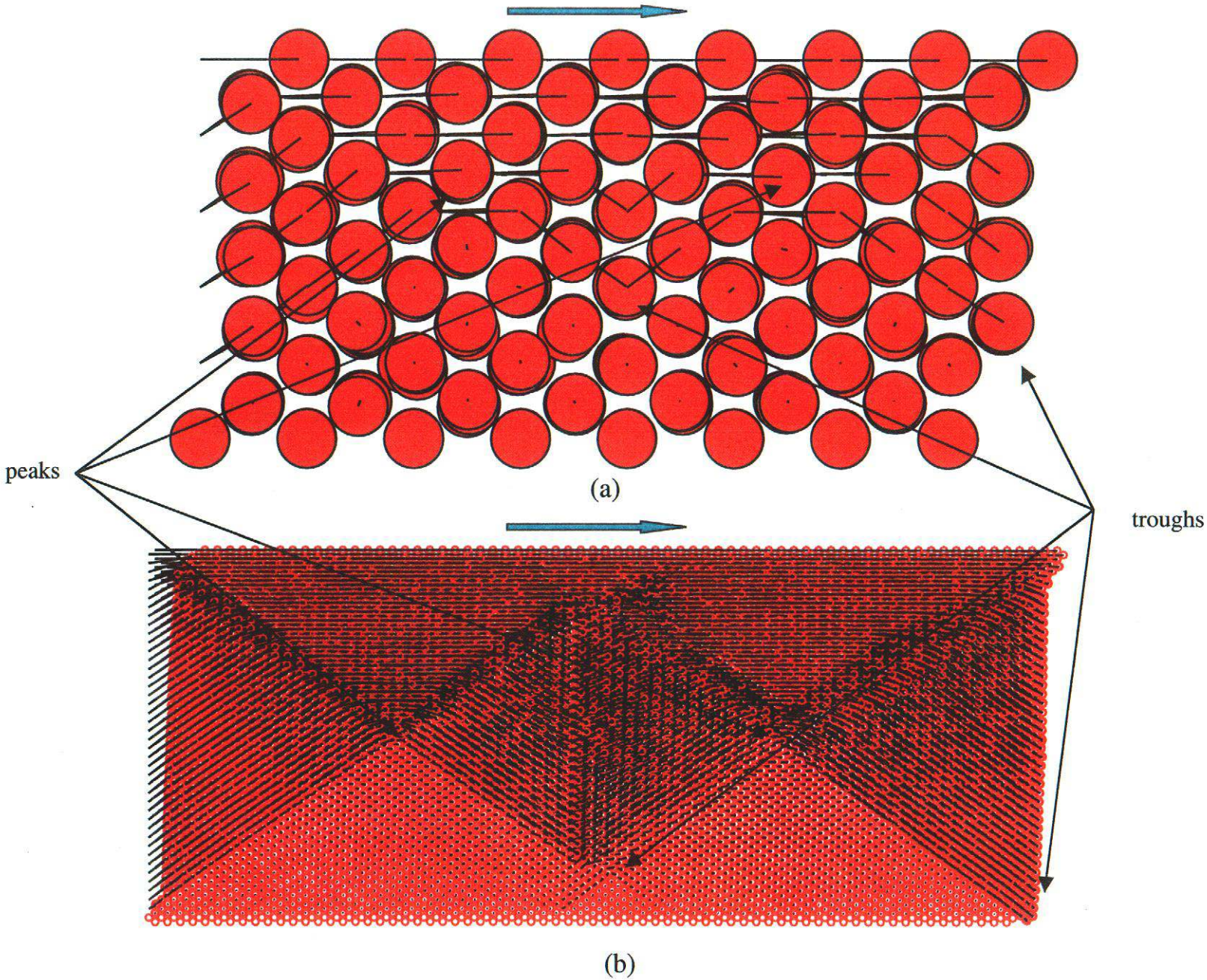

Figure 2.59. Plot of atoms showing relative displacements from original positions with (a) small specimen and (b) large specimen under simple shear.

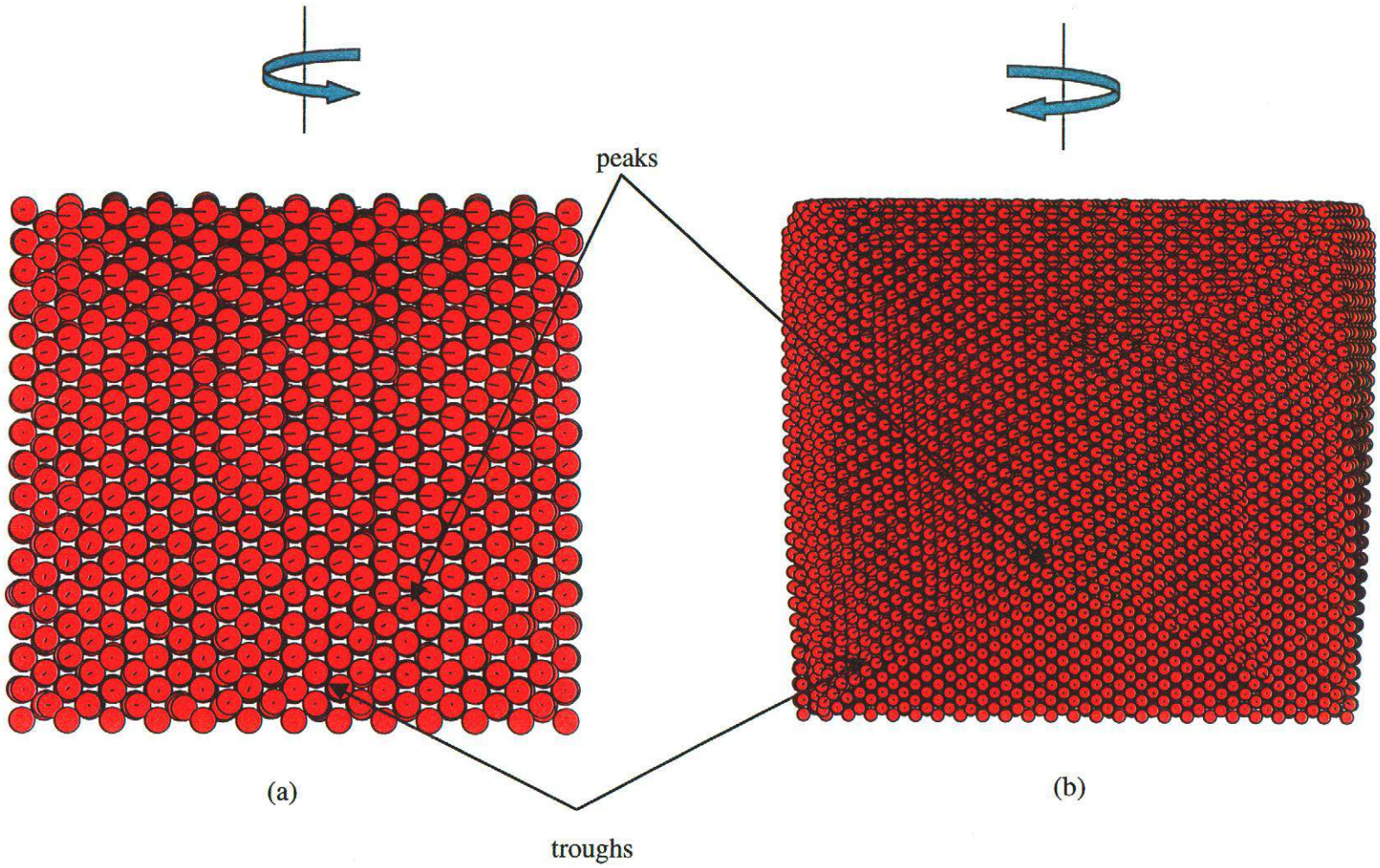

Figure 2.60. Plot of atoms showing relative displacements from original positions with (a) small specimen and (b) large specimen under torsion.

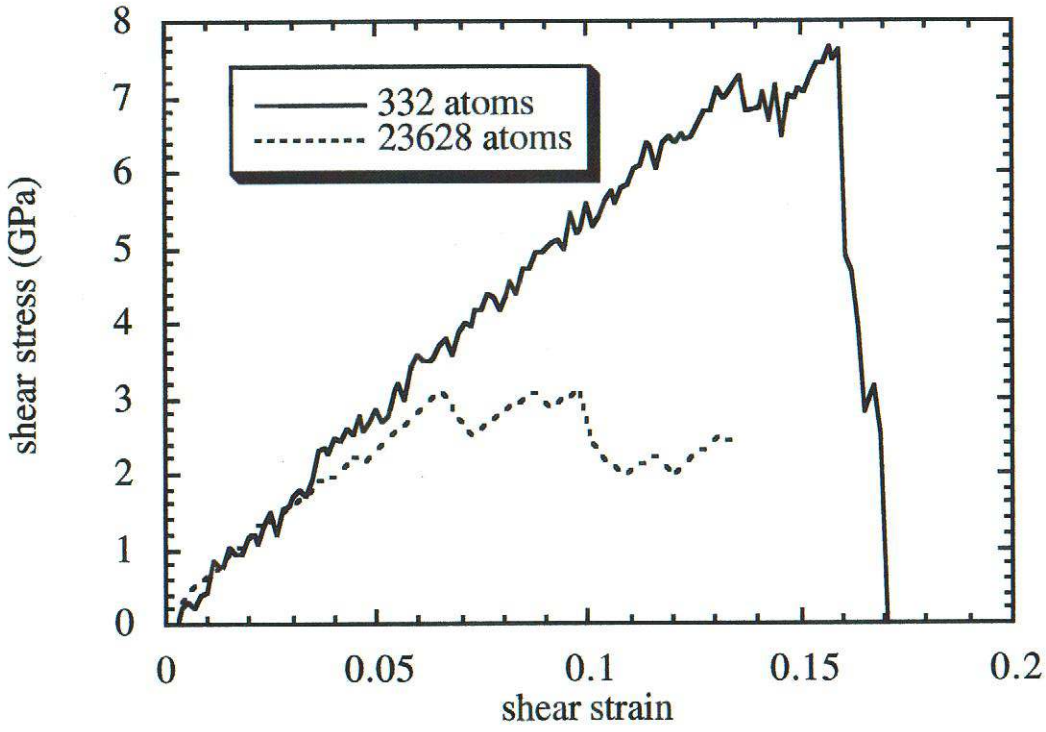

Fig. 2.61. Stress-strain responses of small block of atoms.

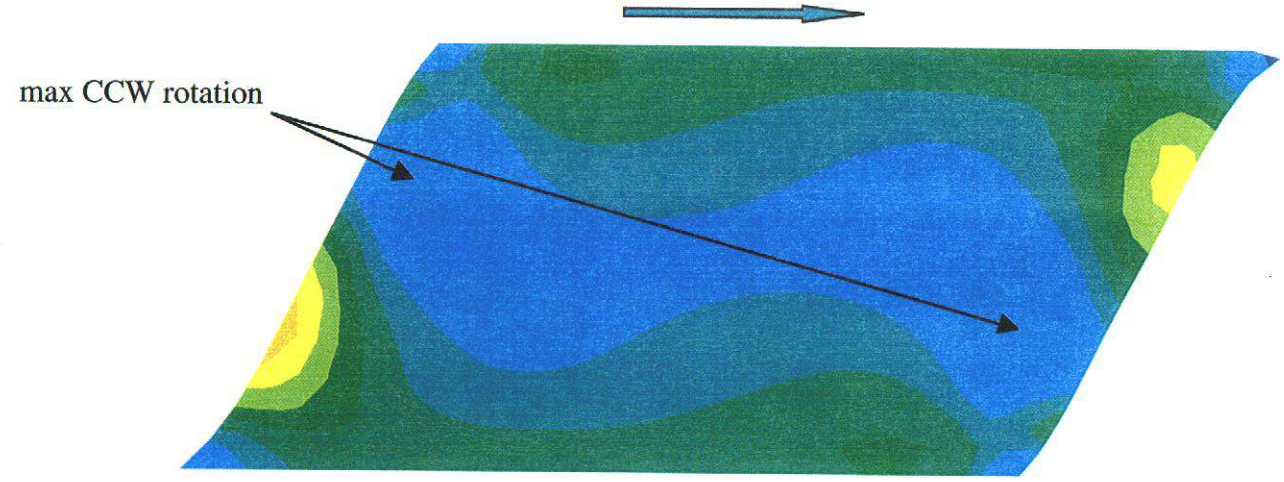

(a)

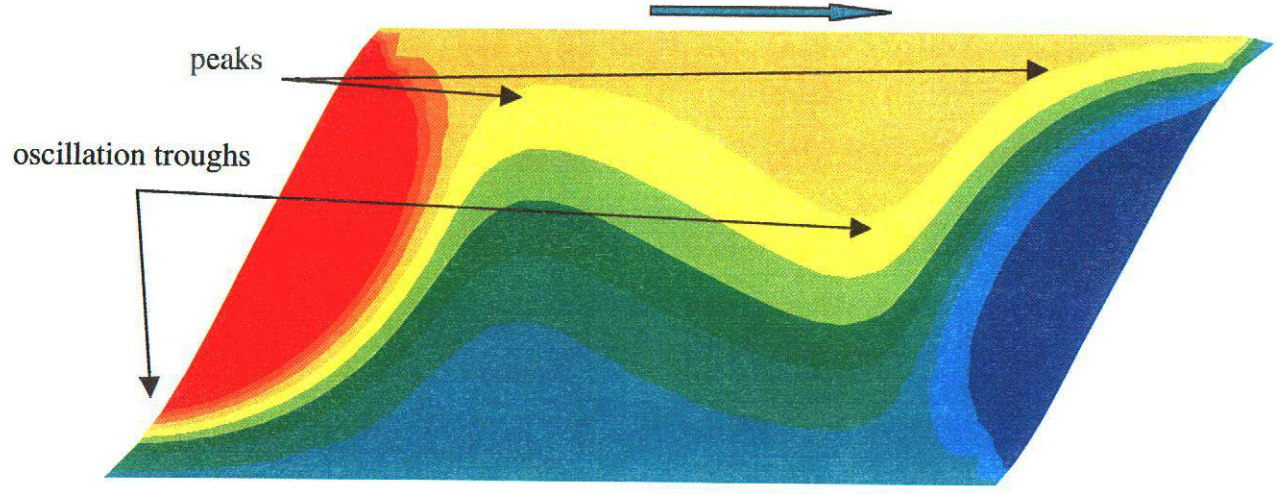

(b)

Fig. 2.62. Finite element simulation of torsion single crystal Cu showing (a) one Euler angle and (b) the correlating displacements to illustrate the oscillating pattern in simple shear.

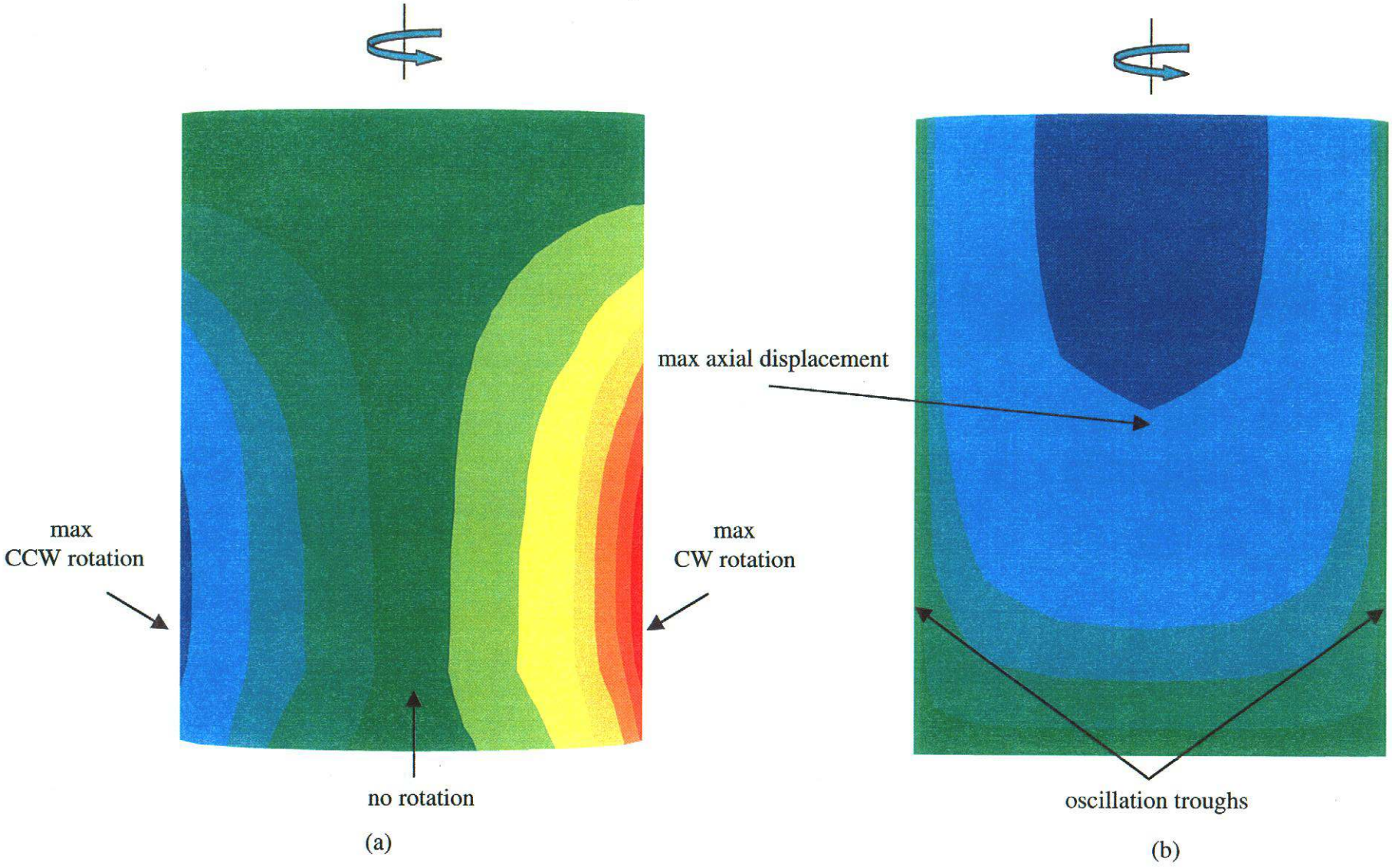

Fig. 2.63. Finite element simulation of torsion single crystal Cu showing (a) one Euler angle and (b) the correlating displacements to illustrate the oscillating pattern in torsion.

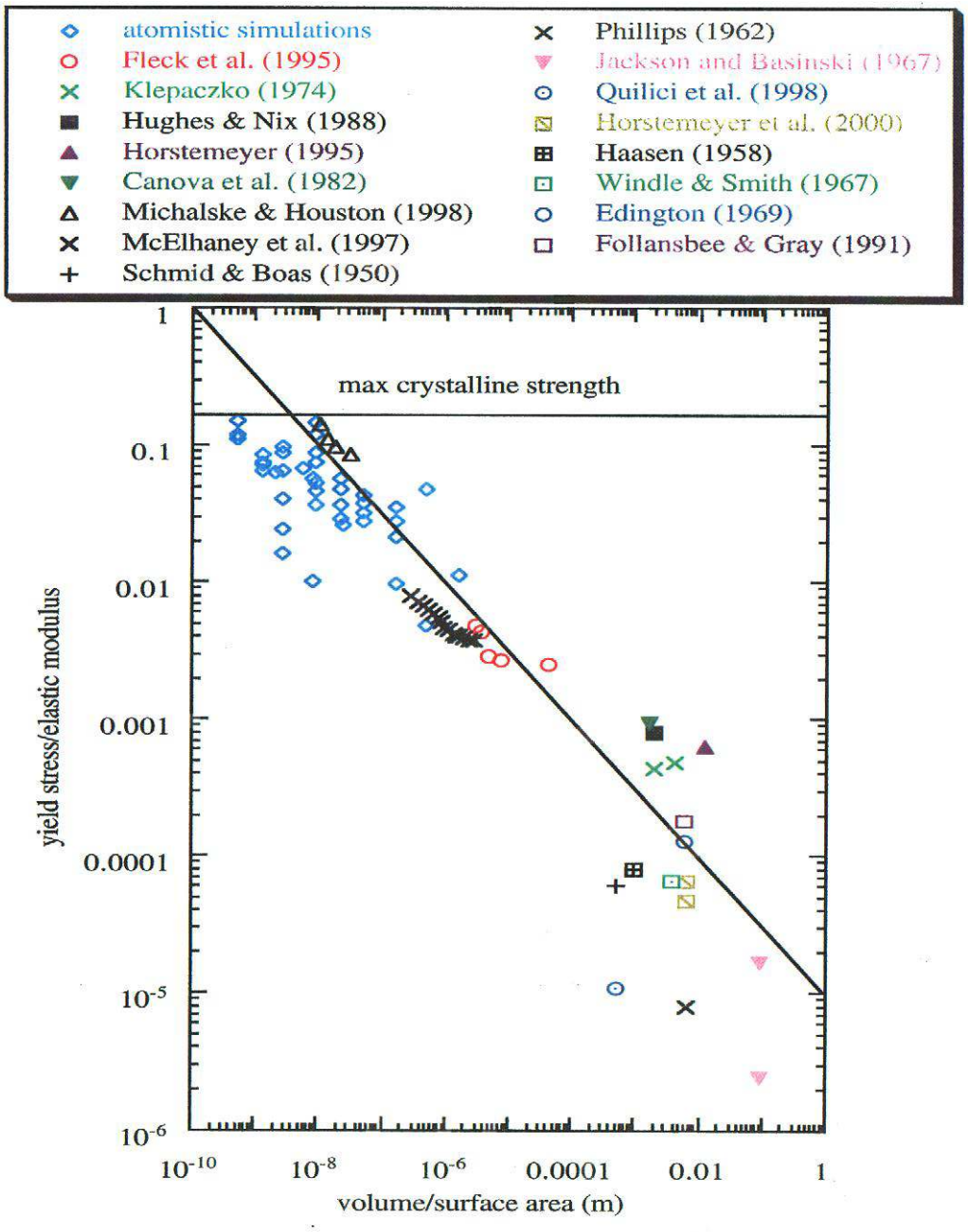

Fig. 2.64. Yield stress/elastic modulus versus volume/surface area (m) for nickel and copper for various experiments and numerous atomistic simulations.

CHAPTER 2 REFERENCES

Anand, L. and Kalidindi, S.R., "The Process of Shear Band Formation in Plane Strain Compression of FCC Metals: Effects of Crystallographic Texture," *Mech. Mater.*, Vol. 17, p. 223, (1993).

Angelo, J.E., Moody, N.R., and Baskes, M.I., "Trapping of Hydrogen to Lattice Defects in Nickel," *Modelling and Simul.. Mater. Sci. Eng.*, Vol. 3, pp. 289-307, (1995).

Armstrong, P.J. and Frederick, C.O.,*CEGB Report RD/B/N*, p. 731, (1996).

Asaro, R.J., *J. Appl. Mech.*, 50, p. 921, (1983).

Bammann, D.J. and Aifantis, E.C., "A Model for Finite Deformation Plasticity," *Acta Mechanica*, Vol. 69, p. 97, (1987).

Bammann, D.J. and Dawson, P.R., "Effects of Spatial Gradients in Hardening Evolution upon Strain Localization," *Physics and Mechanics of Finite Plastic and Viscoplastic Deformation*, eds. A.S. Khan, p. 9, (1997).

Bammann, D.J., *Appl. Mech. Rev.*, 1, p. 312, (1990).

Bammann, D.J., Chiesa, M.L., and Johnson, G.C., *The. App. Mech.*, eds. Tatsumi, Wannabe, and Kambe, Elsevier Science, p. 259, (1996).

Bammann, D.J., Chiesa, M.L., Horstemeyer, M.F., and Weingarten, L.I., "Failure in Ductile Materials Using Finite Element Methods," Structural Crashworthiness and Failure, eds. Norman Jones and Tomasz Weirzbicki, pp. 1-55, (1993).

Bammann, D.J., Chiesa, M.L., Horstemeyer, M.F., and Weingarten, L.I. *Structural Crashworthiness and Failure*, eds. N. Jones and T. Weirzbicki, Elsevier Applied Science, p. 1, (1993).

Baskes, M.I. and Daw, M.S., "The Effects of Impurities on Dislocation Dynamics and Fracture: An Atomistic Study," in Hydrogen Effects on Material Behavior, eds. N. R. Moody and A. W. Thompson,, (The Minerals, Metals & Materials Society, Warrendale, PA), pp. 717-32, (1990).

Baskes, M.I., Angelo, J.E., and Moody, N.R., Hydrogen Effects in Materials, eds A. W. Thompson, N. R. Moody, (The Minerals, Metals & Materials Society, Warrendale, PA) pp. 77-90, (1996).

Baskes, M.I., Sha, X., Angelo, J.E., and Moody, N.R., "Comment: Trapping of Hydrogen to Lattice Defects in Nickel," *Modell. Simul. Mater. Sci. Eng.*, Vol. 5, p. 651, (1996).

Begley, M.R. and Hutchinson, J.W., "The Mechanics of Size-Dependent Indentation," *J. Mech. Phys. Solids*, Vol. 46, No. 10, pp. 2049-2068, (1998).

Boukadia, J. and Sidoroff, F., *Arch. Mech.*, Vol. 40, No. 5-6, p. 497, (1988).

Bourcier, R.J., Sniegowski, J.J., and Porter, V.L., *A Novel Method to Characterize the Elastic/Plastic Deformation Response of Thin Films*, SAND96-1794, Sandia National Laboratories Report, (1996).

Box, G.E., Hunter, W.G., Hunter, J.S., *Statistics for Experimenters*, John Wiley and Sons, Inc., (1978).

Brenner, D.W., "Chemical Dynamics and Bond-Order Potentials," *MRS Bulletin*, p. 36, (1996).

Brenner, D.W., *Growth and Perfection of Crystals*, ed. R.R. Doremus *et al.*, Wiley, New York and London, p. 157, (1956).

Calnan, E.A. and Clews, C.J.B., *Phil Mag.*, Vol. 42, p.616, (1951).

Canova, G.R, Shrivastava, S., Jonas, J.J., and G'Sell, C., "The Use of Torsion Testing to Assess Material Formability," *Formability of Metallic Materials*, ASTM STP753, eds. J.R. Newby and B.A. Niemeier, pp. 189-210, (1982).

Cheung, K.S. and Yip, S., "Atomic Level Stress in Inhomogeneous System," *J. Appl. Phys.*, Communications, Vol. 70, No. 10, p. 5688, (1987).

Chin, G.Y. and Mammel,W.T., *Trans. TMS-AIME*, Vol. 239, p. 1400, (1967).

Coleman, B.D. and Gurtin, M.E., *J. Chem.Phys.*, 47, p. 597, (1967).

Cosserat, E. and Cosserat F., *Theorie des corps deformables*, Herman, Paris, Fr., (1909).

Cuitino, A.M. and Ortiz, M., *Modelling Simul. Mater. Sci. Eng.*, 1, p. 225, (1992).

Davis, R.S., Fleischer, R.L., Livingston, J.D. and Chalmers, B., "Effect of Orientation on the Plastic Deformation of Aluminum Single Crystals and Bicrystals," *J. Metals*, p. 136, (1957).

Daw, M.S, Foiles, S.M., and Baskes, M.I., "The Embedded-Atom Method: A Review of Theory and Applications," *Materials Science Reports*, A Review Journal, Vol. 9, No. 7-8, p. 251, (1993).

Daw, M.S. and Baskes, M.I., *Phys. Rev.*, Vol. B29, p. 6443, (1984).

Daw, M.S., Foiles, S.M., and Baskes, M.I., "The Embedded Atom Method: A Review of Theory and Applications," *Materials Science Reports, A Review Journal*, Vol. 9, No. 7-8, pp. 251-310, (1993).

Daw, M.S., Foiles, S.M., and Baskes, M.I., *Materials Science Reports, A Review Journal*, Vol. 9, No. 7-8, p. 251, (1993).

Diehl, J., "Zugverformung von Kupfer-Einkristallen," *Z. Metallk.*, Vol. 47, p. 331, (1956).

Driver, J.H., Juul Jensen, D., and Hansen, N., *Acta Mater.*, Vol. 42, p. 3105, (1994).

Edington, J.W., "The Influence of Strain Rate on the Mechanical Properties and Dislocation Substructure in Deformed Copper Single Crystals," *Phil. Mag*, Vol. 19, No. 162, p. 41, (1969).

Fleck, N.A. and Hutchinson, J.W., "A Phenomenological Theory for Strain Gradient Effects in Plasticity," *J. Mech. Phys. Solids*, Vol. 41, pp. 1825-1857, (1993).

Fleck, N.A. and Hutchinson, J.W., "Strain Gradient Plasticity," *Advances in Applied Mechanics*, eds. J.W. Hutchinson and T.Y. Wu, Academic Press, New York, Vol. 33., (1997).

Fleck, N.A., Muller, G.M., Ashby, M.F., and Hutchinson, J.W., "Strain Gradient Plasticity: Theory and Experiment," *Acta Metall. Mater.* Vol. 42, p. 475, (1993).

Foiles, S.M., *Phys. Rev.* B32, p. 7685, (1985).

Follansbee, P.S. and Gray, G.T., "The Response of Single Crystal and Polycrystal Nickel to Quasistatic and Shock Deformation," *Int. J. Plast.*, Vol. 7, pp. 651-660, (1991).

Follansbee, P.S., "High Strain Rate Deformation of FCC Metals and Alloys," *Metallurgical Applications of Shock Wave and High Strain Rate Phenomena*, eds. L.E. Murr, K.P. Staudhammer, and M.A. Meyers, Marcel Dekker, Inc.a, pp. 451-479, (1985).

Follansbee, P.S., "The Rate Dependence of Structure Evolution in Copper and Its Influence on the Stress-Strain Behavior at Very High Strain Rates," *Impact Loading And Dynamic Behavior of Materials*, eds. C.Y. Chiem, H.D. Kunze, L.W. Meyer, Informationsgesellschaft-Verlag, p. 315, (1988).

Follansbee, P.S., *Metallurgical Applications of Shock Wave and High Strain Rate Phenomena*, eds. L.E. Murr, K.P. Staudhammer, and M.A. Meyers, Marcel Dekker, Inc., p. 451, (1985).
Freidel, J., *Phil. Mag.*, Vol. 43, p. 153, (1950).

Godfrey, A., Juul Jensen, D., and Hansen, N., "Slip Pattern, Microstructure and Local Crystallography in an Aluminum Single Crystal of Brass Orientation {110}<112>," *Acta Mater.*, Vol. 46, No. 3, p. 823, (1997).

Gray, G.T., Chen, S.R., Wright, W., and Lopez, M.F., *Constitutive Equations for Annealed Metals Under Compression at High Strain Rates and High Temperatures*, Los Alamos National Laboratory, LA-12669-MS, (1994).

Haasen, P., "Plastic Deformation of Nickel Single Crystals at Low Temperatures," *Phil. Mag.*, Vol. 3, p. 384, (1958).

Hall, E.O., *Proc. Roy. Lond. Soc.* B, Vol. 64, Part 9, 381B, p. 747, (1951).

Hardy, R.J., "Formulas for Determining Local Properties in Molecular-Dynamics Simulations: Shock Waves," *J. Chem. Phys.*, Vol. 76, p. 622, (1982).

Harren, S., Lowe, T.C., Asaro, R.J., and Needleman, A., "Analysis of Large Strain Shear in Rate Dependent Face Centered Cubic Polycrystals,": Correlation of Micro- and Macro-mechanics," *Phil. Trans. R. Soc. London*, Vol. A238. p. 443, (1989).

Hibbitt, Karlsson, and Sorensen, Inc., ABAQUS 5.8, (1998).

Hoagland, R.G. and Baskes, M.I., "An atomistic study of the effects of stress and hydrogen on a dislocation lock in nickel," *Scripta Mater.*, Vol. 39 (#4-5), pp. 417-422, (1998).

Holian, B.L. and Lomdahl, P.S., "Plasticity Induced by Shock Waves in Nonequilibrium Molecular-Dynamics Simulations," *Science*, Vol. 280, N5372, pp. 2085-2088, (1998).

Holian, B.L., "Large Scale Molecular Dynamics Simulations of Plastic Deformation," *Radiation Effects and Defects in Solids*, Vol. 129, p. 41, (1994).

Honeycombe, R.W.K., *The Plastic Deformation of Metals*, Edward Arnold, p. 20, (1984).

Hoover, W.G., *Phys. Rev.*, Vol. A31, p. 1695-1697, (1985).

Horstemeyer, M.F. and Baskes, M.I., "Atomistic Finite Deformation Simulations: A Discussion on Length Scale Effects in Relation to Mechanical Stresses," *J. Engin. Mater. Tech.*, Vol. 121, pp. 114-119, (1999).

Horstemeyer, M.F. and Baskes, M.I., *J. Engn. Mater. Tech.*, Vol. 121, p. 114, (1999).

Horstemeyer, M.F. and McDowell, D.L., "Modeling Effects of Dislocation Substructure in Polycrystal Elastoviscoplasticity," *Mech. Matls.*, Vol. 27, p. 145, (1998).

Horstemeyer, M.F. and Ramaswamy, S., "On Factors Affecting Void Growth in Ductile Metals: A Parametric Study," in press Int. J. Damage Mech., (2000).

Horstemeyer, M.F., Baskes, M.I., and Plimpton, S.J., "Yield and Plastic Flow as a Function of Size and Time Scales," to be submitted, (2000).

Horstemeyer, M.F., Lim, T.J., Lu, W.Y., Mosher, D.A., Baskes, M.I., and Prantil, V.C. "Torsion/Simple Shear of Single Crystal Copper", to be submitted, (2000).

Horstemeyer, M.F., McDowell, D.L., and McGinty, R.D., "Design of Experiments for Constitutive Model Selection: Application to Polycrystal Elastoviscoplasticity," *Modell. Simul. Materl. Sci. Eng.*, Vol. 7, p. 253, (1999).

Huang, X. and Hansen, N., "Grain Orientation Dependence of Microstructure in Aluminum Deformed In Tension," *Scripta Mater.*, Vol. 37, No. 1, p. 1, (1977).

Huang, X., Liu, Q., and Hansen, N., "Grain Subdivision on Different Length Scales During Plastic Deformation," *Proc. 19th Int. Symposium on Matls. Science, Modelling of Structure and Mechanics of Materials from Microscale to Product*, eds. J.V. Cartensen, T. Leffers, T. Lorentzen, O.B. Pedersen, B.F. Sorensen, and G. Winther, Riso National Laboratory, Roskilde, Denmark, (1998).

Hughes, D.A. and Nix, W.D., "The Absence of Stread-State Flow During Large Strain Plastic Deformation of Some FCC Metals at Low and Intermediate Temperatures," *Metall. Trans. A*, Vol 19a, pp. 3013-3024, (1988).

Hughes, D.A., "Grain Subdivision and Moderate to High Angle Boundaries," Proc. ReX96, *The Third Int. Conf. On Recrystallization and Related Phenomena*, ed. T.R. McNelley, p. 171, (1994).

Hutchinson, J.W.,*Proc. R. Soc. Lond.*, Vol. A 348, p. 101, (1976).

Irving, J.H. and Kirkwood, J.G., "The Statistical Mechanical Theory of Transport Processes. IV. The Equations of Hydrodynamics," *J. Chem. Phys.* Vol. 18, p. 817, (1950).

Jackson, P.J. and Baskinski, *Canadian J. Physics*, Vol. 45, p. 707, (1967).

Johnson, G.C. and Bammann, D.J., "A Discussion of Stress Rates in Finite Deformation Problems," *Int. J. Solids and Structures*, Vol. 20, No. 8, p. 725, (1984).

Johnson, G.R. and Holmquist, T.J., "Test Data and Computational Strength and Fracture Model Constants for 23 Materials Subjected to Large Strains, High Strain Rates, and High Temperatures," Los Alamos National Laboratory Report, LA-11463-MS, (1988).

Kelchner, C., Plimpton, S., and Hamilton, "Dislocation nucleation and defect structure during surface indentation," *J. Phys. Rev.*, B. Vol. 58, pp. 11085, (1998).

Kitamura, T., Yashiro, K., and Ohtani, R. "Atomic Simulation on Deformation and Fracture of Nano-Single Crystal of Nickel in Tension," *JSME Int. Journal*, Series A, Vol. 40, No.4, pp. 430-435, (1997).

Kochendorfer, A., "Neue Ergebnisse uber die Verfestigung bei der plastischen Verformung von Kristallen," *Z. Metall.*, Vol. 41, p. 265, (1950).

Kocks, U.F., Tome, C., and Wenk, H.R., *Texture Anisotropy: Preferred Orientation in Polycrystals and Their Effects on Material Properties*, Cambridge University Press, (1998).

Lange, H. and Lucke, K., "Störungen der Gleitung bei Aluminiumeinkristallen," *Z. Metall.*, Vol. 44, p. 183, (1953).

Leibfried, G. *Z. Phys.*, Vol. 127, p. 344, (1950).

Lipkin, J. and Lowe, T.C., "Axial Effects During Reverse Torsional Deformation," *Advances in Plasticity*, eds. A.S. Khan and M. Tokuda, Pergamon Press, Oxford, p. 625, (1987).

Liu, Q. and Hansen, N., "Macroscopic and Microscopic Subdivision of a Cold Rolled Aluminum Single Crystal of Cubic Orientation," *Proc. R. Soc. London*, Vol. 454, p. 2555, (1998).

Ludwig, P. and Sheu, R., *Stahl U. Eisen*, Vol. 45, p. 373, (1925).

Ma. Q. and Clarke, D.R. "Size dependent hardness of silver single crystals," *J. Mater. Res.*, Vol. 10, pp. 853-863, (1995).

Masumura, R.A., Hazzledine, P.M., and Pande, C.S., "Yield Stress of Fine Grained Materials," *Acta Metall.*, Vol. 46, No.13, pp.4527-4534, (1998).

Matsuda, A., "The Plastic Deformation of Iron Single Crystals with Shear Tests in {110}<111> and {112}<111> Slip Systems," *Trans. JIM*, Vol. 18, p. 213, (1977).

McElhaney, K.W., Vlassak, J.J., and Nix, W.D., "Determination of Indentor Tip Geometry and Indentation Contact Area of Depth-Sensing Indentation Experiments," *J. Mater. Research*,Vol. 13, No. 5, pp. 130-1306, (1998).

Michalske, T.A. and Houston, J.E., "Dislocation Nucleation at Nano-Scale Mechanical Contacts," *Acta. Mater.*, Vol. 46, No. 2, pp. 391-396, (1998).

Montheillet, F., Cohen, M., and Jonas, J.J., *Acta Metall.*, Vol. 32, p. 2077, (1984).

Nabarro, F.R.N., Basinski, Z.S. and Holt, D.B., "The Plasticity of Pure Single Crystals," *Advances in Physics*, Vol. 13, p.193, (1964).

Nagtegaal, J.C. and DeJong, J.E., "Some Aspects of Nonisotropic Work Hardening in Finite Strain Plasticity," *Plasticity Metals at Finite Deformation*, eds. E.H. Lee and R.L. Mallett, p. 65, (1980).

Neale, K.W., Toth, L.S, and Jonas, J.J., "Large Strain shear and torsion of rate sensitive fcc polycrystals," *Int. J. Plasticity*, Vol. 6, p. 45, (1990).

Nix, W.D. and Gao, H. "Indentation Size Effects in Crystalline Materials: A Law for Strain Gradient Plasticity," *J. Mech. Phys. Solids*, Vol. 46, No.3, pp. 411-425, (1998).

Nose, S., *Mol. Phys.*, Vol. 50, pp.255-268, (1984).

Peirce, D, Asaro R.J., and Needleman ., *Acta Metall.*, Vol. 30, p. 1087, (1982).

Petch, N.J., *J. Iron Steel Inst.*, Vol. 174, (1), p.25, (1953).

Phillips, W.L., "Aluminum and Copper Tested in Direct Shear," *Trans. Metall. Soc. of AIME*, Vol. 224, p. 845, (1962).

Plimpton, S.J., "Fast Parallel Algorithms for Short-Range Molecular Dynamics", *J Comp Phys,* Vol.117, pp.1-19, (1995)

Prantil, V.C., Jenkins, J.T., and Dawson, P.R., "An Analysis of Texture and Plastic Spin for Planar Polycrystals," *J. Mech. Phys. Solids*, Vol. 41, No. 8, p. 1357, (1993).

Quilici, S., Forest, S., and Cailletaud, G., *J. Phys. IV France*, Vol. 8, p. 325, (1998).

Rauch, E.F., Hashimoto, S. and Baudelet, B., "Simple Shear Deformation of Iron-Silicon Single Crystals," *Scripta Metal.*, Vol. 24, pp. 1082-1085, (1989).

Reid, C.N., "Deformation Geometry for Materials Scientists," *Int. Series on Matls. Sci. and Tech.*, Vol. 11, p. 172, (1973).

Rice, J.R., *J. Mech. Phys. Solids,* Vol. 9, p.433, (1971).

Rowlinson, J.S., "Thermodynamics of Inhomogeneous Systems," *Pure and Applied Chem.*, Vol. 65, p. 873, (1993).

Schmid, E. and Boas, W., *Plasticity of Crystals*, Hughes, London, (1950).

Schmid, E. and Boas,W., *Kristallplastizität*, Springer Verlag, Berlin, (1935).

Schmid, E., *Z. Elektrochem.*, Vol. 37, p. 447, (1931).

Staubwasser, W., "Über die Verfestigung von Aluminium Einkristallen (99.99% Al) und Ihre Deutung," *Acta Metall.*, Vol. 7, p. 43, (1956).

Stoneham, M., Harding, J., and Harker, T., "The Shell Model and Interatomic Potentials for Ceramics," *MRS Bulletin*, Feb. 1996, p. 29, (1996).

Stott, M.J. and Zaremba, E., *Phys. Rev.*, B22, p. 1564, (1980).

Tabor, D., *The Hardness of Metals*, Clarendon Press, Oxford, (1994).

Taylor, G. I., "Plastic Strain in Metals," *J. Insit. Metals*, Vol. 62, p.307 (1938).

Windle, A.H. and Smith, G.C. "The Effect of Hydrogen on the Plastic Deformation of Nickel Single Crystals," *Metal Science Journal*, Vol. 2, No. 50, pp. 187-191, (1968).

Yoshida, K., Goto, Y., and Yamamoto, M., *J. Phys. Soc.* Japan, Vol.21, p. 825, (1966).

Zhou, S.J., Carlsson, A.E., and Thomson, R., "Dislocation Core-Core Interaction and Peierls Stress in a Model Hexagonal Lattice," *Phys. Rev. B*, Vol. 49, No. 10, p. 6451, (1994).

Chapter 3

Atomistic Calculations of Diffusion Rates: Compact Surface Cluster Diffusion by Concerted Rotation and Translation

Island diffusion on surfaces has historically been explained by single atom mechanisms including edge-running and evaporation-condensation. More recently, cooperative mechanisms for island diffusion including glide[1], dislocations[2], and dimer-shear[3] have been proposed theoretically although experimental evidence for some of these mechanisms remains limited. Island glide, defined as the nearly simultaneous translation of all island atoms parallel to the surface, could be related to friction,[4,5] since both phenomena require a layer of one material to slide past another material. The detailed atomic mechanisms for island glide and friction represent a challenging problem for theoretical and experimental investigation.

Field ion microscopy studies[6,7] of 19-atom Ir clusters on the Ir(111) surface have documented several remarkable diffusion behaviors as follows: 1) The clusters exhibit an excess of long jumps (i.e. beyond nearest stable fcc configurations) relative to single jumps. 2) The prefactor for diffusion is almost four orders of magnitude larger than usual prefactors. 3) Edge-running and evaporation-condensation apparently can be ruled out as mechanisms for diffusion. These unusual experimental observations motivate a detailed theoretical examination of the possibility raised by Ehrlich and coauthors [6,7] that the clusters glide by simultaneous translation of the cluster atoms over bridge sites.

The experimental results show that an 18-atom cluster moves by periphery diffusion, but that a compact hexagonal 19-atom cluster moves by some other mechanism. The compact hexagonal clusters are of special interest because of the high diffusion prefactors and novel diffusion mechanisms. For this reason we will limit ourselves here to the motion of compact hexagonal clusters by collective mechanisms including but not limited to bridge glide. This chapter has two main sections. First we consider the energy of a pseudomorphic monolayer of Ir on Ir(111). This is relevant since a compact 19-atom Ir cluster is a pseudomorphic island. We find, in dramatic contrast to a single adatom, that a pseudomorphic monolayer has a low-lying local energy minimum at the on-top position. This raises the novel possibility that on-top sites could easily be involved in island glide. In the second section we examine island glide in detail and propose a new mechanism, "cartwheel-shuffle", for island glide. This mechanism involves concerted rotation and translation of the cluster as a whole. We have investigated four possible glide mechanisms for long jumps of the 19-atom cluster. Of these, cartwheel-shuffle has the lowest activation energy.

The first principles energies presented here were calculated within the generalized gradient approximation (GGA).[8] We used the plane wave (E_{cut} = 191eV) and ultrasoft pseudopotential[9] based code, VASP, developed by G. Kresse and J. Furthmuller.[10] All activation energies for diffusion have been calculated using the nudged elastic band method.[11]

As mentioned previously, a 19-atom compact Ir island on Ir(111) is basically a hexagonal portion of a pseudomorphic Ir monolayer on Ir(111). The island will differ from a pseudomorphic film mainly at its perimeter where the atoms will relax inward slightly. Because of the similarity between island glide and monolayer shear, it is relevant to calculate the energies required to shear a pseudomorphic monolayer of Ir across an Ir(111) surface. In table 3.1, we contrast these energies for a pseudomorphic film with the energies for an adatom in the fcc, hcp, bridge and on-top sites. All of the energies are expressed per atom in meV/atom and were calculated using first principles. For an adatom, the calculations of the relative fcc, hcp, and bridge energies are within about 10% of the experimental measurements.[12] This gives us considerable confidence in these first principles calculations. As expected, the energy is a maximum at the on-top site and an adatom will avoid that site. The calculations for the pseudomorphic monolayer present a very different story. The energy required to place the layer in the on-top site is only slightly larger than the hcp energy and is much less than the bridge energy. Surprisingly, the on-top site is metastable for the pseudomorphic monolayer. To our knowledge this is the first time that this behavior has been reported for a transition metal. As shown here, it is different from the well known behavior of a single adatom. It is also different from the well known slip behavior of bulk fcc metals represented in table 3.1 by a bulk calculation with 5 and 4 layers of iridium on the sides of a (111) slip plane, which reproduces the measured bulk stacking fault energy with fortuitously good agreement.

We have also performed semiempirical many-body calculations with two different iridium potentials.[13,14] These calculations fail to predict the important metastable on-top state and differ from first principles calculations by almost an order of magnitude for the energy of this state.[15] Thus, relying on semiempirical calculations (e.g. embedded atom method [EAM], effective medium theory [EMT], or Finnis-Sinclair potentials) to provide even a qualitative understanding of Ir island glide on Ir(111) seems unwise. We did resort to semiempirical calculations to perform exhaustive preliminary searches for metastable states of rotated and translated clusters and to estimate prefactors for diffusion since such calculations are presently well beyond the capability of first-principles methods.

In figure 3.1 we show the energy per atom of an iridium adatom and of a pseudomorphic iridium monolayer plotted as a function of position. These plots are based on the calculations given in table 3.1 and on calculations at intermediate positions. This figure

emphasizes the dramatic difference between moving a single atom across a surface and moving a pseudomorphic overlayer over a surface. For a single atom, diffusion will occur from an fcc site to an hcp site and then to an fcc site. The probability of a long jump over the top site is insignificant. For a monolayer of iridium atoms (as in a pseudomorphic island), one can imagine other paths, such as diffusion from an fcc site to the metastable on-top site and then to the opposite hcp site. Since the energy surface is relatively flat for the monolayer, it also seems conceivable that an island could rotate in addition to translating across the surface. Simultaneous translation and rotation can produce a cartwheel-like motion. Cartwheel-like motion has been reported for gold nanocrystal diffusion on graphite[16], but to find it possible in a homoepitaxial pseudomorphic island is unexpected.

In figure 3.2 we show four different collective diffusion mechanisms which we have studied using first principles calculations of activation energies. (We have also considered a mechanism in which the cluster first rotates, then translates several times, then rotates again. Since this mechanism also has a high activation energy, we will not discuss it here). The first two mechanisms, bridge-glide and top-glide, are almost pure translational mechanisms. The second two mechanisms, cartwheel-shuffle and cartwheel-glide, involve simultaneous translation and rotation. These mechanisms are shown for the 19-atom cluster. For the 7-atom cluster the mechanisms are similar except that cartwheel-shuffle and cartwheel-glide both involve a 30° rotation to reach a metastable state. For the 7-atom cluster cartwheel-shuffle and cartwheel-glide are equivalent by symmetry if jumps in and out of the metastable state are uncorrelated. The first principles activation energies for these glide diffusion mechanisms are given in table 3.2. In all cases the stable island configuration has all atoms near the fcc sites in agreement with experiment. The calculations suggest that bridge-glide is the favored diffusion mechanism with an activation energy of 1.54 eV in excellent agreement with the 1.49 eV measured experimentally. The experimental data shows no excess of "long jumps". Our calculations and the experimental data appear consistent with bridge-glide as a cluster diffusion mechanism for the 7-atom cluster.

For the 19-atom cluster, the calculations show that top-glide and cartwheel-glide can be ruled out as diffusion mechanisms, since their activation energies of 5.2 and 5.1 eV, respectively, are much higher than for bridge-glide and cartwheel-shuffle. The experimental activation energy for diffusion of the 19-atom cluster is 2.54 eV. This is significantly lower than the 3.2 eV and 3.6 eV activation barriers calculated for bridge-glide and cartwheel-shuffle respectively. The discrepancy between experiment and theory may be due to computational inaccuracies which we were forced to accept in order to perform first principles calculations for such a large number of atoms. The intensive computational requirements limited the first

principles nudged elastic band calculation to a small unit cell and sparse k-point sampling. The errors associated with these compromises are difficult to quantify without exceeding all available computational resources. Since the calculations are not fully converged, we cannot make a definitive conclusion regarding whether bridge-glide or cartwheel-shuffle has the lower activation energy. It is also conceivable some other diffusion mechanism may exist which has a lower activation energy than bridge-glide or cartwheel-shuffle.

What theoretical conclusions can we draw with confidence regarding glide mechanisms of a 19-atom cluster? First, we are sure that the cartwheel-shuffle and bridge-glide have a much lower activation energy than the on-top glide or cartwheel-glide. The low activation energy of the cartwheel-shuffle can be understood by noticing that several of the atoms in the cluster remain near the fcc sites during the transition from the fcc to the metastable configuration. The other atoms in the cluster move over on-top sites in an asynchronous fashion as the cluster moves in a cartwheel fashion from fcc to the metastable state. This means that only a portion of the atoms in the cluster will be in energetically unfavorable positions at any time during the cartwheel-shuffle. We suspect that cartwheel shuffle has the lowest activation energy of all mechanisms involving glide of the center of mass of the cluster over the top site. Returning to the experiments on diffusion of 19-atom Ir clusters on Ir(111), we consider possible explanations for the long jumps. We are not able to understand how bridge-glide could produce an excess of long jumps, since it moves a cluster from an fcc site to an adjacent hcp site (and then to an adjacent fcc site). For this reason we believe that cartwheel shuffle (probably in combination with bridge-glide) should be given serious consideration as a possible explanation for the remarkable experimental observations.

Finally we consider the high prefactors measured experimentally for diffusion of compact clusters. Prefactors for diffusion can be calculated from the harmonic approximation to transition state theory using the result derived by Vineyard,[17]

$$\nu = \prod_{n=1,m} \nu_{fcc} \Big/ \prod_{n=1,m-1} \nu_{ts}$$

where ν_{fcc} are the phonon frequencies at the fcc configuration and ν_{ts} are the phonon frequencies at the transition state. Unfortunately, calculation of the phonon frequencies is well beyond the capability of first principles calculations for systems of this size. Figure 3.3 shows the energy as a function of position during the cartwheel-shuffle diffusion process. In this plot the energy rises abruptly from the global minimum at the fcc cluster configuration. However the energy varies very slowly in the vicinity of the maxima (the transition states) on this curve. This is consistent with the type of flat energy surface shown in figure 3.1b and suggests that some of the phonon modes (other than the reaction coordinate) at the transition state may have lower frequencies than the phonon modes at the fcc state, thereby producing a high prefactor.

In order to estimate the prefactors for diffusion of Ir clusters on Ir(111) we used two semiempirical potentials. The calculated prefactors for various mechanisms and two different potentials are given in table 3.3. We also compare these results to the experimental values for diffusion of single atoms, 7-atom and 19-atom clusters. One can only hope for a qualitative prediction here, both because of the inaccuracies involved in the semiempirical approach and possible errors associated with the harmonic approximation. Nonetheless, we find that the prefactors for cartwheel-shuffle and bridge-glide are much larger than for single atom diffusion. We also performed this prefactor calculation for Au, Ag, Cu, Ni, Pd, and Pt using 18 different commonly used EAM and EMT potentials. For a 19-atom cluster, the prefactors for bridge glide ranged from 1×10^{12} to 2×10^{15} whereas the prefactors for cartwheel-shuffle ranged from 1×10^{14} to 1×10^{18}. This shows that the high theoretical prefactors for these cooperative mechanisms are not just an artifact of the particular iridium potentials used.

To summarize, we find that a monolayer of Ir on Ir(111) is metastable in the on-top configuration. This low on-top energy suggests that some cluster atoms may pass close to on-top sites during diffusion by a glide mechanism. In particular, a cartwheel-shuffle mechanism is proposed which may be competitive with other diffusion mechanisms. This mechanism, probably in combination with bridge-glide, appears capable of explaining the long jumps and high prefactors observed in diffusion experiments. In view of the complexity of this problem, additional theoretical and experimental investigation (perhaps examining the intermediate-sized, compact 12 atom cluster and/or other FIM metals) will doubtless be required to determine a definitive diffusion mechanism.

We gratefully acknowledge help plotting figure 3.1 by Vidvuds Ozolins.

TABLE 3.1

Calculated relative energies (meV/atom) for a single adatom, for a pseudomorphic monolayer, and for four pseudomorphic layers in high symmetry sites. Experimental values (adatom from reference 12, bulk from reference 18) are given in parenthesis. All energies are referenced to the energy of the stable configuration. Note the remarkably low energy for the metastable on-top monolayer.

	Fcc	Hcp	Bridge	On-Top
Adatom	18 meV (22)	0 meV (0)	251 meV (269)	1565 meV
Mono-layer	0 meV	81 meV	243 meV	113 meV
Bulk	0 meV (0)	120 meV (120)	234 meV	403 meV

TABLE 3.2: Calculated activation energies for glide by mechanisms shown in figure 3.2. For 7-atom cluster calculations should be reasonably accurate. For 19-atom cluster, computational requirements limited calculation to a 19-atom cluster on a 3 layer slab with 2 fixed layers, limited lateral dimensions for the periodic cell, and limited k-point sampling. Thus 19-atom cluster calculations are only approximations.

Cluster Size	Bridge - Glide	Top-Glide	Cartwhe el-Shuffle	Cartwheel Glide
7-atoms	1.54 eV	3.02 eV	1.92 eV	1.92 eV
19-atoms	3.2 eV	5.2 eV	3.6 eV	5.1 eV

TABLE 3.3: Prefactors calculated using semiempirical potentials from references 13 and 14. All prefactors are in Hz. Values from experiments are also given.

	1 atom	7-atoms	19-atoms
hopping[13]	2×10^{12}		
hopping[14]	3×10^{12}		
bridge-glide[13]		7×10^{13}	2×10^{16}
bridge-glide[14]		1×10^{14}	7×10^{16}
cartwheel-shuffle[13]		7×10^{14}	8×10^{16}
cartwheel-shuffle[14]		5×10^{14}	1×10^{17}
experiment[7]	7×10^{11}	3×10^{15}	2×10^{16}

FIG. 3.1: Relative energy per atom as a function of position for a single Ir atom on Ir(111) (left plot) and for a pseudomorphic Ir monolayer on Ir(111) (right plot). This figure illustrates the dramatic difference between diffusing a single Ir atom on Ir(111) and shearing an Ir monolayer across Ir(111). For example, the top site is unstable for an adatom and metastable for the monolayer. Contour intervals are 100 meV/atom in both plots. The gray scale is choosen to emphasize the portions of the energy surface most likely to be visited during diffusion. Plots are Fourier fits to computed data.

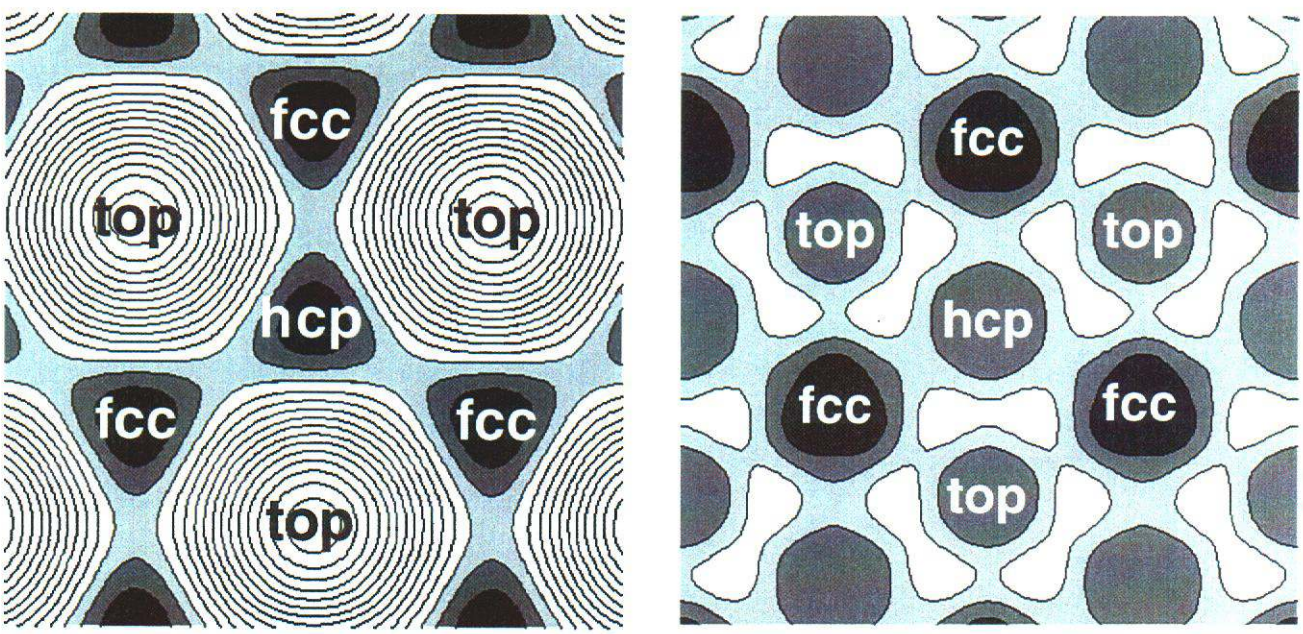

FIG 3.2: Cluster glide mechanisms discussed in this paper. Bridge-glide and top-glide involve nearly simultaneous translation of all cluster atoms over the bridge and on-top sites respectively. Top-glide was considered as one possible mechanism for long jumps. Cartwheel-glide involves a simultaneous translation of the center atom over the on-top site while the cluster rotates by 60°. Cartwheel-shuffle involves translation of the center atom to the on-top site while the cluster rotates by ~15° to form a metastable state. The cluster then translates to another hollow site while rotating back by ~15°.

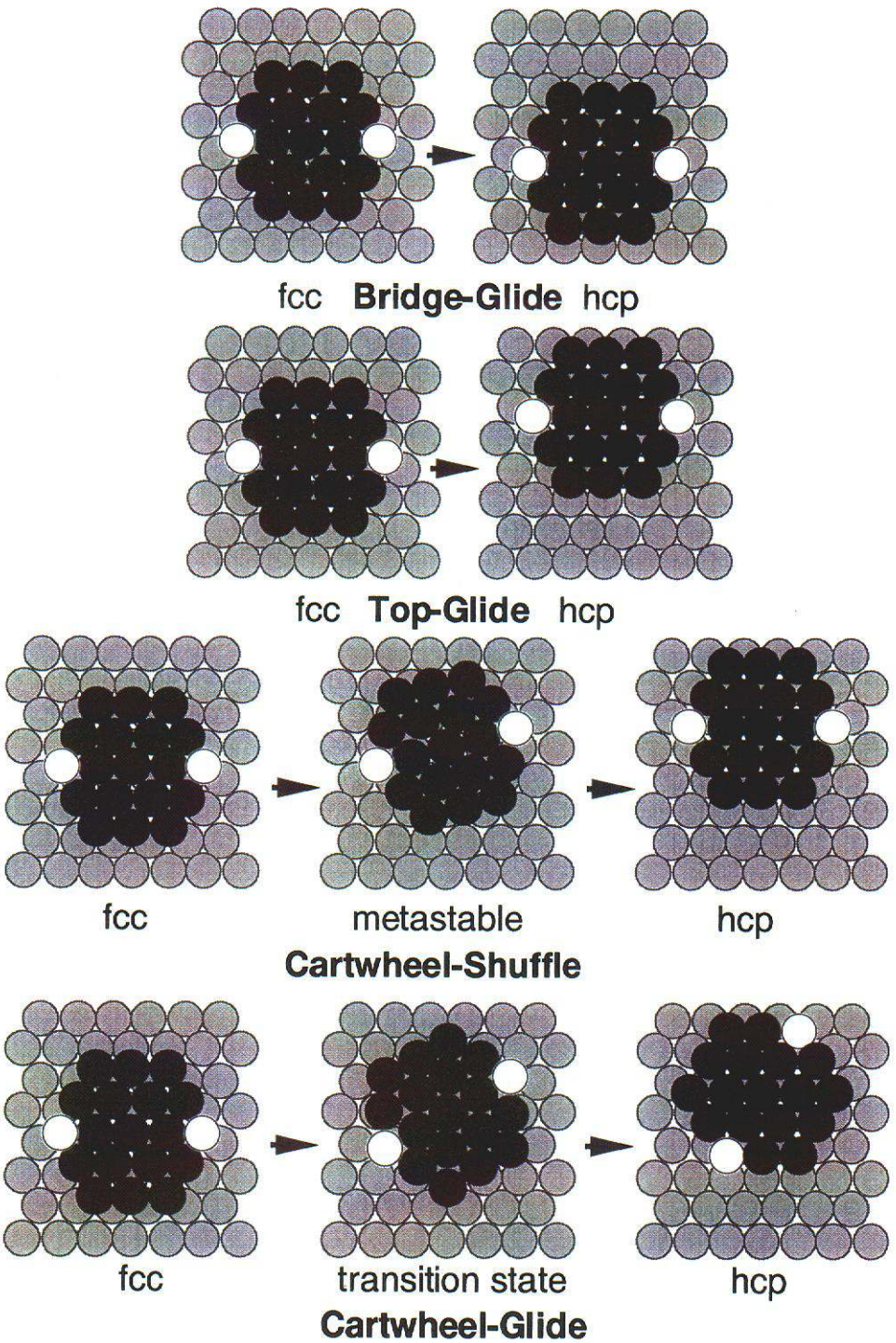

FIG 3.3: Calculated energy as a function of translation and rotation during cartwheel-shuffle shown in figure 3.2. Note that the curve is very flat near the maxima (transition states), and steep near the fcc and hcp minima.

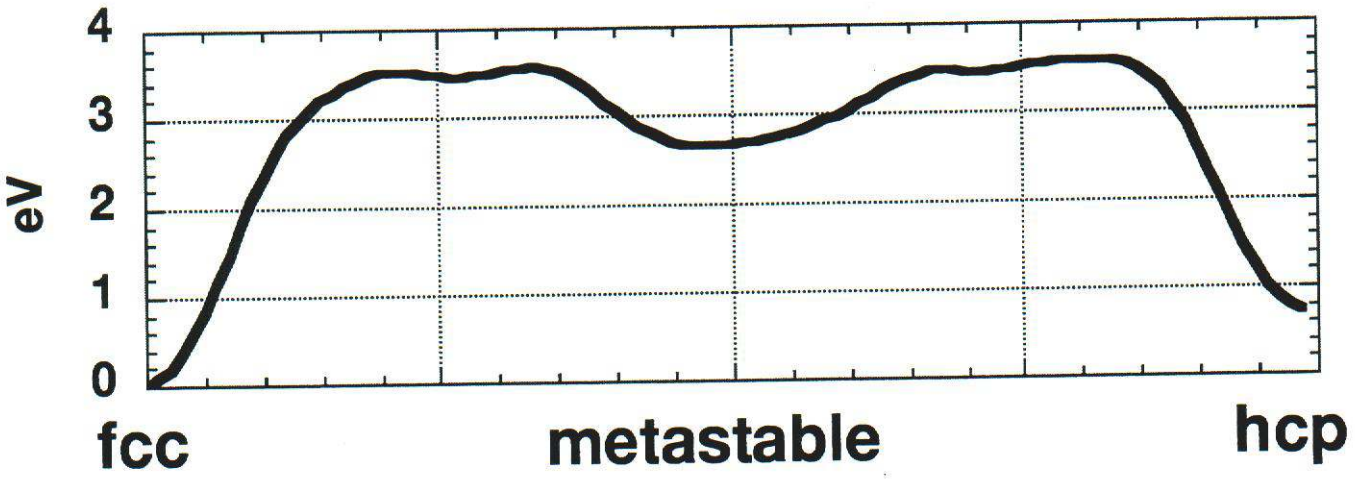

[1] C.L. Liu and J.B. Adams, Surf. Sci **268**, 73 (1992)

[2] J. C. Hamilton, Phys. Rev. Lett. **77**, 885 (1996)

[3] Z.P. Shi, Z. Zhang, A. K. Swan, and J. F. Wendelken, Phys. Rev. Lett. **76**, 4927 (1996).

[4] M. Enachescu, R.J.A.van den Oetelaar, R.W. Carpick, D.F.Ogletree, C.F.J. Flipse and M. Salmeron, Phys. Rev. Lett. **81**, 1877 (1998)

[5] J. S. Ko, A. J. Gellman, T. A. Lograsso, and P. A. Thiel, Surf. Sci. **423**, 243 (1999)

[6] S. C. Wang and Gert Ehrlich, Phys. Rev. Lett. **79**, 4234 (1997).

[7] S. C. Wang, Ulrike Kürpick, and Gert Ehrlich, Phys. Rev. Lett. **81**, 4923 (1998).

[8] J. P. Perdew, K. Burke, and M. Ernzerhof, Phys. Rev. Lett **77**, 3865 (1996)

[9] D. Vanderbilt, Phys. Rev. B **41** 7892 (1990); the GGA pseudopotentials used in this work were developed by G. Kresse.

[10] G. Kresse and J. Hafner, Phys. Rev. B **47**, 558 (1993); ibid. **49**, 14 251 (1994). G. Kresse and J. Furthmuller, Comput. Mat. Sci. **6**, 15 (1996); G. Kresse and J. Furthmuller,Phys. Rev. B **54**, 11169 (1996).

[11] H. Jónsson, G. Mills, and K. W. Jacobsen, "Nudged Elastic Band Method for Finding Minimum Energy Paths of Transitions", in *Classical and Quantum Dynamics in Condensed Phase Simulations*, ed. B. J. Berne, G. Ciccotti, and D. F. Coker (World Scientific, 1998).

[12] S. C. Wang and Gert Ehrlich, Phys. Rev. Lett. **68**, 1160 (1992).

[13] A. P. Sutton and J. Chen, Phil. Mag. Lett. **61**, No. 3, 139 (1990).

[14] S. P. Chen, Phil. Mag. A **66**, No. 1, 1 (1992).

[15] For both an adatom and a monolayer the Finnis-Sinclair potential of reference 13 gives ~0meV for the fcc and hcp sites. For the monolayer, the bridge energy is 150 meV and the on-top energy is 680 meV. For the adatom, the bridge energy is 210 meV and the on-top energy is 1070 meV respectively. Using the EAM potential of reference 14 gives the same fcc and hcp energies. For the monolayer, the bridge energy is 210 meV and the on-top energy is 780 meV. For the adatom, the bridge energy is 350 meV and the on-top energy is 1690 meV respectively.

[16] W. D. Luedtke and Uzi Landman, Phys. Rev. Lett. **82**, 3835 (1999).

[17] G. H. Vineyard, J. Phys. Chem. Solids **3**, 121 (1957).

[18] J. P. Hirth and J. Lothe, "Theory of Dislocations" Krieger Publishing Co., Malabar, Florida (1992).

Chapter 4

Multiscale Modeling of Grain Boundary Roughening: A First Order Phase Transition by Atomic Shuffle

A multiscale theory of a grain boundary de-faceting phase transition in aluminum has been developed. At an atomic scale, molecular dynamics (MD) calculations revealed that the grain boundary can move only by a concerted shuffle of several atoms. This elementary excitation allowed rapid motion and equilibration of the grain boundary. The atomic understanding of the grain boundary motion then was mapped onto a simple lattice model which exhibited a first order phase transition. The results provide the first detailed understanding of an experimentally observed grain boundary de-faceting transition including the cooperative atomic mechanism and a statistical mechanical description.

Grain boundaries are the interfaces separating differently oriented crystallites in polycrystalline minerals, ceramics, and metals. Many important materials properties including fracture strength, impurity diffusion, and corrosion resistance are dramatically affected by grain boundary structure. Because grain boundary structure can be governed by thermodynamics (1, 2), equilibrium grain boundary phase transitions should have major effects on materials properties. However, there are very few reliable experiments on equilibrium grain-boundary transitions and existing experimental techniques cannot resolve their atomic mechanisms. The classic experimental observation of a reversible grain-boundary phase transition was made by Hsieh and Balluffi (3, 4). In their experiment, a grain boundary in aluminum, originally faceted at room temperature, became smooth upon heating the sample to ~400K, and faceted again upon cooling. Attempts to understand such transitions have been limited to a phenomenological mean-field theory (5). Here we discuss the relevant atomic processes of the grain-boundary de-faceting transition and provide a thermodynamic and statistical mechanical description.

We first examined this de-faceting transition by embedded atom method (6) (EAM) MD simulations with Voter-Chen aluminum potentials (7). Initially we used an aluminum bicrystal slab having dimensions 100Å by 42Å by 80Å with a grain boundary perpendicular to the $[01\bar{1}]$ direction. This is identical with the average boundary orientation studied experimentally by Hsieh and Balluffi (3). The temperature was ramped from 0K to 500K and back to 0K at a rate of 1K/ps. At around 50K the grain boundary rapidly formed small {112} facets. Fig. 4.1A shows the cross section of two of these low energy grain boundary facets and their junction.

The boundary structure agrees with the calculated _3 grain boundary structure reported in previous first principles calculations (8), including the 0.7Å offset between the (111) planes of the upper and lower grain (8, 9). As we increased the temperature, some disorder began to appear in the vicinity of the facet junctions. At about 400K, the morphology of the grain boundary changed dramatically from the faceted to a smooth, but atomically disordered structure. During cooling, facets re-formed at about 400K, and the disorder at facet junctions disappeared below 200K. The transition occurred abruptly and remarkably little hysteresis was seen even at the extremely high simulated heating and cooling rates. This de-faceting behavior is in excellent agreement with the experiment (3).

The reversibility of de-faceting indicates that the transition is governed by thermodynamics. Thus, we aim to investigate the equilibrium properties of the system with the help of a lattice model and Monte Carlo simulations. The first step towards formulating the lattice model is to find the relevant atomic processes involved in grain boundary de-faceting. By examining the MD simulations and performing energy calculations for metastable states of the system, we identified the elementary excitation responsible for the rapid equilibration of the grain boundary structure observed in both MD simulation and experiment. It involves cooperative atomic motions as shown in Fig. 4.1A and can occur only at facet junctions. The elementary excitation changes the basis of one primitive cell of the coincidence site lattice (CSL), thereby transforming that primitive cell from the lower grain to the upper grain. (The CSL is the lattice of all points common to both grains if they are shifted such that the two grains have a point in common. A primitive cell of the CSL is shown schematically in Fig. 4.1A.) Fig. 4.1C shows the schematic structure of the grain boundary after an elementary excitation which introduces two extra lengths of facet junction and two extra areas of (111) twin boundary. Because elementary excitations can form only at the grain boundary facet junctions, the resulting defects of the grain boundary are localized near the original junctions at low temperatures. Our atomistic calculations enabled the discovery of this elementary excitation, a cooperative atomic shuffle that cannot be observed directly with existing experimental techniques.

Based on the local and discrete nature of the elementary excitation, we next formulate a lattice model and use it to study the thermodynamics of the transition. We define a coordinate system with x, y, and z axes in the $[\bar{2}11]$, [111], and $[01\bar{1}]$ directions, respectively. We replace the surface of the grain boundary z=h(x,y) by a discrete function h(i,j) where i and j are indices representing the corresponding x and y coordinates of the cells. We scale h such that it takes integer values and the height difference between the neighboring cells in the x direction is always unity. In this notation, a grain boundary facet junction with a single elementary excitation can be represented by a matrix as shown in Fig. 4.1C. A junction corresponds to a

local maximum or local minimum in h as a function of x (at constant y). The elementary excitation turns a local maximum into a local minimum and vice versa. Thus, at a local maximum, h can only be reduced by 2, whereas at a local minimum, h can only be increased by 2.

An elementary excitation increases the total junction length by twice the y dimension of the CSL primitive lattice cell. It also adds two small parallel twin boundaries each having the xz area of the rhombus bounding the CSL primitive lattice cell (see Fig 4.1C). It is important to note that the elementary excitation does not increase the total {112} grain boundary area in the system. Using EAM calculations we determined the total energy of systems with different total junction length and/or total (111) twin areas. We approximated the total energy as $E = E_o + n_{junc}E_{junc} + n_{twin}E_{twin}$, where E_0 is the total energy of the faceted, defect free grain boundary, n_{junc} is the total number of elementary junction segments with associated energy, E_{junc}, and n_{twin} is the total number of elementary twin boundary areas, with associated energy, E_{twin}. The linear approximation was excellent for the junction energy, giving E_{junc}=30meV. The twin energy showed a considerable size dependence. The linear fit gave E_{twin}=30meV for reasonably large values of n_{twin}, which was consistent with experimental twin energies (33meV) (10). However, for the smallest possible twin boundary area we obtained E_{twin} =60meV. This size dependence can be attributed to strain effects. To keep the lattice model numerically tractable, we used the above linear approximation. Expressing n_{junc} and n_{twin} as functions of the height variable $h_{i,j}$ we can write the total scaled energy of the system as:

$$\varepsilon = \varepsilon_o + \frac{1}{2}\sum_{i,j}\left|\mathbf{h}_{i+1,j} - 2\mathbf{h}_{i,j} + \mathbf{h}_{i-1,j}\right| + \frac{1}{2}\alpha\sum_{i,j}\left|\mathbf{h}_{i,j+1} - \mathbf{h}_{i,j}\right|,$$

where $\varepsilon = E/E_{junc.}$, $\varepsilon_0 = E_0/E_{junc.}$, and the energy ratio $\alpha = E_{twin}/E_{junc}$ is the only parameter of the model. The second term measures the total energy of the facet junctions, while the third term accounts for the energy of the twin boundaries.

In order to investigate the nature of the de-faceting transition, we performed MC simulations using this lattice model. Our initial grain boundary, with $(01\bar{1})$ average orientation, consisted of two {112} facets. We found that this grain boundary remained fully faceted at low temperatures with only a few isolated elementary excitations present along the facet junctions (Fig. 4.2A). At high temperatures, the grain boundary facets disappeared and a highly disordered structure formed (Fig 4.2B). This dramatic morphological change took place abruptly with the temperature and the observed behavior is in good agreement with experiment (3) and with our MD simulations. We characterized this de-faceting by measuring the average mean-square deviation of the height profile in the x direction:

$$w = \sqrt{\frac{1}{N_y}\sum_{j=1}^{N_y}\frac{1}{N_x}\sum_{i=1}^{N_x}(h_{i,j}^2 - \bar{h}_j^2)},$$

where N_x and N_y are the number of lattice sites in the x and y directions, respectively, and $\bar{h}_j = \sum_{i=1}^{N_x} h_{i,j}/N_x$. It is convenient to use the dimensionless quantity w/w_o where w_o is the mean-square deviation at zero temperature. The inset of Fig. 4.2 shows w/w_o as a function of the temperature for the N_x=80, N_y=48, _=1 system. The mean-square deviation decreases rapidly from w/w_o=1 to $w/w_o \gg 0.2$ at the de-faceting transition.

It is of importance to find the order of the de-faceting phase transition since it determines how the shape of the grain boundary evolves during the transition (2). To this purpose and to find the transition temperature more accurately we studied the finite size scaling of the maxima of the heat capacity curves (11). The observed linear scaling behavior suggests that this is a first-order phase transition. The de-faceting transition temperature was found to be $t_d^{MC} = k_B T_d^{MC}/E_{junc} = 1.62$, for _=1. For E_{junc}=E_{twin}=30meV, this corresponds to a transition temperature of 570K, in reasonable agreement with both experiment and molecular dynamics.

Both the experiment (3) and our MD simulations show that the flat $(01\bar{1})$ interface is not stable at low temperatures and forms {112} grain boundaries separated by grain boundary facet junctions. These facets are stable since introducing a monoatomic height step wandering across a facet in the [111] direction increases the total free energy of the system. However, at some elevated temperature, introducing such a step will cost no extra free energy. Then steps can form in the system leading to de-faceting. The low-temperature faceted structure becomes metastable above the de-faceting transition temperature and is replaced by an unfaceted, atomically-disordered $(01\bar{1})$ grain boundary. To calculate the change in the free energy of the system we first consider the partition function of a monoatomic height step with y dimension N_y and with free boundary conditions at its end points:

$$Z_{N_y} = \left(e^{-\frac{2}{t}}\sum_{i=-\infty}^{\infty} e^{-\frac{\alpha}{t}|i|}\right)^{N_y} = \left(e^{-\frac{2}{t}}\left(\frac{2}{1-e^{-\frac{\alpha}{t}}} - 1\right)\right)^{N_y},$$

where α=E_{twin}/E_{junc} and $t=k_BT/E_{junc}$ is the scaled temperature. Thus, the scaled extra free energy per unit length of an infinitely long step is

Solving Δf=0 provides the de-faceting phase transition temperature, t_d as a function of

$$\Delta f \equiv \lim_{N_y\to\infty}\frac{\Delta F/E_{junc}}{N_y} = -\lim_{N_y\to\infty}\frac{t\ln Z_{N_y}}{N_y} = 2 - t\ln\left(\frac{2}{1-e^{-\frac{\alpha}{t}}} - 1\right).$$

the energy parameter _. We found that the analytically derived phase transition temperature and its ___dependencare in excellent agreement with the MC results. (The differences were less than two percent.) Since _f(t) has a finite slope at t_d, where _f=0, the phase transition is of first order in the analytic model. Thus, the functional agreement with the MC simulations brings further evidence that de-faceting is a first order phase transition. Even though _f vanishes at the de-faceting transition temperature, the step free energy with respect to the {112} facets remains positive at t_d, due to the fact that introducing a monoatomic step on a single (112) facet with fixed facet boundaries would increase the total (112) facet area and thus the total free energy. This behavior is strikingly different from the infinite order surface roughening transition where the corresponding step free energy vanishes continuously at the roughening temperature.

Our results show that the grain boundary de-faceting phase transition is governed by a local atomic shuffle mechanism. The simplicity of this elementary excitation and the generic nature of the derived lattice model suggest that shuffle mechanism assisted phase transitions can be quite common at faceted interfaces.

Fig. 4.1. Elementary excitation along the grain boundary facet junction. (A) The arrows show the atomic displacements associated with the elementary excitation. The atoms also move perpendicular to the plane of the figure because of the 0.7Å offset in the (111) planes between the upper and lower grain. The blue rhombus represents the base of the coincidence site lattice (CSL) primitive cell. (B) The elementary excitation transforms one CSL primitive cell at the grain boundary junction from the lower grain to the upper grain. (C) Schematic view of the elementary excitation that introduces two extra lengths of facet junctions and two extra areas of (111) twin boundary. The corresponding height matrix **h** is also shown.

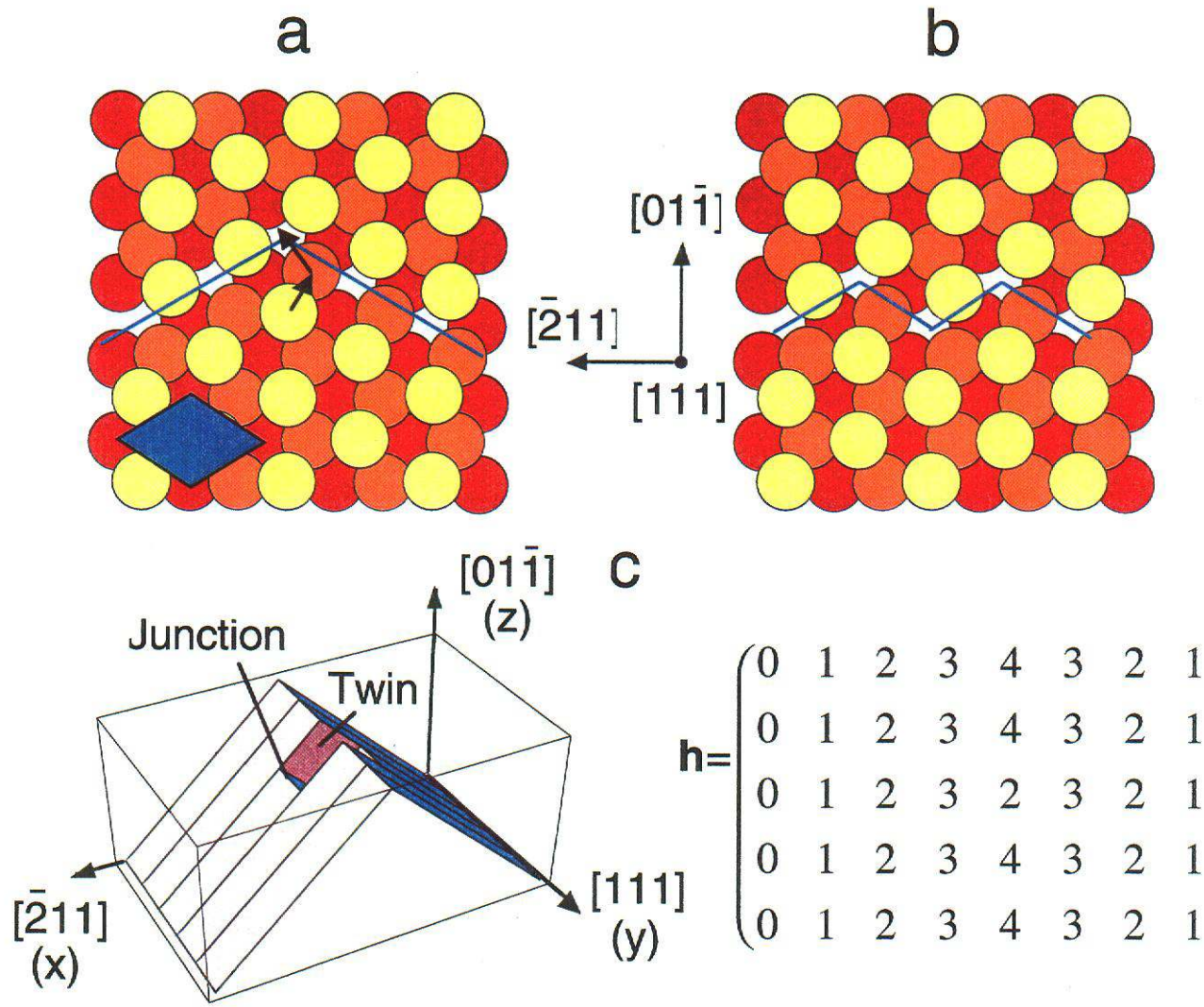

Fig. 4.2. Morphology of the grain boundary obtained by Monte Carlo simulations. We used N_x=80, N_y=48, and α=1 in this calculation. (A) At lower temperatures the grain boundary is faceted as shown here at k_BT/E_{junc}=1.55. (B) Above the de-faceting phase transition temperature a highly disordered structure forms as shown here at k_BT/E_{junc}=1.68. The inset illustrates the normalized average mean-square deviation of the height profile (defined in text). The abrupt change in grain boundary width at $t=k_BT/E_{junc} \approx 1.6$ is characteristic of the de-faceting phase transition.

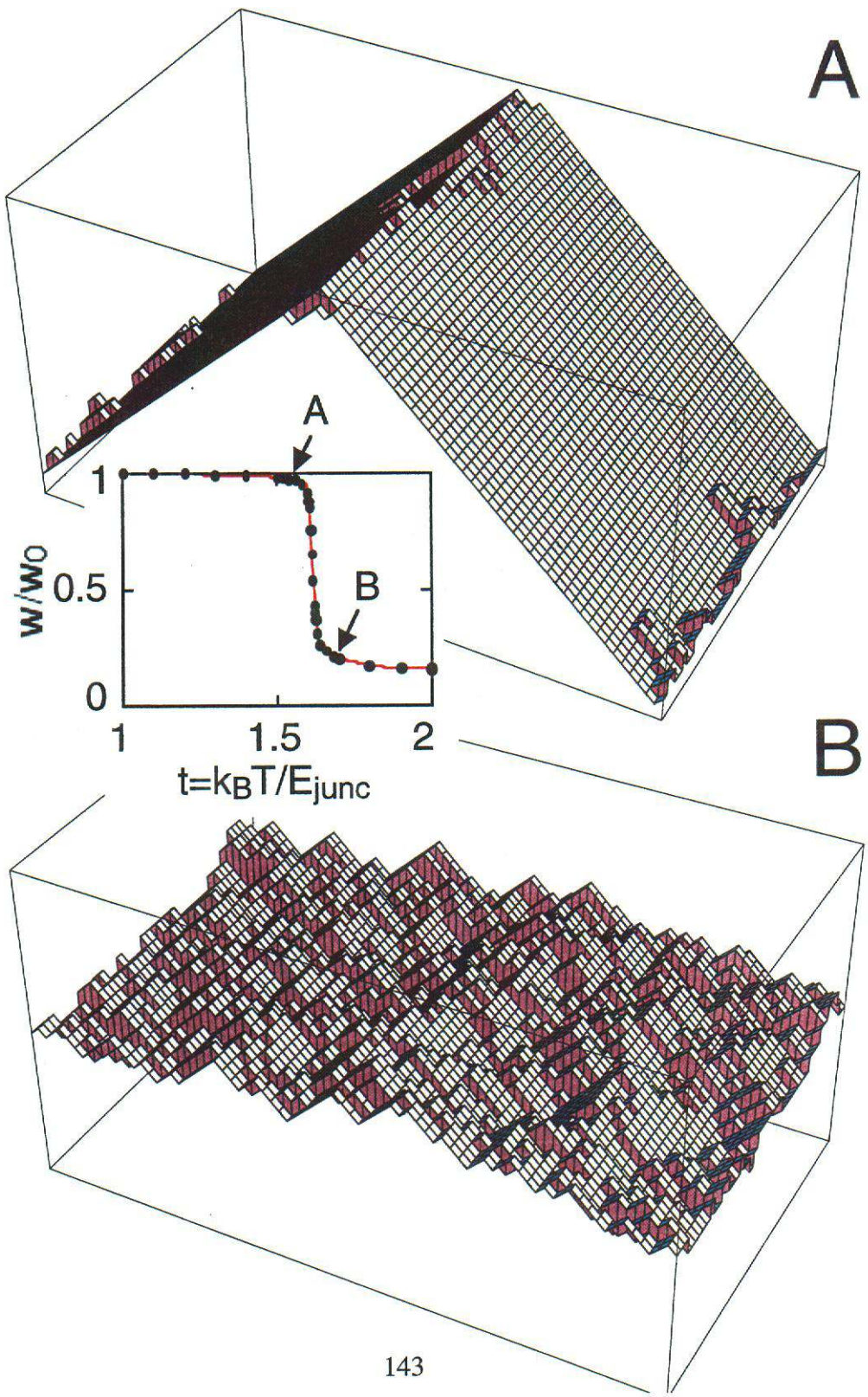

REFERENCES CHAPTER 4

1. J. W. Cahn, *J. Phys.* **43**, C6-199 (1982).

2. C. Rottman, M. Wortis, *Phys. Rep.* **103**, 59 (1984).

3. T. E. Hsieh, R. W. Balluffi, *Acta Metall.* **37**, 2133 (1989).

4. A. P. Sutton, R. W. Balluffi, *Interfaces in Crystalline Materials* (Clarendon Press, Oxford, 1995), pp. 372-401.

5. A. Brokman, V. I. Marchenko, *Scripta Met.* **30**, 639 (1994).

6. M. S. Daw, S. M. Foiles, M. I. Baskes, *Mat. Sci. Rep.* **9**, 251 (1993).

7. A. F. Voter, S. P. Chen, in *Characterization of Defects in Materials,* R. W. Siegel, J. R. Weertman, R. Sinclair, Eds. (Mat. Res. Soc., Pittsburgh, PA, 1987), pp. 175-180.

8. A. F. Wright, S. R. Atlas, *Phys. Rev. B* **50**, 15248 (1994).

9. R. C. Pond, V. Vitek, *Proc. Royal Soc. London B* **357**, 453 (1977).

10. J. P. Hirth, J. Lothe, *Theory of Dislocations* (Krieger Publishing Company, Malabar, Florida, ed. 2, 1992), p. 839.

11. K. Binder, D. W. Heermann, *Monte Carlo Simulation in Statistical Physics* (Springer-Verlag, Berlin, ed. 3, 1997), pp. 57-64.

12. We have benefited from useful comments and discussions with N. C. Bartelt, S. M. Foiles, and D. L. Medlin. This work was supported by the Office of Basic Energy Science, Division of Materials Science, of the U.S. Department of Energy.

Chapter 5

Single Particle Activated Transport in Amorphous Materials

Transport of small molecules through amorphous materials such as non-crystalline polymers can often be characterized by a hopping process. The molecule will remain trapped within a single cavity for a substantial period of time, and then jump to an adjacent cavity. The overall rate of transport is controlled by the jump rate and the distance jumped. In the case of amorphous polymers, this picture has been confirmed by molecular dynamics simulation. However, the observed jump rates vary over many orders of magnitude from one cavity to the next. The jump distances show a moderate variation. Molecular dynamics simulations, while very useful for rapidly diffusing systems, become computationally expensive for diffusion coefficients slower than 10^{-10} cm^2/s, as the required length of the simulation is roughly inversely proportional to the diffusion coefficient. Transition state theory (TST) provides an alternative way of predicting diffusion rates. The jump rate from one cavity to the next can be expressed as the ratio of the partition function for the dividing surface (transition state) between the two cavities divided by the partition function for the initial cavity (reactant state). Both of these quantities can be evaluated efficiently using equilibrium simulation methods, and the computational effort is independent of the actual diffusion coefficient. The accuracy of the TST method is very dependent on how it is implemented. Most important of all is the choice of which degrees of freedom to include in the partition functions. This is particularly important in the case of diffusion in polymers, where neglect of polymer mobility effectively eliminates all solute transport.

This chapter is divided into two sections. In the first, a method for exhaustively finding *all* the cavities and dividing surfaces in a polymer sample is described. Only the solute coordinates are treated explicitly. The polymer motion is either ignored or treated in a mean-field manner (isotropic harmonic approximation). The computationally efficient kinetic Monte Carlo method is then used to simulate diffusion on the resultant network of cavities. Results from the isotropic harmonic approximation for oxygen in EPDM are comparable to the results from a direct molecular dynamics simulation. In the second section, a method is described for finding transition states in which the polymer coordinates

are treated explicitly. This provides a very accurate description of particular cavity-cavity transitions, and is used to examine the competing roles of entropic and energetic selectivity for nitrogen and oxygen diffusing in polypropylene.

5.1 Determination of Cavities and Transition States in 3-D Space

5.1.1 Cavity Analysis Code

The basic problem is to divide up the 3-D configurational space into a set of cavities, and then to evaluate the volume configurational integral for each cavity, and the surface configurational integral for each pair of adjacent cavities. Our approach to this problem is the same as that used by Gusev and Suter [30], and by June, Bell and Theodorou [31], which rests on sampling the energy on a 3-D grid of points with a sufficiently fine spacing to converge to the result that would be obtained in the limit of infinite resolution. There are three novel features of the current implementation. Firstly, assignment of grid-points to cavities was done using just two sweeps across the entire grid, with no additional energy evaluations required. This method works because the set of grid-points belonging to a cavity is mathematically equivalent to a directed tree graph, a fact which was came out of discussions with Steve Plimpton and David Greenberg. Previous implementations assigned grid-points to cavities using an off-grid steepest-descent search from each grid-point to the nearest minimum, requiring many additional energy-evaluations per grid-point. Secondly, the calculation is implemented in a parallel scheme which is embedded within the LAMMPS MD code. This streamlines the preparation of the polymer samples, and also enables the treatment of very large samples, which would easily exceed the memory available on a single workstation. Thirdly, we have used sub-grid sampling to obtain a higher accuracy for the configurational integrals without using more grid-points.

The 3D configurational space was discretized as a cubic grid of volume elements or voxels, with a grid spacing a. The energy of interaction $U_{poly-pen}$ between the polymer and a penetrant particle located at the center of each voxel was calculated. Voxels with energies beyond a cut-off value of 75kT were dropped from the subsequent analysis. For each voxel, the lowest energy was determined from the 27 values occurring in the 3x3x3 cube centered on the current voxel. If the central voxel has the lowest energy, then this point is a local

minimum. Ties were resolved by always choosing the voxel, which occurs later in the arbitrary ordering of the voxels by position.

Once this has been done, it is computationally inexpensive to partition the voxels into a set of cavities, which cover the entire three-dimensional volume of the polymer. To understand this, it is helpful to imagine an arrow drawn from each voxel to its minimum energy neighbor. According to the procedure described above, a voxel can have zero, one, two or more arrows entering it, but only arrow leaving, or zero if it is a minimum. These properties result in the arrows forming a set of arborescences, which are directed graphs with no loops and only one root. Hence there is a one-to-one correspondence between cavities and root voxels. In addition, all points belonging to a given cavity can be found by starting at the root voxel, and finding all the voxels, which are connected to it. Computationally, this was done by identifying which of the twenty-six neighbors of the root voxel had it as their minimum energy neighbor. These voxels belong to the same cavity as the root voxel. Their neighbors were checked in turn, and the process was repeated in an iterative fashion until no more members of the current cavity are found. By repeating this for all the root voxels, every voxel is attributed to one and only one cavity.

Once the voxels have been partitioned into cavities, we can proceed to evaluate properties of the cavities, and the dividing surfaces between cavities. The physical volume V_i of cavity i is simply the number of voxels in the cavity, multiplied by a^3. The partition function Q_i of cavity i is the integral of the Boltzmann factor $\exp(-U_{poly\text{-}pen}/kT)$ over the cavity volume. We computed this by summing the Boltzmann factors calculated for each voxel:

$$Q_i = \int_{V_i} \exp\left(-U_{poly-pen}/kT\right) d\mathbf{r} \cong a^3 \sum_{k \in V_i} e_k \qquad (5.1)$$

where e_k is the Boltzmann factor for voxel k located in cavity i. In our implementation, we obtained improved accuracy for a given grid spacing by using subgrid Monte Carlo sampling. Instead of just using the value of the energy at the midpoint of each voxel to estimate e_k, we sampled the Boltzmann factor at N_s randomly selected points within each voxel volume, and then stored the average value.

$$e_k \cong \frac{1}{N_s} \sum_{l=1}^{N_s} \exp\left(-U_{poly-pen}(\mathbf{r}_{lk})/kT\right) \qquad (5.2)$$

The reason for doing the integrals in this way is that the resolution required to identify cavity boundaries is significantly less than that required to accurately evaluate the important parts of the Boltzmann integral. Since the memory-intensive grid structure is required only for the first task, it makes sense to use subgrid sampling for the second task. Typically, the value used for N_s was 100.

In order to find transition states, it is first necessary to locate the boundaries or dividing surfaces between cavities. We define cavity boundaries by boundary voxels, for which one or more of the six nearest neighbors belongs to a different cavity. The physical area of a dividing surface between two cavities i and j was calculated as the sum of the areas of all the voxels belonging to the set S_{ij}, which have nearest-neighbors in j.

$$A_{ij} \cong a^2 \sum_{k \in S_{ij}} f(n_k) \tag{5.3}$$

where $f(n)$ is a factor which accounts for the increased surface area which exists when a voxel has n neighbors on the other cavity. Values of 1, $\sqrt{2}$, and $\sqrt{3}$ for one, two and three neighbors respectively ensure that the areas of the 100, 110 and 111 cutting planes are exactly reproduced. Once the grid spacing is smaller than the curvature of the boundary, larger values of n occur rarely, and so in these cases we used the same value as was used for three neighbors. The partition function for the dividing surfaces was evaluated in the same manner as the cavity partition functions.

$$Q_{ij} = \int_{S_{ij}} \exp\left(-U_{poly-pen}/kT\right) d\mathbf{r} \cong a^2 \sum_{k \in S_{ij}} f(n_k) e_k \tag{5.4}$$

According to transition state theory k_{ij} the first-order rate constant for hopping from cavity i to cavity j is

$$k_{ij} = \sqrt{\frac{kT}{2\pi m}} \frac{Q_{ij}}{Q_i} \tag{5.5}$$

Finally, the transition state between two cavities is approximated by the boundary voxel with the lowest energy.

$$E_{ij}^{\mp} = \min_{k \in S_{ij}} \min_{l=1,N_s} U_{poly-pen}(\mathbf{r}_{lk}) \tag{5.6}$$

The location of the transition state is taken to be the center of the minimum energy voxel.

The finite grid spacing inevitably results in small differences between the calculated values of Q_{ij} and Q_{ji}, $E^{\mp}_{ij}$ and $E^{\mp}_{ji}$, as well the location of the transition states.

The above cavity analysis is implemented as a module with the LAMMPS MD code. It is run using the command "`tst`" in the LAMMPS input script. The arguments are as follows:

```
tst  q     type grid e_cut      r_min      temp ns    iseed
     delrms     delr
```

where

`q` = the charge on the penetrant species (e)

`type` = the atom type of the penetrant species

`grid` = the spacing for the energy grid (Å)

`e_cut` = the maximum grid energy (kT)

`r_min` = the hard-core separation (Å)

`temp` = the temperature (K)

`ns` = the number of subgrid points sampled

`iseed` = the seed used for the subgrid random number generator

The calculation assumes that periodic boundaries are in effect in all three directions. Before issuing the **`tst`** command, LAMMPS must load a configuration of "matrix" atoms, either from a LAMMPS data file or a restart file, and the appropriate pair interaction potentials must have been specified. The primary output of the cavity analysis is the file **`cavity_tst.dat`**. This contains a list of all the cavities, including position, physical volume, configurational integral and minimum energy, followed by a list of all the dividing surfaces, including the physical area, the configurational integral, the location of the transition state and the transition state energy.

5.1.2 Clustering and Percolation Analysis

Once the set of all cavities and surfaces has been generated, the problem is much more manageable, and all further analysis is done on a single workstation. The many millions of energy grid-points have been reduced to a few hundred cavities. To further refine the data, we perform to three additional operations: clustering, separation and percolation analysis. Clustering is used to filter out very high transition rates between cavities that are separated by very small energy barriers. Such cavities are referred to as microcavities, and can be grouped together to form a macrocavities without changing the overall diffusion rate. A variety of different criteria can be used to determine when two cavities should be clustered. We have used the size of the dividing surface configurational integral, as it is symmetric w.r.t. i and j. For typical polymer-penetrant systems, a value of 10 $Å^2$ gives good results. When two cavities are combined, their configurational integrals are summed, and the new position for the macrocavity is calculated as the weighted average of the microcavity positions, with the configurational integrals used as weighting factors. Three or more cavities can be combined by using these pairwise rules. Separation is used to filter out very low transition rates, by removing these transition states from the network. Once again, we use the dividing surface configurational integral as the threshold criterion. For polymer-solute systems, 10^{-11} $Å^2$ gives good results. Hence only surfaces lying on the range 10^{-11} $Å^2 < S_{ij} < 10$ $Å^2$ remain after clustering and separation has been completed. At this point, the system can be viewed as a graph consisting of vertices (macrocavities, from now on referred to as cavities) and edges (dividing surfaces). The graph may not be fully connected, and typically contains many disconnected components. In order for diffusion to occur, at least one of the components must span the system volume, so that penetrant particles hopping on the network can move indefinitely in the x, y, and z directions. To determine if this is so, we perform a percolation analysis. Two different measures of percolation are considered, SPAN and WRAP, which differ in how the periodic boundaries are treated. The first step is to map all the connected clusters, without regard to whether they cross periodic boundaries. We call these the PERIODIC clusters.

To check SPAN, we then map APERIODIC clusters, with connectivity across periodic boundaries turned off. The number of edges crossing each of the six boundaries are counted for that cluster, and stored in nspan_tmp(idir). If nspan_tmp(idir) > 0 for idir=1 and

2, the cluster SPANS in the x-direction, likewise for y, z. If spanning occurs, then these boundary connections are added to the total sum nspan(idir) for the periodic cluster to which the aperiodic cluster belongs. The final count nspan(idir) for a given periodic cluster reflects the number of edges at each boundary from which a path leads to the other side of the box. So a periodic cluster SPAN percolates in the x-direction when nspan(idir) > 0 for i = 1 AND 2. NOTE: In general, nspan(1) will not equal nspan(2), but if one of them is zero, then they both are. However, they will tend to come out roughly equal for a homogeneous network.

To check WRAP, we also use the aperiodic clusters. In this case we count edges crossing each boundary which connect to the same aperiodic cluster. Each bond where this occurs will actually be encountered twice, at the upper and lower boundaries, but will only be recognized the second time. Hence the assignment to the upper or lower boundary is entirely arbitrary, and there is no real need to differentiate them but we do. Once again, the counts for the aperiodic clusters are summed to the underlying periodic cluster. A periodic cluster WRAP percolates in the x-direction when nwrap(idir) > 0 for i = 1 OR 2. NOTE: nwrap(1) and nwrap(2) depend on the order of the search, but their sum is a fixed property of the network. There is a tendency for one to be much larger than the other, because the search order spatially correlated. Given the above discussion, I have decided that it makes sense to report only the pair sums for both SPAN and WRAP. The following inequality holds: nspan(1)+nspan(2) $\geq$ 2 (nwrap(1)+nwrap(2)).

Note: WRAP is a sufficient condition for an infinite random walk on the periodic network. SPAN is neither sufficient not necessary, but is still a pretty useful indicator. For physically reasonable systems, most of the sites belong to a single large cluster which satisfies both SPAN and WRAP in all three directions. For the purposes of kinetic Monte Carlo simulation, sites in the remaining non-percolating clusters are ignored.

5.1.3 Kinetic Monte Carlo Simulation of Diffusion

For systems with a well-defined structure, such as zeolites, the macroscopic transport properties can be deduced directly from the local hopping rates, assuming that successive hops are uncorrelated. For amorphous materials, similar arguments can be made, provided that good estimates for the average hopping rate and hopping distance can be made.

However, in the case of light gases diffusing in polymers, we see hopping rates distributed over many orders of magnitude, and so the definition of an average rate becomes problematic. To avoid this problem, we can directly simulate diffusion on the network using the kinetic Monte Carlo method. In this method, a set of penetrant particles are placed on different cavities of the network, according to the equilibrium distribution. The particles do not interact with each other, and are assumed to hop from one cavity to each of the neighboring cavityies with rates given by Eq. (5.5). For a sufficiently large number of particle hops on a percolated network, the average mean-square displacement of the particles from there starting points should increase linearly with time. The basic scheme that we have used to simulate this model is as follows.

1. Set the time $t = 0$. For each of N particles, randomly assign it to one of the cavities of the percolating cluster, chosen with probability proportional to Q_i. The number particles is arbitrary, but it makes sense to choose N roughly equal to the number of cavities.
2. For each cavity i, record the number of particles N_i, the hopping rate to each of its neighbors $R_{ij} = N_i k_{ij}$, the total hopping rate for the cavity $R_i = \Sigma R_{ij}$, and the total hopping rate for the system $R_{tot} = \Sigma R_i$.
3. Increment the time by a waiting time Δt chosen with probability density $R_{tot} \exp(-\Delta t\, R_{tot})$. This is done by choosing a uniform random number $\xi \in (0,1)$, and then calculating $-\ln(\xi)/R_{tot}$.
4. Select a move with the correct probability. The simplest way to do this is to select a cavity with probability R_i/R_{tot}, a transition state with probability R_{ij}/R_i, and then select one of the N_i particles with equal probability.
5. Perform the move, update R_i, N_i for the old and new cavities, as well as R_{tot}. Record the new cavity of the particle, and increment the periodic image counter for the particle if a boundary has been crossed.
6. Repeat Steps 2,3, and 4 N_{block} times, then output t and the particle positions using the current cavity and image counter.
7. Repeat Step 6 N_{block}/N_{step} times.

This scheme enables a very large number of moves to be performed on a workstation, e.g. $5x10^8$ moves with 1000 particles on a network of 1000 cavities takes about 10 hours on an SGI R10000 workstation. For systems of this size, most of the time is spent selecting a cavity, as this requires a loop over all cavities, and so scales with the volume of the system. This could be improved upon by using a binary search tree to select a particle instead of a cavity, which would then scale logarithmically with system volume.

5.1.4 Results

The first problem that the code was applied to was very simple: a single Lennard-Jones atom moving in a fixed cubic array of identical atoms, with the potential energy cut and shifted at r_c:

$$u_{LJ}(r) = 4\varepsilon\left[\left(\frac{\sigma}{r}\right)^{12} - \left(\frac{\sigma}{r}\right)^{6}\right] - 4\varepsilon\left[\left(\frac{\sigma}{r_c}\right)^{12} - \left(\frac{\sigma}{r_c}\right)^{6}\right], \quad r \le r_c \qquad (5.7)$$

$$= 0, \quad r > r_c$$

We chose the lattice spacing to be $2a$, $\sigma=1.4a$, and $r_c=2a$, where a is an arbitrary unit of length. This resulted in a simple potential energy surface with a minimum at the center of each cubic cell, and a saddle point on each face. Figure 5.1 shows a comparison of the residence time within one of the cubic cells versus reduced inverse temperature. The TST result from the cavity analysis is compared with the analytic results of harmonic TST, which assumes a quadratic energy surface at the minimum and saddle points. The two calculations agree well at low temperatures, where the harmonic approximation is very accurate. At higher temperatures, the full TST result gives lower residence times, due to the non-quadratic shape of the Lennard-Jones potential.

As a second test, we used the cavity analysis code to map out the cavities and dividing surfaces for a nitrogen molecule in the zeolite 3A. The zeolite forms a cubic array of α-cages, each connected to six neighboring cages by an eight-member ring of oxygen atoms. We used an eight unit cell sample, approximately 24.6Å on each side. Figure 5.2 shows how the estimated diffusion coefficient for nitrogen decreases with increasing level of resolution, until a converged value is reach at a grid-spacing of 0.125Å.

We then applied the code to the calculation of oxygen diffusion in EPDM, which is a polymer widely used in the nuclear stockpile for rubber o-ring seals. EPDM is a random copolymer of ethylene and propylene monomers. United-atom sites were used to represent each methyl and methylene group, and the TraPPE forcefield was used for all the non-bond and bonded interactions. The oxygen molecule was represented by a pair of Lennard-Jones atoms, with a fixed bond length. We used the SIGNATURE builder to construct a large cubic sample of EPDM, approximately 60 Å on a side. The sample consisted of 65 linear polymer chains, containing on average 25 ethylene and 25 propylene monomers, to give a total of 8026 united-atom sites, and a density of 0.86 g/cc. We used a 0.5 Å grid-spacing and 10 sub-grid samples, requiring a total of about 20 million energy calculations. This calculation required about 10 minutes on 64 nodes of ASCI Red.

Figure 5.3 shows the network which is obtained from the cavity analysis. Dividing surfaces are drawn as cylinders joining the centers of adjacent cavities. The radius of each cylinder is scaled proportionally with the logarithm of the configurational integral for the dividing surface, and so gives a measure of the jump rate for that dividing surface. The cavities themselves are not drawn explicitly. The key observation from this of this image is that there is no percolation cluster, which was confirmed using percolation analysis. This demonstrates that if the mobility of the polymer is not accounted for, the diffusion coefficient of oxygen in EPDM is essentially zero.

Figure 5.4 shows a plot of mean square displacement versus time for $-CH_2-$ groups in EPDM, obtained from a molecular dynamics simulation using the same model as described above. The plot shows a distinctive plateau in the range 1-10 picoseconds, where the mean square displacement is constant at about 1 $Å^2$. This is indicative of a vibrational mode which is probably due to oscillation of the backbone dihedral angles back and forth with a particle *trans* or *gauche* conformation. Regardless of the cause, Figure 5.4 suggests that the motion of the polymer over a significant time range can be well represented by the motion of a particle trapped in a quadratic energy well. This is exactly what

was done by Gusev and Suter[9]. They further assumed that the trapping potential was spherically symmetric, and referred to this assumption as the isotropic elastic approximation, which highlights the connection with the thermal motion of solids. The effective interaction u_α^{eff} between a penetrant atom and an isotropic elastic polymer atom α can then be formally written as:

$$u_\alpha^{eff}(s) = -kT \log\left[\frac{1}{\left(2\pi\langle\Delta_\alpha^2\rangle\right)^{3/2}}\int d\ddot{A}_\alpha \exp\left[-\frac{\Delta_\alpha^2}{2\langle\Delta_\alpha^2\rangle} - \frac{u_\alpha(\mathbf{s}-\ddot{A}_\alpha)}{kT}\right]\right] \tag{5.8}$$

where s is the vector distance from the penetrant site to the average position of the polymer atom, and Δ_α is the displacement of the polymer atom from its equilibrium position. $\langle\Delta_\alpha^2\rangle$ is an adjustable parameter describing the mean square displacement of the polymer atom. $u_\alpha(r)$ is the bare interaction potential between the penetrant atom and the polymer site α. The integral is over the entire three-dimensional volume. For very small values of $\langle\Delta_\alpha^2\rangle$, this potential is identical to the bare potential. As $\langle\Delta_\alpha^2\rangle$ is increased, the effective potential becomes more smeared; the attractive well becomes shallower, and the repulsive interaction increases less steeply at short separations. By switching to bipolar coordinates, we can reduce this down to a one-dimensional integral:

$$u_\alpha^{eff}(s) = -kT \log\left[\frac{1}{\sqrt{2\pi}\,y}\int_0^\infty x \exp\left[-u_\alpha\left(x\langle\Delta_\alpha^2\rangle\right)\right]\left(e^{-(x-y)^2/2} - e^{-(x+y)^2/2}\right)dx\right] \tag{5.8}$$

where $y = s/\langle\Delta_\alpha^2\rangle$. For a particular interaction potential $u_\alpha(r)$ and mean square displacement $\langle\Delta_\alpha^2\rangle$, the effective potential function is evaluated numerically at the start of the cavity analysis and stored in a look-up table. $\langle\Delta_\alpha^2\rangle$ is assumed to be the same for all the polymer sites. To implement this with the LAMMPS code, two additional arguments were added to the `tst` command:

`delrms` = the root mean square displacement of the polymer atoms (Å)

`delr` = $\langle\Delta_\alpha^2\rangle^{1/2}$, the grid spacing for the tabulation of u_α^{eff} (Å)

If `delrms` is set to zero, then the bare potential is used as before.

We applied the isotropic elastic approximation to the 60 A EPDM sample with three different choices for $\langle\Delta_\alpha^2\rangle^{1/2}$: 0.6 Å, 0.9 Å and 1.2 Å. Note that the plateau in Figure 5.4 occurs at about 1.4 Å^2, which corresponds to $\langle\Delta_\alpha^2\rangle^{1/2}$ = 1.2 Å. As before, we used a 0.5 Å grid-spacing and 10 sub-grid samples. The calculations took a little longer, about 40 minutes on 64 nodes of ASCI Red. The longer run-time was due to the significantly larger number of points with energies less than $75kT$, which account for most of the computational effort. Figure 5.6 shows a visualization of the cavity network obtained for $\langle\Delta_\alpha^2\rangle^{1/2}$ = 1.2 Å. Most of the cavities belong to a single highly-percolated network. The same was found for $\langle\Delta_\alpha^2\rangle^{1/2}$ = 0.9 Å and 0.6 Å. So clearly adding in even a small amount of polymer mobility has a large impact on the transport properties. For each of the three cases, we performed a kinetic Monte Carlo simulation consisting of 5x10^8 moves with 1000 particles. The mean square displacement of the particles from their starting positions are shown in Figure 5.6. The very large number of timesteps simulated ensures that the asymptotic regime is reached in all cases, so that we can calculate the diffusion coefficient for oxygen using $D_{O2}=\langle\Delta r^2\rangle/6t$. The resultant diffusion coefficients are plotted versus $\langle\Delta_\alpha^2\rangle^{1/2}$ in Figure 5.7. The dependence on $\langle\Delta_\alpha^2\rangle^{1/2}$ is very strong. D_{O2} increases roughly as the fourth power of $\langle\Delta_\alpha^2\rangle$. This is to be expected, The figure also shows a diffusion coefficient obtained by molecular dynamics simulation, and using $\langle\Delta_\alpha^2\rangle^{1/2}$ = 1.2 Å, taken from Figure 5.4. This point lies close to the TST "master curve", suggesting that the TST calculation is fairly accurate. However, the extreme sensitivity of the diffusivity to the input parameter $\langle\Delta_\alpha^2\rangle^{1/2}$ makes it difficult to use the theory as a predictive tool, although it computationally a lot more efficient than molecular dynamics.

5.2 Determination of Multidimensional Transition States in Flexible Polymers

5.2.1 Introduction

Permeation of small molecules in polymers occurs via the "solution-diffusion" mechanism.[1] As the name suggests, in this mode, permeation occurs in two distinct steps: solvation of the penetrant in the polymer matrix and subsequent diffusion of the same through the polymer. Hence the permeability P can be written concisely as $P = D\,S$, where D

is the diffusivity and S is the solubility of the penetrant. In a binary mixture of gases A and B, the selectivity of A with respect to B is given by

$$\alpha_{A/B} = \frac{P_A}{P_B} = \frac{D_A}{D_B}\frac{S_A}{S_B} \tag{5.9}$$

Both permeability and selectivity are important in evaluating the performance of a material. Whereas the former is equivalent to the throughput of a separation process, the latter measures the effectiveness of separation. Equation (5.9) clearly shows that selectivity is affected by two separate quantities: diffusivity and solubility. Although these quantities in general are functions of gas composition across the membrane, at low gas loadings such dependencies may be neglected, and $\alpha_{A/B}$ is referred to as the ideal selectivity.

When dealing with mixtures of non-polar gases of similar sizes, separation based on solubility is not very attractive. In such cases, one instead exploits differences in the diffusivities of the components. To understand the process of penetrant diffusion through glassy polymers, the microstructure in these materials can be pictured as a network of free volume packets. These packets, where the penetrant molecules spend most of their time, are connected by narrow constrictions or "necks." Diffusion occurs as thermal motion of the polymer and/or thermal activation of the penetrant allows crossings through these necks. Hence, the diffusivity of a penetrant depends on the physico-chemical properties of the polymer matrix, such as the fractional free volume (determined by the interchain packing) and the stiffness of the polymer backbone (related to the glass transition temperature, T_g). An ideal membrane material would be composed of high free volume that facilitates diffusion and tight constrictions that provide effective sieving. Glassy polymers, which possess these favorable characteristics, have been successfully used as membranes in effecting several industrially important separations. Rubbery polymers, on the other hand, give high permeation rates but are poor sieves due to the absence of rigid necks.[2,3]

Much success has been gained by chemically modifying polymers to create better materials for gas separation.[2,3] However, the performance of diffusion-selective polymers has been observed to be limited by an inverse relationship between permeability and selectivity. Conceptually, this occurs because the magnitudes of the diffusion barriers are generally increased when enhancing the selectivity. Robeson[4] carried out an extensive

survey of the performance of polymeric membranes in separating several pairs of gases, clearly demonstrating this permeability-selectivity tradeoff. Singh and Koros[5] further analyzed Robeson's data to point out that the performance of the available polymeric membranes falls short of the economically attractive region currently occupied by zeolites and molecular sieves.

Singh and Koros[5] reasoned that this difference in performance between polymers and inorganic molecular sieves is caused by the superior entropic selectivity offered by the latter materials. Using transition-state theory (TST), the ratio of diffusivities of species A and B in a gas mixture can be written as

$$\frac{D_A}{D_B} = \exp\left(\frac{\Delta S_{A,B}}{k_B}\right)\exp\left(-\frac{\Delta U_{A,B}}{k_B T}\right) \tag{5.10}$$

where k_B is the Boltzmann constant, T is the temperature, and $\Delta S_{A,B}$ and $\Delta U_{A,B}$ are, respectively, the differences in entropy and energy barriers encountered by species A and B

$$\Delta S_{A,B} = \Delta S_A - \Delta S_B \tag{5.11a}$$

$$\Delta U_{A,B} = \Delta U_A - \Delta U_B \tag{5.11b}$$

Loosely speaking, the activation entropy for a jump event is a measure of the difference in confinement of the molecule between the transition state and the minimum. The first exponential term on the right-hand side of Eq. (5.10) is the entropic selectivity, while the second exponential term is the energetic selectivity. By correlating experimentally measured O_2/N_2 separation data using Eq. (5.10), Singh and Koros concluded that whereas 4A zeolite and carbon molecular sieves offer significant entropic as well as energetic selectivities, even the best current polymers (*e.g.* polypyrrolone) offer entropic selectivities close to unity.

Singh and Koros[5] hypothesized that this loss in entropic selectivity is consistent with the picture of a penetrant being relatively "unconfined" by a sieving neck in a polymer, due to the relatively large thermal motion of the polymer chains. That is, the local structure of the polymer will relax during a penetrant hopping event, allowing the penetrant significant rotational freedom in the transition state. Zimmerman and Koros[6] subsequently presented several other possible molecular-level scenarios, based on free volume arguments, that would lead to a lack of entropic selectivity. They pointed out that situations where the penetrants

are tightly confined in the *minima* might be expected in polymers, and that this would tend to decrease the entropic barriers for the individual penetrants as well as the entropic selectivity.

The reason for the relatively small entropic selectivities of polymers is still a matter of speculation, especially with regard to the relative contributions of free volume and inherent molecular-level flexibility. The main aim of this paper is to begin using molecular-level modeling to address these issues, by studying the effects of matrix flexibility on the entropic and energetic selectivities in model glassy polymers. Such analysis will yield valuable information regarding the significant factors that contribute to the performance of polymer membranes. This in turn could provide new directions in research aimed at design of better polymers with superior separation capabilities.

Molecular modeling, and molecular dynamics simulation in particular, have developed into useful tools for probing penetrant diffusion in polymers.[7] Because of the time-scale limitations of molecular dynamics, several groups have recently developed alternative theoretical approaches based on combinations of TST and molecular models;[8-12] these approaches have allowed time scales on the order of mircoseconds, and even milliseconds, to be accessed. Gusev and coworkers used TST to study gas diffusion in polymer models which were perfectly rigid[8] and which included mean-field thermal motion;[9] inclusion of the thermal motion of the polymer atoms was seen to have a significant impact on the calculated diffusion coefficients. Greenfield and Theodorou[11,12] devised a novel way to directly include the polymer degrees of freedom (d.o.f.'s) that contribute to the diffusive jump of a penetrant in the TST formalism. Using this methodology, a number of hopping events of a spherical methane molecule in glassy atactic polypropylene (aPP) were studied, and rates of hopping were calculated by making a harmonic approximation in all relevant degrees of freedom. In this work, we used their method to study the entropic selectivity offered by aPP in the sieving of O_2 and N_2, but our penetrants are modeled as rigid dumbbells with their rotational degrees of freedom explicitly included, as opposed to idealized spheres.

A brief discussion of the transition-state theory formulation of Greenfield and Theodorou[12] is presented in the next section. Details of the model systems are given in Section 5.2.3. The calculation details are described in Section 5.2.4. Section 5.2.5 discusses the results of the present study, and conclusions are given in Section 5.2.6.

5.2.2. Transition-state theory

Transition-state theory addresses the rate of occurrence of rare events, such as penetrant diffusion in glassy polymers, where adjacent sorption sites are separated by energy barriers much greater than the thermal energy.[13-15] These events happen on time scales that are beyond the range amenable to study by conventional molecular dynamics simulations. For an activated process, the rate of occurrence can be written as[16,17]

$$k^{TST} = \frac{k_B T}{h}\frac{Q^{\ddagger}}{Q^0} = \frac{k_B T}{h}\exp(-\beta\Delta A) \tag{5.12}$$

where k^{TST} is the rate constant (with units of inverse time), Q is the partition function, ΔA is the free energy barrier, $\beta = 1/k_B T$, and h is the Planck constant. The superscripts $\ddagger$ and 0 indicate the transition state and the minimum respectively. Using the definition of Helmholtz free energy, this equation can be used to derive the selectivity equation, Eq. (5.10).

Previous molecular dynamics studies have revealed the involvement of the torsional motion of chains in the hopping motion of the penetrant during diffusion in polymers.[18] Hence it is important to incorporate the polymer d.o.f.'s in the search for transition states and the subsequent evaluation of the partition functions and the rate constants. As mentioned above, Greenfield and Theodorou[11,12] studied a number of hopping events of a (spherical) methane molecule in atomic-level models of glassy polymer structures. The authors developed an efficient technique to incorporate polymer degrees of freedom, such as torsional motions and bond angle vibrations, in a self-consistent manner when describing the motion of the penetrant during diffusion. The authors also derived an expression for the rate of hopping within the harmonic approximation; the potential energy of the system was treated as a simple harmonic function in all d.o.f.'s, including those of the participating polymer segments, in the transition state and the minimum.[19] Due care was taken to ensure that the end result was independent of the coordinate system used. Using the quantum mechanical vibrational partition function, the resulting rate expression for a hop involving a total of n d.o.f.'s was given by

$$k^{TST} = k_0 \exp(-\beta\Delta U) \tag{5.13a}$$

where

$$k_0 = \frac{k_B T}{h} \frac{\prod_{i=1}^{n} \left[1 - \exp\left(\frac{-h\nu_i^0}{k_B T} \right) \right]}{\prod_{i=2}^{n} \left[1 - \exp\left(\frac{-h\nu_i^{\ddagger}}{k_B T} \right) \right]} \tag{5.13b}$$

and

$$\Delta U = \left(U^{\ddagger} - U^0 \right) \tag{5.13c}$$

with ν_i^0 the vibration frequency of mode i in the minimum and $\nu_i^{\ddagger}$ the vibration frequency of mode i in the transition state. Note that in the denominator of Eq. (5.13b), $i = 1$ corresponds to the diffusion direction (along which the vibration frequency is imaginary), so this term is not included in the product. The entropy barrier ΔS can be calculated using the relation[12]

$$\Delta S / k_B = \ln\left(\frac{h k_0}{k_B T} \right) - 1 \tag{5.14}$$

Given a jump event of a penetrant from one minimum energy position to another through a transition state, the energy and entropy barriers can be determined from Eq. (5.13c), (5.13b), and (5.14), and the total rate for that jump event can be obtained from Eq. (5.13a).

The approach taken in this paper will be to consider individual jump events, calculate the energetic and entropic barriers for each penetrant (O_2 and N_2) separately, and then use Eq. (5.11) to estimate an entropic and an energetic selectivity for each jump. Since the macroscopic selectivity is ultimately determined by the selectivities of individual hopping events, our results will provide insight on macroscopic behavior. However, note that we do not actually predict a ratio of macroscopic diffusion coefficients. Such macroscopic properties could be estimated, but significantly more effort and statistical analysis is necessary; this will be the subject of future work.

In order to proceed with our analysis of transport in a polymer, we must first prescribe an atomic-level model of a polymer/penetrant system, including interaction potentials. Then we must locate transition states and associated minima to define hopping events, and evaluate rate constants based on the information at the transition states and minima.

5.2.3. Model and potential details

The atactic polypropylene (aPP) models used in this study were very similar to those used by Greenfield and Theodorou.[11,12] These structures were parameterized in terms of the various bond lengths, Eulerian, bond, and torsional angles, and chain-start positions following Theodorou and Suter.[20] We review only the most important features here; the interested reader is referred to their publications for details. We employed polymer structures with three polymer chains of 50 monomers each at a density of 0.892 g/cm^3; this is equal to the experimental density at 233 K, which is ca. 20 K below the T_g of aPP.[20] The polymer model, which was cubic and periodic in all three dimensions, had a side length of 22.79Å. The repeat unit of the polymer is depicted in Figure 5.8; we followed the previous authors[11,12,20] in using the "united atom" model for the methyl units, and explicit atom models for the rest of the species. The C-C and C-H bond lengths are constrained at their mean values. Whereas Greenfield and Theodorou[11,12] considered the bond-angles to be flexible, we considered them also to be constrained at their mean values to reduce the computational requirement. A molecular dynamics study by van Gunsteren and Karplus[21] demonstrated that the assumption of rigid bond-angles can affect the dynamics of complex model molecules, damping positional fluctuations and dihedral angle transition rates relative to those in unconstrained models. Our flexible polymer model will therefore be somewhat less flexible than that of Greenfield and Theodorou,[11,12] but we expect that our comparative study of flexible and perfectly rigid polymers will not be qualitatively affected by this assumption.

The initial polymer structures were generated at the given density and temperature using the Polymer Builder module of the CERIUS^2 software from Molecular Simulations Inc.[22] This module samples the torsional angles using the RIS method[23] while avoiding significant overlaps between polymer atoms.[20] After the polymer structure was built, the Energy Minimizer module of the software was used to obtain a preliminary glassy matrix. The AMBER force-field was employed during this step, with the bond-length and angle-bending spring constants modified to very high values; this led to a minimized structure with

bond lengths and angles essentially fixed at the desired values. The final glassy polymer structure was created by further minimizing the potential energy in terms of only the torsional angles, chain start positions, and Eulerian angles.[24] The BFGS algorithm, as implemented in FORTRAN by Byrd *et al.*,[25] was used for this purpose; no penetrants were present in the polymer matrix during energy minimization. The penetrant jump results presented here were obtained from studies carried out in three independently-built glassy polymer structures.

The diatomic penetrant molecules, O_2 and N_2, were modeled as rigid dumbbells with the two force centers separated by a distance equal to the equilibrium bond-length (1.0166 Å and 1.0897Å respectively). Unlike spherical molecules, these penetrants have five degrees of freedom: the three Cartesian coordinates of its center of mass and two Eulerian angles.[24]

The total energy of the penetrant-polymer system is given by

$$U = U_{tor} + U_{poly-poly} + U_{poly-pen} \tag{5.15}$$

where U_{tor} is the torsional energy associated with the rotation of the skeletal bonds, $U_{poly-poly}$ is a pair-wise sum of the non-bonded interactions between the polymer segments, and $U_{poly-pen}$ is the corresponding quantity evaluated between polymer segments and the two force-centers on the penetrant. The potential energy expressions and most of the parameters employed therein were taken from Theodorou and Suter;[20] these are briefly described below.

The torsional energy is given by

$$U_{tor}(\phi) = \frac{k_\phi}{2}(1 - \cos 3\phi) \tag{5.16}$$

where ϕ is the torsional angle. A value of 2.8 kcal/mol was used for k_ϕ.

The polymer-polymer and polymer-penetrant non-bonded interactions were modeled with the site-site 12-6 Lennard-Jones (LJ) potential. To ensure that the energy function and its first and second derivatives were continuous in the entire range of the center-to-center distance r between two species, the attractive tail of the potential was approximated by a quintic spline.[20] Periodic boundary conditions with the usual minimum image convention[26] were employed to eliminate surface effects.

5.2.4. Details of Calculation

5.2.4.1 Geometric analysis of polymer structures

The first step in studying the hopping motion of a penetrant is the location of the transition state, *i.e.* the lowest-energy point on the (hyper) surface that separates the "reactant" and the "product" states. In general, the transition state is physically located in the vicinity of the neck that separates two adjacent packets of free volume present in a microporous material, such as a polymer. In a material made of atoms arranged in a relatively simple geometrical pattern, *e.g.* in a zeolite with well-defined cages and sieving windows arranged on a regular lattice, the transition states can be located in a straightforward way. In a polymer model, on the other hand, the energy landscape is very complex and hence the location of the transition states is not trivial. This task becomes even more difficult when the polymer d.o.f.'s are considered as flexible, *i.e.* when the polymer structure is allowed to rearrange in response to the presence of the penetrant. Hence the location of transition states in a flexible polymer model requires the use of sophisticated search techniques. The success of these algorithms in yielding a viable transition state depends on the proximity of the initial guess configuration to that in the transition state.

Since the physical "terrain" in a polymer matrix does correspond to the energy landscape (*e.g.* constrictions roughly correspond to the energy maxima), geometric analysis of the polymer structures is useful. Several researcers have employed Delaunay tessellation[27,28] or fine grid maps[29] to visualize the free volume clusters accessible to hard-sphere probes of different diameters, and to locate possible constrictions bridging two adjacent cavities.

In our work, we used the three-dimensional cavity analysis for a single site penetrant in a rigid polymer sample, which is described in section 5.1.1 above.

5.2.4.2 Methods for location of transition states and minima

In the transition state (TS), which is a first order saddle point, all but one of the normal modes (which corresponds to the diffusion direction) have real frequencies. Hence the Hessian (the matrix of second derivatives of total potential energy) evaluated at the TS has a single negative eigenvalue. The work of Cerjan and Miller[32] provides the basis for

most techniques employed in the literature for saddle point searches. Baker[33] summarized the original work along with the later developments and made an algorithmic presentation of the technique, which is popular among researchers. Greenfield and Theodorou[11,12] also employed Baker's algorithm[33] in their work. Wales[34,35] followed a slightly different approach in formulating the optimization problem. Whereas two different shift parameters, referred to as λ_p and λ_n, are used for the maximizing and minimizing modes in Baker's algorithm,[33] Wales introduced separate shift factors along all normal modes; a larger variety of high-dimensional problems could be solved more effectively using Wales' algorithm. In the present work, which involves systems with anywhere from 100 to 200 total d.o.f.'s, Wales' algorithm was also generally found to be more efficient. We caution the readers here that this statement is not intended to be a general prescription since no systematic and thorough comparison of the performance of the two methods was carried out.

Once a TS is located, the corresponding minima were located by following Fukui's intrinsic reaction coordinate (IRC) methodology.[36] Banerjee and Adams[37] appropriately modified the original prescription to make it consistent with the use of generalized coordinates (**q**), as opposed to mass weighted Cartesian coordinates. As mentioned earlier, the generalized coordinates include the five penetrant d.o.f.'s, the polymer torsional and Eulerian angles, and chain start positions. The reaction path involving generalized coordinates is described by the following prescription[12] for a step d**q**

$$\mathbf{a}^0 \, d\mathbf{q} = \nabla_{\mathbf{q}} U \, d\tau \tag{5.17}$$

where $\mathbf{a}^0$ is the covariant metric tensor calculated based on the flexible d.o.f.'s and $d\tau$ is a scaling factor used to adjust the step size. The size of the multidimensional step, ds, was calculated by the equation[12]

$$ds^2 = (d\mathbf{q})^T \mathbf{a}^0 (d\mathbf{q}) \tag{5.18}$$

Since the gradient of potential energy with respect to all flexible d.o.f.'s is zero in the TS, the first step from the TS must be treated differently than prescribed in Eq. (5.17). Generally the pathways to each of the minima were initiated along the eigenvector

corresponding to the single negative eigenvalue of the following generalized eigenvalue problem[12,37]

$$(\mathbf{H}_{qq} - \lambda\, \mathbf{a}^0)\mathbf{dq} = \mathbf{0} \tag{5.19}$$

where $\mathbf{H}_{qq}$ is the Hessian with the derivatives evaluated with respect to the flexible degrees of freedom and λ are the eigenvalues.

5.2.4.3 Implementation of rate calculations

Rigid polymer. Each search for a transition state was initiated by inserting a single penetrant molecule into the energy-minimized polymer structure. The center of mass of the diatomic gas molecule was first placed at the coordinates of a TS located by the geometric analysis detailed above; the orientation of the penetrant was chosen randomly. Since the penetrant used in the geometric analysis was a spherical oxygen molecule, as opposed to a dumbbell model used in the rest of the steps, a new transition state in penetrant d.o.f.'s was found using Wales' algorithm. The two minima associated with this TS were located by following the IRC prescription discussed earlier; a step size ds of 0.001 $(g/mol)^{1/2}\times$Å (calculated using Eq. (5.18)) was used in calculating the diffusion path. Finally the rates of hopping in both directions were evaluated using Eq. (5.13), with the frequencies calculated from the eigenvalues of the Hessian matrix at the appropriate locations.

Flexible polymer. The presence of a penetrant naturally perturbs the polymer structure in its immediate vicinity, and the polymer degrees of freedom, such as torsional motions, in turn affect the hopping process of the gas molecule. Hence determining which of the polymer d.o.f.'s are to be treated as flexible is important for obtaining an accurate estimate of the hopping rate. As pointed out by Greenfield,[38] too many polymer d.o.f.'s cannot be treated as flexible due to the constraints on computational power and, more importantly, to avoid studying the effects of long range chain rearrangements as opposed to the more relevant, local segmental motions. On the other hand, one might expect that at least those polymer segments which enter the potential range of the penetrant during a hop event should be treated as flexible. Following Greenfield and Theodorou,[12] when segment i along the chain is found within the potential cutoff from the penetrant, the nearest six torsional

angles are treated as flexible. If that segment happens to be a chain start, its position as well as the Eulerian angles were also treated as flexible.

Since the penetrant travels significant distances in the course of a hop, it is important to include the polymer d.o.f.'s along the diffusion path. Greenfield and Theodorou[12] addressed this issue by including additional d.o.f.'s in the IRC calculation whenever a new polymer segment was found within the penetrant's sphere of interaction. We believe that it is more desirable to make an *a priori* estimate of all of the d.o.f.'s along the path that need to be treated as flexible, and find the transition state in all of these relevant d.o.f.'s. Our initial estimate for the relevant degrees of freedom is obtained from the hopping event in the rigid polymer model. At the transition state in the rigid polymer, we note all polymer segments that are within the potential cutoff from the two penetrant centers. Subsequently as the penetrant moves along the diffusion path during the rigid-polymer IRC calculation, this list is augmented with the new polymer segments encountered by the penetrant. All degrees of freedom associated with the final list of atoms, after locating the two minima, are treated as flexible in studying the corresponding hop in flexible polymer model.

Next we discuss the actual search for the transition state in this high-dimensional space. Starting with the TS configuration in the rigid polymer and a list of d.o.f.'s from the rigid case, a higher dimensional transition state in the penetrant and polymer d.o.f.'s was found by "releasing" the latter set in an incremental fashion. This procedure is similar to the one suggested by Greenfield and Theodorou,[12] who found that the TS search is much quicker when polymer d.o.f.'s are included in steps than when all were treated as flexible simultaneously. We first picked the five polymer segments closest to each of the centers of the penetrant dumbbell and treated all the torsional angles associated with them as flexible. After the higher dimensional transition state was found, the dimensionality of the problem was further increased by releasing more polymer d.o.f.'s. This process was continued until we treat as flexible all the torsional angles associated with the polymer segments found within the potential cutoff distance from the penetrant. After this we also released all the d.o.f.'s in the list compiled earlier along the IRC path in the rigid polymer, and found the corresponding transition state. Subsequently, the IRC-following was initiated and the two minima were found. As before the rates of hopping were found using Eq. (5.13).

Interestingly, the inclusion of additional degrees of freedom in the calculation (beyond those relevant at the transition state) did not significantly alter the energy and entropy barriers and selectivities.

As a consistency check, a list of d.o.f.'s that should be treated as flexible was compiled along the high-dimensional IRC path in the flexible polymer, and it was compared with the original list based on the rigid polymer. In most cases, fewer than six new torsional angles were added to the list, which on average corresponds to one more polymer segment being treated as flexible. We found that including these new d.o.f.'s further in the transition state search and IRC path evaluation did not alter the rate constant values significantly; hence they were not included in obtaining the results reported here. For those cases where many more new polymer d.o.f.'s were added (about 15% of the total), the spatial locations of the transition state and/or minima were observed to change substantially (> 2 Å) relative to the positions in the rigid case. This indicated that the character and path of the hop had changed significantly upon introducing polymer degrees of freedom. There is nothing physically unrealistic about such a result, so these hops were included in the calculation of aggregate statistics such as median energy and entropy barriers. However, since these hops are no longer correlated with the original hop in the rigid polymer, we chose not to include them when the rigid and flexible polymer models were directly contrasted. Since the nitrogen molecule is larger than the oxygen molecule, more polymer d.o.f.'s are treated as flexible during its hop. The TS configuration found for the latter is used as the initial guess for the former to save computer time.

We studied several hops of the penetrants starting with different initial guesses for the penetrant placement in three independent glassy polymer structures. In almost all cases the negative eigenvalue occurred in one of the penetrant degrees of freedom; similar behavior was also observed by Greenfield.[38] In some instances, the transition state search in the rigid polymer yielded configurations in which the negative eigenvalue was seen along one of the Eulerian angles of the penetrant. These jumps were observed to be not diffusive, but rather related to molecular rotation; the jump length in such cases was virtually zero. Hence we present here only those results where the negative eigenvalue occurs in one of the Cartesian directions of the penetrant. In all, 42 distinct hopping events were studied. Since each jump has two rate constants (forward and reverse) associated with it, we have 84 rate constants.

5.2.5. Results

Energy and entropy barriers in rigid polymer models. The energy and entropy barriers for oxygen in rigid polymer models are plotted against the hopping distance d (*i.e.* displacement of the penetrant center of mass from the transition state to the minimum, which is different from the "path length" of the hop) in Figures 5.9a and b respectively. As can be seen from the plots both barriers take on a range of values: ~ 0.01 to ~ 10 k_BT in the case of ΔU and 1 to 10 k_B in the case of ΔS. The distance d ranges from near 0 to 7.5 Å; this wide range of values signifies the heterogeneity of the local microstructural features within the polymer matrix. We would like to point out that the entropy barriers are negative because the penetrant is more constrained and hence has lower entropy in the transition state compared to when it is in the minimum. Similar ranges of activation barriers were seen by Greenfield and Theodorou[12] during the hopping of a spherical methane molecule.

Based on the free energy values of the two minima, each of the two rates in a given jump event can be assigned a direction. By analogy with chemical kinetics, the "forward" event is defined as movement from the minimum of higher free energy to that of lower free energy, and the "reverse" event is of course defined as the opposite. A significant correlation between the direction of motion and the magnitude of the energy barrier might be expected, but none was detected in this work; the "forward" and "reverse" rate data were well-mixed in plots like Figure 5.9 (not explicitly shown).

We can see from Figures 5.9a and b that both ΔU and $-\Delta S$ are positively correlated with distance d. Interestingly, the energy and entropy barriers exhibit different behaviors above and below a d of ~ 2 Å. Typically, ΔU's below this hop distance are less than or close to k_BT. Hence the corresponding hops are not activated. Entropy barriers also behave differently above and below a d of 2 Å. For $d < 2$ Å, ΔS values do not show much scatter, but tend to be in a narrow range between -2 and -4 k_B. Based on the small distances, these jumps likely occur within the sorption site; they are so-called "intra-macrostate" hops that do not contribute to the overall diffusion of the penetrant.[12] The hops with $d > 2$ Å are likely the "inter-macrostate" jumps that take the penetrant from one sorption site to an adjacent one.

A similar range of values for barriers and hopping distances were seen for nitrogen. The ΔU values for oxygen are plotted versus those for nitrogen in Figure 5.10a; a corresponding plot of ΔS values is given in Figure 5.10b. By comparing the data against the $y = x$ lines given on the plots, one can see that whereas ΔU values for O_2 are in general lower than those for N_2, no such trend is obvious in the case of ΔS. The former observation can be explained based on the sizes of the penetrants: since nitrogen is larger than oxygen, it overlaps more with the polymer atoms comprising the neck, thus possessing higher potential energy in the transition state. In the cavity, depending on the local packing of polymer segments, nitrogen may have higher or lower energy compared to oxygen. Since the difference in penetrant energies in the minimum are expected to be much smaller compared to that in the transition state, the energy barrier itself is higher for nitrogen compared to that of oxygen.

Based on the sizes of the penetrants, one would expect that nitrogen would also have a higher entropy barrier. Judging from the magnitudes of the normal-mode frequencies, nitrogen is indeed more constrained (*i.e.* has lower entropy) in the transition state compared to oxygen. However, our data indicated that nitrogen is often more constrained compared to oxygen in the *minimum* as well, leading to a decrease in the overall entropic selectivity for the hopping event. Further discussion of this phenomenon and its consequences for the selectivity behavior will be given below.

Energy and entropy barriers in flexible polymer models. Flexibility of the polymer matrix is expected to lower the energy barriers, since the polymer segments can rearrange to reduce overlaps with the penetrant. The same effect is expected in the case of entropy barriers, since the penetrant presumably is trapped less tightly in a flexible polymer compared to a rigid one. The energy barrier values for oxygen in the flexible polymer are plotted against those in the rigid models in Figure 5.11a; the corresponding plot of entropy barriers is shown in Figure 5.11b.

As expected, these plots show that both activation energies and activation entropies decrease as a result of polymer flexibility; however, the effect is seen to be more pronounced in the case of energies, where order of magnitude differences can be seen. Interestingly, when the energy barriers are relatively low ($< \sim 3\ k_BT$), the values in flexible and rigid models seem to be equal to each other. In the case of entropy barriers, similar behavior tends

to occur when ΔS is in the range between −2 and −4 k_B. This is probably another indication that the these jumps are happening within a macrostate.

Rates of hopping. Now we shall consider the rate constants calculated for various hops in this study. Figures 5.12a and b show the hopping rates k^{TST} plotted against d for oxygen and nitrogen respectively; values in both rigid and flexible models are shown in these plots. We can see that k^{TST} values are spread over a wide range; this is a direct consequence of the wide spread in the energy and entropic barriers seen earlier. A similar range of values for rate constants was seen by Greenfield and Theodorou[11,12] for methane in flexible model systems. Since both barriers are lower in the flexible polymer case than in the rigid one, the rates of hopping are generally faster in the former case. We can also see that the nitrogen hops are, in general, slower compared to those of oxygen; this is consistent with the experimental observation that the former species has a lower diffusion coefficient in polymers compared to the latter species.

The behavior of k^{TST} values for $d < 2$ Å requires some discussion. The rate constants in this region have similar values, in the range of 10^5-10^6 μs^{-1}, for both penetrants; a very similar range of values was seen by Greenfield and Theodorou[12] for the hopping of methane in the course of intra-macrostate jumps. This behavior seems to suggest that intra-macrostate hops do not closely distinguish between penetrants. Interestingly, hopping rates in this region seem to be unaffected by the flexibility of the polymer matrix.

Energetic and entropic selectivities. As given in Eq. (5.10), selectivity is the exponential of the difference between the corresponding barriers for oxygen and nitrogen. Hence the simple difference between ΔU's (or ΔS's) for the two gases is enhanced when converted into the corresponding selectivity. Energetic and entropic selectivities for the different hops are plotted against d in Figures 5.13a and b respectively. We can see from Figure 5.13a that energetic selectivity, in general, is greater than unity, *i.e.* relative to nitrogen, oxygen encounters smaller potential energy barriers during diffusion. In this plot, we can also see the clear difference in behavior in going from a rigid polymer to a flexible model; evidently, rigidity of the constriction helps to distinguish the two penetrants much more effectively based on potential energy barriers. As the polymer is made locally flexible and capable of responding to the penetrant's presence, the overlaps are decreased, leading to a substantial lowering of the energy barriers, and as a consequence the difference between

ΔU's also decreases. One statistic that illuminates this discussion is the median value of the energy barriers in different situations: the median values of ΔU's in the rigid polymer models for O_2 and N_2, respectively, are 7.48 and 12.42 k_BT, whereas the corresponding values in the flexible case are 3.89 and 4.96 k_BT. These findings are consistent with the hypothesis developed by Koros and co-workers[2] that the activation energy for penetrant diffusion should increase with segmental rigidity.

In contrast to energetic selectivity, entropic selectivity (Figure 5.13b) cannot be said to be always favorable to oxygen relative to nitrogen. Again looking at the median values of entropy barriers for oxygen and nitrogen, in the rigid models the values are –5.46 and –5.47 k_B respectively, and in flexible models the values are –4.59 and –4.30 k_B respectively. We can also see from these numbers that rigid and flexible polymer models do not seem to be much different in terms of the entropic selectivity they offer. To look more closely at the effect of flexibility on the two kinds of selectivity, we consider the ratio of the selectivity value in the flexible polymer to the corresponding value in a rigid matrix. Figures 5.14a and b, respectively, show energetic and entropic selectivity ratios plotted against *d*. Figure 5.14a clearly shows that the flexible polymer has a significantly smaller energetic selectivity than the rigid one, except for jump lengths smaller than ~ 2Å (likely intra-macrostate jumps). We believe that this is an indication that polymer d.o.f.'s do not participate significantly in a intra-macrostate jump; similar results were seen by Greenfield and Theodorou.[11,12]

In contrast to the energetic selectivity ratio, Figure 5.14b shows that the entropic selectivity ratio is never very small, and in fact is often greater than unity. There is also a great deal of scatter in the data. This would seem to suggest that polymer flexibility does not have a significant effect on entropic selectivity, although the contributions for the individual penetrant species are affected (ref. Figure 5.11b). There also appears to be some difference in the magnitude of the scatter for the intra- and inter-macrostate jumps, with less scatter below $d = 2$ Å.

5.2.6 Discussion

First we shall summarize the results of the current study. We saw above that a variety of penetrant hopping events is possible in polymers, in which the activation entropies and energies assume a wide range of values. These events are seen to fall into two general

categories: ones that occur within a cavity and those that occur across cavities. Both energy and entropy barriers are lower in the former cases, where the minima are located typically within 2 Å from the transition state. Moreover, since polymer degrees of freedom do not seem to participate in these hops, barrier and selectivity values are not affected due to flexibility of the polymer matrix. The intra-cavity hops do not contribute to the overall diffusion of the penetrant, and hence are relatively unimportant for us. In contrast, the inter-cavity jumps do contribute to diffusion and will be discussed further below.

For jumps that occur across cavities, where the penetrant passes through a constricting neck to move to an adjacent packet of free volume, the activation barriers are typically higher. Whereas the energetic selectivity is seen to be favorable to oxygen compared to nitrogen, the entropic selectivity fluctuated about unity. The introduction of matrix flexibility substantially lowers the energy barriers and the corresponding selectivities. As mentioned above, this observation is consistent with the hypothesis of a positive correlation between penetrant activation energy and polymer segmental rigidity, as developed in the literature by Koros and coworkers.[2] The entropy barriers for each penetrant are also lowered due to matrix flexibility, although the effect is not as substantial as in the case of energy barriers. However, entropic selectivities are apparently not influenced strongly, or in any particular direction, by flexibility.

The lack of clear effect of polymer flexibility on entropic selectivity is directly at odds with the view of Singh and Koros,[5] who proposed that thermal motion of the polymer chains leads to loss of entropic selectivity in these materials. However, our result is perhaps not very surprising in view of a recent simulation study by Rallabandi and Ford[39], who calculated diffusivity selectivities for the oxygen/nitrogen separation in model sieving windows. Their approach was based on statistical mechanics and transition-state theory, and did not use the harmonic approximation to evaluate the partition functions. Instead, the required free energy differences were directly estimated using a Monte Carlo scheme proposed by Voter.[40] Molecular-level flexibility was included by tethering the solid atoms to their equilibrium positions with harmonic springs. Simulations were performed at several window widths and flexibilities, *i.e.* different values of the spring constants (values as low as ~ 0.01 of the C-C bond strength were used). The results from that study showed that while the energetic part of the total selectivity was quite sensitive to the window flexibility, the

change in entropic contribution was never more than about 20%, even for very flexible windows.

As mentioned above, our data indicated that nitrogen is often more constrained than oxygen in the *minimum* as well as in the transition state, leading to a decrease in the overall entropic selectivity for the hopping event. These findings support the hypothesis of Zimmerman and Koros[6] that the small cavity volumes associated with the minima in polymers can have a significant negative impact on entropic selectivity. In particular, our results generally support the picture in Figure 4 of Zimmerman and Koros,[6] where the entropy barrier of nitrogen is lowered due to a high degree of confinement in the minimum. Therefore we believe that the apparent lack of entropic selectivity in polymers is more likely caused by factors associated with the molecular-level distribution of the free volume, rather than the inherent rigidity of the matrix.

The relatively good entropic selectivity in inorganic materials can also be explained on the basis of free volume.[6] The microstructure of inorganic materials such as zeolites and carbon molecular sieves differs substantially from that of polymers. In the inorganic materials, the structure often consists of wide cages (radius ~ 6 Å or more) where the motion of small molecules is relatively free, joined by small windows that provide the sieving.[41] In polymers, the distribution of free volume is believed to be much different, although direct experimental determination of free volume distribution in polymers is not a straightforward task. Positron annihilation lifetime spectroscopy (PALS) measurements in polymers revealed that the average hole radius in polymers typically ranges from 2.8 to 3.7 Å.[42] We note that there has been some criticism of the assumptions made in interpreting PALS results,[43] so these reported cavity sizes should be regarded with some caution. Molecular modeling using hard-sphere penetrant probes provides another method for estimating the free volume distribution in polymers.[27-29,44-48] These studies, performed on a range of polymer types, have revealed that the accessible free volume fraction is a sharply decreasing function of probe size and that very little of the unoccupied volume is accessible to probes having radii greater than ca. 2 Å. Of course, larger cavities do exist and can have a significant impact on the overall transport properties. However, based on the results of either PALS or molecular modeling, the typical free volume elements in polymers are expected to be much smaller than

the cages seen in the inorganic materials. This scenario may mean that nitrogen tends to be more confined compared to oxygen not only in the sieving neck, but also in the cavity. These differences tend to offset those in the transition state, resulting in an overall decrease in entropic selectivity.

If these conclusions are accurate, materials design efforts for increasing entropic selectivity in polymers should not be targeted towards increasing rigidity *per se*, but rather towards manipulating the free volume. The ideal would be to create structures similar to those of inorganic molecular sieves, with cavities which are large enough to allow free movement (rotation) of the penetrants. This idea has been considered before.[3] In fact, Zhang[49] synthesized isotactic polyphenyl silsequioxane, a polymer containing 8-member silicone rings; unfortunately, this polymer did not show much higher selectivities in the separation of O_2/N_2 and CO_2/CH_4 than other silicone polymers with similar permeabilities.[50] In light of our results, such approaches may be worthy of reconsideration by experimentalists.

Energetic and entropic selectivities for oxygen over nitrogen were calculated in atomic models of glassy atactic polypropylene, built following Theodorou and Suter.[20] Geometric and energetic analyses were performed on these structures with a spherical probe molecule to gain knowledge of the microstructure in the models; the locations of possible sieving constrictions, to be used as initial guesses in the transition state searches, were also located in this step. The transition-state theory method developed by Greenfield and Theodorou[11,12] was used to incorporate the polymer degrees of freedom in the simulation of the penetrant hopping process. Almost 100 diffusive hops of oxygen and nitrogen were studied in rigid as well as flexible models and rate constants were evaluated within the harmonic approximation. Subsequently the separation selectivity of each hop was partitioned into distinct energetic and entropic contributions.

Our data showed a wide range of activation barrier values; consequently, the observed rates of hopping varied over several orders of magnitude. A strong positive correlation between energetic selectivity and polymer rigidity was observed, in accordance with previous literature discussions.[2] Furthermore, our model polymer offered low entropic selectivity, in accordance with the observations of Singh and Koros.[5] However, the entropic selectivity was not correlated with rigidity of the polymer, as speculated by those authors. Rather, our

data indicated that entropic selectivity is lost due to the fact the cavities in polymers tend to be smaller than those in inorganic materials, as proposed by Zimmerman and Koros.[6] The nitrogen molecule was confined more than oxygen not only in the necks but also in the cavities, thus the entropic selectivity seen in the neck regions is offset by a comparable selectivity in the cavities. The key to improving the performance of polymer membranes seems to lie in producing larger free volume packets and not just in improving the rigidity of the necks.

We note that the results obtained in this study depend on the validity of the harmonic approximation, which is difficult to estimate. This approximation, which assumes small oscillations about a stationary point, might not be applicable in situations where the frequencies of oscillations are low, and hence the corresponding modes might explore configurations away from the stationary point of interest.[38] Hence it is desirable to calculate the rates of hopping using free energy methods, analogous to the one adopted in our previous study[39]. However, attempts in that direction require considerably more complex calculations and computational power. Efforts are currently underway in our group to implement methods to rigorously evaluate free energy barriers to penetrant hopping in polymer matrices. We also plan to study more technologically relevant polymers and state conditions.

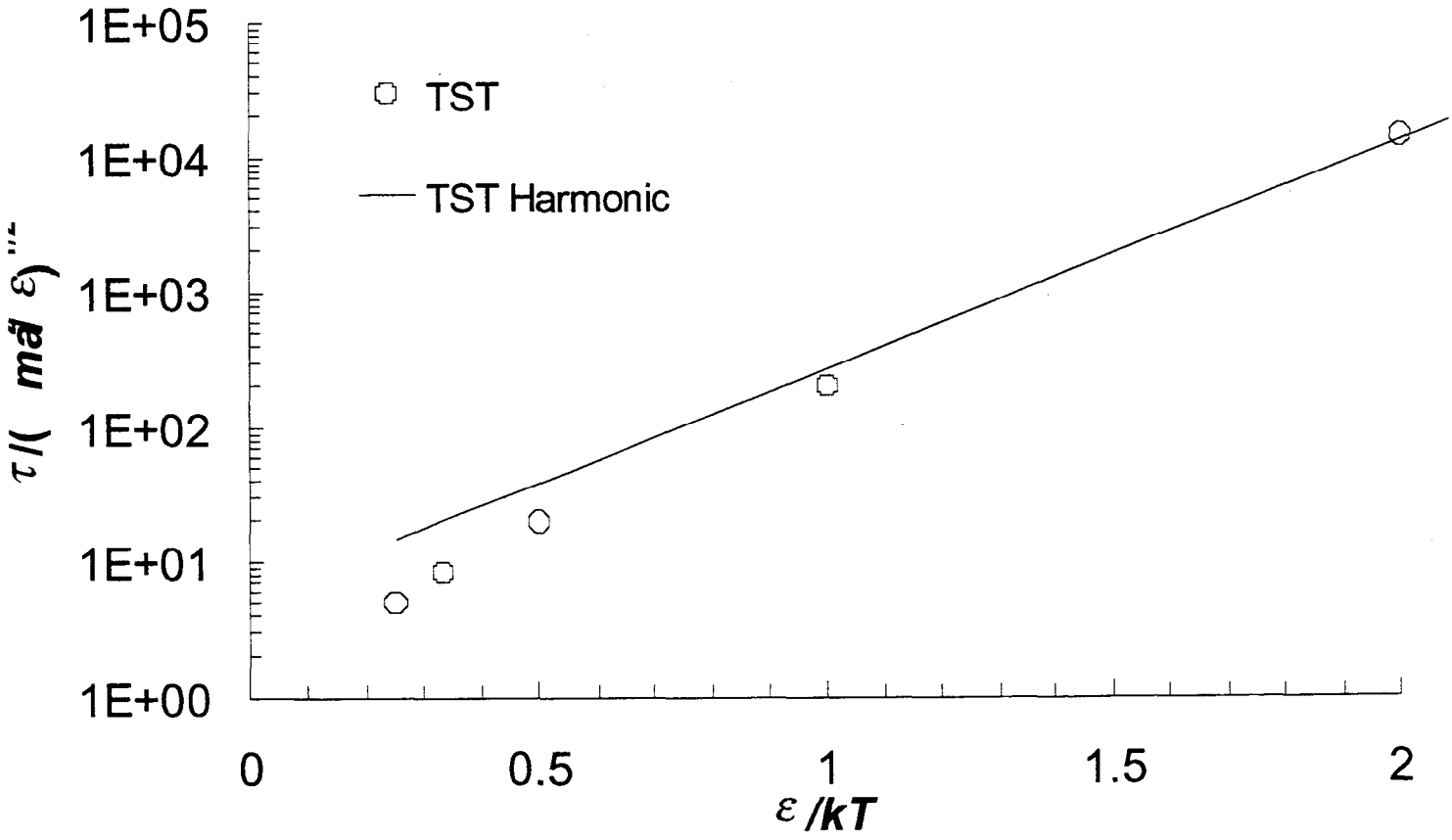

Figure 5.1: Residence time versus reduced inverse temperature for a single Lennard-Jones particle moving within a fixed cubic array of identical particles. The figure compares the results of the full 3-D transition state theory calculation (circles) with the harmonic approximation (squares and line). The full TST calculation mapped a periodic cell containing 8 atoms and 8 cavities using a grid-spacing of $0.03125a$, or 2 million points.

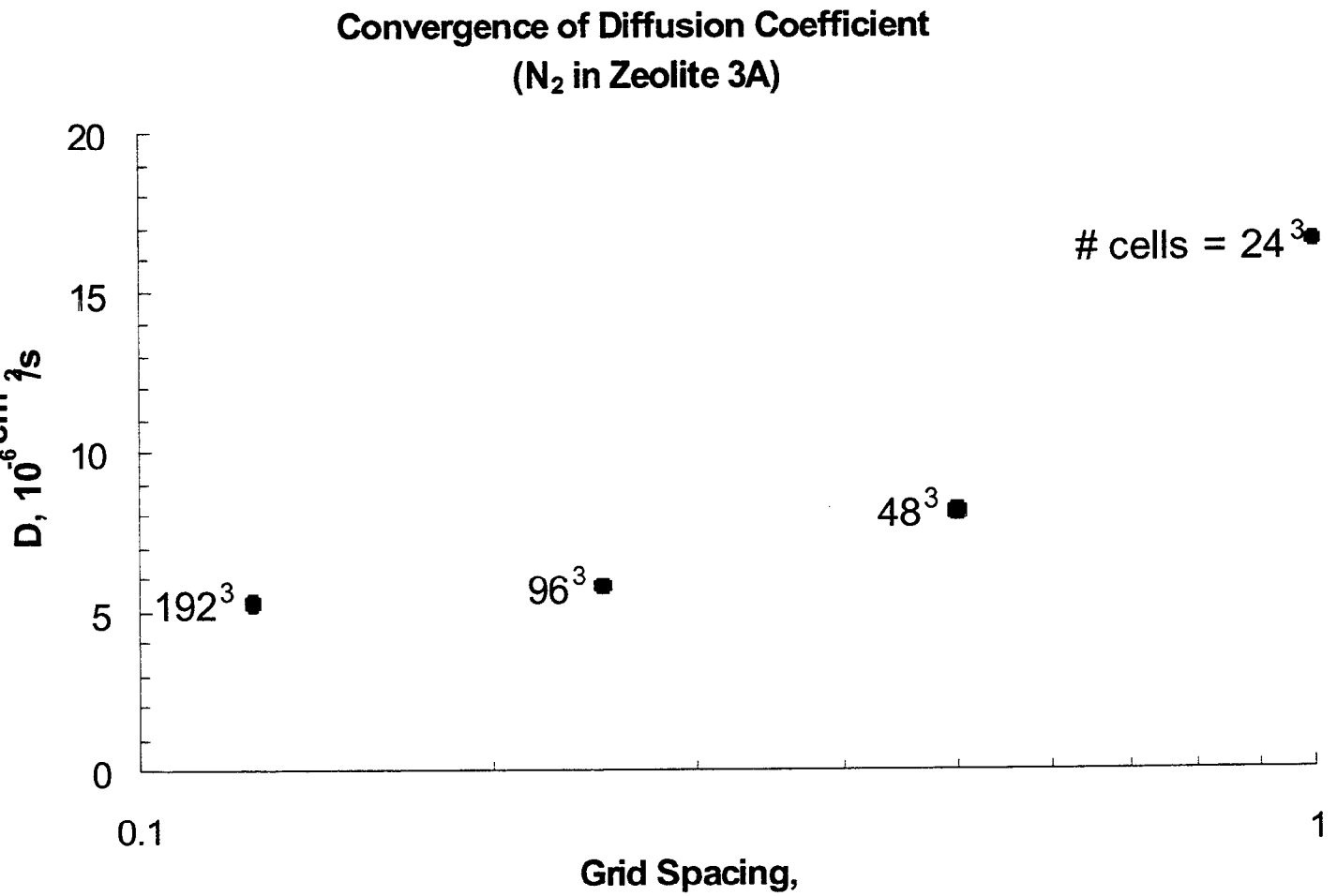

Figure 5.2: Plot of the calculated diffusion coefficient of nitrogen in zeolite 3A versus the number of grid-points used. The calculation used a 24.6Å x 24.6Å x 24.6Å sample containing 8 unit cells and 8 macrocavities.

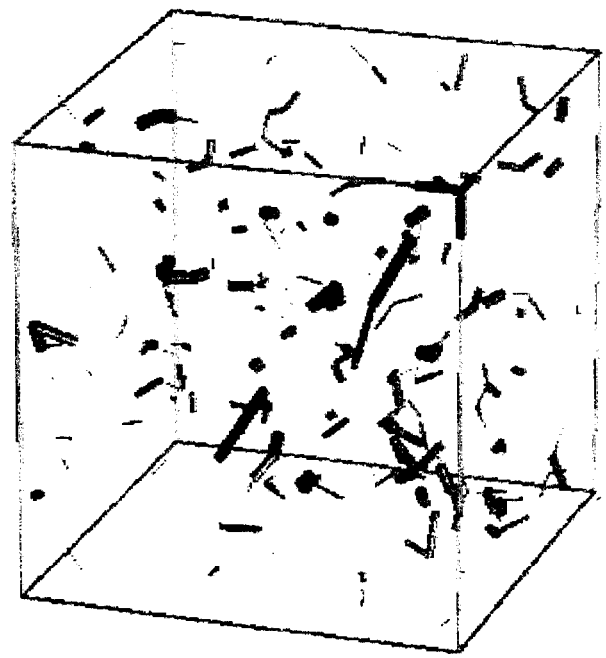

Figure 5.3: Visualization of the dividing surfaces obtained using cavity analysis for oxygen in a 60 Å x 60 Å x 60 Å sample of EPDM, assuming no polymer motion. Dividing surfaces are drawn as cylinders joining the centers of adjacent cavities. The radius of each cylinder is scaled proportionally with the logarithm of the configurational integral for the dividing surface, and so gives a measure of the jump rate for that dividing surface. The cavities themselves are not drawn explicitly. The dividing surfaces do not form a percolated network

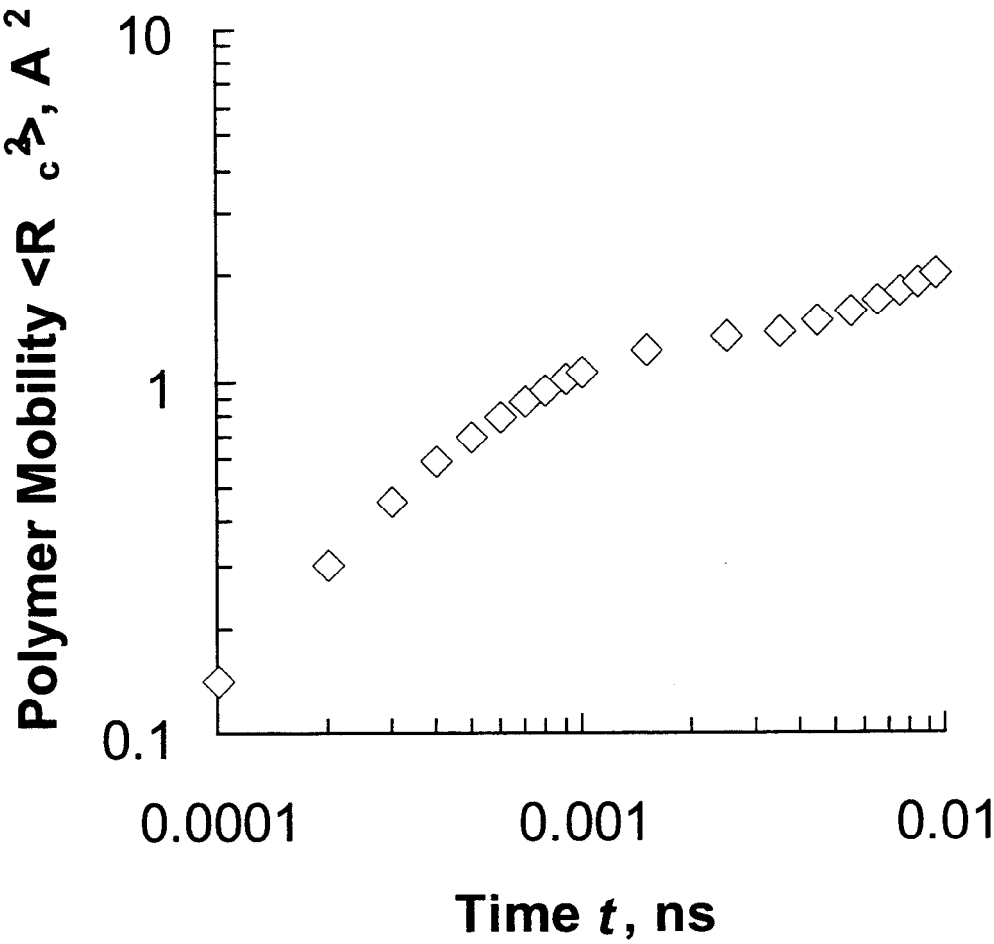

Figure 5.4: Plot of mean square displacement versus time for $-CH_2-$ groups in EPDM, obtained from a molecular dynamics simulation.

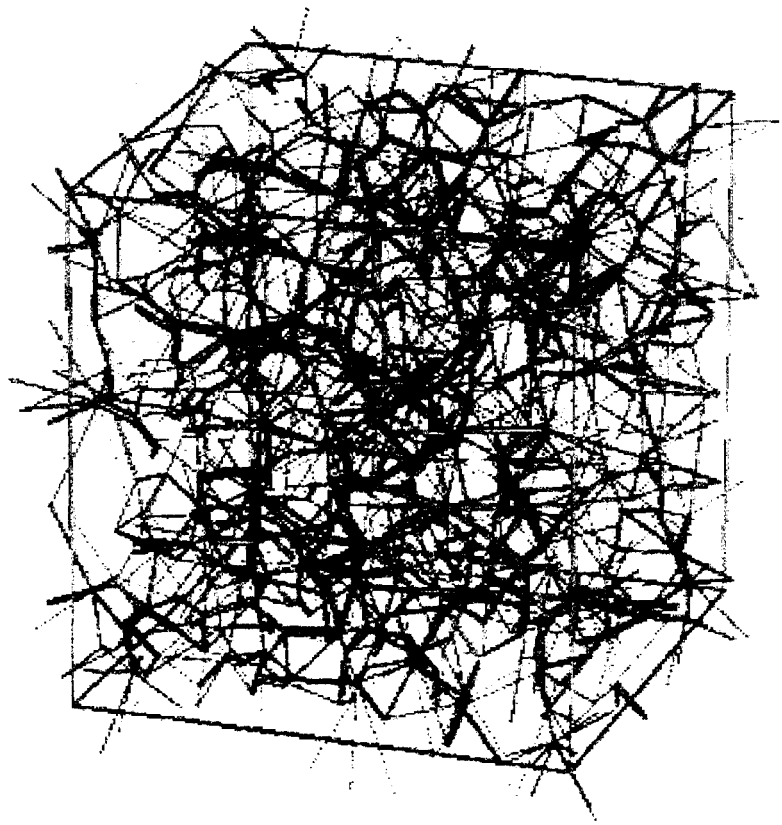

Figure 5.5: Visualization of the dividing surfaces obtained using cavity analysis for oxygen in a 60 x 60 x 60 sample of EPDM. The polymer motion was represented using the isotropic elastic approximation, with $\langle \Delta_\alpha^2 \rangle^{1/2} = 1.2$. Dividing surfaces are drawn as cylinders joining the centers of adjacent cavities. The radius of each cylinder is scaled proportionally with the logarithm of the configurational integral for the dividing surface, and so gives a measure of the jump rate for that dividing surface. The cavities themselves are not drawn explicitly. The dividing surfaces form a strongly percolated network.

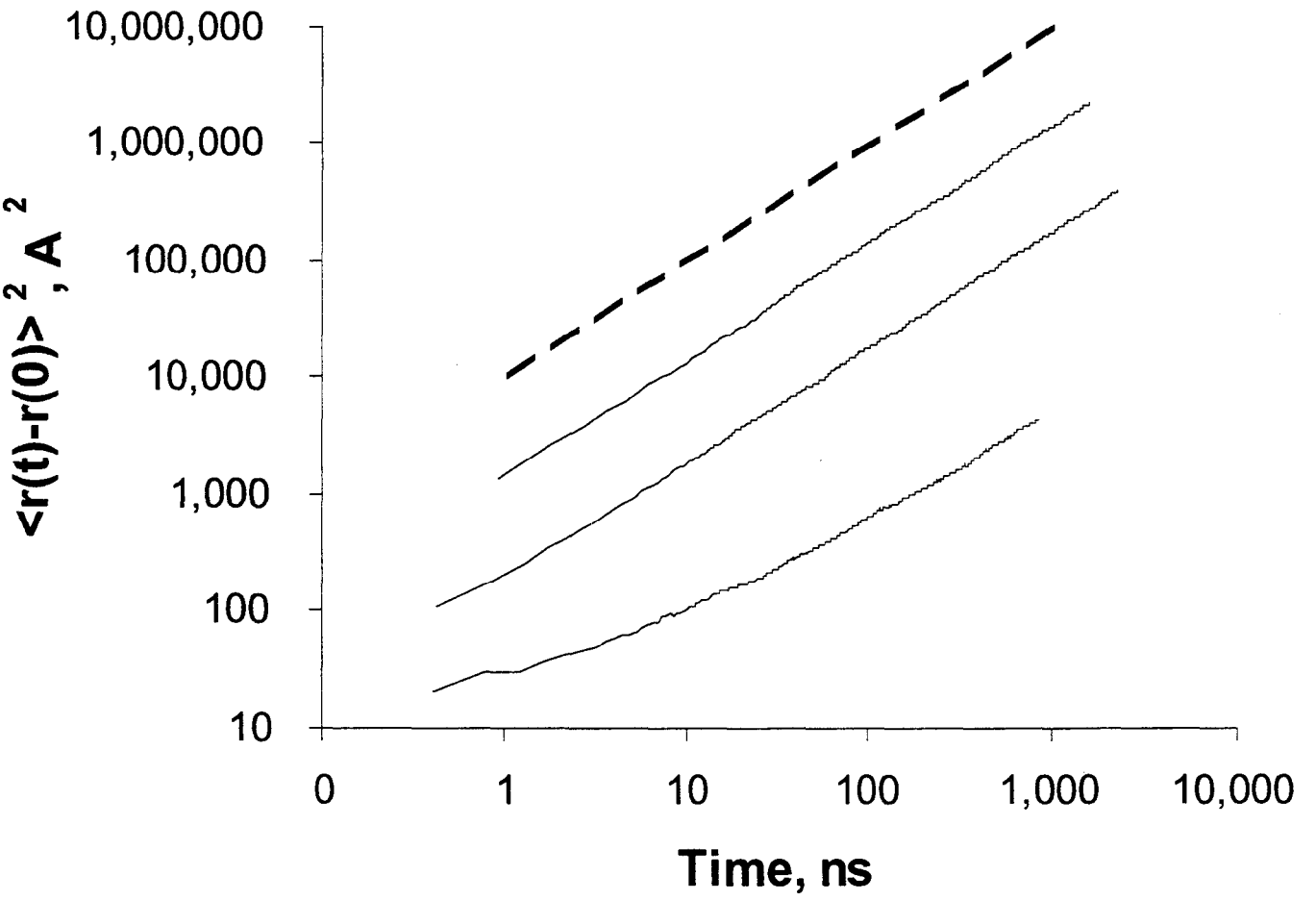

Figure 5.6: Plot of mean square displacement of oxygen molecules in EPDM versus time obtained by kinetic Monte Carlo simulation. The three curves are for $\langle \Delta_\alpha^2 \rangle^{1/2} = 0.6$, 0.9 and 1.2 , going from bottom to top. The thick dashed line serves only to illustrate the expected asymptotic linear behavior.

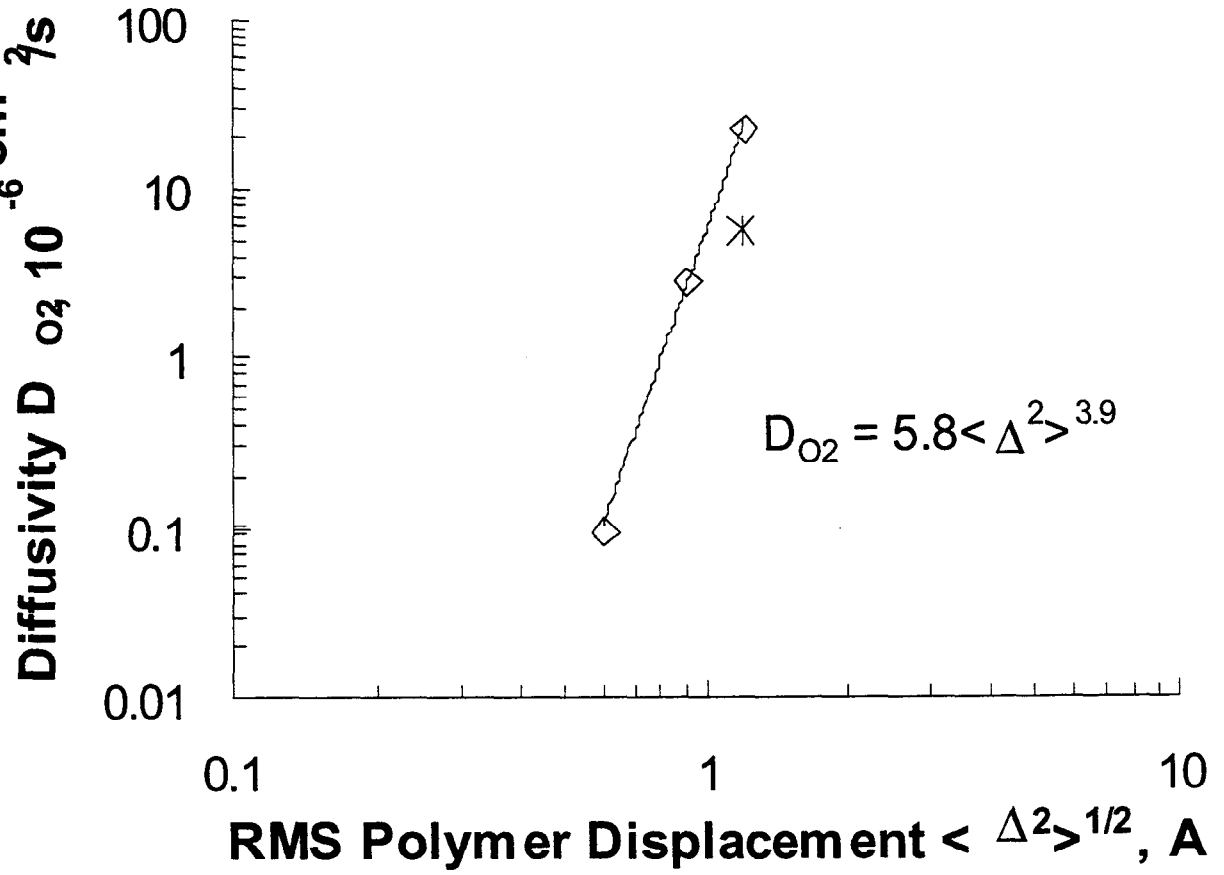

Figure 5.7: Plot of oxygen diffusion coefficient in EPDM versus RMS polymer displacement. The diamonds are from the kinetic Monte Carto simulations. The star is from molecular dynamics. The straight line is a power law fit to the kinetic Monte Carlo data.

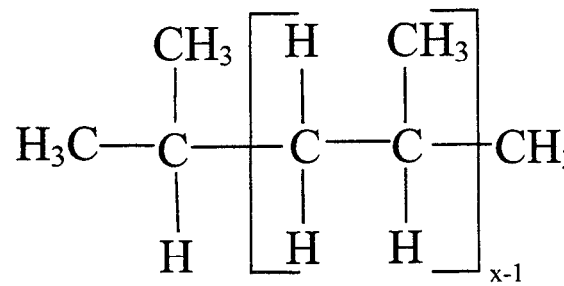

Bond lengths ( )	
C-C	1.53
C-H	1.10
C-CH_3	1.53

Bond angle supplements (degrees)		
intradyad C-C-C	66.0	
interdyad C-C-C	68.0	
intradyad C-C-H	71.0	
interdyad C-C-CH_3		68.0
interdyad C-C-H	73.2	

Figure 5.8.

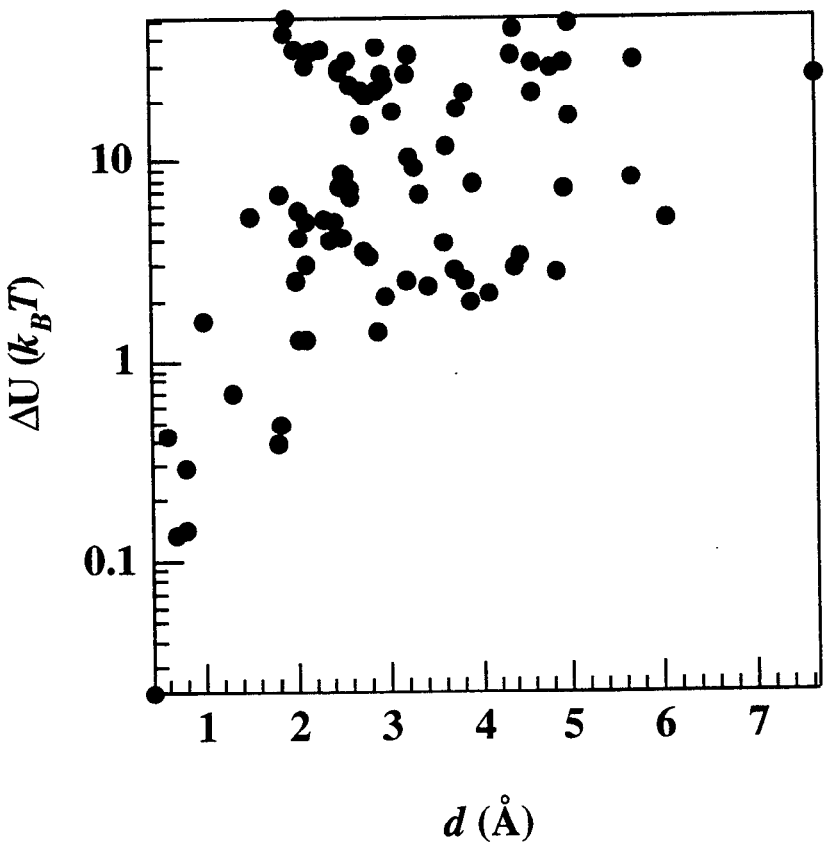

Figure 5.9a.

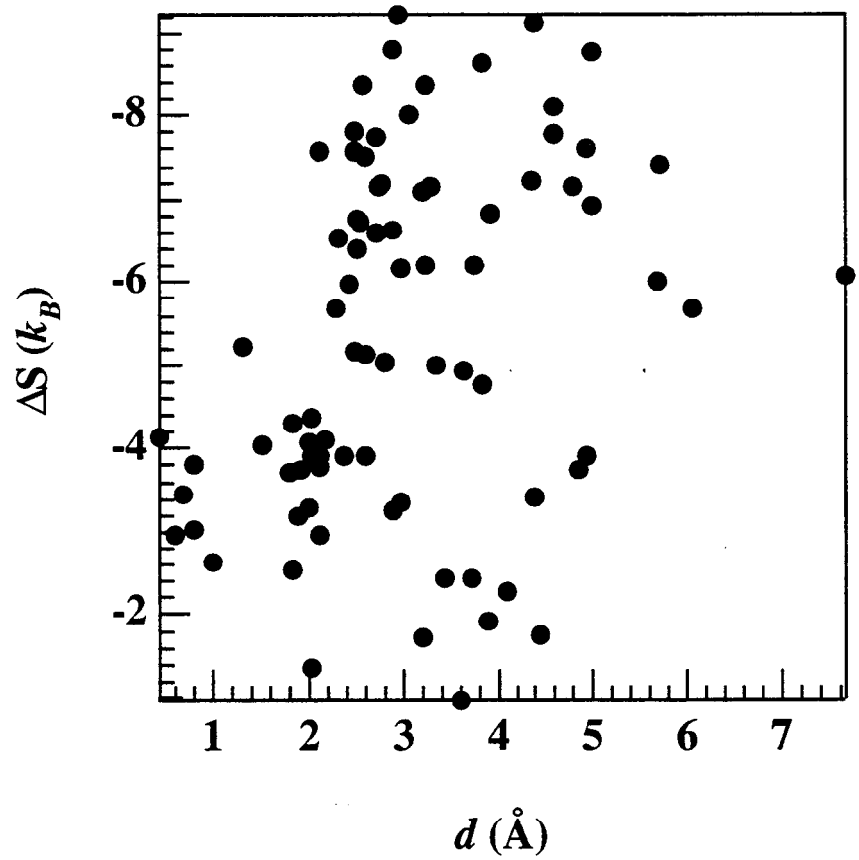

Figure 5.9b.

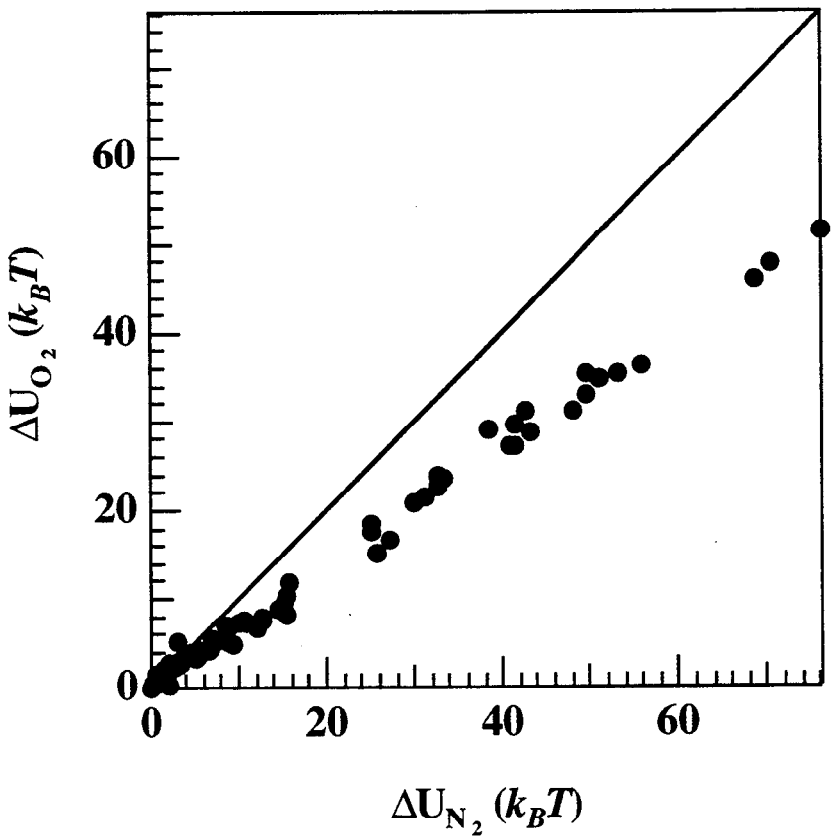

Figure 5.10a.

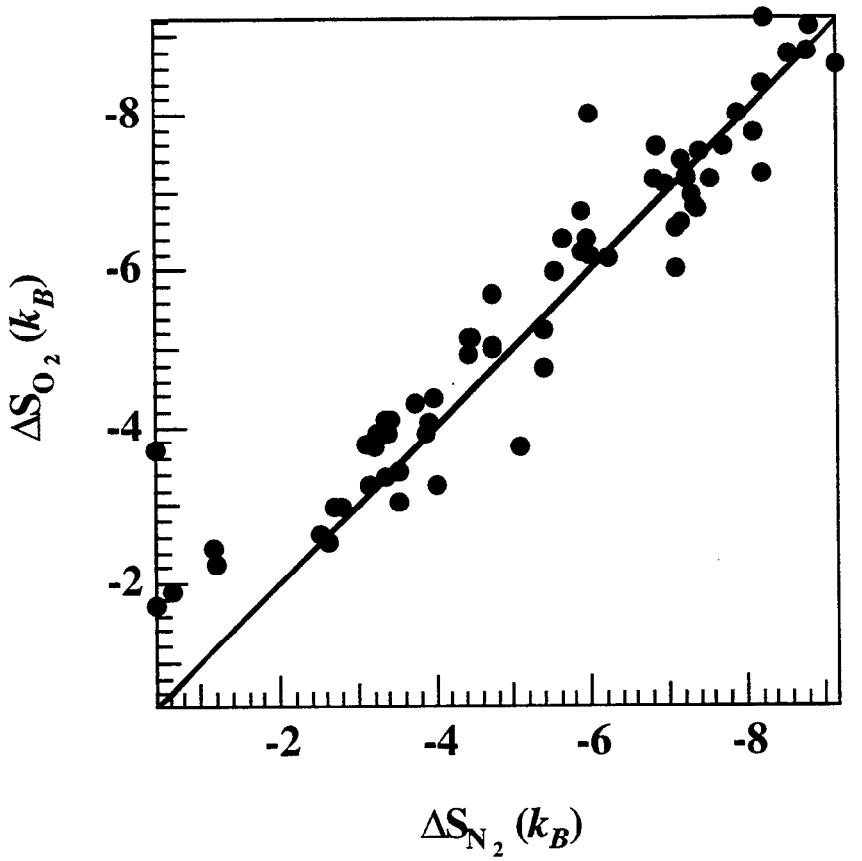

Figure 5.10b.

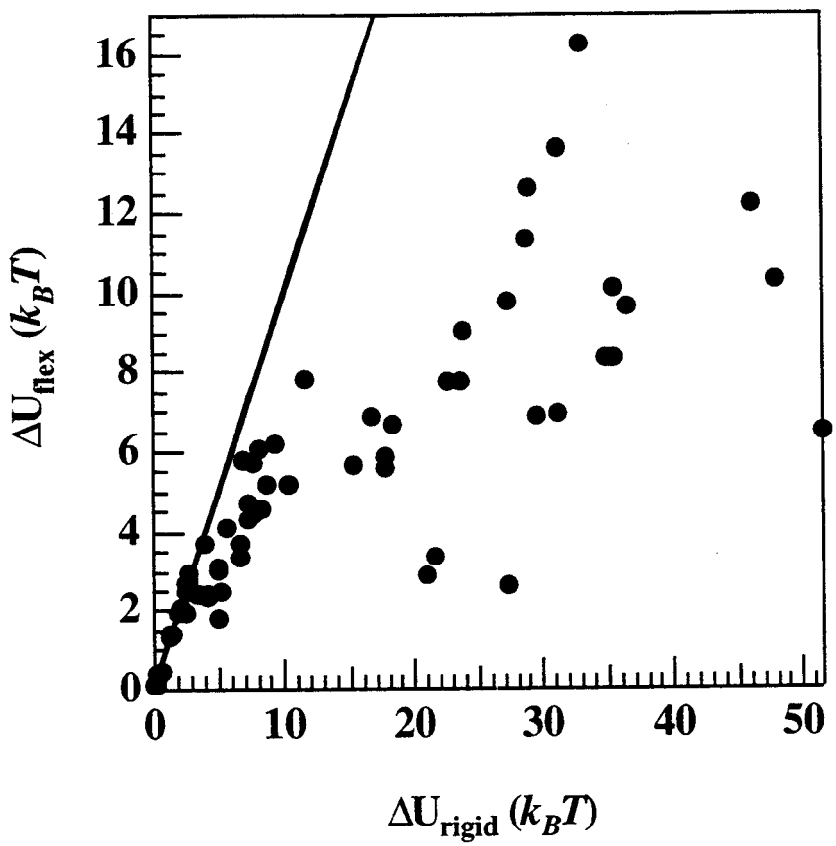
16
14
12
10
8
6
4
2
0
0
10
20
30
40
50
ΔU_{flex} (k_BT)
ΔU_{rigid} (k_BT)

Figure 5.11a.

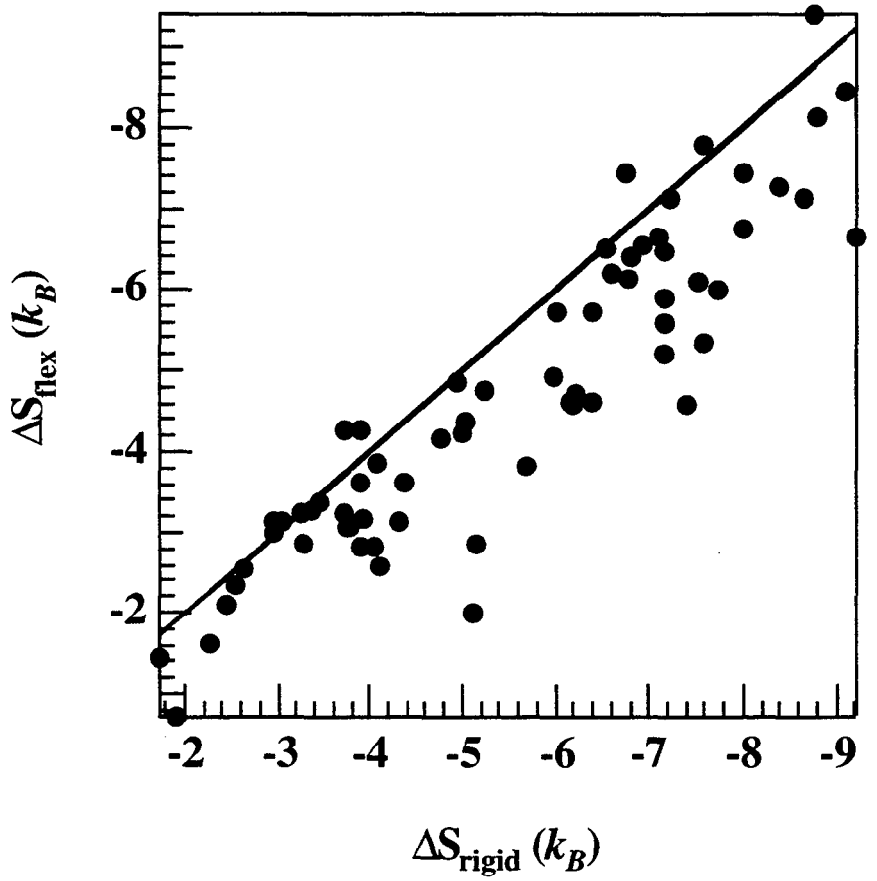

Figure 5.11b.

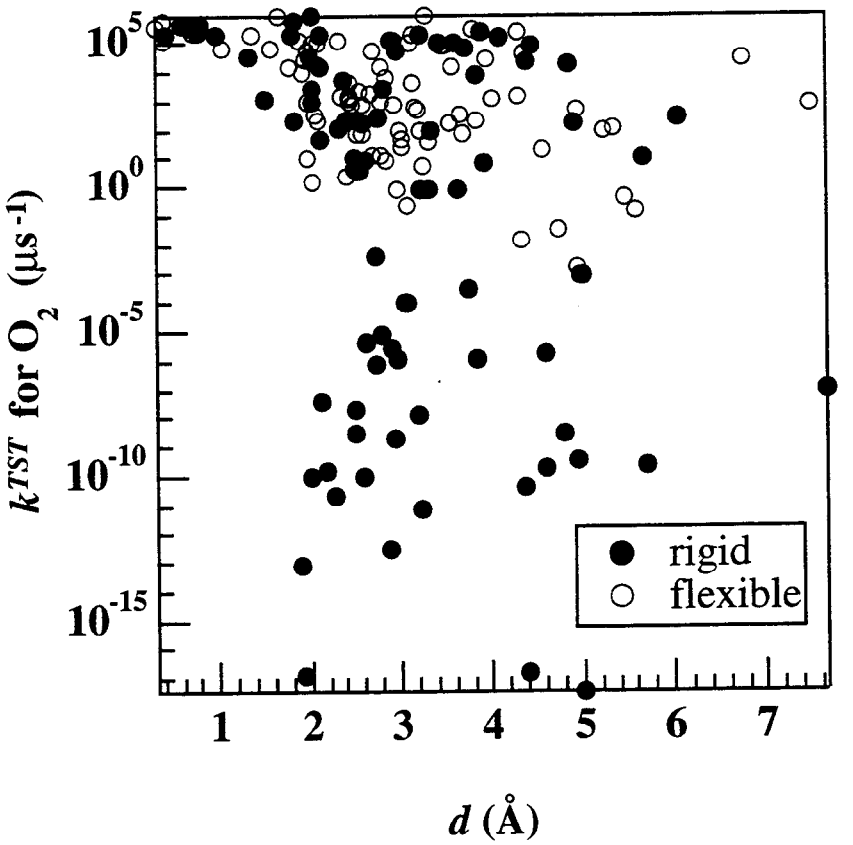
10^{5}
10^{0}
10^{-5}
10^{-10}
10^{-15}
k^{TST} for O_2 (μs^{-1})
rigid
flexible
1
2
3
4
5
6
7
d (Å)

Figure 5.12a.

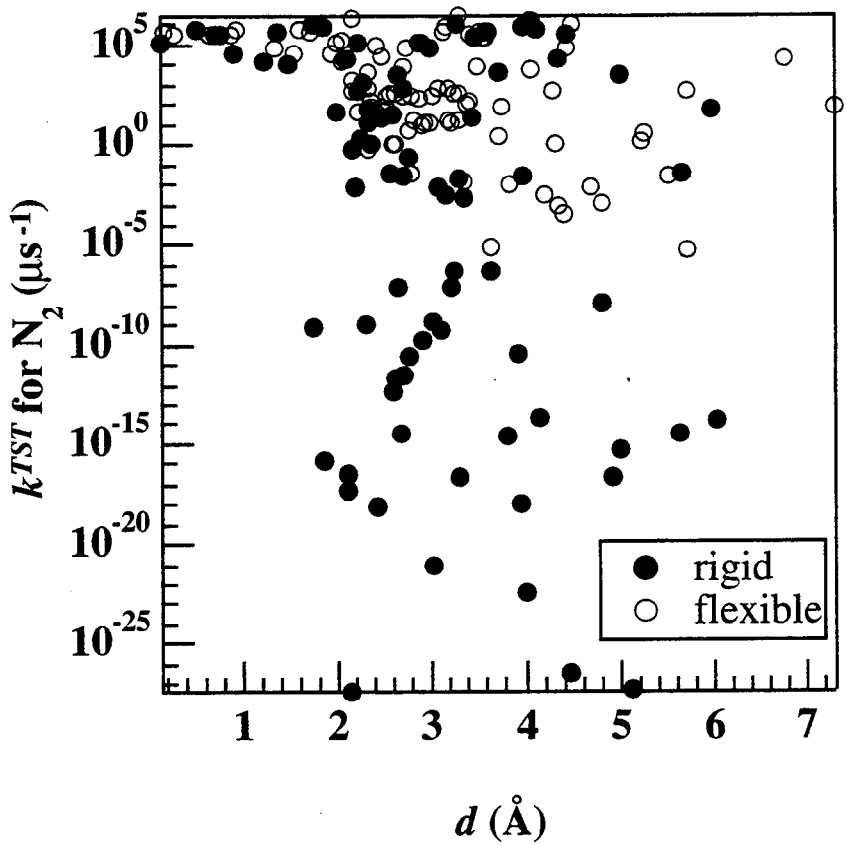
10^{5}
10^{0}
10^{-5}
10^{-10}
10^{-15}
10^{-20}
10^{-25}
k^{TST} for N_2 (μs^{-1})
1
2
3
4
5
6
7
d (Å)
rigid
flexible

Figure 5.12b.

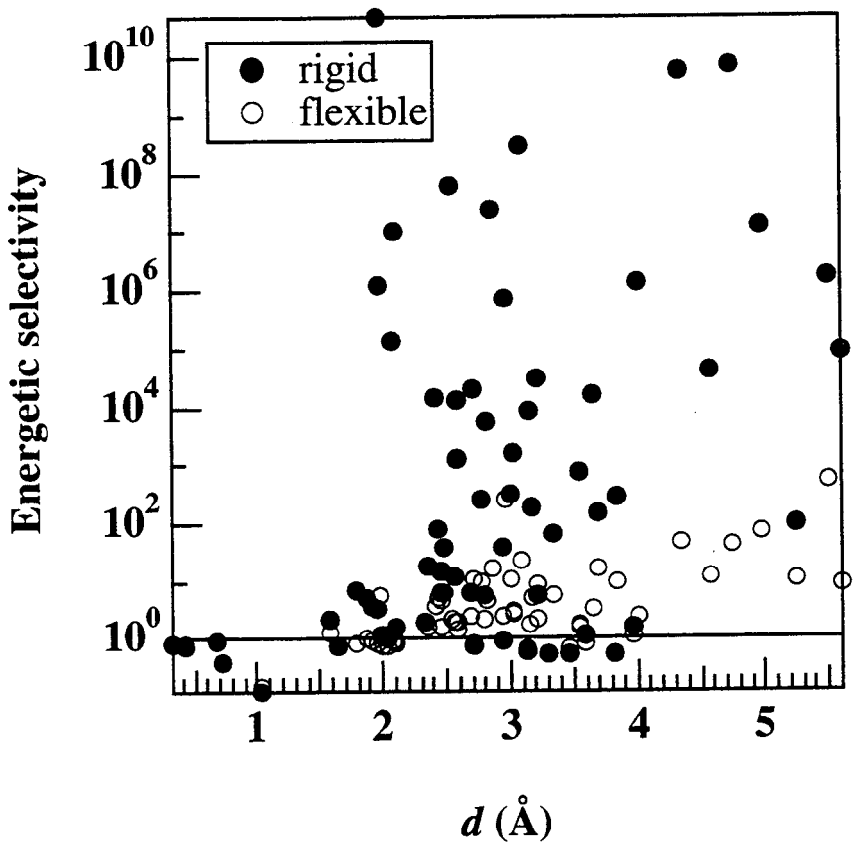
rigid
flexible
Energetic selectivity
10^{10}
10^{8}
10^{6}
10^{4}
10^{2}
10^{0}
1
2
3
4
5
d (Å)

Figure 5.13a.

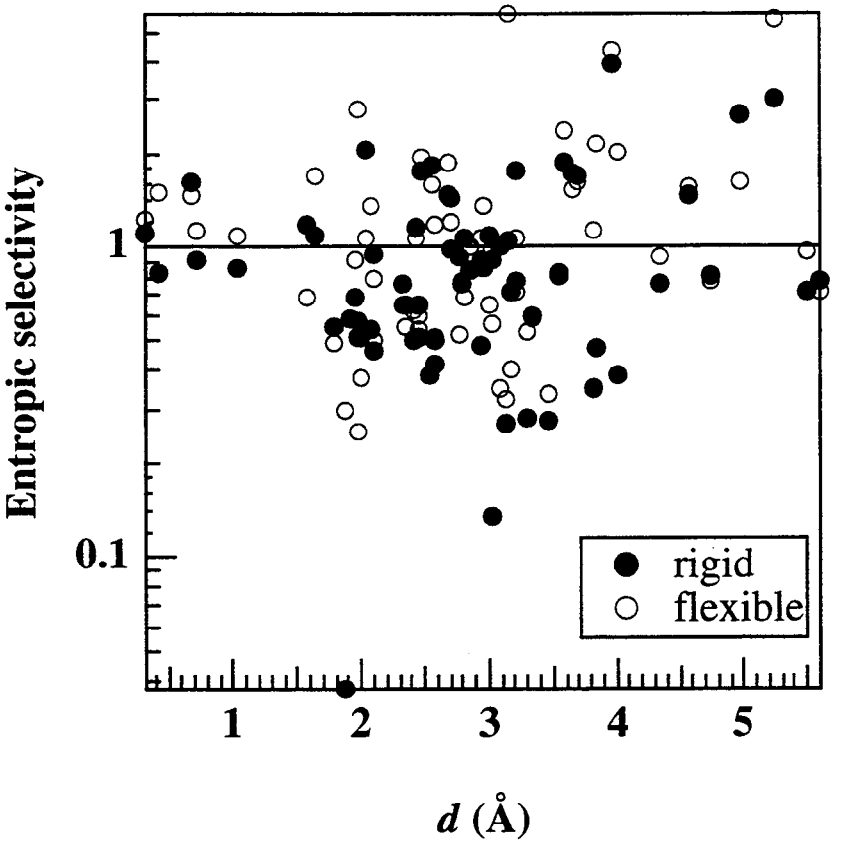

Figure 5.13b.

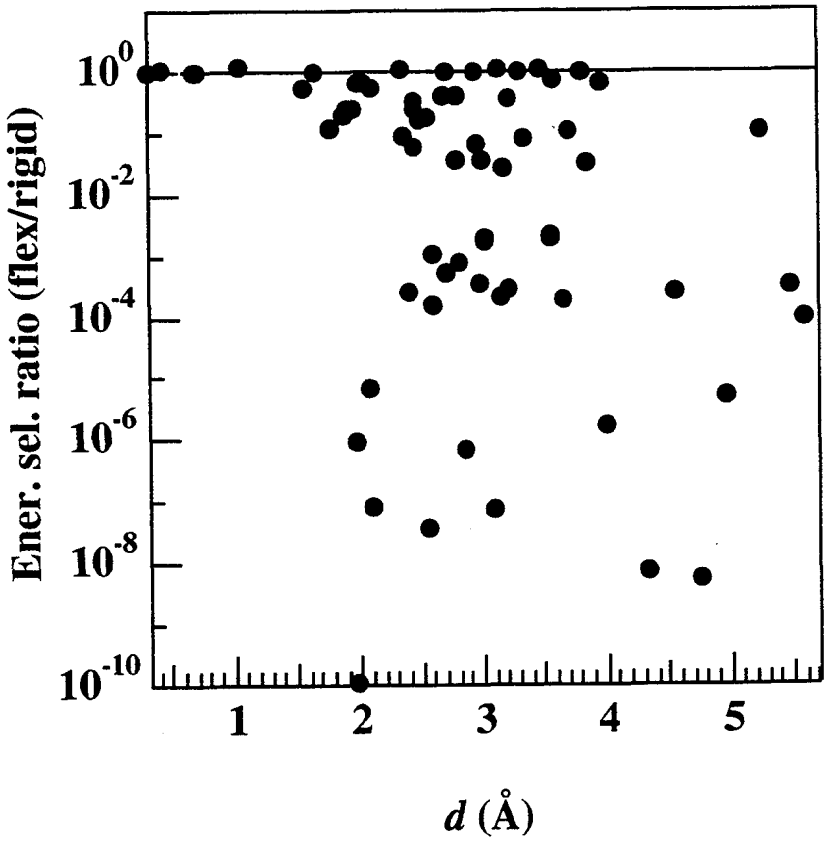

Figure 5.14a.

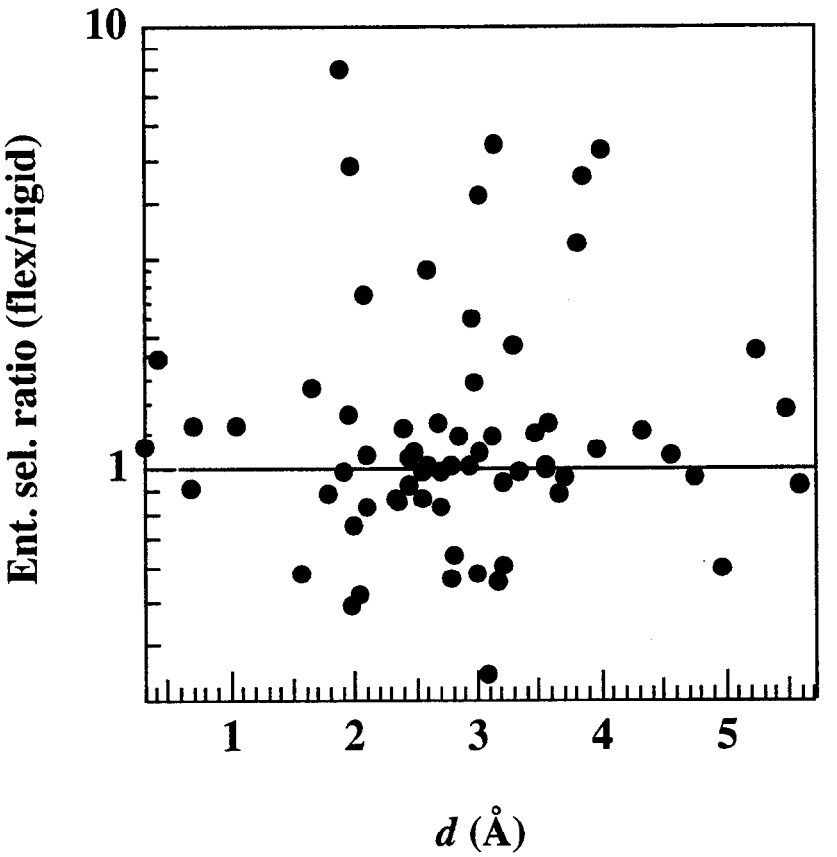

Figure 5.14b.

Chapter 5 REFERENCES

(1) Kesting, R. E.; Fritzsche, A. K. *Polymeric Gas Separation Membranes*; John Wiley & Sons, Inc.: New York, 1993.

(2) Koros, W. J.; Fleming, G. K. *J. Membrane Sci.* **1993**, *83*, 1-80.

(3) Stern, S. A. *J. Membrane Sci.* **1994**, *94*, 1-65.

(4) Robeson, L. M. *J. Membrane Sci.* **1991**, *62*, 165-185.

(5) Singh, A.; Koros, W. J. *Ind. Eng. Chem. Rès.* **1996**, *35*, 1231-1234.

(6) Zimmerman, C. M.; Koros, W. J. *Macromolecules* **1999**, *32*, 3341-3346.

(7) Muller-Plathe, F. *Acta Polymer* **1994**, *45*, 259-293.

(8) Gusev, A. A.; Arizzi, S.; Suter, U. W.; Moll, D. J. *J. Chem. Phys.* **1993**, *99*, 2221-2227.

(9) Gusev, A. A.; Suter, U. W. *J. Chem. Phys.* **1993**, *99*, 2228-2234.

(10) Gusev, A. A.; Muller-Plathe, F.; van Gunsteren, W. F.; Suter, U. W. *Adv. Polym. Sci.* **1994**, *116*, 207-247.

(11) Greenfield, M. L.; Theodorou, D. N. *Mol. Sim.* **1997**, *19*, 329-361.

(12) Greenfield, M. L.; Theodorou, D. N. *Macromolecules* **1998**, *31*, 7068-7090.

(13) Chandler, D. *J. Chem. Phys.* **1978**, *68*, 2959-2970.

(14) Voter, A. F.; Doll, J. D. *J. Chem. Phys.* **1985**, *82*, 80-92.

(15) Berne, B. J.; Borkovec, M.; Straub, J. E. *J. Phys. Chem.* **1988**, *92*, 3711-3725.

(16) Hill, T. L. *An Introduction to Statistical Thermodynamics*; Dover: New York, 1986.

(17) Snurr, R. Q.; Bell, A. T.; Theodorou, D. N. *J. Phys. Chem.* **1994**, *98*, 5111-5119.

(18) Takeuchi, H. *J. Chem. Phys.* **1990**, *93*, 2062-2067.

(19) Vineyard, G. H. *J. Phys. Chem. Solids* **1957**, *3*, 121-127.

(20) Theodorou, D. N.; Suter, U. W. *Macromolecules* **1985**, *18*, 1467-1478.

(21) van Gunsteren, W. F.; Karplus, M. *Macromolecules* **1982**, *15*, 1528-1544.

(22) MSI. Cerius2 User Guide; March 1997 ed.; Molecular Simulations Inc.: San Diego, 1997.

(23) Flory, P. J. *Statistical Mechanics of Chain Molecules*; Wiley: New York, 1969.

(24) Goldstein, H. *Classical Mechanics*; Addison-Wesley: Reading, 1950.

(25) Byrd, R. H.; Lu, P.; Nocedal, J.; Zhu, C. *SIAM J. Scientific Comput.* **1995**, *16*, 1190-1208.

(26) Allen, M. P.; Tildesley, D. J. *Computer Simulation of Liquids*; Clarendon Press: Oxford, 1987.

(27) Arizzi, S.; Mott, P. H.; Suter, U. W. *J. Polym. Sci. Polym. Phys. Ed.* **1992**, *30*, 415-426.

(28) Greenfield, M. L.; Theodorou, D. N. *Macromolecules* **1993**, *26*, 5461-5472.

(29) Misra, S.; Mattice, W. L. *Macromolecules* **1993**, *26*, 7274-7281.

(30) Gusev, A. A.; Suter, U. W. *Phys. Rev. A* **1991**, *43*, 6488-6494.

(31) June, R. L.; Bell, A. T.; Theodorou, D. N. *J. Phys. Chem.* **1991**, *95*, 8866-8878.

(32) Cerjan, C. J.; Miller, W. H. *J. Chem. Phys.* **1981**, *75*, 2800-2806.

(33) Baker, J. *J. Comput. Chem.* **1986**, *7*, 385-395.

(34) Wales, D. J. *Mol. Phys.* **1991**, *74*, 1-25.

(35) Wales, D. J. *J. Chem. Phys.* **1994**, *101*, 3750-3762.

(36) Fukui, K. *Acc. Chem. Res.* **1981**, *14*, 363-368.

(37) Banerjee, A.; Adams, N. P. *Int. J. Quantum Chem.* **1992**, *43*, 855-871.

(38) Greenfield, M. L. Molecular Modeling of Dilute Penetrant Gas Diffusion in a Glassy Polymer using Multidimensional Transition-State Theory. Ph.D. Thesis, University of California at Berkeley, 1996.

(39) Rallabandi, P. S.; Ford, D. M. *AIChE Journal* **2000**, *46*, 99-109.

(40) Voter, A. F. *J. Chem. Phys.* **1985**, *82*, 1890-1899.

(41) Karger, J.; Ruthven, D. M. *Diffusion in Zeolites and Other Microporous Solids*; John Wiley & Sons, Inc.: New York, 1992.

(42) Shantarovich, V. P.; Azamatova, Z. K.; Novikov, Y. A.; Yampolskii, Y. P. *Macromolecules* **1998**, *31*, 3969-3966.

(43) Yu, Z.; McGervey, J. D.; Jamieson, A. M.; Simha, R. *Macromolecules* **1995**, *28*, 6268-6272.

(44) Shah, V. M.; Stern, S. A.; Ludovice, P. J. *Macromolecules* **1989**, *22*, 4660-4662.

(45) Rigby, D.; Roe, R. J. *Macromolecules* **1990**, *23*, 5312-5319.

(46) Trohalaki, S.; DeBolt, L. C.; Mark, J. E.; Frisch, H. L. *Macromolecules* **1990**, *23*, 813-816.

(47) Boyd, R. H.; Pant, P. V. K. *Macromolecules* **1991**, *24*, 6325-6331.

(48) Bharadwaj, R. K.; Boyd, R. H. *Polymer* **1999**, *40*, 4229-4236.

(49) Zhang, X.-S. . Ph.D. Dissertation, Academia Sinica at Beijing, 1987.

(50) Mi, Y.; Stern, S. A. *J. Polym. Sci., Part B: Polym. Phys.* **1991**, *29*, 389-393.

(51) Fischer, J.; Lago, S. *J. Chem. Phys.* **1983**, *78*, 5750-5758.

Chapter 6

Multi-Particle Activated Transport of Small Molecules in Ordered Nanoporous Materials

6.1. INTRODUCTION

A major challenge for TST is the prediction of the concentration dependence of diffusion rates in nanoporous materials. This is generally a difficult problem because the TST partition functions increase in dimensionality with the number of particles involved in a hopping event, and just defining the limits on the integrals may quickly become unfeasible.[3] The development of practical and accurate approximations is therefore necessary, but the type of approximation that will be adequate depends strongly on the nature of the particular system being modeled.[3-6] A recent example is the use of mean-field corrections to treat many-body effects in benzene-NaX systems, where the sorbate-sorbate interactions are perturbations on the very strong sorbate-host interactions.[2]

In a recent paper, (also funded under this LDRD, but due to space-limitations we have not included it in this report; instead we summarize the results below) Tunca and Ford[1] have addressed a different situation, where adsorption is not highly localized and the sorbate-sorbate interactions are comparable in strength to the sorbate-host interactions. Such a situation can be realized within the cages of highly siliceous zeolites or within the nanopores of carbon materials. Tunca and Ford modeled the particular case of methane and xenon escaping from a loaded α cage in aluminum-free ZK4 into empty neighboring cages. They developed a physically reasonable "low-dimensional approximation" to make the many-dimensional TST partition functions tractable, and they solved the integrals with a method introduced by Kaminsky[7] that employs Widom[8] test insertions. Although the nested approach of Kaminsky avoided problems associated with the inefficiencies of inserting many particles, the single-particle Widom insertions still suffered from statistical inefficiencies at higher loadings.

Recently, expanded ensemble methods (EEMs) have been developed and used successfully to calculate the chemical potentials of dense fluids and polymers.[9-17] The basic idea is to have one particle in the system that couples to the rest of the particles in

incremental stages, with sampling of these stages included in the Monte Carlo walk. Although the intermediate configurations of the test particle do not contribute directly to the statistics, they provide a smooth pathway between a full particle and a ghost particle. Furthermore, transitions along this pathway are greatly enhanced with the use of bias functions that equalize the occupation probabilities of the stages. Improvements of many orders of magnitude in statistical quality can be achieved with EEM in chemical potential calculations for dense and complex fluids.

There are two main goals of this work. One goal is to extend our study of escape rates to cases where neighboring cages are occupied; this is of course necessary for the development of realistic stochastic models of diffusion. We will meet this goal by calculating the rate of adsorbate hopping between two adjacent cages, each at an arbitrary loading. Another goal is to incorporate an EEM into Kaminsky's scheme for evaluating multidimensional partition functions of fluids in pores. To our knowledge, this work is the first to use an EEM to evaluate such partition functions. In Sec. 6.2, we present the necessary background and develop our extended theory. In Sec. 6.3, the model systems and calculational details are described. The results are presented and discussed in Sec. 6.4. Conclusions are outlined in Sec. 6.5.

6.2. THEORY

6.2.1. Background

Vineyard[4] has derived the following classical TST rate expression for a system with F degrees of freedom. For two adjacent local potential energy minima, denoted by i and j, the average transition rate from i to j (in units of inverse time) is given by

$$\Gamma_{i\to j}^{\mathrm{TST}} = (2\pi\beta)^{-1/2} \frac{\int_S dy_1 \ldots dy_F \, e^{-\beta U}}{\int_V dy_1 \ldots dy_F \, e^{-\beta U}} \tag{6.1}$$

where $\beta=1/k_BT$ with T the temperature and k_B the Boltzmann constant, S is the hypersurface connecting minimum i with minimum j, V is the hypervolume associated with minimum i, y_k is the mass-weighted coordinate for the degree of freedom k, and U is the potential energy of the system. The denominator of Eq. (6.1) is an F-dimensional integral with the system constrained to hypervolume V. The numerator of Eq. (6.1) is an (F-1)-dimensional integral

with the system constrained to the hypersurface S. For a single spherical molecule in a rigid zeolite matrix, there are three degrees of freedom, so the numerator will be two-dimensional and the denominator will be three-dimensional.

6.2.2. Low-dimensional (LD) approximation

Equation (6.1) is rigorous, but not always useful in practice. As mentioned above, for large F it is difficult to even define the limits on the integrals, much less calculate them. Tunca and Ford[1] developed a useful approximate expression for the case of spherical molecules escaping from a loaded cage to neighboring empty cages. Here we extend the derivation of that "low-dimensional" (LD) approximation to include arbitrary loading in the neighboring cages. More specifically, we consider the rate of transition of molecules from one cage (A) to a single neighboring cage (B), as a function of loading in both A and B. As will be discussed later, we believe that such a "pairwise" consideration of cages is justified.

First, we assume that the (three-dimensional) volume associated with each cage, and the (two-dimensional) surface which joins the two cages, are well-defined. This information may be obtained through geometric considerations, or through calculations using a single spherical adsorbate probe molecule.[1,18] Next, we consider a system with N spherical molecules distributed between the two cages A and B. In particular, we consider the state where N_A molecules are in cage A, and $N_B = N - N_A$ molecules are in the neighboring cage B. Within the LD approximation, the transition rate from this state to the state where one molecule has moved from A to B (i.e., the state where $N_A - 1$ molecules are in A and $N_B + 1$ molecules are in B) is given as

$$(\Gamma^{\mathrm{TST}}_{A\to B})_{\mathrm{LD}} = (2\pi m\beta)^{-1/2}\,\frac{N_A\int_{S_{AB}}\int_{V_A}\cdots\int_{V_A}\int_{V_B}\cdots\int_{V_B} d\mathbf{r}_{1A}^{\{2\}}d\mathbf{r}_{2A}^{\{3\}}\ldots d\mathbf{r}_{N_AA}^{\{3\}}d\mathbf{r}_{1B}^{\{3\}}\ldots d\mathbf{r}_{N_BB}^{\{3\}}\,e^{-\beta U}}{\int_{V_A}\cdots\int_{V_A}\int_{V_B}\cdots\int_{V_B} d\mathbf{r}_{1A}^{\{3\}}\ldots d\mathbf{r}_{N_AA}^{\{3\}}d\mathbf{r}_{1B}^{\{3\}}\ldots d\mathbf{r}_{N_BB}^{\{3\}}\,e^{-\beta U}} \tag{6.2}$$

In Eq. (6.2), m is the mass of a molecule, S_{AB} is the two-dimensional surface joining the two cages, V_A is the three-dimensional volume of cage A, V_B is the three-dimensional volume of cage B, and $\mathbf{r}_{kK}$ is the position of the kth molecule in cage K. The notation $A \to B$ indicates that a molecule is leaving cage A and going to the surface S_{AB}. The superscripts on the integration variables give the dimensionality of the corresponding

integrals. The integral in the numerator is over the positions of all N adsorbate molecules, with molecule 1 from cage A constrained to the surface S_{AB}, and the rest of the molecules constrained to their respective cage volumes. The integral in the denominator is also over the positions of all N adsorbate molecules, with all of them constrained to their respective cage volumes. Thus, in writing Eq. (6.2), we have approximated the true ($3N$-1) dimensional hypersurface by the hypersurface on which one of the molecules is confined to the dividing surface S_{AB}, and the rest of the molecules are confined to their cage volume. Likewise, we have approximated the true $3N$-dimensional hypervolume by the hypervolume in which all of the molecules are confined to their cage volume. Note that for the case of $N_B = 0$, Eq. (6.2) reduces to Eq. (2) from Ref. 1.

In writing Eq. (6.2) from Eq. (6.1), we have assumed that the intra-cage dynamics are always fast compared to inter-cage hopping events and that the potential energy barriers at the cage windows are not much perturbed by the presence of multiple molecules. Thus, the LD approximation works best for cages that are large enough to allow multiple occupancy, connected to each other by very narrow necks, and energetically "uncorrugated."[1]

Recognizing that the numerator and denominator of Eq. (6.2) represent configurational partition functions, we can re-write the equation in more convenient notation as

$$(\Gamma^{\mathrm{TST}}_{A\to B})_{\mathrm{LD}} \equiv (2\pi m\beta)^{-1/2} N_A \frac{Z_S(N_A,N_B)}{Z_V(N_A,N_B)} \tag{6.3}$$

Although the LD approximation makes the problem tractable in terms of providing well-defined partition function integrals, those integrals are still challenging to evaluate. We have previously employed[1] a method introduced by Kaminsky,[7] in which the partition functions are built up in a sequential fashion using single-particle Widom insertions. For example, the ratio of the volume integrals involving N_A and N_A-1 adsorbates in cage A, at constant loading of cage B, can be written as

$$\frac{Z_V(N_A,N_B)}{Z_V(N_A-1,N_B)} = V_A\left\langle e^{-\beta u_t}\right\rangle_{N_A-1,N_B} \tag{6.4}$$

where u_t is the potential energy of a single inserted test molecule and the brackets represent an average over a canonical Monte Carlo (MC) simulation. In this example, the MC

simulation would consist of N_A-1 molecules sampling cage A and N_B molecules sampling cage B, and the Widom test insertions would be performed in cage A. An equation analogous to Eq. (6.4) can also be written for the ratio of area integrals. Given that the $N_A = 1$ integral can be determined accurately through crude MC (or some other technique), Eq. (6.4) provides an efficient step-wise route to all integrals with $N_A \geq 2$.

Although this method was used in our previous work (for $N_B = 0$), it began to suffer from statistical inefficiencies at higher loadings in A, as reflected in the error bars of Figs. 2 and 3 of Ref. 1. This is a well-known phenomenon when applying Widom's technique to very dense fluids.[15] In the present work, we use a more efficient technique, expanded ensembles, to evaluate the partition function ratios.

6.2.3. Expanded ensemble methods (EEMs)

EEMs improve the efficiency with which free energy differences (i.e., partition function ratios) are determined.[9-17] The basic idea is to employ intermediate states which connect the two end states of interest, and sample these states throughout a single simulation. The intermediate states themselves are generally not of interest, but they can greatly facilitate sampling between the two end points, especially when bias functions are employed.

For example, to determine the free energy difference between two canonical systems that differ by exactly one molecule (as in Eq. (6.4) above), one begins by writing the partition function for an expanded ensemble as[12,13,17]

$$\Omega(\lambda) = \sum_{n=0}^{M} \exp(\eta_n) Z(\lambda_n) \tag{6.5}$$

where λ is a parameter that represents the degree of coupling of one molecule to the rest of the system, n is an index over the possible λ states (with M the total number of such states), η is a bias function, and $Z(\lambda)$ is the configurational canonical partition function of the system in a particular λ state. The number of intermediate λ states and their characteristics can be chosen in different ways, but the two end points, n=0 and n=M, should correspond to fully decoupled and coupled states.

A MC walk is then performed over the degrees of freedom of the expanded ensemble. This involves two types of moves. One is the usual displacement of molecules at a fixed

value of n, and the other is the change of n at fixed coordinates of the molecules. The transition probability for either type of move is given by the Metropolis criterion for the expanded ensemble,[10] $\min\{1,\exp[\Delta(U+\eta)]\}$.

The probability of visiting a particular state λ_n during the MC walk is

$$p_n = \frac{\exp(\eta_n)Z(\lambda_n)}{\Omega} \tag{6.6}$$

so that the ratio of partition functions for two arbitrary states i and j is given by

$$\frac{Z(\lambda_i)}{Z(\lambda_j)} = \frac{p_i \exp(-\eta_i)}{p_j \exp(-\eta_j)} \tag{6.7}$$

The partition function ratio for two systems that differ by one molecule can then be calculated by simply counting the number of times that each of the two end states (n=0 and n=M) is sampled during the MC walk. To gain the maximum benefit from the EEM, the bias factors should be optimized. Certain λ states will be naturally less favored than others, and such disparities generally cause bottlenecks in sampling that result in poor connection between the two end points. The goal is to select values of the η_n such that all λ_n states have roughly equal probabilities of occupation during the walk; the states are then smoothly and equally sampled, and statistical efficiency is high. Corrections for the biasing are present in Eq. (6.7).

Applying the EEM concept to our example of two systems which differ by one molecule in cage A at constant loading of cage B (Sec. 6.2.2), we find that the ratio of volume integrals can be written as

$$\frac{Z_V(N_A,N_B)}{Z_V(N_A-1,N_B)} = V_A \frac{p_M \exp(-\eta_M)}{p_0 \exp(-\eta_0)} \tag{6.8}$$

Here, we would perform an extended ensemble MC simulation with N_A-1 full molecules sampling cage A and N_B full molecules sampling cage B; in addition, one special "coupling" molecule would sample different states and positions within cage A. The ratio of probabilities of the fully coupled (M) and fully decoupled (0) states of this molecule, corrected by the applied bias factors, yields the partition function ratio. As in Eq. (6.4), the factor of V_A in Eq. (6.8) represents the ideal contribution of the N_A-th molecule to the configurational integral; even if this molecule has no interaction with the others, it

contributes one factor of volume to the partition function. An equation analogous to Eq. (6.8) can be written for the ratio of area integrals. For that calculation, one molecule would be confined to the surface between cages, and the coupling molecule would still be placed in the volume of cage *A*.

6.3. MODEL SYSTEMS

6.3.1. Zeolite and adsorbate models

The same model zeolite employed previously,[1] pure silica (cation-free) ZK4, was used here. Spherical methane was the model adsorbate. For this model system, we previously concluded that the rate-limiting step in methane diffusion is the hop between two neighboring α cages through the 8-membered oxygen ring. Using an atomic-level model of the ZK4 and a single methane probe, we mapped out the relevant volume of an α cage and the surface joining two neighboring cages, using the voxel method of June *et al.*[18] Those volume and surface data will be used here; the reader is referred to Ref. 1 for details.

Our zeolite model consisted of a full unit cell of ZK4, which had eight α cages and an edge length of 24.6 Å. Two directly neighboring cages within this model, denoted as *A* and *B*, were used for the calculations. Periodic boundary conditions were employed when calculating the adsorbate-zeolite interactions. However, they were turned off for the adsorbate-adsorbate interactions, because we wanted to model a single, isolated pair of occupied cages.

One small difference between the present and previous results should be noted. In the previous work,[1] we presented transition rates from one α cage to any of the 6 empty neighboring cages. In this paper, we are considering only the jump to one specific neighboring cage, *B*. Therefore, the values for the transition rates to an empty *B* cage reported here are systematically lower (by a factor of 6) than the escape rates given in the previous paper.

6.3.2. Potentials

Since the silicon atoms are shielded by oxygen atoms in the zeolite framework, only the oxygen atoms were taken into account in the calculation of potential energy. The zeolite

lattice was assumed to be rigid. The methane molecules were taken as spherical. The 12-6 Lennard-Jones potential was used to calculate methane-methane and methane-oxygen interactions.

$$u_{ij}(r) = 4\varepsilon_{ij}\left[\left(\frac{\sigma_{ij}}{r}\right)^{12} - \left(\frac{\sigma_{ij}}{r}\right)^{6}\right], \quad r \le r_{cut}$$

$$= \qquad 0, \quad r \le r_{cut} \tag{6.9}$$

The potential parameters are listed in Table I. The cutoff was taken to be $r_{cut}=2.5\sigma_{ij}$.

6.3.3. Evaluation of integrals

The nested scheme indicated by Eq. (6.8) was used to evaluate the TST integrals, with the area and volume integrals determined separately. Loadings of up to 12 molecules/cage were considered in both A and B. For convenience, the area or volume integrals can be indexed as elements in a matrix, $Z(N_A,N_B)$. Since the A cage cannot be empty (there must be at least one molecule to make the transition) but the B cage can be empty, N_A ranges from 1 to 12 and N_B ranges from 0 to 12. Thus we have a 12x13 matrix for both the area and volume integrals. Due to the fact that the A and B cages are structurally equivalent, both matrices have a great deal of symmetry, which reduces the computational requirements.

For the volume integrals, the symmetry relationship is simple: $Z_V(N_A,N_B)$ is equal to $Z_V(N_B,N_A)$. The starting points for the nested scheme, $Z_V(1,0)$ and $Z_V(1,1)$, were calculated using crude MC integration. From these points, we explicitly calculated volume integrals for the rest of the columns $Z_V(N_A,0)$ and $Z_V(N_A,1)$ using Eq. (6.8). Due to symmetry, the row $Z_V(1,N_B)$ was then also known, from the column $Z_V(N_A,1)$. Next we generated the $Z_V(N_A,2)$ column with Eq. (6.8), starting from the known element $Z_V(1,2)$. The row $Z_V(2,N_B)$ was then also known by symmetry. We continued in this fashion, calculating parts of columns and generating corresponding symmetric parts of rows, until we obtained all the matrix elements. Thus, it was sufficient to explicitly calculate only those volume integrals on and below the matrix diagonal.

For the area integrals, the symmetry relationship is slightly more complex. The integral $Z_S(N_A,N_B)$ corresponds to having N_A-1 molecules in A, one molecule on the surface between A and B, and N_B molecules in B. The equivalent "mirror" conformation has N_B molecules in A, one molecule on the surface, and N_A-1 molecules in B, and is thus denoted by $Z_S(N_B+1,N_A-1)$. The area matrix was obtained in a similar way to that described above for the volume integrals, with a few small differences. Only one starting point, $Z_S(1,0)$, was required from crude MC integration. The remainder of the column $Z_S(N_A,0)$ was then calculated using Eq. (6.8); by symmetry, this yielded the row $Z_S(1,N_B)$ as well. The known $Z_S(1,1)$ was then used as the starting point for calculation of the column $Z_S(N_A,1)$ by Eq. (6.8). Calculation of column $Z_S(N_A,1)$ also yielded elements in the row $Z_S(2,N_B)$ by symmetry. Again, we continued in this fashion until the area matrix was complete. We note that for the area matrix, we needed to calculate integrals for N_A=13 (for N_B values from 0 to 11) to obtain the desired elements $Z_S(N_B+1,12)$. For the area matrix, it was sufficient to explicitly calculate only those elements below the matrix diagonal.

For the area integrals, one molecule was confined to the surface and the remaining ones were confined to their respective α cage volume. For the volume integrals, all of the penetrants were confined in their respective α cage volume. The "coupled particle" in the EEM was always constrained to the A cage. The constraint of a molecule to a volume (surface) was accomplished by rejecting MC moves that attempted to place this molecule outside that volume (surface). The corresponding rate constants were then calculated using Eq. (6.3).

The potential parameters for the intermediate states of the coupled methane particle were taken from Kaminsky's paper.[13]

$$\sigma^{(n)} = \sigma(n/M)^{1/4} \quad \text{for } 1 \le n \le (M-1)$$
$$\varepsilon^{(n)} = \varepsilon(n/M)^{1/3} \quad \text{for } 1 \le n \le (M-1) \tag{6.10}$$

The total number of states, M, was taken as 8. Lorentz-Berthelot mixing rules[19] were used for the interactions between full and intermediate methane.

The procedure given by Wilding and Müller[12] was employed to determine optimum values for the bias factors η_n. First, an estimate of the probability of each state was obtained,

using a short MC simulation of 100,000 steps with all bias factors set to zero. Those probabilities were plugged into the following equation to get an initial estimate of the bias factor for each n.

$$\eta_n' = \eta_n - \ln p(\lambda_n) \tag{6.11}$$

Another short MC simulation was then performed with the updated bias factor to obtain new probabilities. This procedure was repeated until every state had roughly equal probability of being visited. Usually two iterations were sufficient to accomplish this. Four different long runs (10^7 MC steps) with different starting states were then initiated to get final probabilities for n=0 and n=8. Those results were used to calculate the ratio of partition functions, using Eq. (8).

6.4. RESULTS AND DISCUSSION

Figure 6.1 shows the escape rate of methane from A to B as a function of N_A, for three values of N_B. The escape rate increases strongly with increasing N_A, covering three orders of magnitude. This increase in escape rate is due to the decrease of available free volume upon addition of adsorbate molecules in cage A. This entropic effect is apparently quite dominant over the attractive adsorbate-adsorbate interactions, which should tend to decrease the potential energy (and the escape rate) with increased loading. Although the rates are clearly not as sensitive to N_B as they are to N_A, an interesting non-monotonic trend is seen in Fig. 6.1, with the N_B=0 curve lying between the N_B=6 and N_B=12 curves.

Figure 6.2 provides more insight into the effects of loading in cage B. Initially, the escape rates increase slightly with N_B. This is due to the fact that the molecule on the surface is "stabilized" by attractive interactions with the molecules in cage B. However, as cage B becomes increasingly crowded, the surface molecule becomes "de-stabilized" by excluded volume interactions with those molecules. This leads to the decreases in escape rate seen at higher N_B values. This behavior explains the non-monotonic trend seen in Fig. 6.1 with varying N_B. Note that the standard deviations are very small in Figs. 1 and 2 even at high loadings, due to the use of the EEM.

Further insight on the transition rate behavior can be obtained by examining the area and volume contributions independently. Figure 6.3 shows the values of the area and volume

integrals as a function of N_A for three values of N_B. Note that the integral values grow very quickly as either N_A or N_B increases, because each molecule in the system carries one factor of α-cage volume (1165.8 Å^3). For example, for N_A =1 and N_B =6, the volume integral is on the order of $V^7 \sim 10^{21}$ Å^3. Although the general order of magnitude of the integrals is set by the total number of molecules, the important physics is captured in the Boltzmann factor integrand, $\exp(-\beta U)$, which determines the shape of the curves in Fig. 6.3. There are three main points to note about these curves: (1) for a given N_B, the volume curves lie above the area curves, (2) the slope of each curve decreases with increasing N_A, and (3) for a given N_B, this decrease in slope is greater for the volume integral than the area integral, causing the two curves to become closer at higher N_A.

These observations can be understood in the following way. The volume integrals tend to have higher values than the corresponding area integrals for two reasons. First, the volume integrals contain an extra factor of cage length (~ 10 Å). Second, the molecule constrained to the dividing surface in an area integral typically has a higher potential energy than its counterpart in the volume integral, so the average value of the Boltzmann factor is lower for the area integral. This energy effect becomes less important at higher loadings, as will be discussed momentarily. The slope of each curve decreases with increasing N_A because of entropic effects; there are more "overlap" configurations in the integrals at higher N_A, and the average value of the Boltzmann factor decreases. The magnitude of this decrease in slope is slightly smaller for the area integrals because one of the molecules is confined to the surface, leaving more free space in the cage. Because of this difference in slope, the area and volume curves for a given N_B approach each other at higher N_A; in principle, the curves could cross, although this was not observed for the loadings studied here. Note that this behavior leads directly to the increases in escape rate with N_A observed in Fig. 6.1.

Another issue of interest is how strongly the molecules in one cage are affected by the presence of molecules in the neighboring cage. To study this, we employed MC simulations with an empty A cage and different numbers of methane molecules in cage B. During these MC walks, Widom test insertions of a methane molecule were performed either in the empty A cage, or on the surface between the two cages. The average Boltzmann factors for the inserted molecule are shown in Fig. 6.4. Clearly, the test insertions in the volume were not affected by the loading in cage B, except very slightly at the highest loadings. This is very

interesting because it indicates a high level of screening of inter-cage adsorbate-adsorbate interactions by the zeolite atoms, which in turn suggests that a "cage-pairwise" additivity of the free energy will be quite accurate for these model systems. The Boltzmann factors for the test insertions on the surface showed a non-monotonic behavior similar to that seen in Fig. 6.2. There is an initial increase due to favorable energetic interactions with the molecules in B, but crowding in the B cage eventually leads to less favorable energetic interactions and a consequent decrease in the Boltzmann factor. The results in Fig. 6.4 suggest that focusing on one pair of cages at a time will be sufficient in this model system; other nearby cages, not directly involved in the hopping event, will not perturb that event significantly.

Finally, we note that the results and conclusions reported here are based on TST rate constants that have not been dynamically corrected. That is, our rate constants assume no fast barrier recrossings. However, such recrossings may be important in our model system, especially at higher loadings in cage B. Calculations of dynamical correction factors are underway and will be presented in a future paper.

6.5. CONCLUSIONS

Transition rates of molecules between adjacent zeolite cages at arbitrary loadings were calculated using an approximate multidimensional TST approach. An extended ensemble method within a nested integral scheme was used to calculate the partition functions of interest. This proved to be an efficient combination, producing low standard deviations in the rate constants even at very high loadings. The rate constants increased sharply with the number of molecules in the original cage but exhibited a weaker, non-monotonic dependence on the loading in the destination cage. These trends were explained in terms of the behavior of the individual area and volume integrals, based on entropic and energetic arguments. Furthermore, our results indicated that a "cage-pairwise" additivity of free energy is a good approximation in our model system, which should greatly simplify future analysis.

Work is in progress to calculate dynamical correction factors to the transition-state theory rate constants. The corrected rate constants will then be used as input in a stochastic

dynamics simulation to obtain self-diffusivities as a function of loading. Future work will also examine cases where diffusion occurs under a concentration gradient across the zeolite lattice.

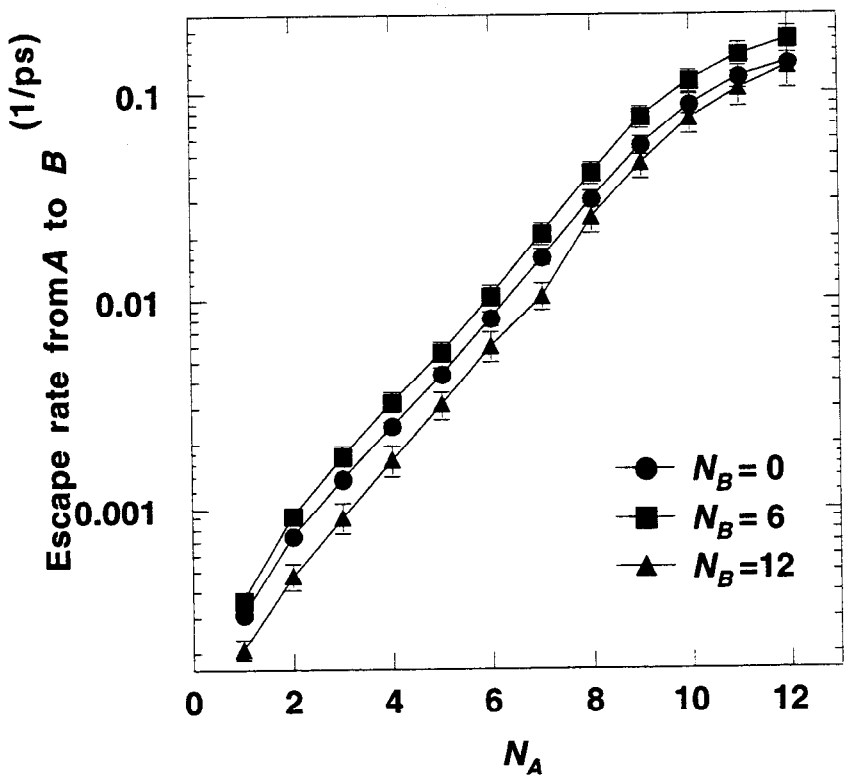

FIG 1. Tunca and Ford

Figure 6.1

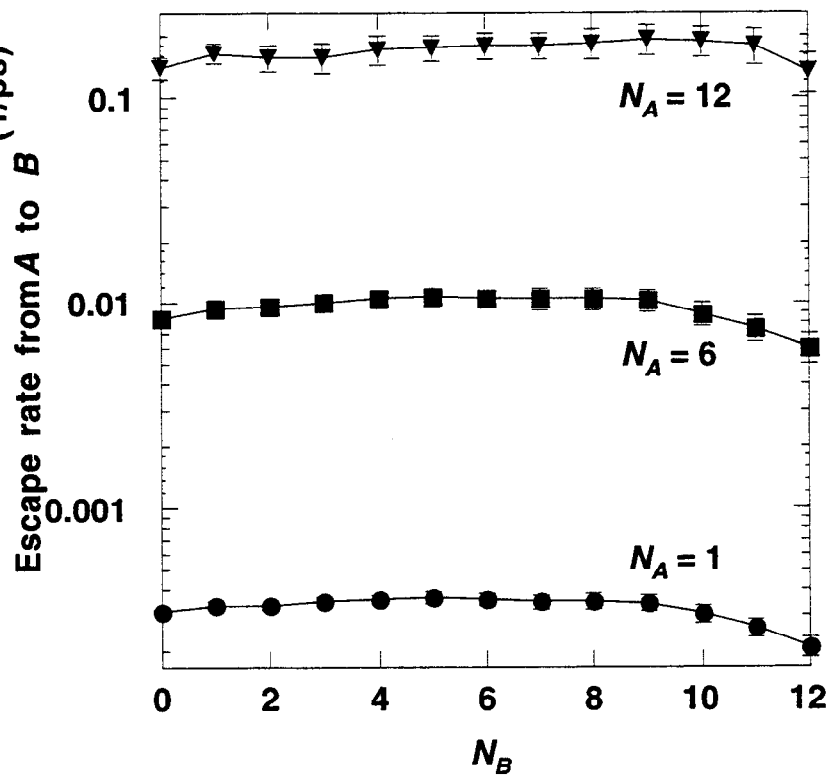

FIG 2. Tunca and Ford

Figure 6.2

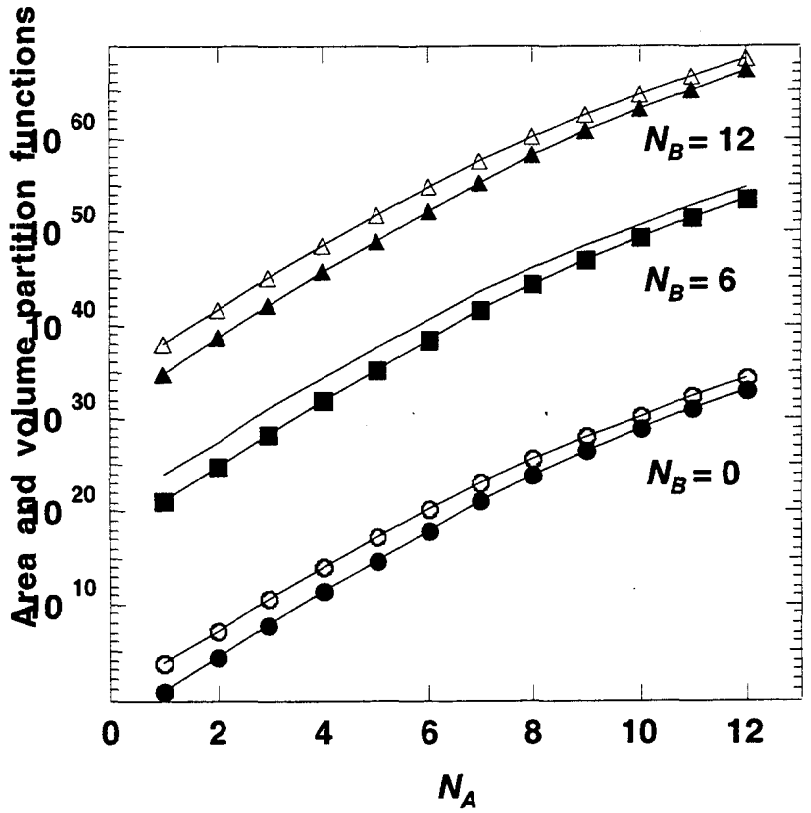

FIG 3. Tunca and Ford

Figure 6.3

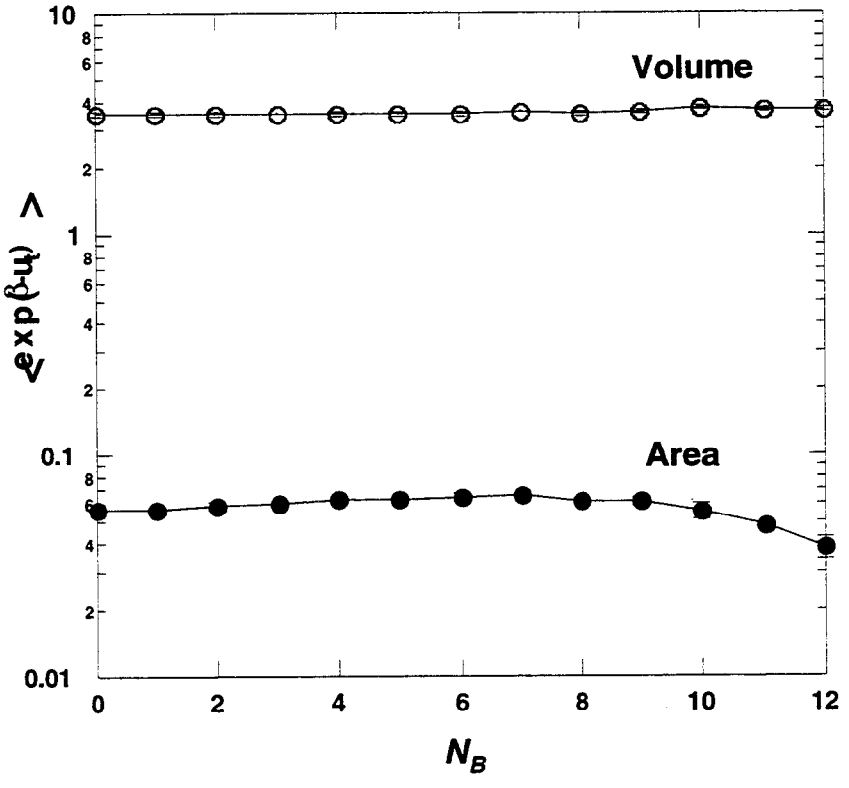

FIG 4. Tunca and Ford

Figure 6.4

Chapter 6 REFERENCES

1 C. Tunca and D. M. Ford, *J. Chem. Phys.* **111,** 2751-2760 (1999).

2 S. M. Auerbach, *Int. Rev. Phys. Chem.* **19,** 155-198 (2000).

3 E. M. Sevick, A. T. Bell, and D. N. Theodorou, *J. Chem. Phys.* **98,** 3196-3212 (1993).

4 G. H. Vineyard, *J. Phys. Chem. Solids* **3,** 121-127 (1957).

5 A. F. Voter and J. D. Doll, *J. Chem. Phys.* **82,** 80-92 (1985).

6 F. Jousse and S. M. Auerbach, *J. Chem. Phys.* **107,** 9629-9639 (1997).

7 R. D. Kaminsky, *Mol. Phys.* **84,** 69-88 (1995).

8 B. Widom, *J. Chem. Phys.* **39,** 2808-2812 (1963).

9 A. P. Lyubartsev, A. A. Martsinovski, S. V. Shevkunov, and P. N. Vorontsov-Velyaminov, *J. Chem. Phys.* **96,** 1776-1783 (1992).

10 A. P. Lyubartsev, A. Laaksonen, and P. N. Vorontsov-Velyaminov, *Mol. Phys.* **82,** 455-471 (1994).

11 P. Attard, *J. Chem. Phys.* **98,** 2225-2231 (1993).

12 N. B. Wilding and M. Muller, *J. Chem. Phys.* **101,** 4324-4330 (1994).

13 R. D. Kaminsky, *J. Chem. Phys.* **101,** 4986-4994 (1994).

14 F. A. Escobedo and J. J. de Pablo, *J. Chem. Phys.* **103,** 2703-2710 (1995).

15 D. A. Kofke and P. T. Cummings, *Mol. Phys.* **92,** 973-996 (1997).

16 J. J. de Pablo, Q. Yan, and F. A. Escobedo, *Annu. Rev. Phys. Chem.* **50,** 377-411 (1999).

17 A. A. Khare and G. C. Rutledge, *J. Chem. Phys.* **110,** 3063-3069 (1999).

18 R. L. June, A. T. Bell, and D. N. Theodorou, *J. Phys. Chem.* **95,** 8866-8878 (1991).

19 M. P. Allen and D. J. Tildesley, *Computer Simulation of Liquids* (Clarendon Press, Oxford, 1987).

7. Achievements

The most significant achievements in our LDRD were the following:

1) determined yield stress as a function of size scale

2) distinguish pertinent parameters influence on mechanical state with respect to each other (strain rate, temperature, crystal orientation, specimen size, deformation path)

3) developed mechanistic model to capture size scale, strain rate, and orientation effects.

4) explored the use of accelerated molecular dynamics methods to solve materials problems.

5) used first-principles nudged elastic band method to calculate activation barriers for complex materials process and verified calculations by comparison with experiment.

6) developed mesoscale model of grain boundary defaceting phase transition.

7) developed a parallel code for locating 3-D cavities transition states in amorphous materials

8) determined that for oxygen/nitrogen transport, entropic selectivity is much weaker in polymeric materials than in nanoporous solids.

9) developed an accurate and efficient transition state theory approach to transport in zeolites at non-zero loading

Appendix A: **Publications Resulting from this LDRD**

1. Horstemeyer, M.F. and Baskes, M.I., "High Strain Rate Single Crystal Atomistic Simulations," International Conf. On Plasticity, ed. A. Khan, Cancun, Mexico 1999.

2. Somerday, B.P, Pattillo, P.D., Horstemeyer, M.F., and Baskes, M.I., "Atomistic Modeling of Void Growth and Coalescence in Ni+H," MRS Conf, Boston, 1999.

3. Horstemeyer, M.F., Baskes, M.I., "Strain Tensors at the Atomic Scale," MRS, Boston, 1999.

4. Horstemeyer, M.F. and Baskes, M.I., "Atomistic Finite Deformation Simulations: A Discussion on Length Scale Effects in Relation to Mechanical Stresses," JEMT, ASME, Vol. 121, p. 114, 1998.

5 Horstemeyer, M.F. Baskes, M.I., Hughes, D.A., and Godfrey, A. "Orientation Effects on the Stress State of Molecular Dynamics Large Deformation Simulations," accepted in Int. J. Plasticity

6. Horstemeyer, M.F., Philliber, J., and Baskes, M.I., "Large Strain Molecular Dynamics and Finite Element Simulations of Fixed-End Simple Shear," in MSMSE.

7. M.F. Horstemeyer, J. Lim, W.Y. Lu, D.A. Mosher, M.I. Baskes, "Torsion/Simple Shear of Single Crystal Copper," submitted to JEMT.

8. M. F. Horstemeyer, M. I. Baskes, S. J. Plimpton, "Length Scale and Time Scale Effects on the Plastic Flow of Metals," submitted to Acta Met

9. J. C. Hamilton, M. R. Sorensen, A. F. Voter, "Compact Surface-Cluster Diffusion by Concerted Rotation and Translation," Phys. Rev. B. 61, R5125, 2000.

10. J. C. Hamilton, A. F. Voter, "Failure of 1D models for Ir island diffusion on Ir(111)," Phys. Rev. Lett. 85,1580, 2000.

11 I. Daruka, J. C. Hamilton, "Grain Boundary De-faceting: A First Order Phase Transition by Atomic Shuffle," submitted to Phys. Rev. Lett.

12. P. S. Rallabandi, A. P. Thompson, D. M. Ford, "A molecular modeling study of entropic and energetic selectivities in air separation with glassy polymers", Macromolecules, 33, 3142 (2000).

13. C. Tunca and D. M. Ford, "A Transition State Theory Approach to Adsorbate Dynamics at Arbitrary Loadings", *J. Chem. Phys.* **111,** 2751-2760 (1999).

14. C. Tunca and D. M. Ford, "Modeling Cage-to-Cage Dynamics of Adsorbates at Arbitrary Loadings with Transition-State Theory",accepted in *J. Chem. Phys.*

DISTRIBUTION

1 Kenneth Gall
University of Colorado
Department of Mechanical Engineering
Campus Box 427
Boulder, CO 80309

1 George Johnson
Mechanical Engineering
University of California
Berkeley, CA 94720-1740

1 Bill Nix
Stanford University
Department of Materials Science & Engineering
Stanford, CA 94305

1 K.T. Ramesh
Johns Hopkins University
Department of Materials Science & Engineering
3499 N Charles St.
Balitmore, MD 21218

1 Richard Hoagland
Washington State University
Dept. of Mechanical and Materials Engineering
Pullman, WA 99164-2920

1 Mark Rashid
Department of Civil and Environmental Engineering
University of California at Davis
Davis, CA 95616-5294

1 Mohammed Zikry
Dept. of Mechanical and Aerospace Engineering
North Carolina State University
Raleigh, NC 27695-7910

1 A. Needleman
Brown University
Division of Engineering
Providence, RI 02912-9104

1 John Bassani
University of Pennsylvania
Dept. of Mechanical Engineering and Applied Mechanics
297 Towne Bldg.
Philadelphia, Pa 19104-6315

1 H. Gao
Dept. of Mechanical Engineering
Stanford University
Stanford, CA 94305

1 Arun Gokhale
School of Materials Sciences Engineering
Georgia Tech
Atlanta, Ga 30332-0405

1 Dave McDowell
GWW School of Mech. Engng.
Georgia Tech
Atlanta, Ga 30332-0405

1 Armand Beaudoin
Dept. of Mechanical and Industrial Engineering
University of Illinois at Urbana-Champaign
140 Mechanical Engineering Building, MC-244
1206 West Green Street
Urbana, IL 61801

1 W. K. Liu
Mechanical Engineering Dept.
Northwestern University
Evanston, IL 60208-3109

1 Sunil Saigal
Civil and Environmental Dept.
Carnegie Mellon University
Pittsburgh, Pa 15123-3890

1 Hussein Zbib
Mechanical and Materials Engineering
Washington State University
Pullman, WA 99164-2920

5 David M. Ford
Department of Chemical Engineering
Texas A&M University
College Station, TX 77843

5 Mike I. Baskes
MST-8, MS G755
Los Alamos National Laboratory
Los Alamos, NM 87545

1 MS 0316 S.S. Dosanjh, 9233
1 MS 0316 G.S. Heffelfinger, 9235
1 MS 0826 W.L. Hermina, 9113
1 MS 0847 H.S. Morgan, 9121
5 MS 1111 S.J. Plimpton, 9233
5 MS 1111 A. P. Thompson, 9235
1 MS 1111 H. P. Hjalmarson, 9235
1 MS 1111 M. G. Martin, 9235
1 MS 1111 M. J. Stevens, 9235
1 MS 1411 J. M. Philips, 1802
1 MS 1411 H.E. Fang, 1834
1 MS 1411 S.M. Foiles, 1834

1 MS 9001 M. E. John, 8000
Attn: R. C. Wayne, 2200, MS 9005
J. Vitko, 8100, MS 9004
W. J. McLean, 8300, MS 9054
D. R. Henson, 8400, MS 9007
P. N. Smith, 8500, MS 9002
K. E. Washington, 8900, MS 9003
1 MS 9221 C. M. Hartwig, 8510
1 MS 9405 T. M. Dyer, 8700
Attn: R. Q. Hwang, 8721, MS 9161
K. L. Wilson, 8722, MS 9402
J. C. F. Wang, 8723, MS 9403
G. J. Thomas, 8724, MS 9402
W. A. Kawahara, 8725, 9042
J. L. Handrock, 8727, 9042
M.W. Perra, 8728, 9042
1 MS 9161 D. L. Medlin, 8721
1 MS 9405 D. J. Bammann, 8726
1 MS 9161 E. P. Chen, 8726
10 MS 9161 J.C. Hamilton. 8723
1 MS 9405 B. Somerday, 8724

1	MS 9405	N. Moody, 8725
10	MS 9405	M. F. Horstemeyer, 8726
1	MS 9405	D. A. Hughes, 8726
1	MS 9405	R. E. Jones, 8726
1	MS 9161	P. A. Klein, 8726
1	MS 9161	J. Zimmerman, 8726
1	MS 9405	E. B. Marin, 8726
1	MS 9405	R. A. Regueiro, 8726
1	MS 9042	M. L. Chiesa, 8727
1	MS 9042	J. J. Dike, 8727
1	MS 9012	P. E. Nielan, 8920
1	MS 0188	D. Chavez, LDRD Office, 4001
1	MS 0899	Technical Library, 4916
1	MS 9021	Technical Communications Department, 8511/ Technical Library, MS 0899, 4916
1	MS 9021	Technical Communications Department, 8511 for DOE/OSTI
3	MS 9018	Central Technical Files, 8940-2

This page intentionally left blank